Using Poly(lactide) Crystallization to Probe Nanostructure Morphologies for Biomedical Applications

Liang Sun

Submitted for the degree of Doctor of Philosophy

Department of Chemistry

THE UNIVERSITY OF WARWICK

March 2015

For my dearest parents, Changfa Sun and Guirong Tan

Table of Contents

Acknowledgements

My sincere thanks goes to my supervisors, Professor Rachel O'Reilly and Professor Andrew Dove, not only for their invaluable guidance and advice during my PhD study but also for their support and encouragement. I feel very lucky to work with them in both well-organized research groups.

I would like to thank all of the group members from both groups for their collaborations, especially Dr. Nikos Petzetakis for his kind help at the begginning of my PhD; Dr. Anaïs Pitto-Barry, Dr. Helen Willcock, Dr. Mathew Robin, Yan Kang and Dafni Moatsou for their help and precious advice and discussions during my PhD.

A big thank you goes to my parents, Changfa Sun and Guirong Tan, not only for their financial support of my PhD study but also for their continuous caring and love.

A special thank you goes to my friends, Xionghe Jin, Zhengmin Huang, Jinshuo Zhang, Limin Jin, Yang Li, Linjie Quan, Guohui Zhang, Xiyan Tong, Mi Yi, Yufei Cao, Liping Zhang, Shuai Hou, Juan Wei, Changhui Chen, Haojia Chen, Xingjie Wei; my roommates Ning Jia, Xiaofan Zhang, Yi Tian, Wei Xing, Yuhan Cai, Zedong Hu, Odette Toloza and those from other research groups in the Department of Chemistry in University of Warwick, Yunhua Chen, Muxiu Li and Chongyu Zhu.

Declaration of authorship

This thesis is submitted to the University of Warwick to fulfil the requirements of the degree of Doctor of Philosophy. Unless otherwise stated, the work described in this thesis was carried out by the author from October 2011 to March 2015. Any experiments or data analysis carried out by persons other than the author were clearly stated in each chapter.

List of publications

1. Tuning the Size of Cylindrical Micelles from Poly(*L*-Lactide)-*b*-Poly(Acrylic Acid) Diblock Copolymers based on Crystallization-Driven Self-Assembly, L. Sun, N. Petzetakis, A. Pitto-Barry, T. Schiller, N. Kirby, D. Keddie, B. Boyd, R.K. O'Reilly, A.P. Dove, ***Macromolecules***, 2013, 46, 9074–9082. (Chapter 2)

2. Structural Reorganization of Cylindrical Nanoparticles Triggered by Polylactide Stereocomplexation, L. Sun, A. Pitto-Barry, N. Kirby, T. Schiller, A. Sanchez, M. Dyson, J. Sloan, N. Wilson, R.K. O'Reilly, and A.P. Dove, ***Nature Commun.***, 2014, 5:5746. (Chapter 3)

Summary

Chapter 1 gives the introduction of the main concepts and techniques throughout this thesis.

Chapter 2 describes the control over the dimensions of various poly(*L*-lactide)-*b*-poly(acrylic acid) cylindrical micelles based on crystallization-driven self-assembly. Such change of the dimensions was realized by tuning the compositions of the precursor diblock copolymers. We have also explored the window to access cylindrical micelles as well as the relationship between poly(*L*-lactide) core block and crystallinity of resultant cylindrical micelles.

In **Chapter 3**, we have studied the stereocomplexation between the crystalline-coil poly(*L*-lactide)-*b*-poly(acrylic acid) and poly(*D*-lactide)-*b*-poly(acrylic acid) diblock copolymers in an aqueous system. We have also observed an unexpected morphological transition from homochiral cylindrical micelles to stereocomplex spherical micelles which was proposed to follow a "unimer-exchange" mechanism.

Chapter 4 discusses the preparation of fluorescent dithiomaleimide and aminobromomaleimide labelled polymers and nanoparticles and compares their different fluorescent properties. The potential applications of these fluorescent materials as bioimaging contrast agents were also illustrated.

In **Chapter 5**, we have copolymerized an allyl-functionalized cyclic carbonate monomer with *L*-lactide in order to use the ally groups as versatile handles to modify the core domain of the resultant cylindrical micelles. Benzyl mercaptan was chemically attached to the cores of these cylindrical micelles using photo-initiated thiol-ene radical reactions, illustrating their potential applications as delivery vehicles.

Abbreviations

°C	degrees Celsius
$Đ_M$	molar-mass dispersity
λ	wavelength
δ	chemical shift
AIBN	azobisisobutyronitrile
ATRP	atom transfer radical polymerization
br	broad (^{1}H NMR)
CDSA	crystallization-driven self-assembly
cm^{-1}	wavenumber
CTA	chain transfer agent
CuAAC	copper-catalyzed azide-alkyne cycloaddition
d	doublet (^{1}H NMR)
Da	Daltons
DCM	dichloromethane
DCTB	trans-2-[3-(4-tert-butyl-phenyl)-2-methyl-2-propenylidene] malononitrile
D_h	hydrodynamic diameter
DLS	dynamic light scattering
DMA	*N*,*N*'-dimethylacylamide
DMF	*N*,*N*-dimethylformamide
DMSO	dimethyl sulfoxide
D_n	number-average diameter
DOSY	diffusion-ordered NMR spectroscopy

DP	degree of polymerization
DSC	differential scanning calorimetry
EDC	*N*-(3-dimethylaminopropyl)-*N'*-ethylcarbodiimide
eq.	equivalents
FT-IR	Fourier transform infrared
g	grams
h	hours
HEA	2-hydroxyehthyl acrylate
Hz	hertz
HR-MS	high resolution mass spectroscopy
J	coupling constant (^{1}H NMR)
kDa	kiloDaltons
LLA	*L*-Lactide
L_n	number-average length
L_w	weight-average length
m	meters / multiplet (^{1}H NMR)
MAC	5-methyl-5-allyloxycarbonyl-1,3-dioxan-2-one
MALDI-ToF	matrix assisted laser desorption/ionization time of flight
MHz	megahertz
min	minutes
mg	milligrams
mL	millilitres
mmol	millimoles
M_n	number-average molecular weight
M_w	weight-average molecular weight

mol	moles
NaTFA	sodium trifluoroacetate
nm	nanometers
NMP	nitroxide mediated polymerization
NMR	nuclear magnetic resonance
OEGA	poly(ethylene glycol) methyl ether acrylate
PAA	poly(acrylic acid)
PCL	poly(***ε***-caprolactone)
PLA	poly(lactide)
PLLA	poly(*L*-Lactide)
PD	polydispersity
PDLA	poly(*D*-lactide)
PMMA	poly(methyl methacrylate)
ppm	parts per million
PDMA	poly(dimethylacylamide)
PEG	poly(ethylene glycol)
PFS	poly(ferrocenyldimethylsilane)
PHEA	poly(2-hydroxyethyl acrylate)
PMAC	poly(5-methyl-5-allyloxycarbonyl-1,3-dioxan-2-one)
POEGA	poly(poly(ethylene glycol) methyl ether acrylate)
PS	poly(styrene)
PTHPA	poly(tetrahydropyran acrylate)
q	scattering vector (SAXS)
RAFT	reversible addition-fragmentation chain transfer
RI	refractive index

ROP	ring-opening polymerization
rt	room temperature
s	singlet (^{1}H NMR)
SAXS	small-angle X-ray scattering
SEC	size exclusion chromatography
t	triplet (^{1}H NMR)
TCSPC	time-correlated single-photon counting
TEA	triethylamine
TEGA	triethylene glycol methylether acrylate
TEM	transmission electron microscopy
TEMPO	(2,2,6,6-tetramethylpiperidin-1-yl)oxy
T_g	glass transition temperature
THF	tetrahydrofuran
THPA	tetrahydropyran acrylate
T_m	melting temperature
UV	ultraviolet
WAXD	wide-angle X-ray diffraction

Chapter 1. Introduction

1.1 Overview

This chapter describes a detailed background of concepts and methodologies used throughout this thesis. Firstly, living polymerization, reversible-deactivation radical polymerizations (especially reversible addition-fragmentation chain transfer polymerization) and the ring-opening polymerization of lactide are introduced. These polymerization techniques allow control over polymer synthesis and can be exploited to prepare amphiphilic polymers suitable for solution self-assembly of various nanoparticles. The special stereocomplexation phenomenon between poly(*L*-lactide) and poly(*D*-lactide) is also illustrated. The preparation of cylindrical micelles is discussed with particular focus given to the crystallization-driven self-assembly approach, which is the key concept in this thesis. Finally, the functionalization of nanoparticles is outlined to fulfil numerous applications.

1.2 Living polymerization

As defined by International Union of Pure and Applied Chemistry (IUPAC), a living polymerization is a chain growth polymerization from which both chain transfer and chain termination are absent.[1] A number of experimental criteria have been developed to identify whether a polymerization process is living:[2]

1. Polymerization proceeds until all of the monomer has been consumed and further addition of monomer results in continued polymerization.
2. A linear correlation between number average molecular weight (or number average degree of polymerization (DP)) and conversion should be observed.
3. The number of growing polymer chains and active centers is constant and independent of conversion.
4. The DP of the resultant polymers can be controlled by the ratio of monomer to initiator.
5. Polymers with narrow molecular weight distributions are produced.
6. Chain-end functionalized polymers can be prepared in a quantitative yield.
7. Block copolymers can be prepared *via* sequential addition of a second monomer.

The first living polymerization system was reported by Szwarc who used sodium naphthalenide as an initiator in an anionic polymerization of styrene in 1956.[3] However, this anionic system and other ionic polymerization systems require extremely demanding experimental conditions such as complete removal of oxygen and moisture from the reaction which has limited the accessibility of living ionic polymerizations. Therefore, alternative polymerization techniques such as reversible-deactivation radical

polymerizations have been developed to synthesize polymers with good control over molecular weight and molecular weight distribution.

1.3 Reversible-deactivation radical polymerization

Conventional free radical polymerization has been widely used in research and industry as it can be applied to a variety of monomers, it is tolerant to a range of functional groups and is a relatively simple and inexpensive technique to undertake. In a typical free radical polymerization, a monomer is first initiated by a radical initiator such as azobisisobutyronitrile (AIBN) to generate a reactive monomer radical. Then the successive addition of monomer to the radical chain end results in polymer chain growth. The termination of a free radical polymerization can occur by either recombination or disproportionation. However, there are several drawbacks to conventional free radical polymerizations. For example, the average life of a propagating chain in a free radical polymerization is only a few seconds and this short lifetime will result in difficulties for synthetic manipulation, chain end modification or the synthesis of block copolymers by adding a second monomer. Also, in conventional free radical polymerization initiation is much slower than propagation which means some polymer chains have reached high molecular weights while some are still being initiated.[4] The above disadvantages of free radical polymerization lead to uncontrolled polymer chain growth and further result in unpredictable molecular weights and broad molecular weight distributions.

To overcome the disadvantages of free radical polymerization, several reversible-deactivation radical polymerization techniques have been developed over the past few decades. These include nitroxide-mediated radical polymerization (NMP),[5] atom-transfer radical polymerization (ATRP),[6, 7] and reversible addition-fragmentation chain transfer (RAFT) polymerization.[8, 9] In a typical reversible-deactivation radical polymerization, as there is a rapid

equilibrium between active and dormant species, all polymer chains are given an equal opportunity to grow, enabling controlled polymerization.[4] Therefore, reversible-deactivation polymerization can generate polymers with well-defined architectures along with narrow dispersities, predictable degrees of polymerization and uniform chain compositions.[10]

NMP was the first reversible-deactivation radical polymerization technique to be developed.[5, 11] The NMP equilibrium is based on a principle in which the propagating species are reversibly captured by the free nitroxide radicals to form dormant alkoxyamine species (Scheme 1.1). When this equilibrium is shifted toward the dormant species, the concentration of the active species is low and chain termination is thus avoided. However, NMP often requires high polymerization temperatures (typically > 100 °C) and has shown limited control over methacrylate species.[12]

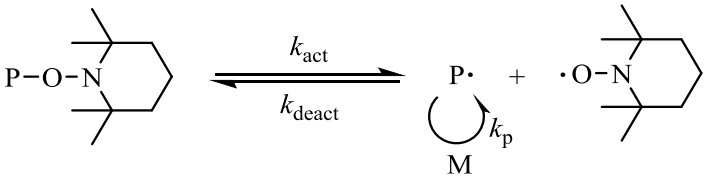

Scheme 1.1. A typical NMP equilibrium using (2,2,6,6-Tetramethylpiperidin-1-yl)oxy (TEMPO).

ATRP was reported simultaneously by Matyjaszewski *et al*.[6] and Sawamoto *et al*.[7] in 1995. ATRP can be mediated by various redox-active transition metal complexes such as Cu, Ru and Fe.[13] The typical ATRP mechanism using Cu(I)/ligand is given in Scheme 1.2. ATRP is based on the reversible end capping process of the propagating polymer chain with a halide leaving group.

To be more specific, the dormant species P-X reversibly reacts with Cu(I)X/ligand which is an activator to intermittently form the propagating radical (P•) and Cu(II)X_2/ligand which is a deactivator. The deactivator then reacts with the propagating radical to reform the dormant species and the activator. As the deactivation process is significantly favored in such an equilibrium, a low concentration of propagating radicals is guaranteed and therefore termination can be minimized and the polymerization is controlled. The structure of the ligand, the polymer/dormant species and the polymerization conditions affect the equilibrium constant and play decisive roles in an ATRP.[14]

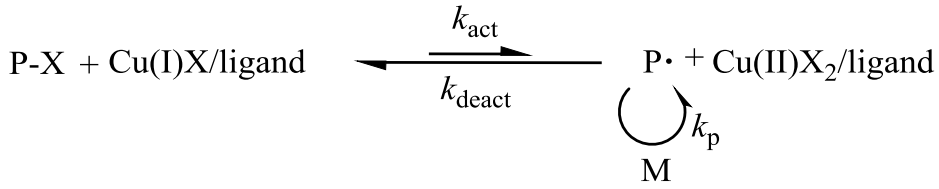

Scheme 1.2. A typical ATRP equilibrium.

1.4 Reversible addition-fragmentation chain transfer (RAFT) polymerization

Reversible addition-fragmentation chain transfer (RAFT) polymerization was reported in 1998 by a group at the Commonwealth Scientific and Industrial Research Organisation (CSIRO) in Australia.[8] In this work, different types of dithioesters were utilized as RAFT chain transfer agents (CTAs) to polymerize a number of monomers including styrene, methyl methacrylate and butyl acrylate in bulk, solution and emulsion respectively. At a similar time, Zard and co-workers reported macromolecular design *via* the interchange of xanthates (MADIX)[9] which follows an identical mechanism to RAFT polymerization, as reported by CSIRO. MADIX is thus considered as a specific type of RAFT polymerization using xanthates as RAFT chain transfer agents.

RAFT is thought to follow the mechanism shown in Scheme 1.3.[15] Firstly, monomer M is initiated by a radical initiator such as AIBN to form a propagating polymer chain P_n•. Then, P_n• undergoes a fast reversible chain transfer equilibrium with a CTA to release another radical R•. R• can re-initiate the monomer to give another propagating chain P_m• which subsequently enters the main chain equilibirum with P_n• *via* reaction with the thiocarbonyl end group. The fast exchange between dormant species, **4** and active species, **5** allows polymer chains to grow simultaneously and narrow molecular weight distributions to be obtained.

The R group of a RAFT CTA, **1** should be a good leaving group in comparison with the growing polymer chain during the reversible chain transfer process. The R group is also required to be a good reinitiating species toward the monomer used and also helps to stabilize the radical intermediate species, **3**,

although to a lesser extent than the Z group.[10] Figure 1.1 illustrates the choices of R groups of a RAFT CTA, starting from the most reactive species.[10]

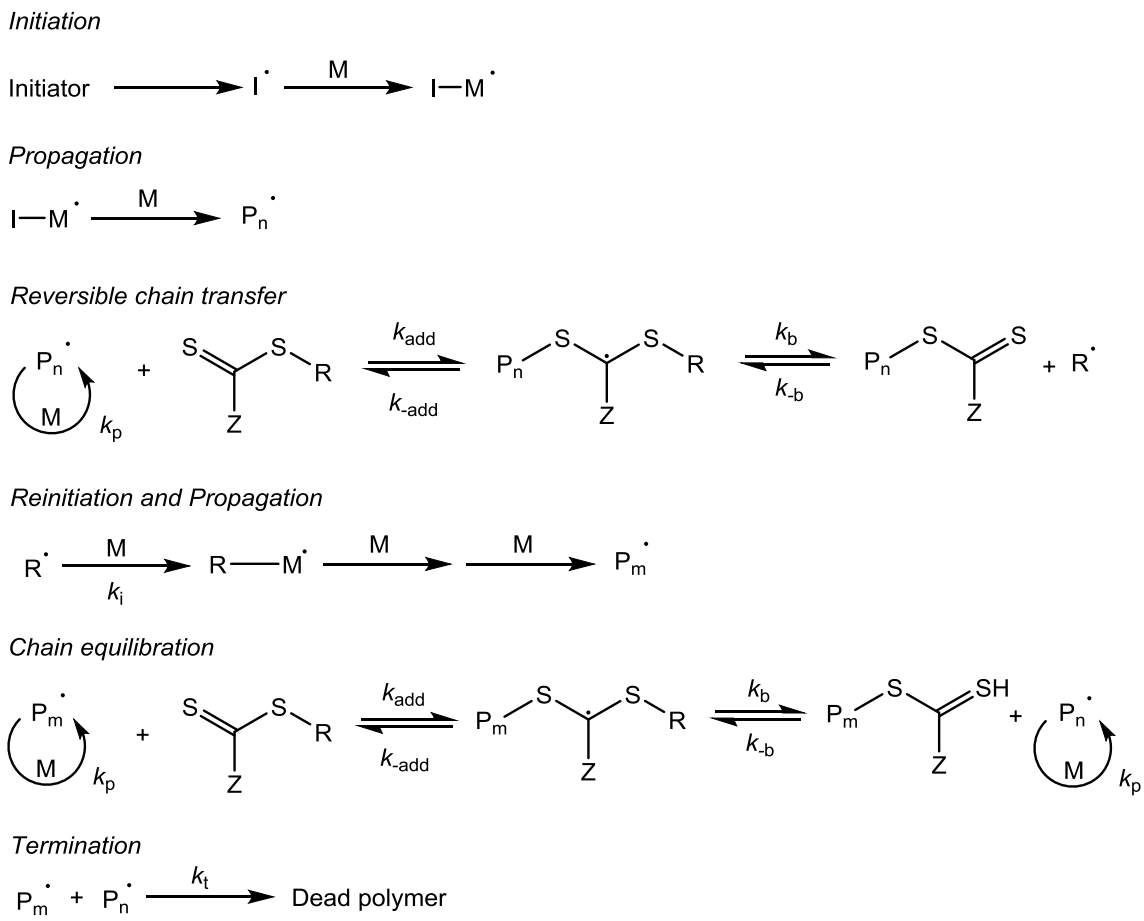

Scheme 1.3. The proposed mechanism of RAFT polymerization.[15]

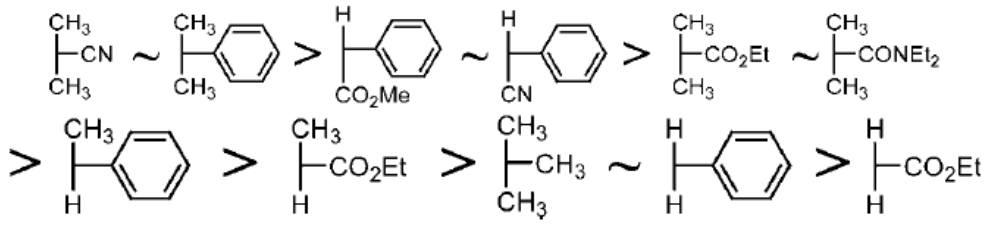

Figure 1.1. R groups of RAFT CTAs. Fragmentation rates decrease from top left to down right.[10]

The function of the Z group of a RAFT CTA, **1** is to stabilize the thiocarbonylthio radical intermediates **3** and **5**. Strong stabilizing Z groups will favour the formation of the intermediate and improve the reactivity of the C=S bond toward radical addition. However, if the intermediate species is too stable, fragmentation to generate the reinitiating radical R• and P_n• will be hindered. Therefore, the choice of Z group is highly important. Figure 1.2 illustrates the choices of Z groups of a RAFT CTA, starting from the most stabilizing species.[10] Based on the different types of Z group, RAFT CTAs can be subdivided into dithioester (C), trithiocarbonate (S), xanthate (O) and dithiocarbamate (N) (Figure 1.3).

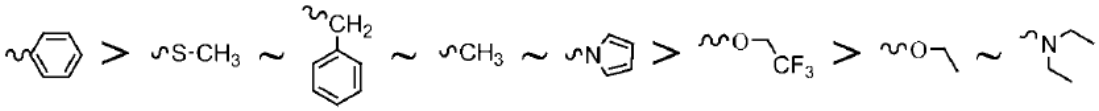

Figure 1.2. Z groups of RAFT CTAs. Fragmentation rates increase from left to right.[10]

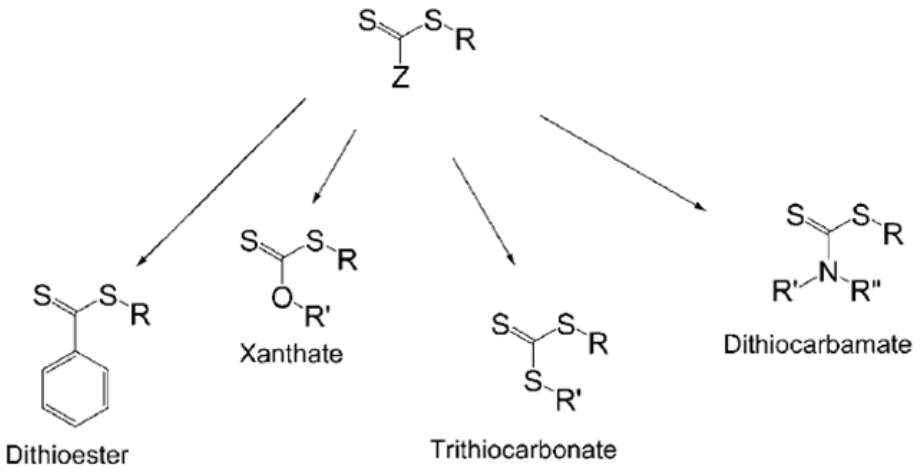

Figure 1.3. General structures of RAFT CTAs with different Z groups.

RAFT polymerization has shown many outstanding advantages. It controls the polymerizations of a variety of monomers in varying solvents including water. It is tolerant to a wide range of functional monomers and therefore allows the facile synthesis of polymer chains with different functionalities. Complicated polymer architectures such as block copolymers, graft copolymers, star-shaped polymers and hyperbranched polymers can be obtained by using RAFT polymerization. It is also compatible to many polymerization methods such as solution, bulk, emulsion, and dispersion.[16]

However, the RAFT polymerization technique still has a few drawbacks. For example, the residual RAFT agents in the polymer often result in colored materials which could be a problem for commercial applications. Several procedures have been developed for RAFT end group removal: radical-induced reduction (reaction with radical species like AIBN), aminolysis (reaction with primary or secondary amines), thermal elimination and hetero-Diels-Alder cycloadditions.[17]

1.5 Poly(lactide)s and controlled ring-opening polymerization of lactide

Poly(lactide) (PLA) is a biodegradable aliphatic poly(ester) which can be derived from renewable resources such as corn or sugarcane. It has attracted great interest given the successful application of PLA in the biomedical and pharmaceutical fields, in areas such as tissue engineering and drug delivery, due to the outstanding biodegradability, biocompatibility and low toxicity of PLA.[18-20] PLA can be synthesized by the ring-opening polymerization (ROP) of the corresponding cyclic ester monomers, *L*-lactide, *D*-lactide, *meso*-lactide or *rac*-lactide. Metal-based catalysts/initiators, such as tin octanoate ($Sn(Oct)_2$), are often utilized for the ROP of lactide.[21] $Sn(Oct)_2$ is an efficient active site precursor to yield PLAs and the ROP process was generally considered to follow a coordination-insertion mechanism.[22] However, using $Sn(Oct)_2$ catalyst during the ROP of lactide has shown to undergo undesirable transesterifications that led to broad molecular weight distributions.[23] Several metal-free catalysts,[24, 25] such like thiourea/(-)-sparteine co-catalyst system (Figure 1.4), offered an alternative route to realize narrow dispersities and precise architectures of PLAs.[26-28] It was found that by using the thiourea/(-)-sparteine co-catalyst system, the ROP of *L*-lactide was highly effective with 95% conversion of monomer achieved after only 2 h when the targeting degree of polymerization (DP) was 100.[27] The proposed mechanism of the thiourea/(-)-sparteine co-catalyst system for ROP is shown in Figure 1.4.[27] The carboxyl group of lactide is activated by the thiourea increasing its electrophilicity, while the initiating alcohol or propagating alcohol is activated by the tertiary amines of (-)-sparteine increasing the alcohols' nucleophilicity.[27] Thus, the metal-free catalyst system promotes the attack of the initiating or

propagating alcohol and the ring-opening of the lactide monomer. It was found that the supramolecular recognition between the thiourea and cyclic lactide ester is in preference to the linear *s-trans* ester so that the initiating or propagating alcohol would avoid attack of the already formed PLA and thus minimal epimerisation and transesterification can be guaranteed.[25, 27] However, as (-)-sparteine is no longer commercially available, a dibenzyl-functionalized bispidine organocatalyst (Figure 1.5) was recently developed to successfully replace (-)-sparteine by Dove and co-workers.[29] The use of the thiourea/dibenzyl bispidine co-catalyst system showed a similar polymerization rate with that of thiourea/(-)-sparteine during the ROP of lactide monomers.[29] Furthermore, the thiourea/dibenzyl bispidine co-catalyst system allowed control over the molecular weight of PLA with minimal transesterification and narrow dispersities.[29]

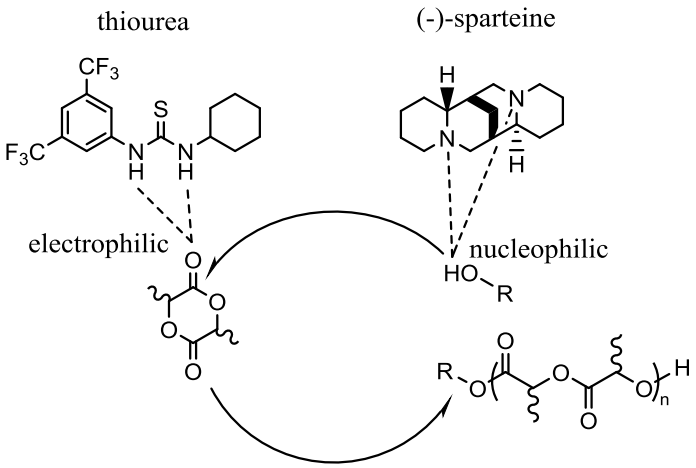

Figure 1.4. Proposed mechanism of ROP by using metal-free thiourea/(-)-sparteine co-catalyst system.[27]

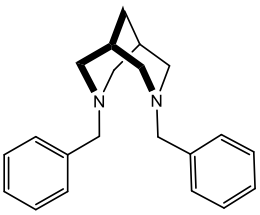

Figure 1.5. Chemical structure of dibenzyl bispidine organocatalyst which can be used to replace (-)-sparteine during the ROP of lactide.[29]

1.6 Stereocomplexation between PLLA and PDLA

The polymerization of pure enantiomeric monomer, *L*-lactide or *D*-lactide, leads to the formation of isotatic poly(*L*-lactide) (PLLA) or poly(*D*-lactide) (PDLA). When semi-crystalline left-handed poly(*L*-lactide) (PLLA) and right-handed poly(*D*-lactide) (PDLA) co-crystallize, stereocomplex formation between PLLA and PDLA occurs. By careful study on the X-ray diffraction patterns of the stereocomplex crystals, it was found that PLLA and PDLA polymer chains adopted 3_1 helical conformations in a triangular stereocomplex crystal (Figure 1.6).[30, 31] The stereocomplex PLA crystallites are stabilized by the CH_3•••O=C hydrogen-bonding interaction between the two opposite homochiral polymer chains, allowing a more compact conformation and more dense polymeric packing than observed for homochiral crystallites.[32]

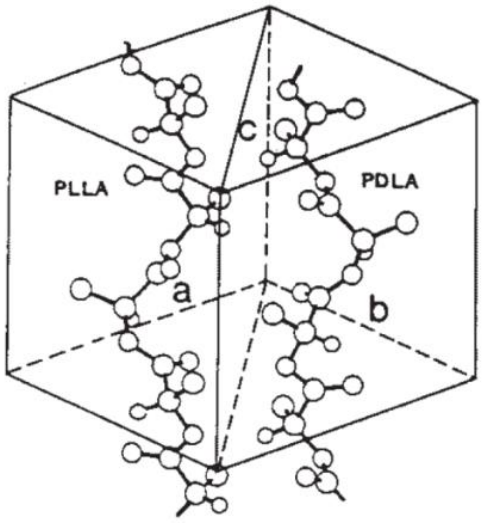

Figure 1.6. Crystal structure of PLA stereocomplexation.[33]

When compared with PLLA or PDLA homopolymer, the stereocomplex formation between PLLA and PDLA has imparted improved thermal and mechanical properties to various materials. For example, stereocomplex blends

of PLLA and PDLA were much more stable and showed a 50 °C higher melting temperature than that of PLLA or PDLA homopolymer as proved by differential scanning calorimetry (DSC) (Figure 1.7).[34] Also, higher values of tensile strength, Young's modulus and elongation at break were observed for the stereocomplex film materials during tensile tests.[35]

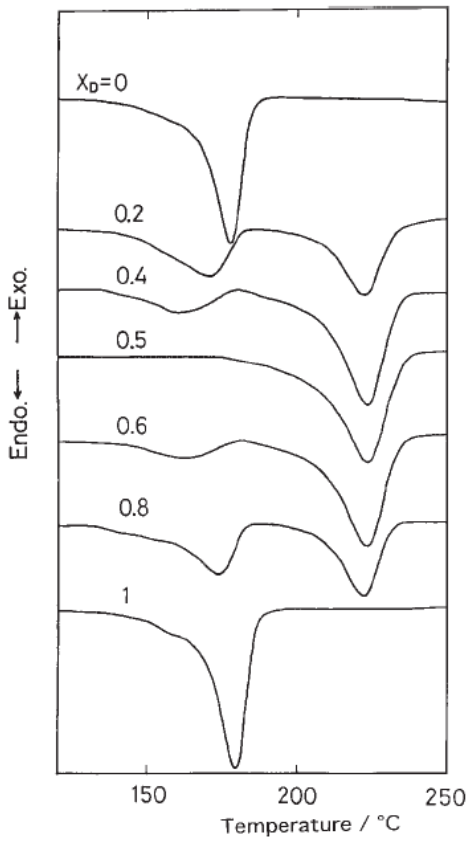

Figure 1.7. DSC thermograms of PLLA/PDLA blends with different compositions of PDLA that highlight that the melting temperature of stereocomplexation is much higher than that of PLLA or PDLA.[34]

The self-assembly of PLLA- and PDLA-containing block copolymers in solution can also induce stereocomplex formation in the resulting assemblies. For instance, the stereocomplex spherical micelles prepared from an equimolar

mixture of poly(*L*-lactide)-*b*-poly(ethylene glycol) (PLLA-*b*-PEG) and poly(*D*-lactide)-*b*-poly(ethylene glycol) (PDLA-*b*-PEG) diblock copolymers in water were reported to promote drug releasing kinetics with improved stability.[36] Stereocomplex micelles prepared from Y-shaped PEG-*b*-PLLA-*b*-PLLA and PEG-*b*-PDLA-*b*-PDLA miktoarm copolymers showed high loadings of paclitaxel.[37] Furthermore, the stereocomplexation of poly(*L*-lactide)-*b*-poly(*N*-isopropylacrylamide) (PLLA-*b*-PNIPAAM) and PDLA-*b*-PEG diblock copolymers were found to possess temperature-responsive behaviour which is suitable for potential delivery vehicles.[38] The stereocomplexation of PLLA and PDLA has also led to many interesting self-assembled morphologies both in solution and in bulk. For example, Hedrick and co-workers obtained patchy polymeric micelles from a mixture of PLLA-*b*-PNIPAM and PDLA-*b*-PEG (Figure 1.8A).[38] Hsiao and co-workers reported onion-like particles due to an imbalance in the surface stress from the stereocomplexation of poly(*L*-lactide)-*b*-poly(ethylene oxide) (PLLA-*b*-PEO) and poly(*D*-lactide)-*b*-poly(ethylene-*co*-1-butene) (PDLA-*b*-PEB), that possessed similar poly(lactide) block lengths but different PEO and PEB block lengths (Figure 1.8B).[39] Jing *et al*. also prepared flower-like particles from stereo multiblock copoly(*rac*-lactide)s by precipitation of the polymer solution into a bad solvent followed by nucleation of the polymer chains (Figure 1.8C).[40] Therefore, the study of stereocomplex formation between PLLA and PDLA is of great significance for the exploration of the resultant structures and furthermore their applications in the nanotechnology area.

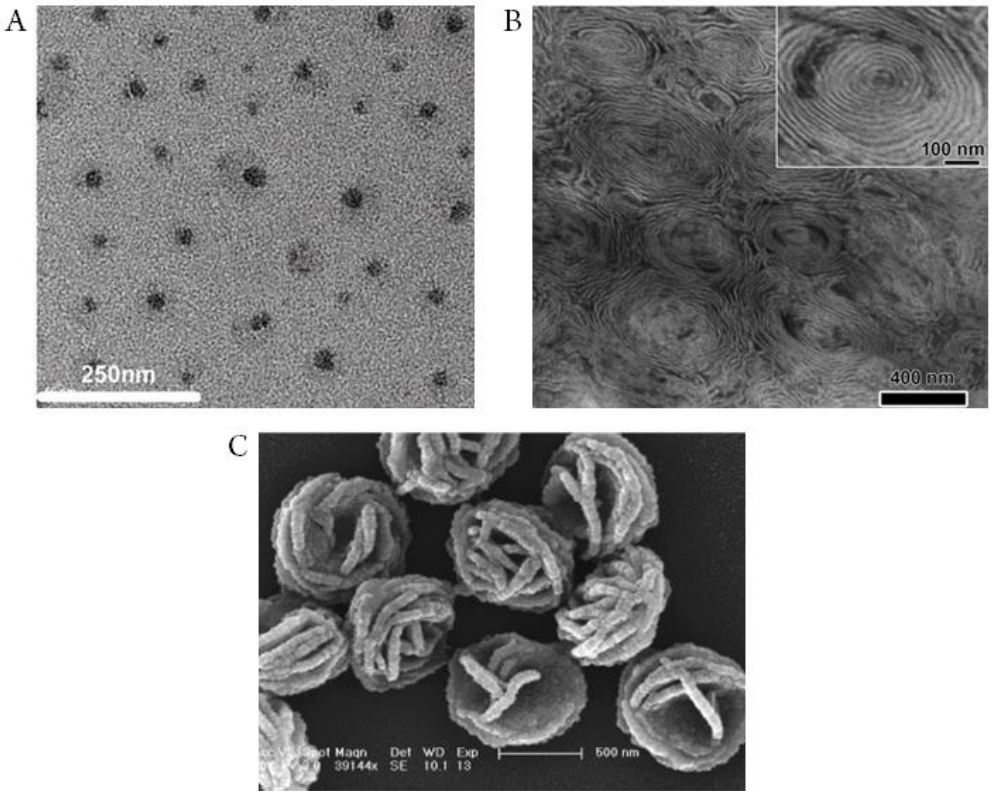

Figure 1.8. Patchy micelles (A, TEM image),[38] onion-like particles (B, TEM image)[39] and flower-shaped particles (C, SEM image)[40] obtained from the stereocomplexation of PLLA- and PDLA- containing polymers in solution or in bulk.

Wide-angle X-ray diffraction (WAXD) can be utilized to characterize the stereocomplexation between PLLA and PDLA. As a consequence of the distinct crystal structures exhibited by the homochiral crystals and stereocomplex crystals of PLA, the resultant Bragg peaks are also different: for the homochiral crystal, the main Bragg peaks are at 15, 17, and 19 2θ angle, which are comparable with the results for a homopolymer chain crystallized in a *pseudo*-orthorhombic unit cell. For the stereocomplex crystal, the most intense Bragg peaks are observed at 12, 21, and 24 2θ angle (Figure 1.9). These peaks are for the PLA stereocomplex crystallized in a triclinic unit cell.[33]

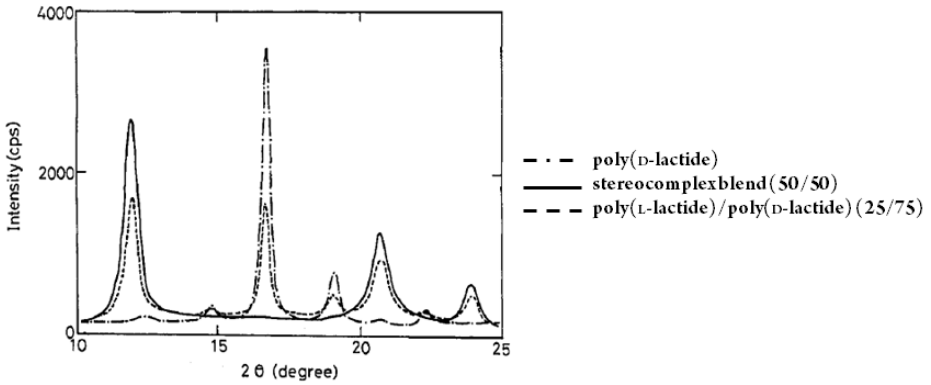

Figure 1.9. Wide-angle X-ray diffraction profiles for PDLA homopolymer and blended polymers: 50/50 PLLA/PDLA blend and 25/75 PLLA/PDLA blend.[41]

Fourier-transform infrared (FT-IR) spectroscopy is another important technique used to prove stereocomplex formation. It was found that the vibration of the carbonyl group of PLA shifted to a lower wavenumber during formation of the stereocomplex.[32] Such a wavenumber shift is attributed to the rearrangement of the PLA chains from a disordered state to an ordered one throughout stereocomplexation, induced by CH_3•••O=C hydrogen-bonding interactions.[42, 43]

1.7 Macromolecular self-assembly in solution

Amphiphilic block copolymers which contain a hydrophilic block and a hydrophobic block can self-assemble in water to form micelle structures. Such a self-assembly process is often driven by the solvophobic effect to minimize the unfavourable interactions between the hydrophobic core block and the solvent. Since Eisenberg and co-workers found that poly(styrene)-*b*-poly(acrylic acid) (PS-*b*-PAA) and polystyrene-*b*-poly(ethylene oxide) (PS-*b*-PEO) could form various self-assembled structures by tuning block lengths twenty years ago,[44-46] macromolecular self-assembly has received increasing attention.

In a coil-coil block copolymer system, the resultant self-assembly morphology depends on three factors: the interfacial tension between the core and the solvent, the stretching of the core-forming block and the interaction of the coronal block.[47] Any contributions such as changing the hydrophilic/hydrophobic ratio of the block copolymer composition[48] and self-assembly conditions (temperature,[49] solvent selectivity[50] and salt concentration[51]) that can affect these three factors will influence the resultant self-assembled structures. A dimensionless packing parameter p ($p = v/al$, where v is the volume of the hydrophobic block, a is the optimal area of interface and l is the length of the hydrophobic chain) can be calculated based on the knowledge of the three factors given above to predict the potential structure of the assemblies. Generally, when $p \leq 1/3$, spherical micelles are favoured; when $1/3 \leq p \leq 1/2$, cylindrical micelles are preferred; while one can obtain vesicular structures when $1/2 \leq p \leq 1$ (Figure 1.10).[52]

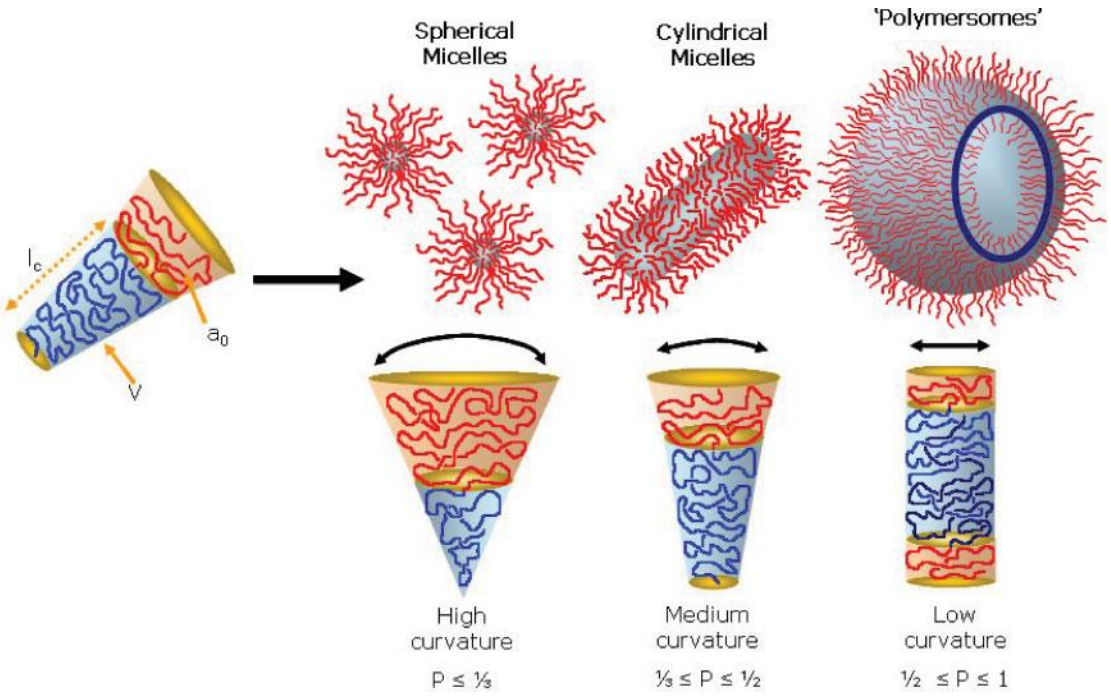

Figure 1.10. Schematic representation of different morphologies obtained from macromolecular self-assembly governed by the packing parameter, *p*.[52]

The most common micelle morphology obtained through macromolecular self-assembly is spherical micelles which possess a soluble shell shielding an insoluble spherical core. Spherical micelles have been intensively studied[44, 48, 53-55] and are often obtained when the weight fraction of the hydrophilic block is larger than that of the hydrophobic block.

Cylindrical micelles have an elongated morphology with a high aspect ratio (the dimension of the length is larger than that of diameter). More information of polymeric cylindrical micelles will be discussed in the next section.

Vesicular micelles are often obtained when the weight fraction of the hydrophilic block is lower than that of the hydrophobic block. Such a morphology possesses a bilayer-type structure with the shorter hydrophilic block located inside and longer hydrophilic block located outside the hydrophobic membrane surface (Figure 1.11).[56] When compared to lipid-based vesicles, polymeric

vesicles are more stable and robust[57] and can be given various properties by careful design of the precursor polymers.[58, 59] Also, the relatively large interior cavities of vesicles allow the encapsulation of water soluble guest molecules.

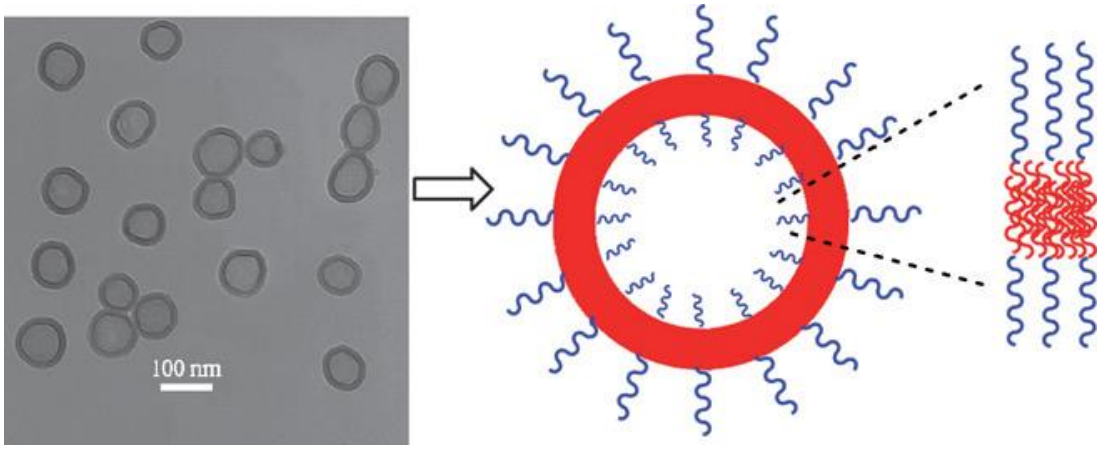

Figure 1.11. TEM image (left) showing the bilayer structure of polymeric vesicular micelles and a schematic representation (right) of their structure.[56]

Unlike a coil-coil block copolymer system, in a crystalline-coil copolymer system, the resultant self-assembly structure depends on the balance between crystallization of the core block and the stretching of the corona block.[60] As the free energy of crystallization is so large and accounts for the majority of the total free energy, the crystalline block has to adopt a folded structure consisting of a crystalline lamellar domain sandwiched by two stretching corona faces to minimize the total free energy.[61] However, if the stretching of the corona block is stronger, cylindrical micelles can be obtained.[62]

In addition to the three conventional morphologies described above, recently, a wide range of polymeric particles with interesting morphologies have been prepared through macromolecular self-assembly. These include Janus

particles,[63-65] multicompartment micelles,[66, 67] core- and shell-crosslinked particles[68, 69] and stimuli-responsive nanoobjects.[70, 71]

The nanostructures realized from polymeric amphiphiles possess various useful features: they can incorporate or encapsulate hydrophilic/hydrophobic compounds in their cores and coronas, they can be designed to be biocompatible and biodegradable and they can be devised to respond to internal or external stimuli.[72] Therefore, the exploration of polymeric materials for macromolecular self-assembly allows potential applications in drug delivery,[73] the preparation of electroactive materials[74] and organocatalytic nanoreactors[75, 76] as well as in the biotechnology arena.[77]

1.8 Polymeric cylindrical nanoparticles

Due to their long dimensions, polymeric cylindrical nanoparticles undergo a much longer *in vivo* circulation time[78] and altered cell internalization pathways[79] when compared to spherical particles and therefore exhibit great potential for biomedical applications. Cylindrical nanoparticles have also been successfully used for ion etching,[80] adding toughness to epoxy resin[81] and in the preparation of metal encapsulated nanoparticles.[82]

One approach to obtain cylindrical nanoparticles is using macromolecular self-assembly. Early in the 1990s, Bates *et al*. observed that poly(ethylene oxide)-*b*-poly(butadiene) diblock copolymers formed cylindrical micelles in water when the PEO weight fraction was 50%, using transmission electron microscopy (TEM) and small-angle neutron scattering (SANS) techniques.[83] Meanwhile, Wu and co-workers reported that poly(styrene)-*b*-poly(isoprene) spherical nanoparticles fused into cylindrical structures when they were extruded through a special membrane with numerous nanoscale pores.[84] Hedrick *et al.* incorporated urea functional groups into PLA-*b*-PEO polymer chains and they noticed that instead of spherical nanoparticles, these polymers self-assembled into cylindrical nanoparticles which were induced by the hydrogen-bonding interaction between the urea functional groups of polymer chains.[85] Polymerization-induced self-assembly was also utilized to prepare cylindrical nanoparticles.[86, 87] For example, Armes and co-workers have reported RAFT aqueous dispersion polymerization of 2-hydroxypropyl methacrylate (HPMA) monomer using a water-soluble poly(glycerol monomethacrylate) (PGMA) macro-CTA.[88] HPMA was found to be water miscible up to 13 *w*/*v*% at room temperature while it formed water-insoluble polymer and therefore, during the

RAFT aqueous dispersion polymerization, various self-assembly nanostructures (spheres, worms or vesicles) were obtained due to the formation of amphiphilic block copolymers with different DP of PHPMA hydrophobic block.[87] Cylindrical nanoparticles can also be obtained from bottle brush copolymers. For example, poly(4-(3-butenyl)styrene) side chains were grown from a PEO-*b*-PLA diblock backbone using RAFT polymerization by Rzayev *et al*. and after cross-linking of the poly(4-(3-butenyl)styrene) side chains, short cylindrical nanoparticles (L_n < 100 nm) were obtained.[89]

In addition to smooth and straight cylindrical morphologies, some other interesting structures of polymeric cylinders have been synthesized to date using both conventional and crystallization-driven self-assembly. For instance, segmented cylinders were obtained due to the phase separation between the fluorinated poly(butadiene) block and poly(4-*tert*-butoxystyrene) block in the core domain of cylindrical micelles (Figure 1.12A).[90] Helical cylinders were also realized using a similar method but with the addition of an organic diamine to complex with the PAA blocks of poly(acrylic acid)-*b*-poly(methacrylate)-*b*-poly(styrene) triblock copolymers (Figure 1.12B).[91] Furthermore, pointed-oval shaped cylinders were achieved *via* crystallization-driven self-assembly of poly(ferrocenyldimethylsilane)-*b*-poly(2-vinylpyridine) (PFS-*b*-P2VP) and poly(ferrocenyldimethylsilane)-*b*-poly(bis(trifluoroethoxy)-phosphazene) (PFS-*b*-PP) (Figure 1.12C).[92]

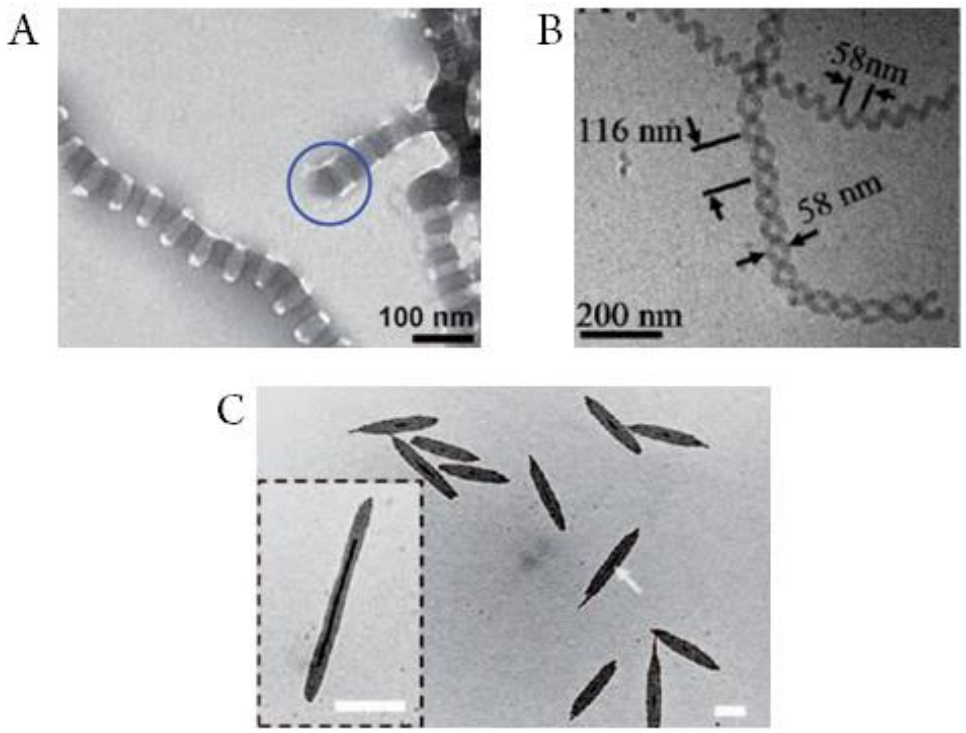

Figure 1.12. TEM images showing segmented cylinders[90] (A), helical cylinders[91] (B) and pointed-oval cylinders[92] (C).

1.9 Crystallization-driven self-assembly to prepare cylindrical nanoparticles

In the late 1990s and early 2000s, Manners, Winnik and co-workers reported that organometallic poly(ferrocenyldimethylsilane) (PFS) containing diblock copolymers, poly(ferrocenyldimethylsilane)-*b*-poly(dimethylsiloxane) (PFS-*b*-PDMS), can undergo a self-assembly process to yield cylindrical nanoparticles in *n*-hexane (a selective solvent for PFS).[93-95] The PFS-*b*-PDMS diblock copolymers used by these researchers were designed with a relatively short PFS core block and a relatively long PDMS corona block (block ratio > 1 : 6) and were expected to form spherical micelles instead.[93] Several subsequent studies have shown that the crystallization of the crystalline PFS core block is the driving force to realize such anisotropic cylindrical micelles rather than the solvophobic effect in the conventional macromolecular self-assembly. Furthermore, when a poly(ferrocenyldimethylsilane)-*b*-poly(dimethylsiloxane) (PFS-*b*-PDMS) block copolymer solution was heated above the T_m of the PFS block to destroy the crystallization ability, spherical micelles rather than cylindrical micelles were observed.[94] These researchers thus described such a self-assembly approach that used the crystallization process of crystalline PFS containing block copolymers to realize cylindrical micelles as crystallization-driven self-assembly (CDSA). By growing the same or other analogous PFS-based unimers on the two active ends of sonicated PFS- based cylindrical micelle nucleis, highly monodisperse cylinders (length dispersity < 1.05) with controlled lengths or multiblocks (Figure 1.13A) were realized *via* living CDSA.[96, 97] In addition to cylindrical structures, other complicated morphologies were also obtained by further exploiting the CDSA concept. For example, multi-armed cylindrical micelles were obtained by growing

poly(ferrocenyldimethylsilane)-*b*-poly(isoprene) (PFS-*b*-PI) unimers from PFS nanocrystals[98] (Figure 1.13B), while scarf-shaped architectures with cylindrical tassels were realized by growing PFS-*b*-PI unimers on PFS-*b*-PI plate-like substrates[99] (Figure 1.13C). Other groups have also explored CDSA using crystalline or semicrystalline poly(3-hexylthiophene),[100, 101] poly(acrylonitrile),[102] poly(ethylene)[103] and poly(*N*-decylglycine)[104] block containing copolymers and CDSA is becoming an increasingly powerful technique to access cylindrical micelles.

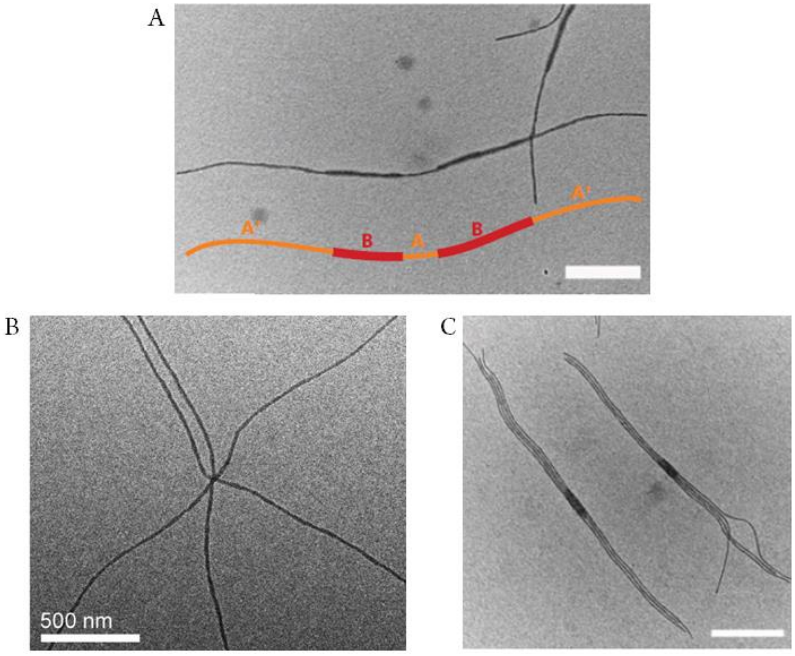

Figure 1.13. TEM images showing A) pentablock co-micelles,[99] B) multi-armed cylindrical micelles,[105] and C) scarf-shaped architectures[99] obtained from CDSA. Scale bar = 500 nm.

Inspired by the seminal work listed above, our group have focused on the use of semi-crystalline poly(L-lactide)-*b*-poly(acrylic acid) (PLLA-*b*-PAA) diblock copolymers to realize polymeric cylinders with a non-metallic core.[106, 107] The

diblock copolymers were synthesized by a combination of the ROP of *L*-lactide and the RAFT polymerization of tetrahydropyran acrylate (THPA). The diblock copolymers were designed with a large fraction of hydrophilic block to access a cylindrical morphology. Hydrolysis of PTHPA in mild acidic conditions whilst heating above the T_g of the lactide block yielded PLLA-*b*-PAA cylindrical micelles. Similar to other CDSA systems,[108] the process of the formation of PLLA-*b*-PAA cylinders followed a sphere-to-rod transition.[107] To be more specific, amphiphilic PLLA-*b*-PAA diblock copolymers formed spherical micelles first which underwent a crystallization process to yield crystalline micelle seeds above the T_g of the PLLA core block. The addition of PLLA-*b*-PAA unimers from the solution onto the two ends of these seeds was thought to cause the resultant cylinder growth. The sphere-to-rod transition was confirmed by TEM (Figure 1.14) and DLS analyses while the crystallization process of the core block during the CDSA was proven by WAXD analysis. The PLLA-*b*-PAA cylinders also showed a linear correlation between micelle length and assembly time whilst heated above T_g indicating a living character in their growth.[106] When using THF as an additive, a good solvent for both PLA and PAA blocks that will destroy the crystallinity of the cylinders, only spherical micelles were obtained emphasizing that crystallinity is an important driving force to induce micelle nucleation and cylinder growth.[107] More interestingly, when the PLLA-*b*-PAA cylinders were air dried, they underwent a structural reorganization process and core hollowed cylindrical structures were obtained, which could be loaded with hydrophobic dyes.[109] The core hollowing phenomenon was proposed to be induced by the hydrogen bonding interaction between the PLLA block and the PAA block. Overtime, this core hollowing effect was completely

erased when the hollow cylindrical micelles were redispersed in water. Instead of PAA, other hydrophilic corona blocks such as poly(4-acryloyl morpholine) (P4AM), poly(ethylene oxide) (PEO) and poly(*N*,*N*-dimethylacrylamide) (PDMA) were utilized to prepare cylindrical micelles, although a mixture of cylinders and spheres was obtained and the formation of cylinders was much slower in these cases.[110]

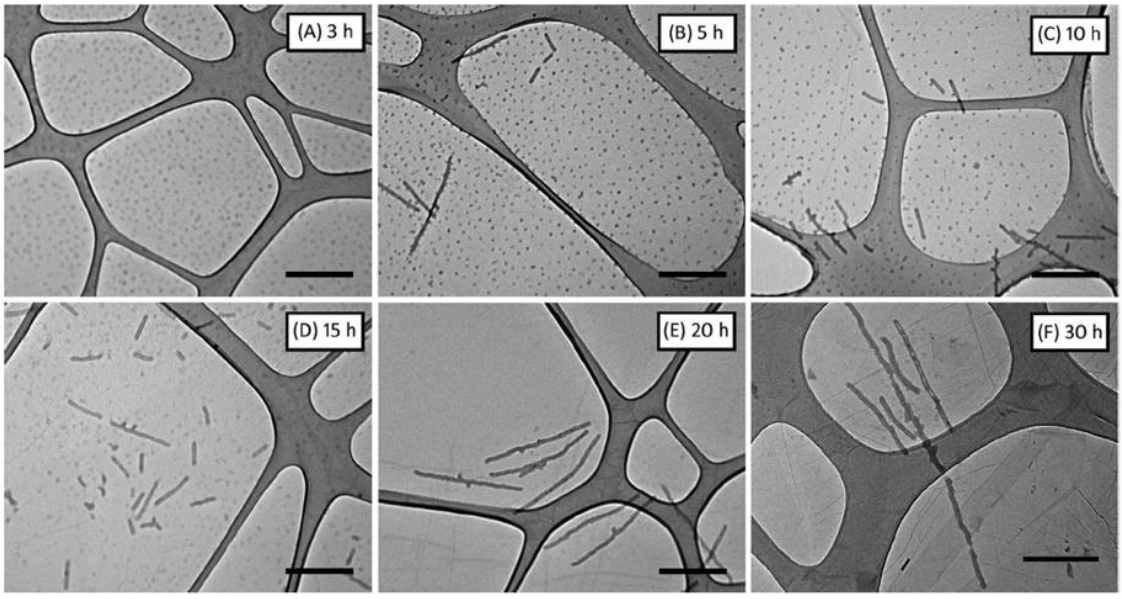

Figure 1.14. TEM images showing the sphere-to-rod transition during the CDSA of PLLA-*b*-PAA diblock copolymers.[107] Scale bar = 500 nm.

1.10 Functionalization of polymeric nanoparticles

To afford nanoparticles with different features and functions, chemical modification is often required. Functionalized nanoparticles can be achieved either by modification of the precursor amphiphilic polymers followed by self-assembly or by direct functionalization of the nanostructures. For the former route, it is more flexible to design a polymer with a specific target but this is time-consuming and requires multiple synthetic steps. In contrast, the post-assembly functionalization of micellar scaffolds is a faster and easier route as it avoids the synthesis and polymerization of new functional monomers and subsequent self-assembly.

A number of chemical modifications have been used to functionalize polymeric nanoparticles. Amidation modification is one of the most widely used methods. For example, Wooley, Welch and co-workers modified PS-*b*-PAA spherical micelles *via* reaction between the PAA shell block and PEG-NH_2 to prepare biocompatible nanostructures.[111] Amidation modification has also been used for cross-linking purposes.[112, 113] Click-chemistry is another important modification route to functionalize polymeric micelles. A variety of click-type reactions have been demonstrated so far. These include the Diels-Alder reaction,[114] thiol-ene reaction,[28, 115] and copper-catalyzed azide-alkyne cycloaddition (CuAAC) reaction.[116]

By using the above modification methods, functionalizations have been realized at different domains of the micellar scaffolds such as the core, shell, surface and core-shell interface to fulfil various functions. For example, our group functionalized both the core and shell of spherical micelles with coumarin and tetrazine functionalities by using the CuAAC reaction and tetrazine-norbornene

reaction respectively.[53] Monteiro *et al*. modified the surface of PNIPAM-*b*-PS cylindrical micelles with PEG by use of the CuAAC reaction.[117] In spite of the limited study on functionalization at the core-shell interface of micelles, our group have recently modified an amphiphilic poly(*dl*-lactide)-*b*-poly(triethylene glycol monomethyl ether acrylate) block copolymer with a fluorescent dithiomaleimide functional group incorporated between the two blocks which can self-assemble in water to yield spherical micelles with a fluorescent core-shell interface.[54]

1.11 Conclusions

In this chapter, living polymerization, reversible-deactivation radical polymerizations and the ring-opening polymerization of lactides, all of which can be used to synthesize well-defined polymers, were introduced. Then, the self-assembly of amphiphilic polymers in solution to obtain various nanostructures was outlined. Crystallization-driven self-assembly to synthesize cylindrical micelles, which is the key concept throughout this thesis, is specifically discussed. Stereocomplex formation between PLLA and PDLA and its application in self-assembly is also described. Finally, the functionalization of nanoparticles to fulfil various applications is detailed.

1.12 References

(1) Jenkins, A. D.; Kratochvíl, P.; Stepto, R. F. T.; Suter, U. W. *Pure Appl. Chem* **1996,** 68, 2287–2311.

(2) Quirk, R. P.; Lee, B. *Polym. Int.* **1992,** 27, 359-367.

(3) Szwarc, M. *Nature* **1956,** 178, 1168-1169.

(4) Braunecker, W. A.; Matyjaszewski, K. *Prog. Polym. Sci.* **2007,** 32, 93-146.

(5) Hawker, C. J. *J. Am. Chem. Soc.* **1994,** 116, 11185-11186.

(6) Wang, J.-S.; Matyjaszewski, K. *J. Am. Chem. Soc.* **1995,** 117, 5614-5615.

(7) Kato, M.; Kamigaito, M.; Sawamoto, M.; Higashimura, T. *Macromolecules* **1995,** 28, 1721-1723.

(8) Chiefari, J.; Chong, Y. K.; Ercole, F.; Krstina, J.; Jeffery, J.; Le, T. P. T.; Mayadunne, R. T. A.; Meijs, G. F.; Moad, C. L.; Moad, G.; Rizzardo, E.; Thang, S. H. *Macromolecules* **1998,** 31, 5559-5562.

(9) Corpart, P. C., D.; Biadatti, T.; Zard, S. Z.; Michelet, D. *PCT Int. Pat. Appl. WO 9858974,* **1998**.

(10) Perrier, S.; Takolpuckdee, P. *J. Polym. Sci., Part A: Polym. Chem.* **2005,** 43, 5347-5393.

(11) Georges, M. K.; Veregin, R. P. N.; Kazmaier, P. M.; Hamer, G. K. *Macromolecules* **1993,** 26, 2987-2988.

(12) Grubbs, R. B. *Polym. Rev.* **2011,** 51, 104-137.

(13) di Lena, F.; Matyjaszewski, K. *Prog. Polym. Sci.* **2010,** 35, 959-1021.

(14) Matyjaszewski, K. *Macromolecules* **2012,** 45, 4015-4039.

(15) Moad, G.; Rizzardo, E.; Thang, S. H. *Aust. J. Chem.* **2005,** 58, 379-410.

(16) Boyer, C.; Bulmus, V.; Davis, T. P.; Ladmiral, V.; Liu, J.; Perrier, S. *Chem. Rev.* **2009,** 109, 5402-5436.

(17) Willcock, H.; O'Reilly, R. K. *Polym. Chem.* **2010,** 1, 149-157.

(18) Rezwan, K.; Chen, Q. Z.; Blaker, J. J.; Boccaccini, A. R. *Biomaterials* **2006,** 27, 3413-3431.

(19) Feng, J.; Zhuo, R. X.; Zhang, X. Z. *Prog. Polym. Sci.* **2012,** 37, 211-236.

(20) Sun, H. L.; Guo, B. N.; Li, X. Q.; Cheng, R.; Meng, F. H.; Liu, H. Y.; Zhong, Z. Y. *Biomacromolecules* **2010,** 11, 848-854.

(21) Dechy-Cabaret, O.; Martin-Vaca, B.; Bourissou, D. *Chem. Rev.* **2004,** 104, 6147-6176.

(22) Ryner, M.; Stridsberg, K.; Albertsson, A.-C.; von Schenck, H.; Svensson, M. *Macromolecules* **2001,** 34, 3877-3881.

(23) Baran, J.; Duda, A.; Kowalski, A.; Szymanski, R.; Penczek, S. *Macromol. Symp.* **1997,** 123, 93-101.

(24) Dove, A. P. *Chem. Comm.* **2008**, 6446-6470.

(25) Dove, A. P. *ACS Macro Lett.* **2012,** 1, 1409-1412.

(26) Dove, A. P.; Pratt, R. C.; Lohmeijer, B. G. G.; Waymouth, R. M.; Hedrick, J. L. *J. Am. Chem. Soc.* **2005,** 127, 13798-13799.

(27) Pratt, R. C.; Lohmeijer, B. G. G.; Long, D. A.; Lundberg, P. N. P.; Dove, A. P.; Li, H. B.; Wade, C. G.; Waymouth, R. M.; Hedrick, J. L. *Macromolecules* **2006,** 39, 7863-7871.

(28) Tempelaar, S.; Mespouille, L.; Dubois, P.; Dove, A. P. *Macromolecules* **2011,** 44, 2084-2091.

(29) Todd, R.; Rubio, G.; Hall, D. J.; Tempelaar, S.; Dove, A. P. *Chem. Sci.* **2013,** 4, 1092-1097.

(30) Brizzolara, D.; Cantow, H.-J.; Diederichs, K.; Keller, E.; Domb, A. J. *Macromolecules* **1996,** 29, 191-197.

(31) Fukushima, K.; Kimura, Y. *Polym. Int.* **2006,** 55, 626-642.

(32) Zhang, J.; Sato, H.; Tsuji, H.; Noda, I.; Ozaki, Y. *Macromolecules* **2005,** 38, 1822-1828.

(33) Tsuji, H. *Macromol. Biosci.* **2005,** 5, 569-597.

(34) Tsuji, H.; Hyon, S. H.; Ikada, Y. *Macromolecules* **1991,** 24, 5657-5662.

(35) Tsuji, H.; Ikada, Y. *Polymer* **1999,** 40, 6699-6708.

(36) Kang, N.; Perron, M. E.; Prud'homme, R. E.; Zhang, Y. B.; Gaucher, G.; Leroux, J. C. *Nano Lett.* **2005,** 5, 315-319.

(37) Nederberg, F.; Appel, E.; Tan, J. P. K.; Kim, S. H.; Fukushima, K.; Sly, J.; Miller, R. D.; Waymouth, R. M.; Yang, Y. Y.; Hedrick, J. L. *Biomacromolecules* **2009,** 10, 1460-1468.

(38) Kim, S. H.; Tan, J. P. K.; Nederberg, F.; Fukushima, K.; Yang, Y. Y.; Waymouth, R. M.; Hedrick, J. L. *Macromolecules* **2009,** 42, 25-29.

(39) Sun, L.; Zhu, L.; Rong, L. X.; Hsiao, B. S. *Angew. Chem. Int. Ed.* **2006,** 45, 7373-7376.

(40) Hu, J. L.; Tang, Z. H.; Qiu, X. Y.; Pang, X.; Yang, Y. K.; Chen, X. S.; Jing, X. B. *Biomacromolecules* **2005,** 6, 2843-2850.

(41) Ikada, Y.; Jamshidi, K.; Tsuji, H.; Hyon, S. H. *Macromolecules* **1987,** 20, 904-906.

(42) Portinha, D.; Boue, F.; Bouteiller, L.; Carrot, G.; Chassenieux, C.; Pensec, S.; Reiter, G. *Macromolecules* **2007,** 40, 4037-4042.

(43) Portinha, D.; Bouteiller, L.; Pensec, S.; Richez, A.; Chassenieux, C. *Macromolecules* **2004,** 37, 3401-3406.

(44) Zhang, L. F.; Eisenberg, A. *Science* **1995,** 268, 1728-1731.

(45) Yu, K.; Eisenberg, A. *Macromolecules* **1996,** 29, 6359-6361.

(46) Yu, K.; Zhang, L. F.; Eisenberg, A. *Langmuir* **1996,** 12, 5980-5984.

(47) Zhang, L. F.; Eisenberg, A. *Polym. Advan. Technol.* **1998,** 9, 677-699.

(48) He, Y. Y.; Li, Z. B.; Simone, P.; Lodge, T. P. *J. Am. Chem. Soc.* **2006,** 128, 2745-2750.

(49) Rank, A.; Hauschild, S.; Forster, S.; Schubert, R. *Langmuir* **2009,** 25, 1337-1344.

(50) Mihut, A. M.; Drechsler, M.; Moller, M.; Ballauff, M. *Macromol. Rapid Commun.* **2010,** 31, 449-453.

(51) He, W. N.; Xu, J. T.; Du, B. Y.; Fan, Z. Q.; Wang, X. S. *Macromol. Chem. Phys.* **2010,** 211, 1909-1916.

(52) Blanazs, A.; Armes, S. P.; Ryan, A. J. *Macromol. Rapid Commun.* **2009,** 30, 267-277.

(53) Hansell, C. F.; O'Reilly, R. K. *ACS Macro Lett.* **2012,** 1, 896-901.

(54) Robin, M. P.; Mabire, A. B.; Damborsky, J. C.; Thom, E. S.; Winzer-Serhan, U. H.; Raymond, J. E.; O'Reilly, R. K. *J. Am. Chem. Soc.* **2013,** 135, 9518-9524.

(55) Zhang, L. F.; Eisenberg, A. *J. Am. Chem. Soc.* **1996,** 118, 3168-3181.

(56) Du, J. Z.; O'Reilly, R. K. *Soft Matter* **2009,** 5, 3544-3561.

(57) Discher, B. M.; Won, Y.-Y.; Ege, D. S.; Lee, J. C.-M.; Bates, F. S.; Discher, D. E.; Hammer, D. A. *Science* **1999,** 284, 1143-1146.

(58) Du, J. Z.; Armes, S. P. *J. Am. Chem. Soc.* **2005,** 127, 12800-12801.

(59) Du, J. Z.; Tang, Y. P.; Lewis, A. L.; Armes, S. P. *J. Am. Chem. Soc.* **2005,** 127, 17982-17983.

(60) Vilgis, T.; Halperin, A. *Macromolecules* **1991,** 24, 2090-2095.

(61) Hamley, I. W. *Adv. Polym. Sci.* **1999,** 148, 113.

(62) Cao, L.; Manners, I.; Winnik, M. A. *Macromolecules* **2002,** 35, 8258-8260.

(63) Moughton, A. O.; Hillmyer, M. A.; Lodge, T. P. *Macromolecules* **2012,** 45, 2-19.

(64) Du, J. Z.; O'Reilly, R. K. *Chem. Soc. Rev.* **2011,** 40, 2402-2416.

(65) Walther, A.; Muller, A. H. E. *Soft Matter* **2008,** 4, 663-668.

(66) Pochan, D. J.; Zhu, J. H.; Zhang, K.; Wooley, K. L.; Miesch, C.; Emrick, T. *Soft Matter* **2011,** 7, 2500-2506.

(67) Dupont, J.; Liu, G. *Soft Matter* **2010,** 6, 3654-3661.

(68) O'Reilly, R. K.; Joralemon, M. J.; Hawker, C. J.; Wooley, K. L. *New J. Chem.* **2007,** 31, 718-724.

(69) Moughton, A. O.; Stubenrauch, K.; O'Reilly, R. K. *Soft Matter* **2009,** 5, 2361-2370.

(70) Chen, W.; Meng, F. H.; Cheng, R.; Zhong, Z. Y. *J. Control. Release* **2010,** 142, 40-46.

(71) Ieong, N. S.; Brebis, K.; Daniel, L. E.; O'Reilly, R. K.; Gibson, M. I. *Chem. Comm.* **2011,** 47, 11627-11629.

(72) Giacomelli, C.; Schmidt, V.; Aissou, K.; Borsali, R. *Langmuir* **2010,** 26, 15734-15744.

(73) Lin, L. Y.; Lee, N. S.; Zhu, J. H.; Nystrom, A. M.; Pochan, D. J.; Dorshow, R. B.; Wooley, K. L. *J. Control. Release* **2011,** 152, 37-48.

(74) Nisisako, T.; Torii, T.; Takahashi, T.; Takizawa, Y. *Adv. Mater.* **2006,** 18, 1152-1156.

(75) Cotanda, P.; O'Reilly, R. K. *Chem. Comm.* **2012,** 48, 10280-10282.

(76) Cotanda, P.; Lu, A.; Patterson, J. P.; Petzetakis, N.; O'Reilly, R. K. *Macromolecules* **2012,** 45, 2377-2384.

(77) Choi, H. J.; Montemagno, C. D. *Nano Lett.* **2005,** 5, 2538-2542.

(78) Geng, Y.; Dalhaimer, P.; Cai, S. S.; Tsai, R.; Tewari, M.; Minko, T.; Discher, D. E. *Nat. Nanotechnol.* **2007,** 2, 249-255.

(79) Zhang, K.; Rossin, R.; Hagooly, A.; Chen, Z. Y.; Welch, M. J.; Wooley, K. L. *J. Polym. Sci., Part A: Polym. Chem.* **2008,** 46, 7578-7583.

(80) Cao, L.; Massey, J. A.; Winnik, M. A.; Manners, I.; Riethmuller, S.; Banhart, F.; Spatz, J. P.; Moller, M. *Adv. Funct. Mater.* **2003,** 13, 271-276.

(81) Liu, J.; Thompson, Z. J.; Sue, H. J.; Bates, F. S.; Hillmyer, M. A.; Dettloff, M.; Jacob, G.; Verghese, N.; Pham, H. *Macromolecules* **2010,** 43, 7238-7243.

(82) Wang, H.; Wang, X. S.; Winnik, M. A.; Manners, I. *J. Am. Chem. Soc.* **2008,** 130, 12921-12930.

(83) Won, Y.-Y.; Davis, H. T.; Bates, F. S. *Science* **1999,** 283, 960-963.

(84) Chen, Q. J.; Zhao, H.; Ming, T.; Wang, J. F.; Wu, C. *J. Am. Chem. Soc.* **2009,** 131, 16650-16651.

(85) Kim, S. H.; Nederberg, F.; Jakobs, R.; Tan, J. P. K.; Fukushima, K.; Nelson, A.; Meijer, E. W.; Yang, Y. Y.; Hedrick, J. L. *Angew. Chem. Int. Ed.* **2009,** 48, 4508-4512.

(86) Sugihara, S.; Blanazs, A.; Armes, S. P.; Ryan, A. J.; Lewis, A. L. *J. Am. Chem. Soc.* **2011,** 133, 15707-15713.

(87) Blanazs, A.; Madsen, J.; Battaglia, G.; Ryan, A. J.; Armes, S. P. *J. Am. Chem. Soc.* **2011,** 133, 16581-16587.

(88) Li, Y.; Armes, S. P. *Angew. Chem. Int. Ed.* **2010,** 49, 4042-4046.

(89) Huang, K.; Rzayev, J. *J. Am. Chem. Soc.* **2009,** 131, 6880-6885.

(90) Fang, B.; Walther, A.; Wolf, A.; Xu, Y. Y.; Yuan, J. Y.; Muller, A. H. E. *Angew. Chem. Int. Ed.* **2009,** 48, 2877-2880.

(91) Zhong, S.; Cui, H. G.; Chen, Z. Y.; Wooley, K. L.; Pochan, D. J. *Soft Matter* **2008,** 4, 90-93.

(92) Soto, A. P.; Gilroy, J. B.; Winnik, M. A.; Manners, I. *Angew. Chem. Int. Ed.* **2010,** 49, 8220-8223.

(93) Raez, J.; Barjovanu, R.; Massey, J. A.; Winnik, M. A.; Manners, I. *Angew. Chem. Int. Ed.* **2000,** 39, 3862-3865.

(94) Massey, J. A.; Temple, K.; Cao, L.; Rharbi, Y.; Raez, J.; Winnik, M. A.; Manners, I. *J. Am. Chem. Soc.* **2000,** 122, 11577-11584.

(95) Massey, J.; Power, K. N.; Manners, I.; Winnik, M. A. *J. Am. Chem. Soc.* **1998,** 120, 9533-9540.

(96) Wang, X. S.; Guerin, G.; Wang, H.; Wang, Y. S.; Manners, I.; Winnik, M. A. *Science* **2007,** 317, 644-647.

(97) He, F.; Gaedt, T.; Manners, I.; Winnik, M. A. *J. Am. Chem. Soc.* **2011,** 133, 9095-9103.

(98) Qiu, H.; Cambridge, G.; Winnik, M. A.; Manners, I. *J. Am. Chem. Soc.* **2013,** 135, 12180-12183.

(99) Gadt, T.; Ieong, N. S.; Cambridge, G.; Winnik, M. A.; Manners, I. *Nat. Mater.* **2009,** 8, 144-150.

(100) Gwyther, J.; Gilroy, J. B.; Rupar, P. A.; Lunn, D. J.; Kynaston, E.; Patra, S. K.; Whittell, G. R.; Winnik, M. A.; Manners, I. *Chem. Eur. J.* **2013,** 19, 9186 - 9197.

(101) Patra, S. K.; Ahmed, R.; Whittell, G. R.; Lunn, D. J.; Dunphy, E. L.; Winnik, M. A.; Manners, I. *J. Am. Chem. Soc.* **2011,** 133, 8842-8845.

(102) Lazzari, M.; Scalarone, D.; Vazquez-Vazquez, C.; Lopez-Quintela, M. A. *Macromol. Rapid Commun.* **2008,** 29, 352-357.

(103) Schmalz, H.; Schmelz, J.; Drechsler, M.; Yuan, J.; Walther, A.; Schweimer, K.; Mihut, A. M. *Macromolecules* **2008,** 41, 3235-3242.

(104) Lee, C.-U.; Smart, T. P.; Guo, L.; Epps, T. H.; Zhang, D. *Macromolecules* **2011,** 44, 9574-9585.

(105) Qiu, H.; Cambridge, G.; Winnik, M. A.; Manners, I. *J. Am. Chem. Soc.* **2013,** 135, 12180-12183..

(106) Petzetakis, N.; Dove, A. P.; O'Reilly, R. K. *Chem. Sci.* **2011,** 2, 955-960.

(107) Petzetakis, N.; Walker, D.; Dove, A. P.; O'Reilly, R. K. *Soft Matter* **2012,** 8, 3408-3414.

(108) Shen, L.; Wang, H.; Guerin, G.; Wu, C.; Manners, I.; Winnik, M. A. *Macromolecules* **2008,** 41, 4380-4389.

(109) Petzetakis, N.; Robin, M. P.; Patterson, J. P.; Kelley, E. G.; Cotanda, P.; Bomans, P. H. H.; Sommerdijk, N. A. J. M.; Dove, A. P.; Epps, T. H.; O'Reilly, R. K. *ACS Nano* **2013,** 7, 1120-1128.

(110) Pitto-Barry, A.; Kirby, N.; Dove, A. P.; O'Reilly, R. K. *Polym. Chem.* **2014,** 5, 1427-1436.

(111) Sun, G.; Hagooly, A.; Xu, J.; Nyström, A. M.; Li, Z.; Rossin, R.; Moore, D. A.; Wooley, K. L.; Welch, M. J. *Biomacromolecules* **2008,** 9, 1997-2006.

(112) Zhang, K.; Rossin, R.; Hagooly, A.; Chen, Z.; Welch, M. J.; Wooley, K. L. *J. Polym. Sci. A Polym. Chem.* **2008,** 46, 7578-7583.

(113) Huang, H.; L. Wooley, K.; E. Remsen, E. *Chem. Comm.* **1998**, 1415-1416.

(114) Shi, M.; Wosnick, J. H.; Ho, K.; Keating, A.; Shoichet, M. S. *Angew. Chem. Int. Ed.* **2007,** 46, 6126-6131.

(115) Onbulak, S.; Tempelaar, S.; Pounder, R. J.; Gok, O.; Sanyal, R.; Dove, A. P.; Sanyal, A. *Macromolecules* **2012,** 45, 1715-1722.

(116) O'Reilly, R. K.; Joralemon, M. J.; Hawker, C. J.; Wooley, K. L. *Chem. Eur. J.* **2006,** 12, 6776-6786.

(117) Jia, Z.; Bobrin, V. A.; Truong, N. P.; Gillard, M.; Monteiro, M. J. *J. Am. Chem. Soc.* **2014,** 136, 5824-5827.

Chapter 2. Tuning the Dimensions of Cylindrical Micelles from Poly(L-Lactide)-containing Diblock Copolymers based on Crystallization-Driven Self-Assembly

2.1 Abstract

In this chapter, a number of poly(*L*-lactide)-*b*-poly(acrylic acid) (PLLA-*b*-PAA) cylindrical micelles were prepared based on crystallization-driven self-assembly (CDSA). It was observed that by simply changing the compositions of PLLA-*b*-PAA diblock copolymers, the dimensions of these cylindrical micelles could be tuned. The precursor poly(*L*-lactide)-*b*-poly(tetrahydropyran acrylate) (PLLA-*b*-PTHPA) was synthesized by a combination of ring-opening polymerization (ROP) and reversible addition-fragmentation chain transfer (RAFT) polymerization. The CDSA process was carried out in a tetrahydrofuran/water (THF/H_2O) mixture during the hydrolysis of PTHPA block at 65°C by using an evaporation method. We found that most PLLA-*b*-PAA diblock copolymers led to cylindrical micelles with narrow size distributions (L_w/L_n < 1.30) by transmission electron microscopy (TEM) analysis. It should be also noted that the length of PLLA block controlled the lengths of resultant cylindrical micelles while the length of PAA block governed their widths. Small-angle X-ray scattering (SAXS) further proved that the length increase of these cylinders was due to the decreasing PLLA block lengths. The crystalline core nature of these polymeric cylindrical micelles was proven by wide-angle X-ray diffraction (WAXD) and the relative core crystallinity was calculated to compare different samples. Finally, we found that both the hydrophobic weight fraction and the relative core crystallinity determined the formation of PLLA-*b*-PAA cylindrical micelles.

2.2 Introduction

Crystallization-driven self-assembly (CDSA) of amphiphilic block copolymers has provided a powerful technique for the selective synthesis of cylindrical or worm-like micelles. While such phases were first reported in the early 1990s,[1, 2] the narrow composition window in which cylindrical micelles can form significantly limits the access to this morphology when using the hydrophobic effect as the main driving force for assembly (within the region 1/3 ≤ packing parameter p ≤ 1/2).[3] In turn, by comparison to spherical[4-6] or vesicular[7-10] micelles, cylinders have received more limited study to date. Despite the difficulty in obtaining pure cylindrical phases, several examples have demonstrated the outstanding advantages of cylinders in numerous applications. For instance, the addition of cylinders into epoxy resin improved its mechanical properties,[11] the encapsulation of metallic nanoparticles inside cylinders yielded templates for electronic materials,[12, 13] while the most notable potential applications are in the biomedical arena due to the *in vivo* long circulation time[14] and altered cell internalization pathways of cylindrical morphologies compared to spherical constructs.[15]

Several methodologies to control particle morphology have been explored to access cylindrical particles. The groups of Wooley and Rzayev studied the preparation of cylinders obtained from bottle brush copolymers by using "grafting through"[16] and "grafting from"[17] methods respectively. Wu and co-workers reported that poly(styrene)-*b*-poly(isoprene) spherical micelles could be extruded through nanoscale pores to realize cylindrical structures,[18] whereas Wang *et al.* utilized inorganic salts to induce the transformation of spherical poly(*ε*-caprolactone)-*b*-poly(ethylene oxide) micelles into cylindrical

micelles.[19] Still, living CDSA of crystalline[20, 21] or semi-crystalline[22, 23] block containing polymers has emerged as one of the most powerful methods to realize cylindrical micelles by altering the conventional rules of self-assembly. The concept was first reported by Manners, Winnik and co-workers who focused on organometallic and crystalline poly(ferrocenylsilane) (PFS)-containing diblock copolymers.[24-28] The general process developed by these researchers was to grow the same or other analogous PFS-based unimers on the two living ends of a PFS-based cylindrical micelle seed to achieve cylinders with increased lengths or cylinders with multiple blocks.[21, 29] Interestingly, when a PFS-containing block copolymer solution was heated above the melting temperature, T_m, of the PFS block to destroy the crystallinity of the core, spherical micelles rather than cylindrical micelles were observed, which indicated the significant importance of crystallinity in defining the cylindrical morphology phase.[30] The key importance of the crystallization process in the formation of cylindrical morphologies in combination with the active nature of the two ends of the micelle nuclei, led to the assembly process being described as a living CDSA.[20, 30] Extension of this concept has enabled the synthesis of other complicated morphologies such like 9-block co-micelles,[29] star-shaped supermicelles,[31] scarf-shaped architectures[32] and multi-armed micelles grown from nanocrystals.[33]

Beyond these seminal works, Schmalz and coworkers utilized the CDSA process to assemble semi-crystalline poly(ethylene)-based diblock or triblock copolymers into patchy cylinders and co-micelles,[34, 35] and other groups utilized poly(3-hexylthiophene),[36, 37] poly(acrylonitrile),[38] poly(ethylene)[39] and poly(*N*-decylglycine)[40] to direct the CDSA process. Recently, our group and others

have also explored CDSA in aqueous systems using semi-crystalline poly(*L*-lactide)-containing diblock copolymers.[41-45] The formation of cylindrical micelles from poly(*L*-lactide)-*b*-poly(acrylic acid) (PLLA-*b*-PAA) copolymers was found to follow a sphere-to-rod transition in which amorphous spheres undergo a crystallization process to yield short crystalline cylindrical seeds that are proposed to grow by a unimer exchange mechanism. Moreover, under high dilution conditions, the PLLA-*b*-PAA cylinders showed a linear correlation between the micelle length and CDSA time, which indicates a living character to their growth.

While several systems have now been reported in this area, the factors that control the dimensions of the micelles have received relatively little study. Only a few examples have been reported to govern the lengths of cylindrical micelles. For example, Manners, Winnik and co-workers have grown unimers onto the short crystalline PFS-containing seeds and by adjusting the unimer to seed ratio, cylinders with accurate lengths were realized.[20, 37] Our group has tuned the lengths of PLLA-*b*-PAA cylinders by varying the ratio of THF in THF/H_2O mixture during CDSA and we found that increasing the amount of THF led to longer cylinders as a consequence of the enhanced mobility of polymer chains.[45] Herein, we demonstrate the first study into the control over the cylinder lengths and widths by changing the compositions of PLLA-*b*-PAA diblock copolymers using CDSA. All of the resultant cylinders showed narrow size distributions (L_w/L_n < 1.30) from transmission electron microscopy (TEM) analysis and the crystalline core nature of these cylinders was revealed by wide-angle X-ray diffraction (WAXD) with further evidence of the relationship

between crystallinity and cylinder formation through small-angle X-ray scattering (SAXS) studies.

2.3 Results and discussion

2.3.1 Synthesis and characterization of PLLA-*b*-PTHPA diblock copolymers

The synthesis of the PLLA-*b*-PTHPA diblock was achieved by a combination of ring-opening polymerization (ROP) and reversible addition-fragmentation chain transfer (RAFT) polymerization from a dual-headed initiator/chain transfer agent as reported previously by the group (Scheme 2.1).[44]

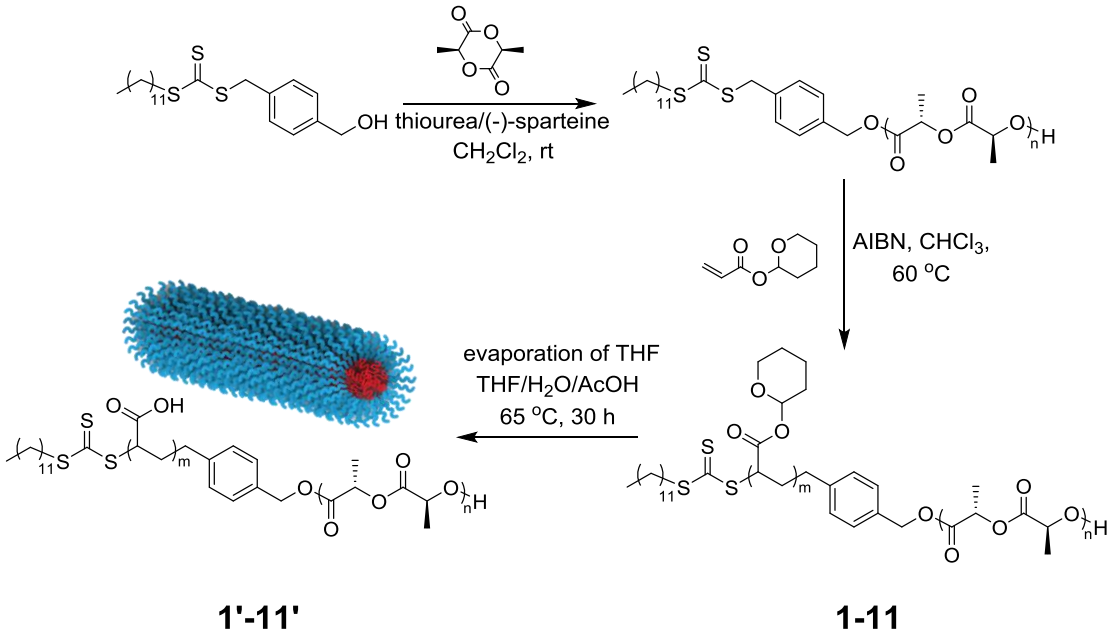

Scheme 2.1. Synthesis and CDSA of PLLA-*b*-PTHPA diblock copolymers.

Firstly, ROP of *L*-lactide was performed using the highly selective 1-(3,5-bis(trifluoromethyl)phenyl)-3-cyclohexyl-thiourea/(-)-sparteine co-catalyst system and initiated from the hydroxyl group of the dual-headed initiator as previously described by the group.[44] ^{1}H NMR spectroscopy (Figure 2.1) indicated the successful synthesis of PLLA with different degree of polymerizations (DPs) (methine resonance of PLLA repeat units observed at *δ*

= 5.30 - 5.40 ppm). SEC analysis revealed narrow dispersities in all cases (Figure 2.2 and Table 2.1). MALDI-ToF MS measurement of the various PLLA macro-initiators was consistent with the expected molar mass and minimal transesterification was observed (Figure 2.3, Table 2.2).

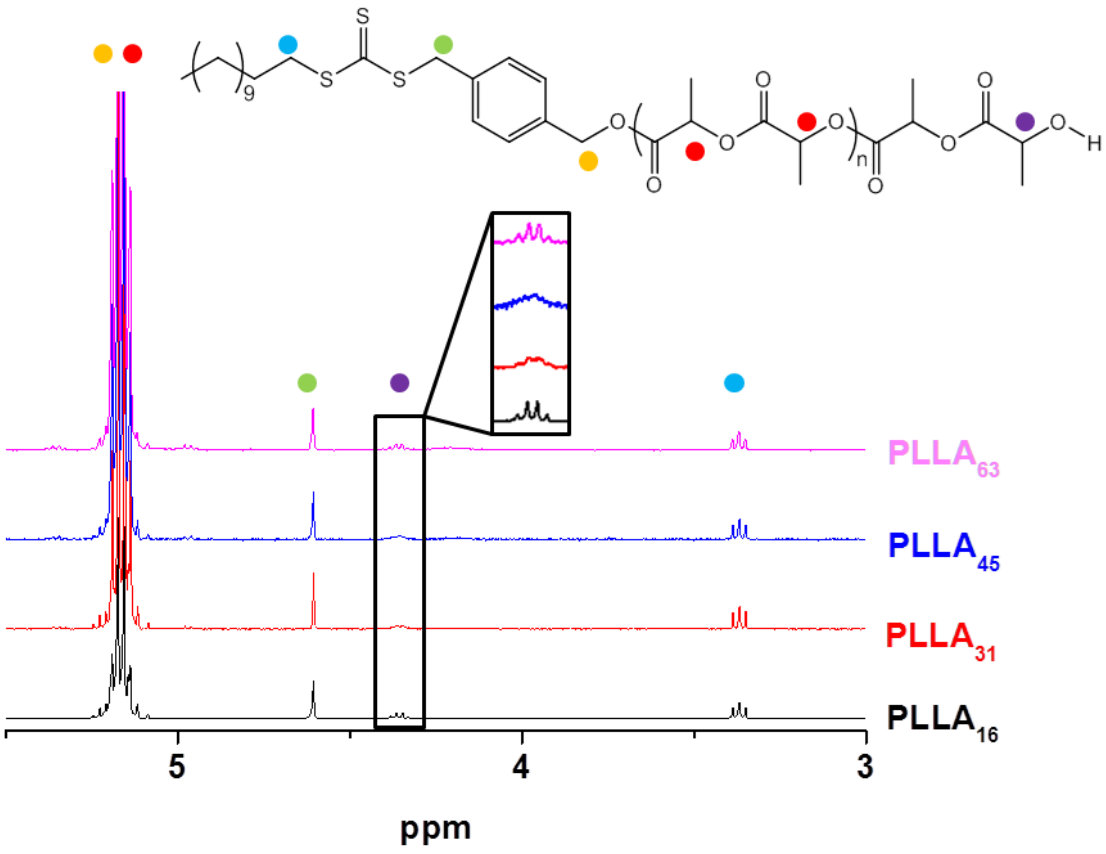

Figure 2.1. ^{1}H NMR spectra (400MHz, $CDCl_3$) of various PLLA macro-initiators with different DPs.

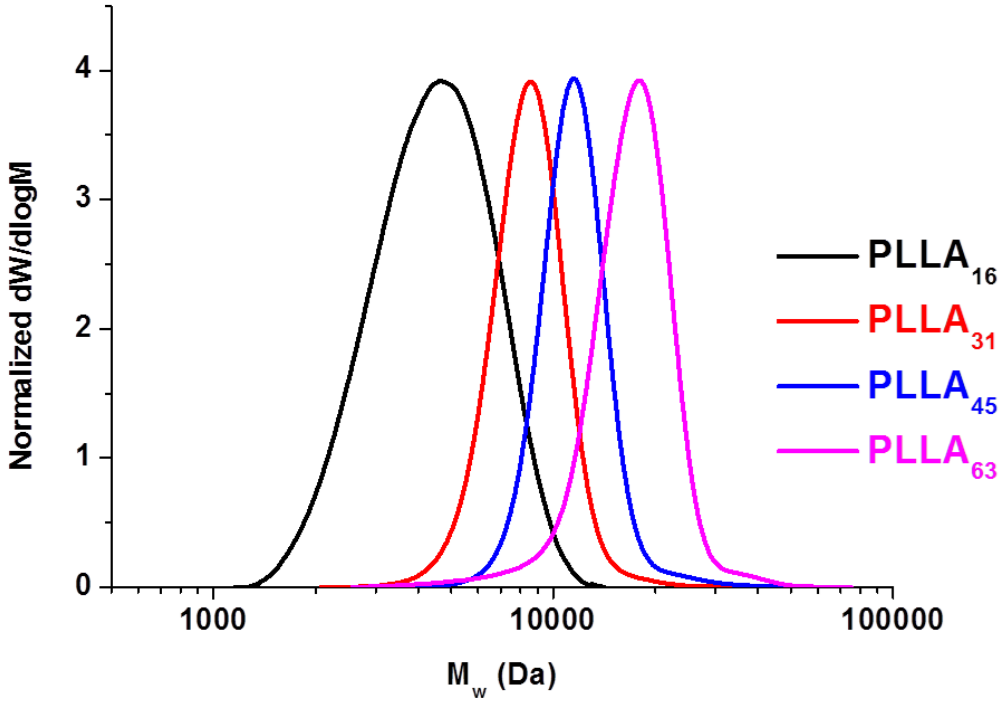

Figure 2.2. SEC chromatograms (THF with 2% TEA as eluent) of various PLLA macro-initiators using RI detector.

Table 2.1. Characterization data of PLLA homopolymers

Polymer	M_n **(kDa)**[a]	$Đ_M$[b]	T_g **(°C)**[c]
$PLLA_{16}$	2.7	1.17	50.5
$PLLA_{31}$	4.9	1.07	51.0
$PLLA_{45}$	6.9	1.06	50.5
$PLLA_{63}$	9.5	1.10	51.0

[a] Measured by ^{1}H NMR spectroscopy in $CDCl_3$. [b] Measured by SEC analysis (THF with 2% TEA as eluent, RI detection). [c] Measured by DSC analysis in the first heating run with a heating rate of 10 °C/min.

PTHPA was subsequently grown from the PLLA macro-initiator by RAFT polymerization of THPA as proved by ^{1}H NMR spectroscopy showing the broad methine resonance of tetrahydropyranyl protecting groups of PTHPA repeat

units at δ = 6.20 - 5.68 ppm (Scheme 1, Figure 2.4 and Figure 2.5). The diblock copolymers, **1** - **5** (Table 2.3), were designed with DP of PLLA but a similar hydrophobic weight fraction, optimized to *ca*. 18% in line with our previous studies.[45] In contrast, diblock copolymers, **6** - **11** (Table 2.3), were targeted with the same DP of PLLA but different DPs of PTHPA to enable exploration of the effect of hydrophobic weight fraction upon the dimensions of the resultant particles. All of the diblock copolymers used in this chapter showed narrow dispersities by SEC analysis ($Đ_M$ < 1.20) (Table 2.3, Figure 2.6 and Figure 2.7) and molar masses close to those predicted, as determined by ^{1}H NMR spectroscopy.

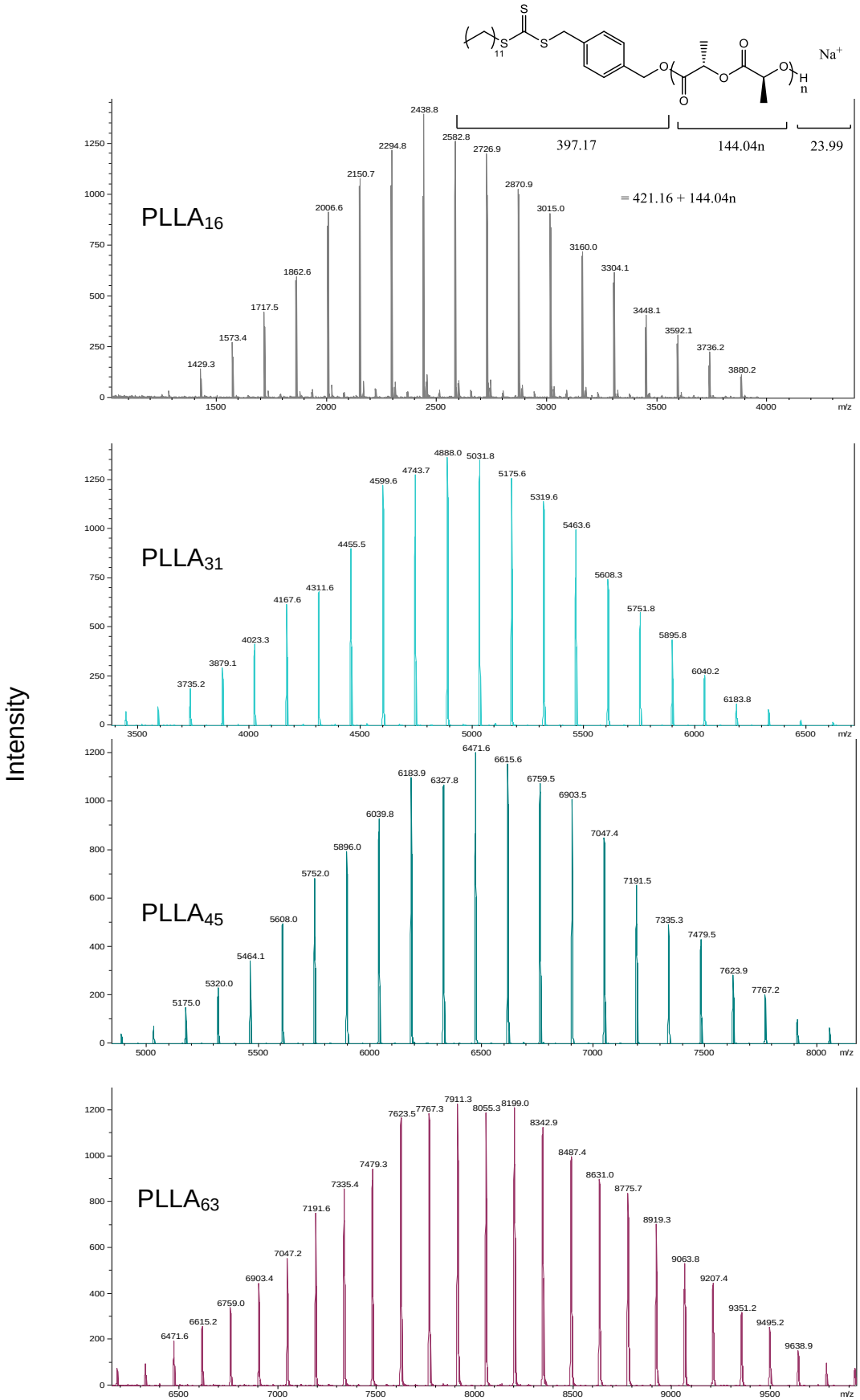

Figure 2.3. MALDI-ToF mass spectra of PLLA macro-initiators.

Table 2.2. Comparisons of theoretical and observed m/z of different PLLA macro-initiators

DP of PLLA	Theoretical m/z of PLLA	Observed m/z of $PLLA_{16}$[a]	Observed m/z of $PLLA_{31}$[a]	Observed m/z of $PLLA_{45}$[a]	Observed m/z of $PLLA_{63}$[a]
10	1861.6	1862.6	–	–	–
15	2581.8	2582.8	–	–	–
20	3302.0	3304.1	–	–	–
25	4022.2	–	4023.3	–	–
30	4742.4	–	4743.7	–	–
35	5462.6	–	5463.6	5464.1	–
40	6182.8	–	6183.8	6183.9	–
45	6903.1	–	–	6903.5	6903.4
50	7623.3	–	–	7623.9	7623.5
55	8343.5	–	–	–	8342.9

[a] Measured by MALDI-ToF mass-spectrometry using trans-2-[3-(4-*tert*-butyl-phenyl)-2-methyl-2-propenylidene] malononitrile (DCTB) as matrix and sodium trifluoroacetate (NaTFA) as cationization agent.

Table 2.3. Characterization data of PLLA-*b*-PTHPA diblock copolymers

Diblock copolymer		M_n (kDa)[a]	$Đ_M$[b]	Hydrophobic %wt[c]
$PLLA_{16}$-*b*-$PTHPA_{151}$	**1**	26.3	1.12	17.5
$PLLA_{31}$-*b*-$PTHPA_{278}$	**2**	48.3	1.13	18.2
$PLLA_{38}$-*b*-$PTHPA_{333}$	**3**	57.9	1.11	18.6
$PLLA_{45}$-*b*-$PTHPA_{393}$	**4**	68.3	1.16	18.6
$PLLA_{63}$-*b*-$PHTPA_{603}$	**5**	103.7	1.20	17.3
$PLLA_{45}$-*b*-$PTHPA_{52}$	**6**	15.0	1.09	63.4
$PLLA_{45}$-*b*-$PTHPA_{156}$	**7**	31.2	1.10	36.6
$PLLA_{45}$-*b*-$PTHPA_{244}$	**8**	45.0	1.11	26.9
$PLLA_{45}$-*b*-$PTHPA_{305}$	**9**	54.5	1.14	22.8
$PLLA_{45}$-*b*-$PTHPA_{514}$	**10**	87.2	1.13	14.9
$PLLA_{45}$-*b*-$PTHPA_{612}$	**11**	102.5	1.17	12.8

[a] Measured by ^{1}H NMR spectroscopy (400 MHz, $CDCl_3$). [b] Measured by THF SEC. [c] PLLA weight fraction in the resultant PLLA-*b*-PAA diblock copolymer.

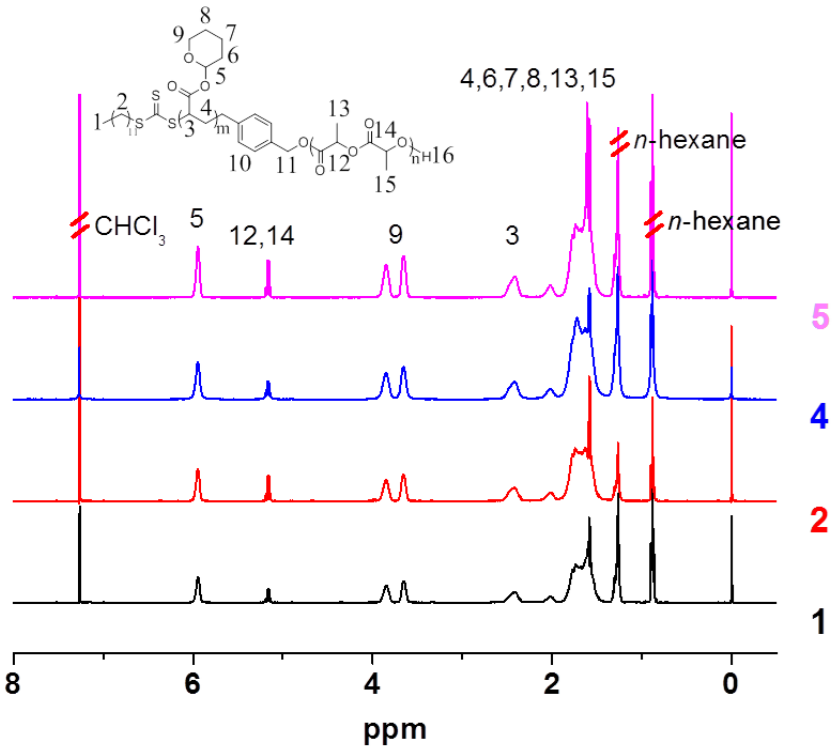

Figure 2.4. ^{1}H NMR spectra (400MHz, $CDCl_3$) of PLLA-*b*-PTHPA diblock copolymers, **1**, **2**, **4**, and **5**.

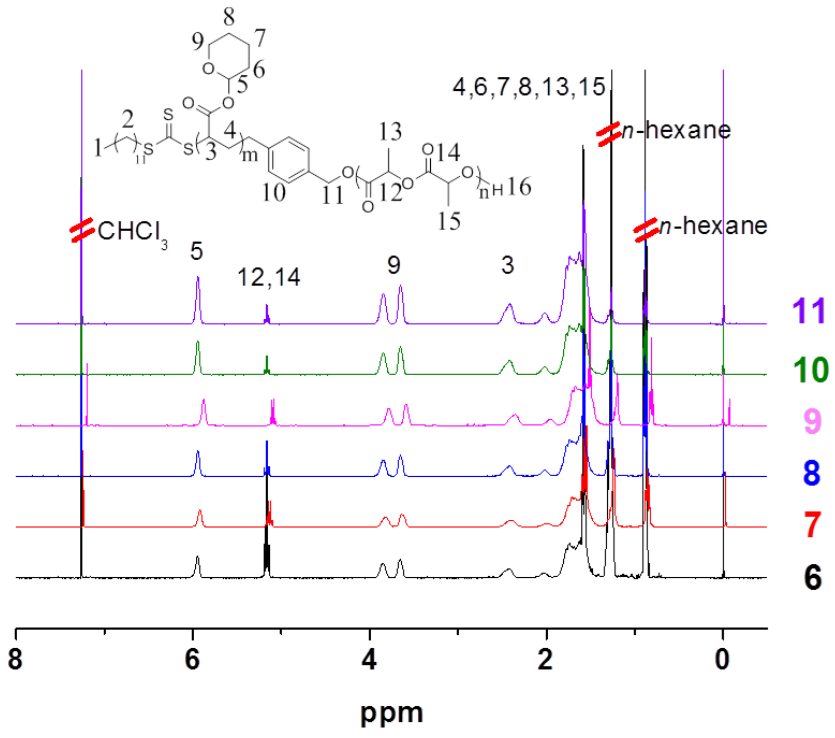

Figure 2.5. ^{1}H NMR spectra (400MHz, $CDCl_3$) of PLLA-*b*-PTHPA diblock copolymers, **6** - **11**.

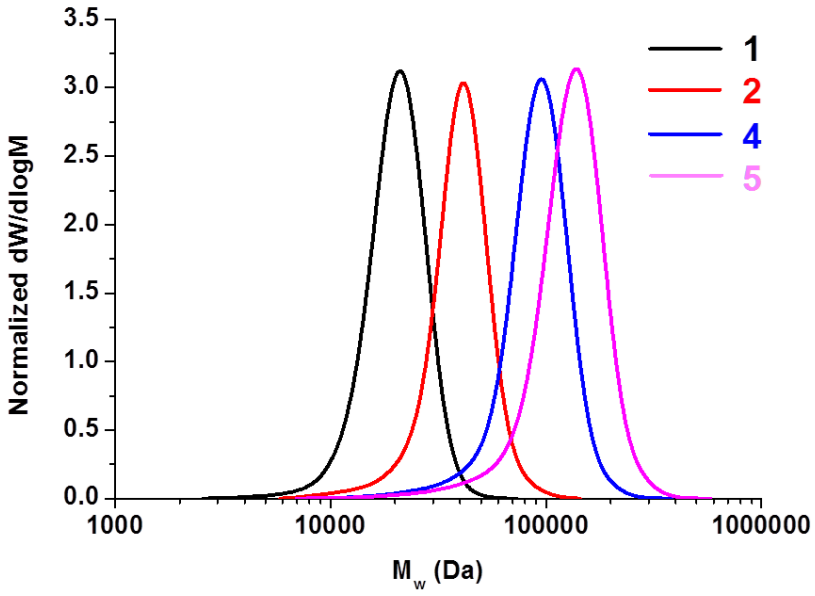

Figure 2.6. SEC chromatograms (THF with 2% TEA as eluent, RI detection) of various PLLA-*b*-PTHPA diblock copolymers with varied block lengths but all with 18% hydrophobic weight fraction. See Table 2.3 for the specific compositions of block copolymers.

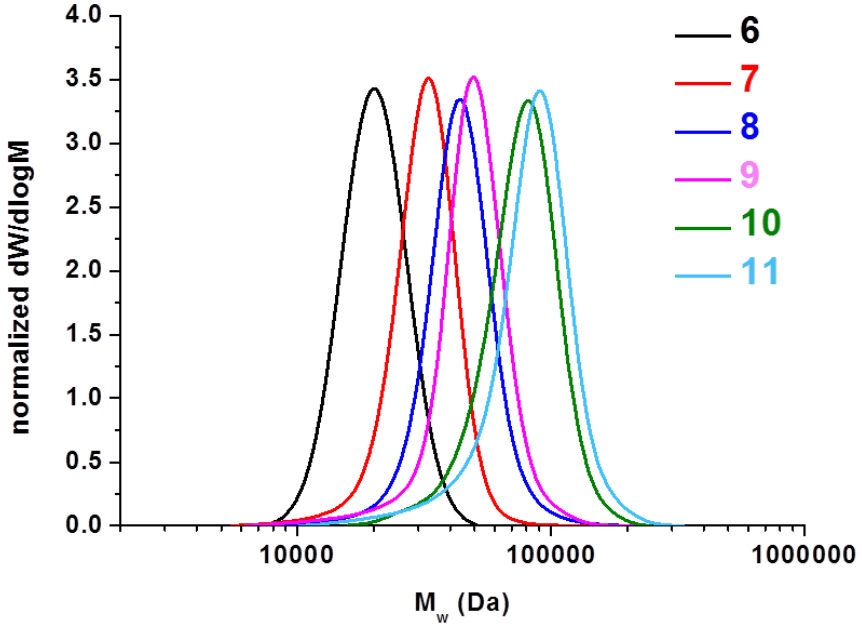

Figure 2.7. SEC chromatograms (THF with 2% TEA as eluent, RI detection) of various PLLA-*b*-PTHPA diblock copolymers with the same DP of PLLA but with different DPs of PTHPA. See Table 2.3 for the specific compositions of block copolymers.

2.3.2 Crystallization-driven self-assembly of various PLLA-*b*-PTHPA diblock copolymers

The one pot deprotection of PTHPA and self-assembly of the resultant PLLA-*b*-PAA diblock copolymers was realized in a THF/H_2O mixture with 20 *v*/*v*% THF, a good solvent for both blocks, at 65 °C (above the T_g of PLLA) to yield micellar solutions (**1'** - **11'** corresponding to each precursor PLLA-*b*-PTHPA diblock copolymer).[44] The successful hydrolysis of PTHPA to PAA was proven by ^{1}H NMR spectroscopic analysis of the polymer in d_6-DMSO, with a loss of peak at *ca*. δ = 6.0 ppm from the methine resonance of tetrahydropyranyl protecting groups of PTHPA repeat units and a new broad peak at *ca*. δ = 12.5 ppm assigned to the protons of carboxyl groups of PAA (Figure 2.8 and Figure 2.9).

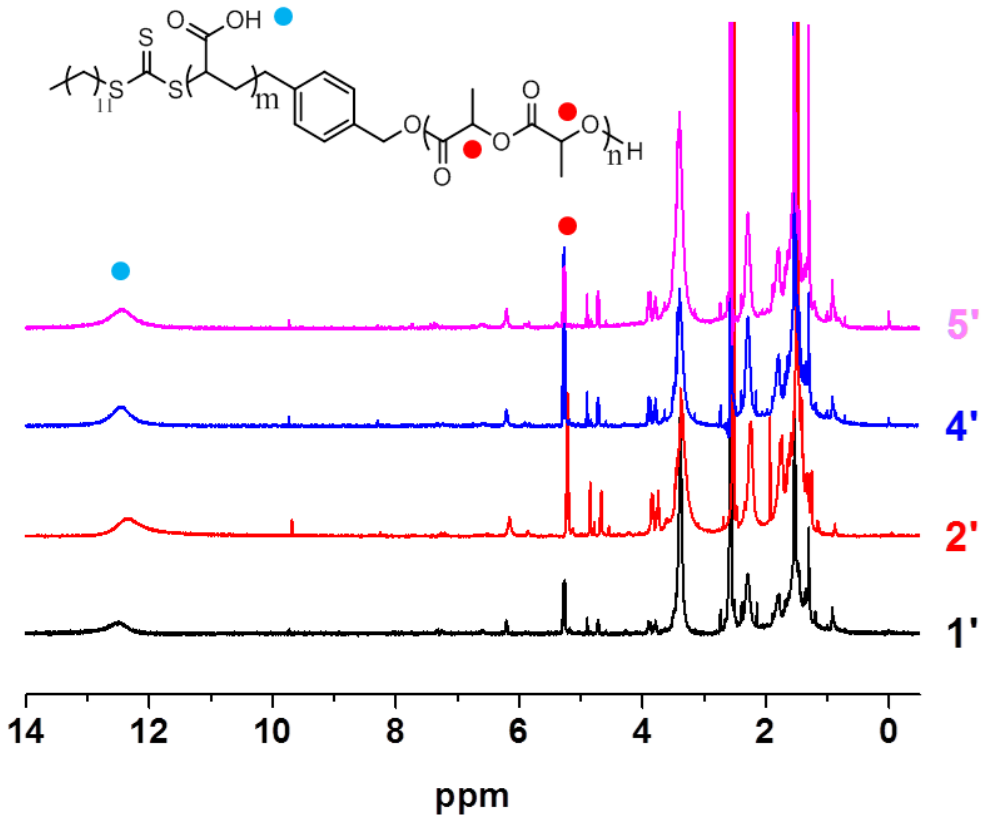

Figure 2.8. ^{1}H NMR spectra (400 MHz, d_6-DMSO) of PLLA-*b*-PAA diblock copolymers.

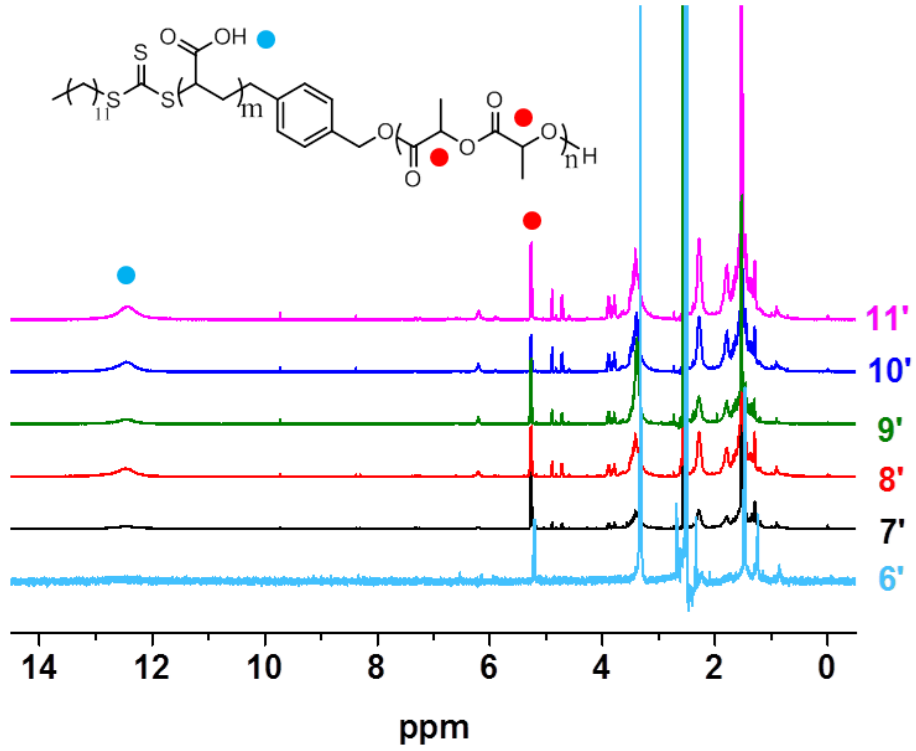

Figure 2.9. ^{1}H NMR spectra (400 MHz, d_6-DMSO) of PLLA-*b*-PAA diblock copolymers.

2.3.3 Tuning the lengths of polymeric cylinders through variation of the hydrophobic PLLA block length

TEM analysis of assemblies formed from the diblock copolymers, **2** - **5** (Figure 2.10), show the cylindrical nature of the micelles formed in all cases. Image analysis reveals that the cylinder lengths are narrowly dispersed (Table 2.4) and dynamic light scattering (DLS) measurements indicate only one population for each of the different copolymer assemblies (Figure 2.11). Notably, assembly of block copolymer, **1**, only led to ill-defined aggregated structures (Figure 2.12), most likely a consequence of the low DP of the PLLA block providing insufficient crystallization to allow CDSA. The hollow cores observed in these cylinders, when imaged on graphene oxide-coated (GO) TEM grids, were caused by hydrogen bonding interactions between the PLLA block and PAA

block during the slow drying of the samples and is in line with a previous report from our group.[46] The widths of the hollow cores of cylinders, **2'** - **5'**, were observed to be very similar (*ca*. 11 nm). As the solvation of PAA makes the cylinder corona invisible on the GO grid, in order to measure the precise sizes of different cylinders, samples were negatively stained using phosphotungstic acid (PTA) (Figure 2.10B, 2.10D, 2.10F, 2.10H). Using these two TEM sample preparation methods, comparison of both results yields more useful information relating to the dimensions of the cylindrical micelles. Increasing the length of the hydrophobic PLLA block from a DP of 31 to 63 (while retaining the overall hydrophobic weight fraction of *ca*. 18%) led to the lengths of cylinders decreasing gradually from 223 nm to 127 nm (Table 2.4). The same trend was further observed by SAXS technique of the nanostructures upon fitting to a Cylinder_PolyRadius (cypr) model (Figure 2.13). The length was fixed as previously determined by TEM analysis (Table 2.4). It appears that the radius from the fit does not correspond to the radius determined by TEM analysis. It seems that the radius by SAXS corresponds better to the radius of the crystalline core. The scattering length density (SLD) value of the solvent (1.10×10^{-5} Å^{-2}) is higher than the one for water alone (9.46×10^{-6} Å^{-2}) which further confirmed that the hydrophilic PAA corona was hydrated with its SLD value has to be included in the SLD of the solvent. The widths of the cylinders in solution state were calculated to be 14 nm (**2'**) and 27 nm (**5'**) by SAXS analysis. The trend of fitted widths followed the result that longer PAA blocks led to wider cylinders and this also proved that the lengths used to fit the SAXS profile were correct. The fitted widths of these cylinders were smaller than the widths from the dry state TEM (Table 2.4) as the coronas of the micelles are hydrated in

solution, and are less visible in solution. It should be noted that SAXS curves were not plotted as I(q) *versus* q^{-1} due to the dispersity of both the radius and the length of cylindrical nanoparticles. Moreover, the form factor is a key factor to obtain a large q values range for which the slope of the curve I(q) *versus* q equals -1. Some examples with various radii for a fixed length and with various lengths for a fixed radius are given in Figure 2.26. It is clearly visible that the q values range for which a slope of -1 is limited.

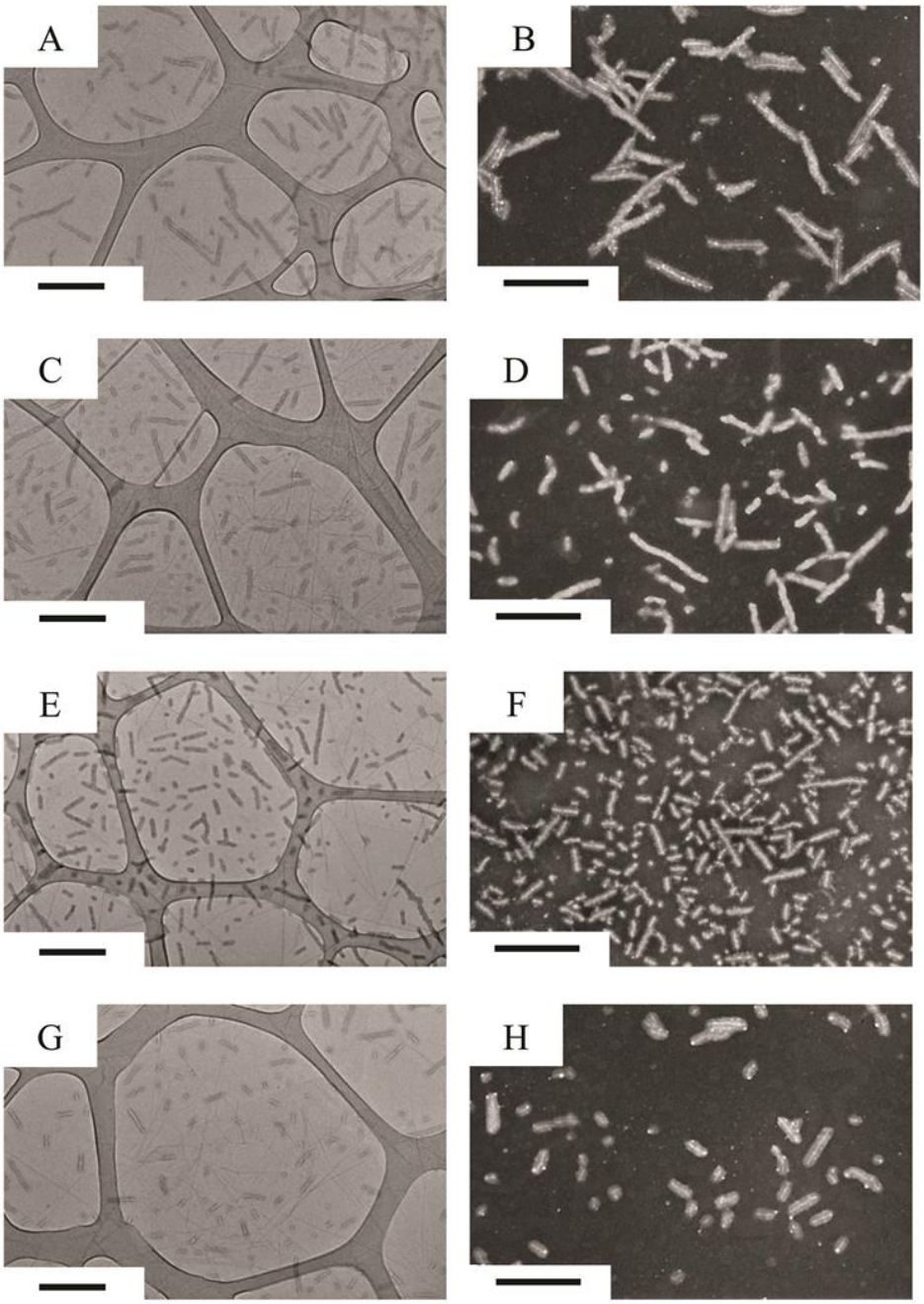

Figure 2.10. Cylindrical micelles achieved from **2'** (A, B), **3'** (C, D), **4'** (E, F) and **5'** (G, H). A, C, E, G prepared by a slow drying method on GO grids[47] and B, D, F, H also prepared by slow drying but with negative staining using PTA. The decrease in lengths of these cylinders could be easily observed when the DP of PLLA increased from 31 to 63. Scale bar = 500 nm.

Table 2.4. Characterization data of cylinder dimensions

Sample	L_n [a] (nm)	L_w [a] (nm)	L_w/L_n	W_n [a] (nm)
1'	—	—	—	—
2'	223	274	1.23	56 ± 6
3'	174	214	1.23	58 ± 5
4'	145	175	1.21	61 ± 6
5'	127	154	1.22	76 ± 6

[a] Determined by TEM analysis from the PTA stained samples.

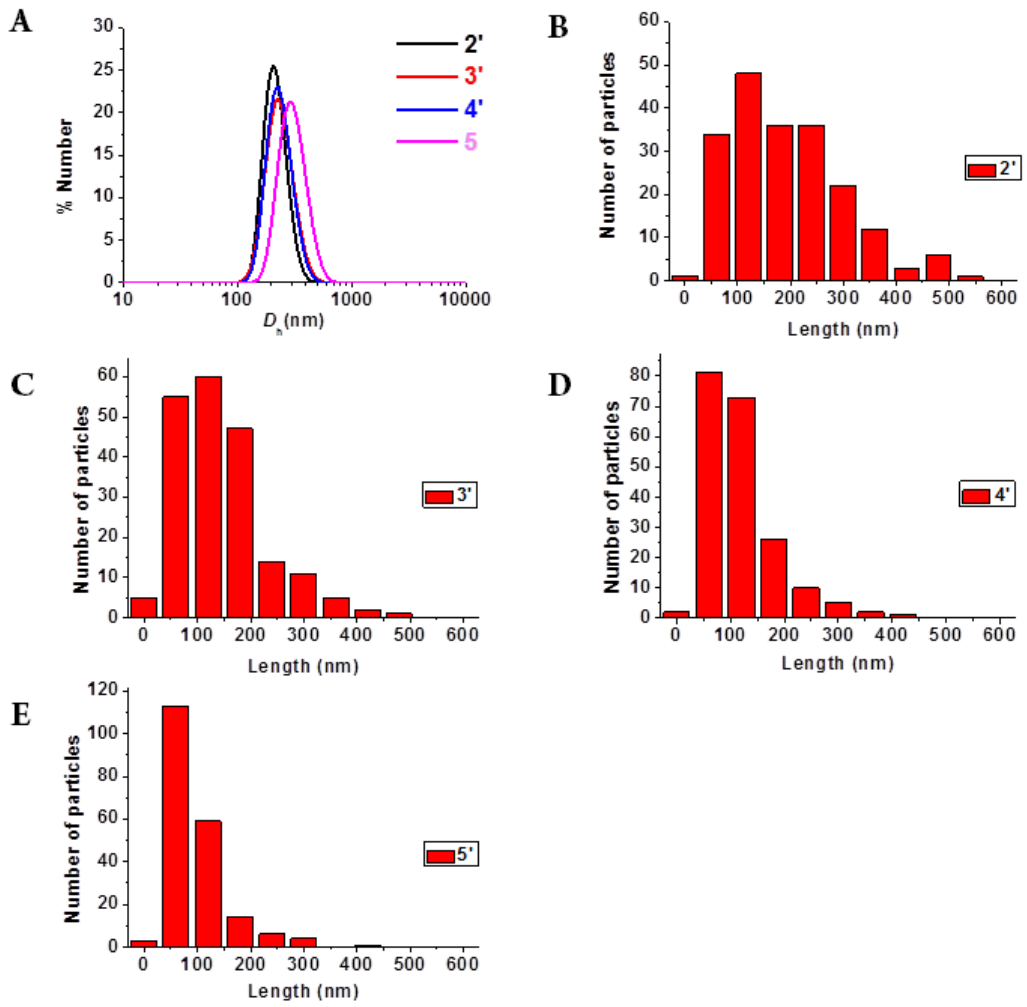

Figure 2.11. A) DLS number distributions of cylindrical micelles self-assembled from diblock copolymers, **2** - **5**. B, C, D, E) Histograms of the lengths of PLLA-*b*-PAA cylindrical micelles, **2'** - **5'**, as determined by TEM analysis.

The shorter cylinder length at higher PLLA DPs is proposed to result from the more facile crystallization of the longer PLLA blocks that leads to increased amounts of crystalline seeds forming from the amorphous spheres that are observed in the early stages of these assemblies,[45] which in turn means that less unimers are available in the system, leading to shorter cylinders. Moreover, according to the chain-folding model of crystalline-coil block copolymers,[48] unimers with longer PLLA segments may be less dynamic and take longer time to fold and thus add onto the two active ends of crystalline seeds, resulting in a relatively shorter size for the resulting nanostructures.

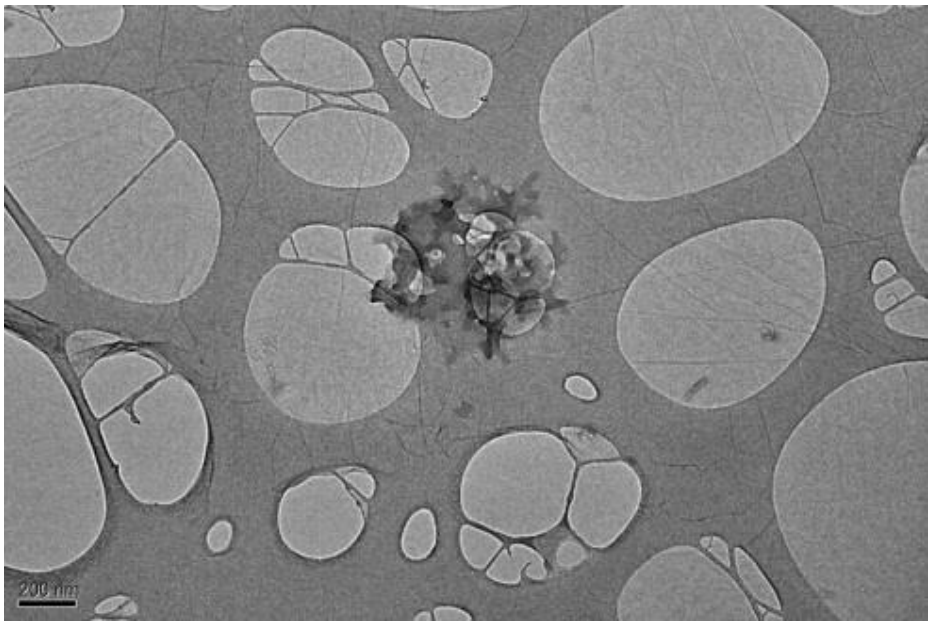

Figure 2.12. TEM image (imaged without staining on GO) showing the aggregated particles obtained from the self-assembly of polymer, **1**. Scale bar = 200 nm.

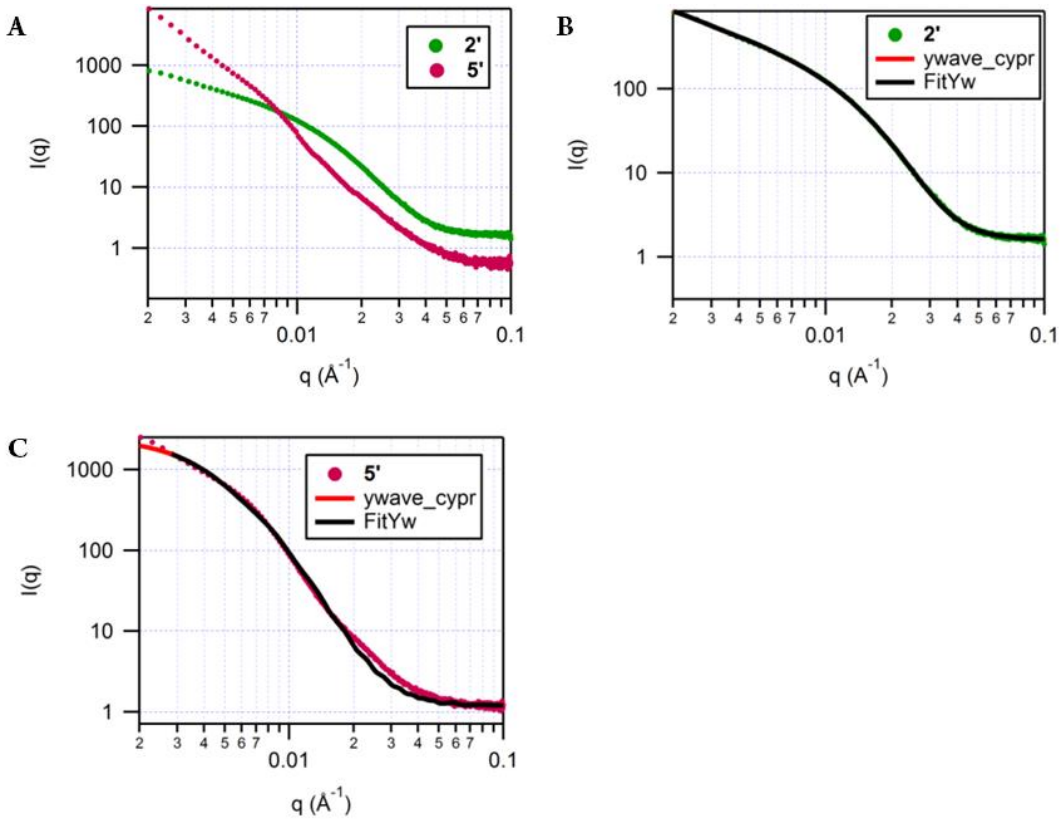

Figure 2.13. A) Overlaid SAXS profiles of **2'** and **5'**, B) form factor fitted SAXS profile of **2'** C) form factor fitted SAXS profile of **5'**.

The widths of these cylindrical micelles only increased slightly from **2'** to **4'** while the cylinders self-assembled from **5** led to much wider cylindrical micelles (*ca.* 76 nm). The obvious increase in width is a result of the much longer PAA block length in polymer, **5**, compared to **2**, **3** or **4**. As a result of the long PAA block, the core-corona structure of cylinders self-assembled from **5** can be easily observed by TEM analysis after being negatively stained by PTA, while it is not easy to observe this structure in the other cylinders (Figure 2.10).

We have previously proposed a sphere-to-rod transition for PLLA-*b*-PAA diblock copolymers[45] and this was confirmed by SAXS analysis of copolymer, **3** (Figure 2.14). The curves at 3, 6 and 8 h cannot be fitted with a simple model, for example, Sphere (sf), Cylinder (cyl), Cylinder_PolyLength (cypl) and Cylin-

der_PolyRadius (cypr), therefore, a sum model was created, being the linear addition of the sf and cypr models. Meanwhile, the curves at 13 h and 20 h can be easily fitted with a cypr model. An evolution of the shapes of the curves is clearly visible between assembly times of 3 h and 8 h, which indicates the successful morphological transition during the CDSA process. By further comparing the two parameters K_0 (scale for the Cylinder PolyRadius model) and K_7 (scale for the Sphere model) at 3 h, 6 h and 8 h in the fitted curves (Figure 2.14, Table 2.5), we noticed a dramatic increasing contribution from cylinders and a decreasing contribution from spheres over this time period which is in accordance with our proposed mechanism based on previous TEM and DLS results.[45]

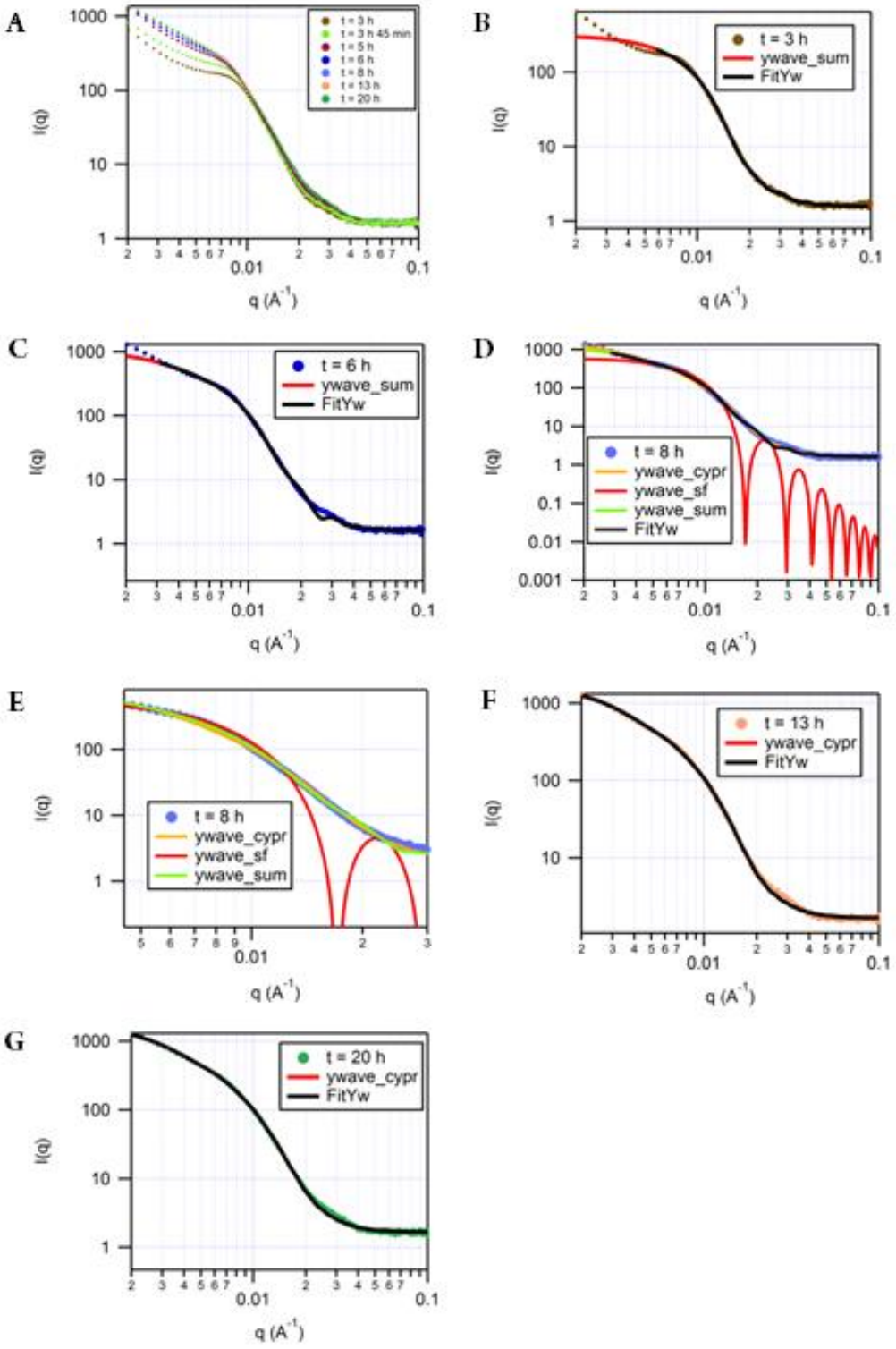

Figure 2.14. SAXS profiles of **3'** at different time points which prove the sphere-to-cylinder transition during the CDSA process: A) 3 h, B) 6 h, C) 8 h, D) zoom profile of 8 h, E) 13 h, F) 20 h.

Table 2.5. Definitions of the parameters K_n and their values in the Cylinder Polyradius model and the Sum model (Cylinder Polyradius + Sphere) of the fitted SAXS profiles of **3'** at different time points.

Parameters K_n	**3 h**	**6 h**	**8 h**	**13 h**	**20 h**
scale for the cypr model, K_0	0.0076	0.0234	0.0455	0.0447	0.0441
radius (Å) for the cypr model, K_1	162	151	149	159	152
length (Å) for the cypr model, K_2	385	1482	1537	1634	1680
polydispersity for the cypr model, K_3	0.16	0.22	0.28	0.30	0.34
SLD cylinder ($Å^{-2}$) for the cypr model, K_4	1.21e-005	1.13e-005	1.09e-005	1.10e-005	1.10e-005
SLD solvent ($Å^{-2}$) for the cypr model, K_5	9.65e-006	9.75e-006	9.68e-006	9.58e-006	9.59e-006
incoherent background (cm^{-1}) for the cypr model, K_6	1.18	1.45	1.51	1.67	1.67
scale for the sf model, K_7	0.0221	0.0194	0.013	———	———
radius (Å) for the sf model, K_8	283	298	303	———	———
SLD cylinder ($Å^{-2}$) for the sf model, K_9	1.05e-005	1.09e-005	1.09e-005	———	———
SLD solvent ($Å^{-2}$) for the sf model, K_{10}	9.65e-006	9.75e-006	9.68e-006	———	———
background (cm^{-1}) for the sf model, K_{11}	0.395	0.180	0.1327	———	———

To further investigate the CDSA process, an experiment was carried out to monitor the influence of changing solvent composition through the self-assembly process as THF evaporated. To this end, a solvent mixture of THF (0.5 mL) and deuterium oxide (D_2O) (2 mL) was studied by ^1H NMR spectroscopy using 3-(trimethylsilyl)-1-propanesulfonic acid (DSS) sodium salt (26.9 mg, 0.02 *eq*. to THF) as an internal standard under identical CDSA conditions. We observed that after 5 h, at which point cylinders are beginning to form in solution and no crystallinity is present, 20% of the initial amount of THF

remained in the solution (Figure 2.15). This further confirms our hypothesis that the good solvent plays a key role in the CDSA process through the production of unimers and their subsequent addition to crystalline seeds to enable CDSA.

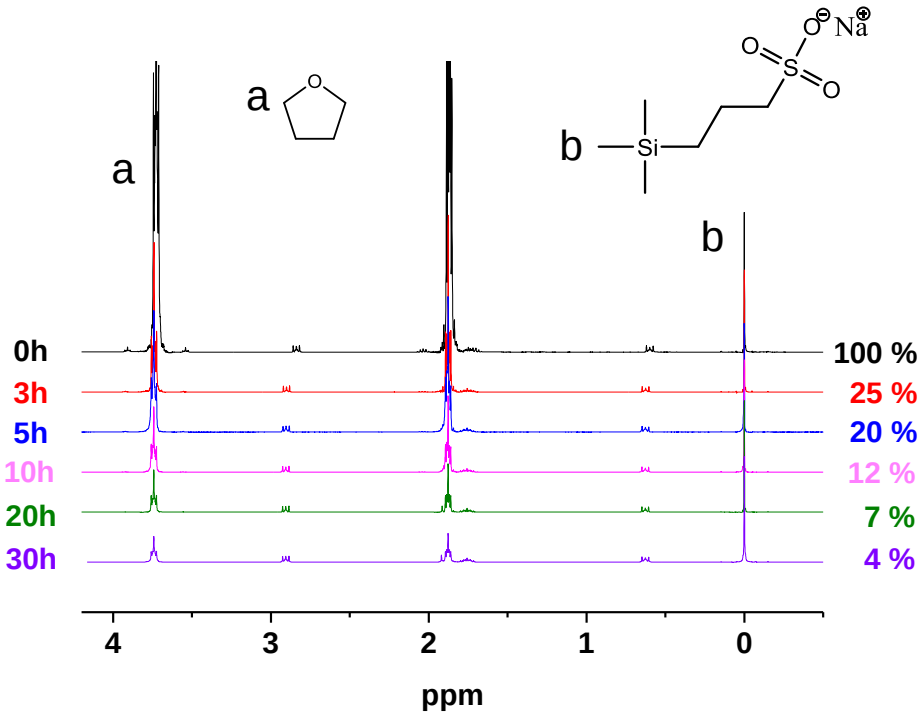

Figure 2.15. ^{1}H NMR spectra (400 MHz, D_2O) monitoring the amount of THF during the normal CDSA process by using DSS sodium salt as a standard. The percentages given were the ratios of THF left in the solution when compared to the initial amount of THF.

The crystalline nature of the core of the cylinders was interrogated by wide-angle X-ray diffraction (WAXD) (Figure 2.16), which revealed the intense crystalline Bragg peak at 16.6° *2θ* angle that corresponds to the reflections of (110)/(200) planes in the crystalline domains of PLLA,[49] in all cases. The relative core crystallinity was calculated as follows. The WAXD diffractogram of each cylinder was simulated using MDI Jade software, the amorphous background was then subtracted from the diffractogram before the main

crystalline peaks at 16.6° and 18.5° *2θ* angles (which arise from the reflections of (110)/(200) and (203) planes)[49, 50] were deconvoluted from the diffractograms. The overall crystallinity was obtained by comparing the area of the crystalline peaks with the total area of the diffractogram. Finally, the overall crystallinity was divided by the PLLA weight fraction of each diblock copolymer to give the reported relative core crystallinity. The core crystallinity of each cylindrical assembly is presented as a relative value rather than the exact value (Table 2.6) with the core crystallinity of cylinder, **5'** (which showed the highest core crystallinity), being defined as 1.00. The relative core crystallinity of the cylindrical constructs prepared from copolymers, **1** - **5**, was calculated to increase gradually from 0.71 to 1.00 as the DP of PLLA blocks was increased from 31 to 63. This observation strongly supports the observation that the decreased cylinder lengths in block copolymers with longer PLLA blocks is consistent with increased levels of crystallinity and most likely arises from the increased probability of the longer chains being able to adjust and align during the chain folding process. Indeed, we attribute the aggregated structure observed by TEM analysis of copolymer, **1**, to the observed low core crystallinity by WAXD analysis.

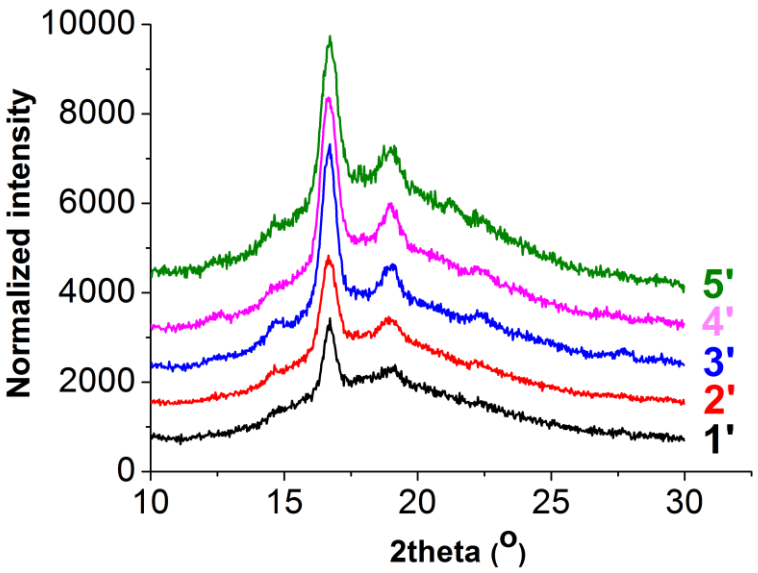

Figure 2.16. WAXD diffractograms of the particles from **1'** - **5'** showing the crystalline core nature.

Table 2.6. Characterization data of the core crystallinity of cylinder, **1'** - **5'**

Sample	Relative core crystallinity [a]
1'	0.45
2'	0.71
3'	0.89
4'	0.92
5'	1.00

[a] Determined by WAXD, relative core crystallinity is defined as crystallinity relative to the most crystalline sample, **5'**.

2.3.4 Tuning the widths of polymeric cylinders through variation of the PAA block length and hydrophobic weight fraction

In order to expand the window for the preparation of PLLA-*b*-PAA cylinders and to compare the sizes of the resultant cylinders with different hydrophobic weight fractions, copolymers, **6** - **11**, were synthesized with the same PLLA block

length but varied PAA block lengths from DP of 52 to 612 (hydrophobic weight fractions from 63.4% to 12.8%, Table 2.1). After the CDSA of these copolymers for 30 h under identical conditions to those outlined previously, **7** - **10** formed smooth and straight cylindrical micelles (Figure 2.17) with narrow size distributions (Table 2.7 and Figure 2.18). This indicates that the hydrophobic weight fraction window for the preparation of PLLA-*b*-PAA cylinders is at least between 14.9% and 36.6%. Interestingly however, diblock copolymer, **6**, with a hydrophobic weight fraction of 63.4% yielded a mixed phase of cylindrical and lamellar particles (Figure 2.19). This observation may be expected given CDSA of polymers with a short coronal block (*i.e.* high hydrophobic weight fraction) in selective solvents has previously been reported to form lamellar structures[27, 28, 32] which are more energetically favorable.[48] Self-assembly of block copolymer, **11** (with the lowest hydrophobic weight fraction), led to the observation of spherical micelles co-existing with cylinders by TEM analysis (Figure 2.20). The failure of the entire transition from sphere-to-rod in this case can be attributed to either the requirement to tune the self-assembly conditions for diblock copolymer, **11** or the low hydrophobic weight fraction of the polymer itself.

The significant changes in the widths of cylinders, **7'** - **11'**, can be easily observed by TEM analysis after negative staining with PTA (Figure 2.17B, 2.17D, 2.17F, 2.17H, 2.17J, 2.17L). Cylinders were noted to display increasing widths as the PAA block lengths increased (Table 2.7). DLS measurements also showed an increasing trend of apparent hydrodynamic diameter (D_h) due to the increased PAA block lengths (Figure 2.18).

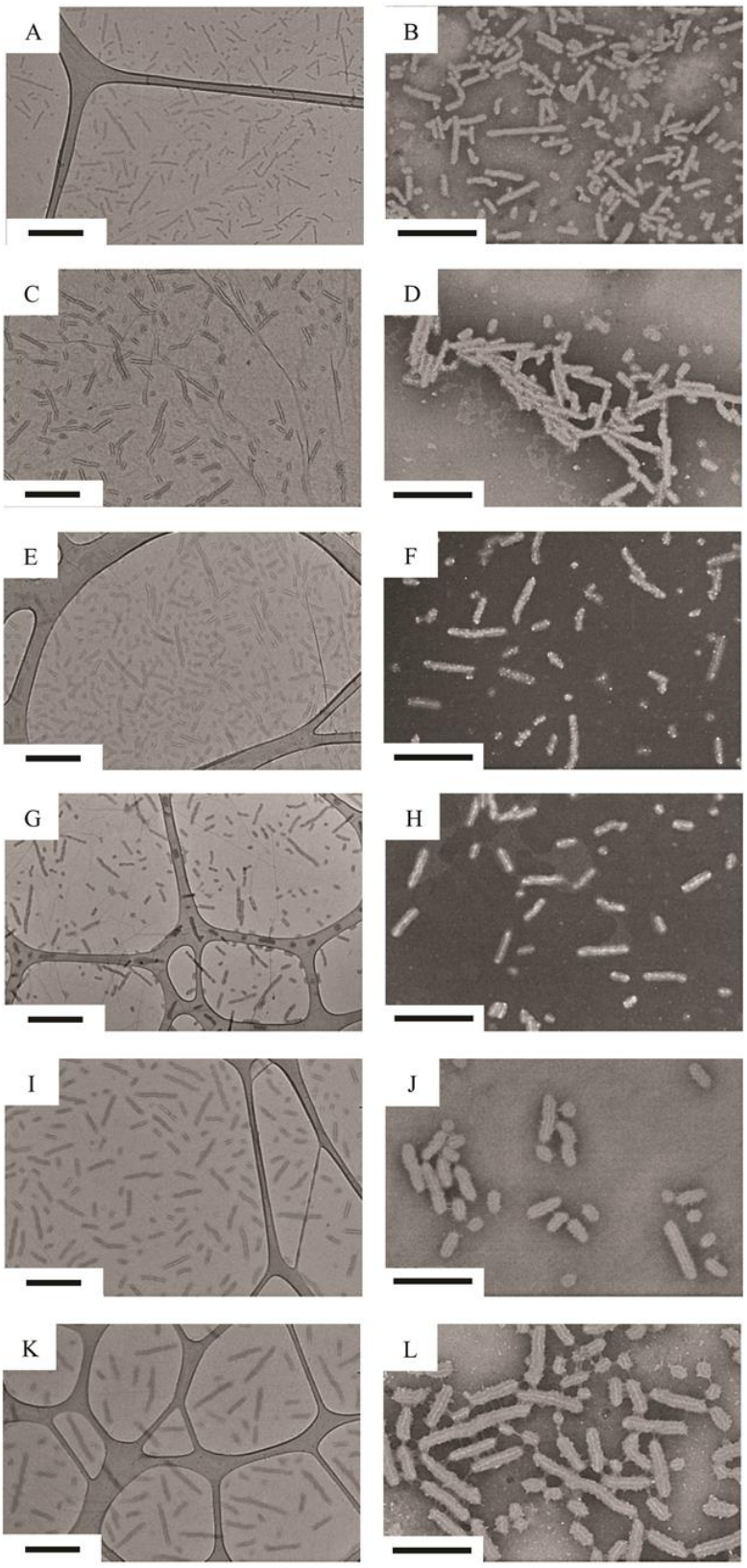

Figure 2.17. Cylindrical micelles obtained from the CDSA of **7** (A, B), **8** (C, D), **9** (E, F), **4** (G, H), **10** (I, J) and **11** (K, L) containing the same hydrophobic block length but different overall hydrophobic weight fractions. Samples A, C, E, G, I, K were prepared

by slow drying on GO grids and imaged without staining. Samples B, D, F, H, J, L were also prepared by slow drying but were negatively stained using PTA. The dramatic increase in the widths of these cylinders, as a result of the increasing PAA block lengths, could be easily observed after stained by PTA. Scale bar = 500 nm.

Table 2.7. Characterization data of cylinder dimensions

Sample	L_n [a] **(nm)**	L_w [a] **(nm)**	L_w/L_n	W_n [a] **(nm)**
7'	134	166	1.24	45 ± 5
8'	157	194	1.24	49 ± 9
9'	141	174	1.24	59 ± 6
4'	145	175	1.21	61 ± 6
10'	225	289	1.28	86 ± 13
11'	251	317	1.26	95 ± 10

[a] Determined by TEM analysis.

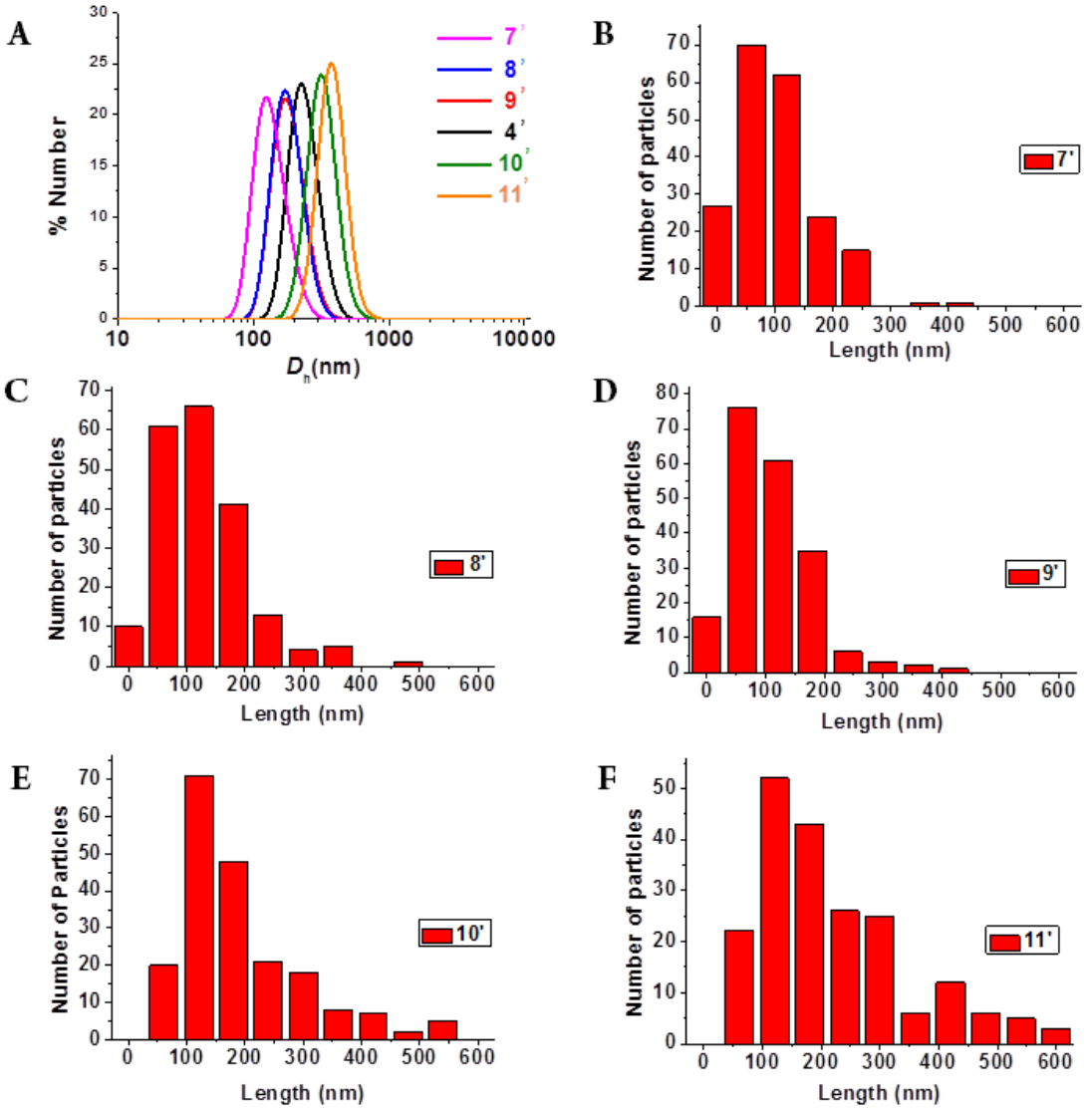

Figure 2.18. A) DLS number distributions of cylindrical micelles self-assembled from diblock copolymers, **4**, **7**, **8**, **9**, **10** and **11**, showing an increasing trend of apparent hydrodynamic diameter when the PAA block length is increased. B, C, D, E, F) Histograms of the lengths of PLLA-*b*-PAA cylindrical micelles, **7'** - **11'**, as determined by TEM analysis.

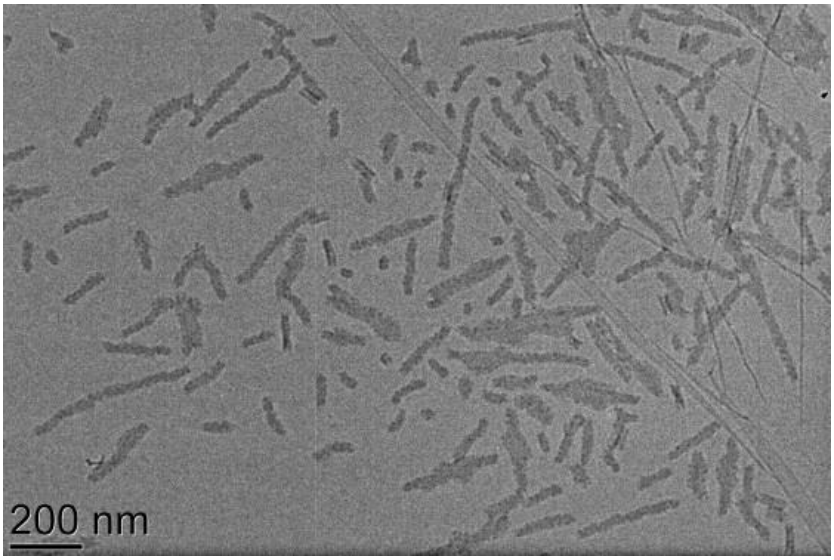

Figure 2.19. TEM image (imaged without staining on GO) showing a mixture of lamellar and cylindrical particles achieved from the self-assembly of polymer, **6**. Scale bar = 200 nm.

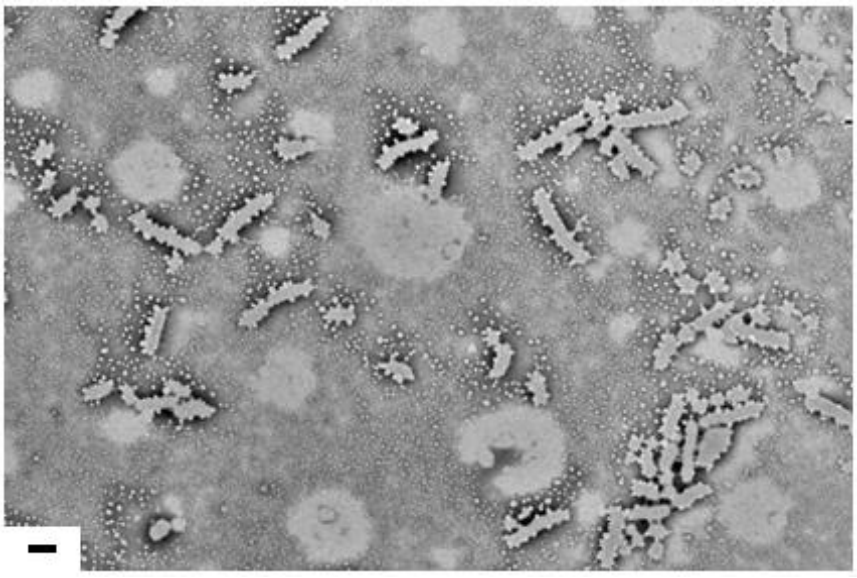

Figure 2.20. TEM image (stained by PTA) showing a mixture of spherical and cylindrical particles achieved from the self-assembly of polymer, **11**. Scale bar = 200 nm.

Measurement of the lengths of the cylindrical micelles in this series resulted in the observation that between 36.6% and 18.6% hydrophobic weight fraction, the lengths were similar (*ca.* 145 nm), most likely a consequence of similar crystallization behavior that resulted from the same PLLA block length in each case. However, at hydrophobic weight fractions below 15%, a dramatic increase in the lengths of **10'** and **11'** were observed. This phenomenon can be explained by the Vilgis and Halperin chain-folding model of crystalline-coil block copolymers.[48] As the longer PAA chains have a larger radius of gyration, they tend to occupy more space[23] and as a result coronal repulsion will increase. In order to decrease the repulsion between the overcrowding PAA chains and to minimize the PAA grafting density on the crystalline core domain, a larger number of PLLA chain folds are favored at a given PLLA chain length, leading to larger dimensions of the PLLA core as observed in the dimensions of the resultant cylinders. Another reason for this dramatic increase in length can be ascribed to the contribution of the PAA corona (end cap) on the contour length as cylinder, **10'** and **11'**, possess much longer PAA blocks than other samples. Combining these observations, it can be concluded that the lengths of PLLA-*b*-PAA cylinders depend mainly on the length of the PLLA core block.

The crystalline nature of the core for each cylindrical micelle was proven by WAXD (Figure 2.21) with the relative core crystallinity calculated using the method described previously. The core crystallinity of **4'** and **7'** - **11'** was found to be similar (*ca.* 0.90; Table 2.8), most likely a result of the block copolymers containing an identical crystallizable PLLA block length. Comparison of **1'** (DP of PLLA = 16; hydrophobic weight fraction = 17.5%; relative core crystallinity = 0.45) with that of **10'** (DP of PLLA = 45; hydrophobic weight fraction = 14.9%;

relative core crystallinity = 0.90), shows that core crystallinity, which is derived from the DP of PLLA, rather than a high hydrophobic weight fraction within the block copolymer, is a critical factor to enable CDSA and afford cylindrical micelles.

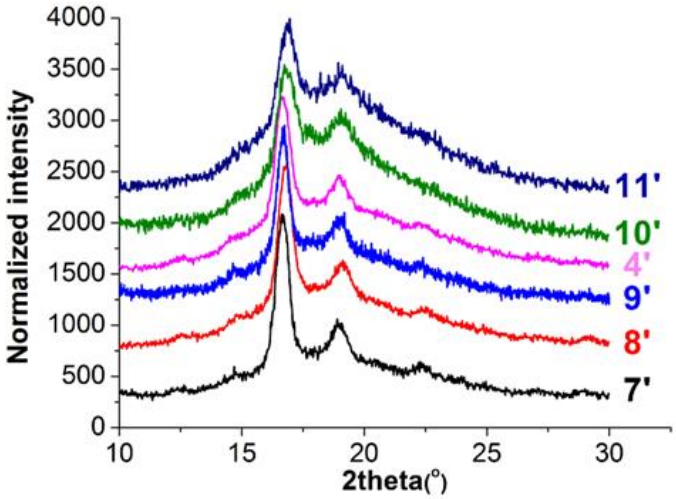

Figure 2.21. WAXD diffractograms for the cylindrical micelles, **4'** and **7'** - **11'**, showing the characterization signals attributable to the crystalline core nature of the nanostructures.

Table 2.8. Characterization data of core crystallinity of cylinder, **4'** and **7'** to **11'**

Sample	Relative core crystallinity [a]
7'	0.95
8'	0.93
9'	0.83
4'	0.92
10'	0.90
11'	0.86

[a] Determined by WAXD, relative core crystallinity is defined as crystallinity relative to the most crystalline sample, **5'**.

However, considering the CDSA results of **1'** (aggregated structures), **6'** (cylinders with lamellar particles) and **11'** (cylinders with spheres), we would reinforce that both the core crystallinity and the hydrophobic weight fraction can determine the assembly window to access PLLA-*b*-PAA cylinders. To be more specific, at a given PLLA block length that can offer sufficient core crystallinity for CDSA, an excess hydrophobic weight fraction (short corona block) provides insufficient coronal repulsions and yields lamellar particles with low interfacial curvature (**6'**) while an inadequate hydrophobic weight fraction (long corona block) gives strong repulsions between PAA chains and leads to spheres with high interfacial curvature (**11'**). Therefore, a moderate hydrophobic weight fraction (between 15 and 35 wt%) is favored to obtain cylindrical micelles. However, if the PLLA block is too short and hence fails to provide sufficient core crystallinity for CDSA, cylindrical structures could not be realized even when the diblock copolymer were designed at a sufficient hydrophobic weight fraction (**1'**).

2.3.5 Study of the effect of different pH values on the PLLA-*b*-PAA cylindrical morphologies

In order to explore the effect of pH on the dimensions of the resultant PLLA-*b*-PAA cylinders, through variation of the coronal volume by adjusting the pH, three CDSAs of diblock copolymer, **3**, were set up using the standard conditions. After 3 h the pH of the CDSA solution was observed to be 2.9. This solution was divided into three and the pH values of two of these solutions were adjusted to 5.7 and 8.3 respectively, the third was not adjusted. After a further 27 h, cylindrical micelles were obtained in all cases and no significant changes

in their dimensions or size distributions were observed by TEM or DLS analysis (Figure 2.22, Figure 2.23, and Table 2.9). These results demonstrate that in this CDSA process, the pH of the coronal block is not a critical factor in the determination of the dimensions of the resultant cylindrical micelles.

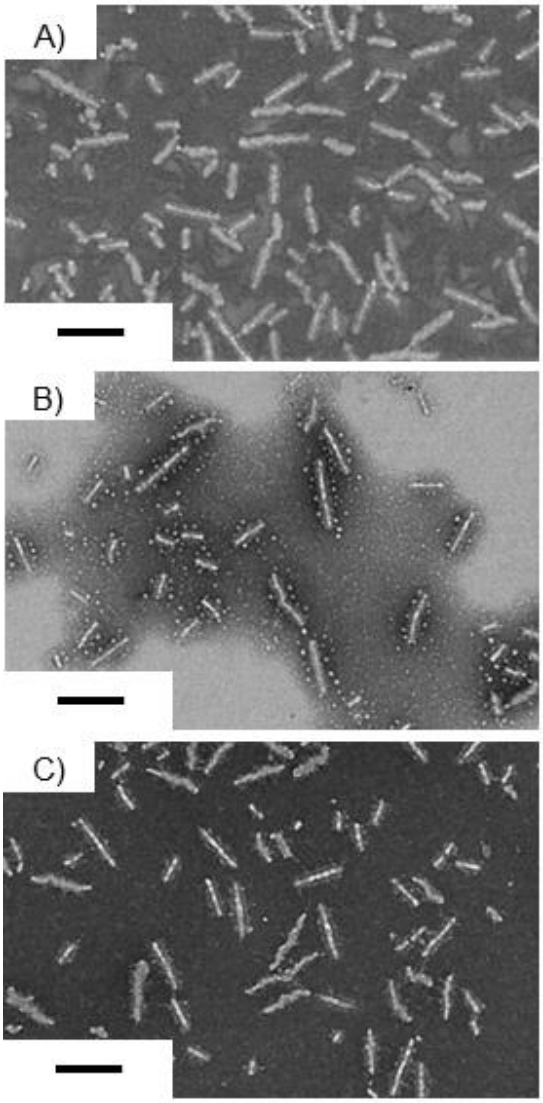

Figure 2.22. TEM images (stained by PTA) showing $PLLA_{38}$-*b*-PAA_{333} cylindrical micelles obtained at different pH conditions. A) pH = 2.9, B) pH = 5.7, C) pH = 8.3. Scale bar = 200 nm.

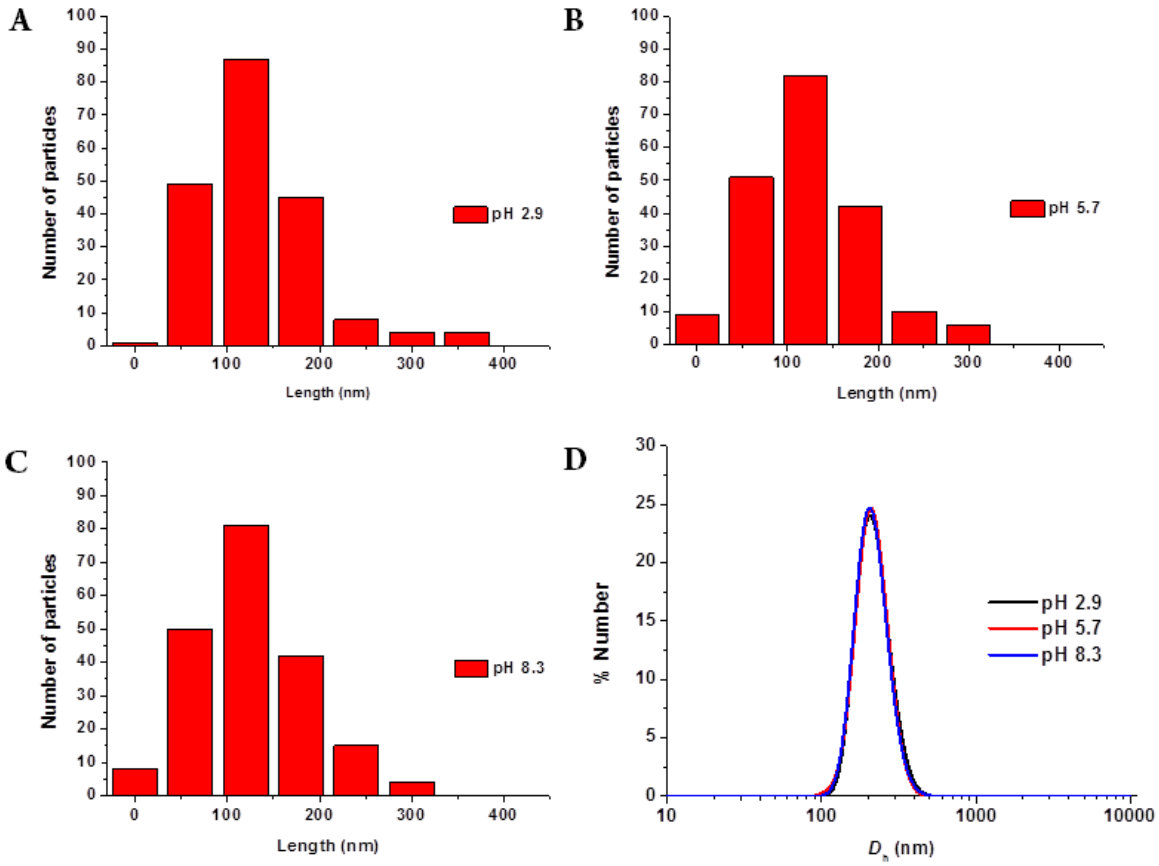

Figure 2.23. A, B, C) Histograms of the lengths of $PLLA_{38}$-*b*-PAA_{333} cylindrical micelles prepared at various pH conditions (determined by TEM analysis). D) DLS data showing the size distributions of $PLLA_{38}$-*b*-PAA_{333} cylindrical micelles obtained at different pH values.

Table 2.9. Characterization data of the size of the $PLLA_{38}$-*b*-PAA_{333} cylinders obtained at different pH values

Conditions	L_n[a]	L_w[a]	L_w/L_n	W_n[a]
pH 2.9	166	193	1.16	60.0 ± 7
pH 5.7	153	174	1.15	63.0 ± 7
pH 8.3	154	179	1.16	57.4 ± 6

[a] Determined by TEM analysis.

2.4 Conclusions

In summary, the window of the formation of PLLA-*b*-PAA cylinders has been shown to be very broad and exist from 14.9% to 36.6% hydrophobic weight fraction (expanded by at least 20% from previous reports). The successful tuning of the lengths and widths of various PLLA-*b*-PAA cylinders was demonstrated by changing the compositions of the diblock copolymers. As such, both the core crystallinity and the hydrophobic weight fraction have been shown to determine the window to access PLLA-*b*-PAA cylinders, with starting copolymers that display a moderate hydrophobic weight fraction favored. All of the resultant cylindrical micelles possessed narrow size distributions as proved by TEM and DLS analysis. Combination of the observed effects of varied PLLA and PAA blocks upon CDSA and the dimensions of the resultant cylindrical micelles emphasized that the contour lengths of PLLA-*b*-PAA cylinders mainly depended on the PLLA core block while the PAA corona governed their resultant widths. Moreover, the block length of crystallizable PLLA played an important role on the core crystallinity and was independent of hydrophobic weight fraction. Furthermore, SAXS analysis further proved that a sphere to cylinder morphological transition occurs in line with the core crystallization. Finally, conducting the CDSA at different pH did not significantly affect the dimensions of the resultant PLLA-*b*-PAA cylinders, providing further evidence that it is the core PLLA block which is critical in the determination of the cylinder dimensions.

2.5 Experimental section

2.5.1 Materials

Chemicals and solvents were purchased from Aldrich, Acros, Fluka, Fisher Chemical, Alfa Aesar or VWR. *L*-Lactide monomer was kindly donated by Corbion-Purac and dried over 3 Å molecular sieves in dichloromethane before recrystallization from toluene and stored in a glove box with inert atmosphere. (-)-Sparteine was distilled over CaH_2 before use and 1-(3,5-bis(trifluoromethyl)phenyl)-3-cyclohexyl-thiourea was prepared and purified as previously reported.[51] Tetrahydropyran acrylate (THPA) was synthesized and purified as described previously.[52, 53] 2,2'-azobis(isobutyronitrile) (AIBN) was recrystallized in methanol and stored at 4 °C.

2.5.2 Instrumentation

^1H NMR spectra were recorded on a Bruker DPX400 spectrometer operating at a frequency of 400 MHz in $CDCl_3$ unless otherwise stated. The chemical shifts are given in ppm with tetramethylsilane (TMS) as an internal reference. Size exclusion chromatography (SEC) was performed in an Agilent 1260 Infinity Multi-Detector SEC System equipped with refractive index and UV detector with THF and 2% triethyl amine as eluent at a flow rate of 1 mL/min. SEC data were calibrated by Cirrus SEC software with poly(styrene) (PS) standards.

Mass spectra were obtained by using Bruker Ultraflex II Matrix-assisted laser desorption/ionization time of flight (MALDI-ToF) mass spectrometer. The MALDI-ToF samples were prepared as follows: trans-2-[3-(4-*tert*-butyl-phenyl)-2-methyl-2-propenylidene] malononitrile (DCTB) was used as matrix while

sodium trifluoroacetate (NaTFA) was used as cationization agent. Typically, DCTB (20 µL of a 40 mg/mL HPLC grade tetrahydrofuran solution), samples (20 µL of a 1 mg/mL HPLC grade tetrahydrofuran solution) and NaTFA (20 µL of a 0.1 mg/mL HPLC grade tetrahydrofuran solution) were added into a small centrifuge tube successively and mixed by a vortex mixer. Traces of mixture were deposited on a MALDI-ToF plate followed by solvent evaporation. The samples were measured in reflectron ion mode and calibrated by SpheriCal (1200 ~ 8000 g/mol) standards.

Transmission electron microscopy (TEM) was performed using a JEOL 2000FX at 200 kV. TEM samples were deposited on graphene oxide (GO)-covered TEM grids, where GO which is almost electron transparent and gives excellent image contrast.[47] Generally, one drop of the sample solution (20 µL) was added onto a GO grid and after 2 min, the solution was blotted away before drying totally. The GO grids were prepared as follows: lacey carbon grids (400 Mesh, Cu, Elektron Technology UK LTD) were cleaned by air plasma from a glow-discharge system (2 min, 20 mA) to improve the hydrophilicity of the lacey carbon. One drop of GO solution (0.10 - 0.15 mg/mL) was deposited on each grid and left to air-dry totally. Phosphotungstic acid (PTA, 2%) was used for the negative staining of TEM samples on formvar/carbon grid (300 Mesh, Cu, Elektron Technology UK LTD). TEM images were analyzed by Image J software and 200 particles were counted for each sample to obtain the number-average length (L_n), weight-average length (L_w) and number-average width (W_n). L_n, L_w and W_n were calculated by using the following equations:

$$L_n = \frac{\sum_{i=1}^{n} N_i L_i^2}{\sum_{i=1}^{n} N_i L_i} \qquad (1)$$

$$L_w = \frac{\sum_{i=1}^{n} N_i L_i^2}{\sum_{i=1}^{n} N_i L_i} \quad (2)$$

$$W_n = \frac{\sum_{i=1}^{n} N_i W_i}{\sum_{i=1}^{n} N_i} \quad (3)$$

where L_i and W_i are the length and the width of each counted cylindrical micelle while N_i is the number of the cylindrical micelles with the length of L_i and the width of W_i.

The hydrodynamic diameter (D_h) of different nanoparticles was determined by dynamic light scattering (DLS). Typically, 0.25 mg/mL aqueous nanoparticle solutions were measured in a Malvern Zetasizer NanoS instrument equipped with a 4 mW He-Ne 633 nm laser module at 25 °C. Measurements were carried out at a detection angle of 173° (back scattering) and the data was further analyzed by Malvern DTS 6.20 software. D_h was calculated by fitting the apparent diffusion coefficient in the Stokes-Einstein equation $D_h = kT/(3\pi\eta D_{app})$, where k is the Boltzmann constant, T is the temperature and η is the viscosity of the solvent. D_h only coincides to the real hydrodynamic diameter when the measured sample is monodispersed spherical particles as D_{app} equals the translational diffusion (D_t). For cylindrical particles, because of their anisotropy, the rotational diffusion is not negligible and contributes to the D_{app}. Therefore, the D_h measured in this study only has a relative value and provides polydispersity information to detect multiple populations.

Small-angle X-ray scattering (SAXS) measurements were carried out on the SAXS/WAXS beamline at the Australian Synchrotron facility at a photon energy of 11 keV. The samples in solution were run by using 1.5 mm diameter quartz capillaries. The reaction took place in heated vials and the solution was circulated through the capillaries *via* a peristaltic pump. Such a set-up allows

living data to be collected *in situ*, which reflects the overall self-assembly. The measurements were collected at sample to detector distance of 7.1 m to give a q range of 0.001 to 0.1 $Å^{-1}$, where q is the scattering vector and is related to the scattering angle (θ) and the photon wavelength (λ) by the following equation:

$$q = \frac{4\pi \sin(\theta)}{\lambda} \qquad (4)$$

The scattering from a blank (THF/H_2O) was measured in the same location as sample collection and was subtracted for each measurement. The two-dimensional SAXS images were converted into one-dimensional SAXS profiles ($I(q)$ versus q) by circular averaging, where $I(q)$ is the scattering intensity.

Wide-angle X-ray diffraction (WAXD) was performed on a Panalytical X'Pert Pro MPD equipped with a Cu Kα1 hybrid monochromator as the incident beam optics. The PiXcel detector enables the statistics to be better counted and the elimination of noise. Typically, *ca*. 30 mg of freeze dried particles after self-assembly was placed in a 10 mm sample holder and standard "powder" 2θ - θ diffraction scans were carried out in the angular range from 10° to 30° 2θ at room temperature. The WAXD diffractograms were processed by MDI Jade software to calculate the crystallinity of different samples.

Differential scanning calorimetry (DSC) analysis was performed on a Mettler Toledo HP DSC827 equipment. Samples were run at a heating or cooling ramp of 10 °C/min in triplicate in series under a nitrogen atmosphere in 40 µL aluminum crucibles. T_g and T_m of various samples were obtained in the first runs and were taken as the midpoint of the inflection tangent.

2.5.3 Synthesis of dual ROP/RAFT initiator dodecyl 4-(hydroxymethyl) benzyl carbonotrithioate

The dual headed initiator was synthesized as reported previously.[44] Typically, 1-dodecanethiol (1.29 g, 6.4 mmol), potassium phosphate (1.48 g, 7 mmol) and carbon disulphide (1.14 mL, 19 mmol) were added into 200 mL acetone. After stirring for 2 h at room temperature, 4-chloromethylbenzyl alcohol (1.00 g, 6.4 mmol) was added into the solution and the mixture was stirred for another 24 h. Acetone was removed *in vacuo* and the resultant solid was dissolved in dichloromethane. The organic layer was washed against HCl (1 M, 200 mL × 1), deionized water (200 mL × 3) and brine (200 mL × 1) before drying over magnesium sulfate. Solids were removed by filtration and the solution was concentrated *in vacuo* before being passed through a silica column (*n*-hexane : ethyl acetate = 60 : 40). The solvent was removed *in vacuo* to yield a yellow solid which was dried over P_2O_5 in a dessicator for 2 days before being transferred into a glove box. ^{1}H NMR (400 MHz, $CDCl_3$, ppm) δ = 7.40 - 7.28 (4H, m, H6 & H7), 4.68 (2H, d, $^{3}J_{H\text{-}H}$ = 5.0 Hz, H8), 4.61 (2H, s, H5), 3.37 (2H, t, $^{3}J_{H\text{-}H}$ = 7.5 Hz, H4), 1.77 - 1.58 (3H, m, H3 & H9), 1.46 - 1.20 (18H, m, H2), 0.88 (3H, t, $^{3}J_{H\text{-}H}$ = 7.0 Hz, H1); ^{13}C NMR (150 MHz, $CDCl_3$, ppm) δ = 223.7 (C5), 140.4 (C7), 134.6 (C10), 129.5 (C8), 127.3 (C9), 65.0 (C11), 41.0 (C6), 37.1 (C4), 32-22 (C2 & C3), 14.1 (C1).

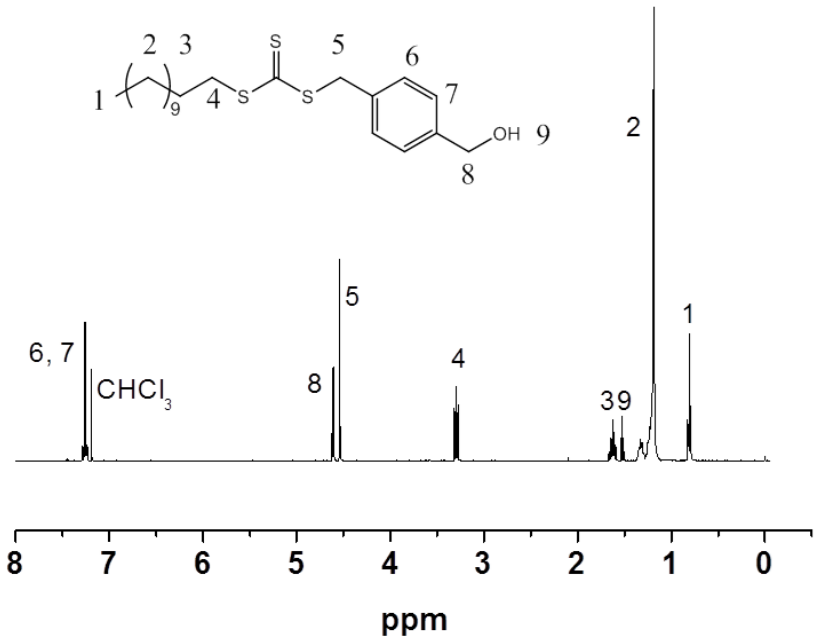

Figure 2.24. ^{1}H NMR spectrum of dual-headed initiator dodecyl 4-(hydroxymethyl) benzyl carbonotrithioate (400 MHz, $CDCl_3$).

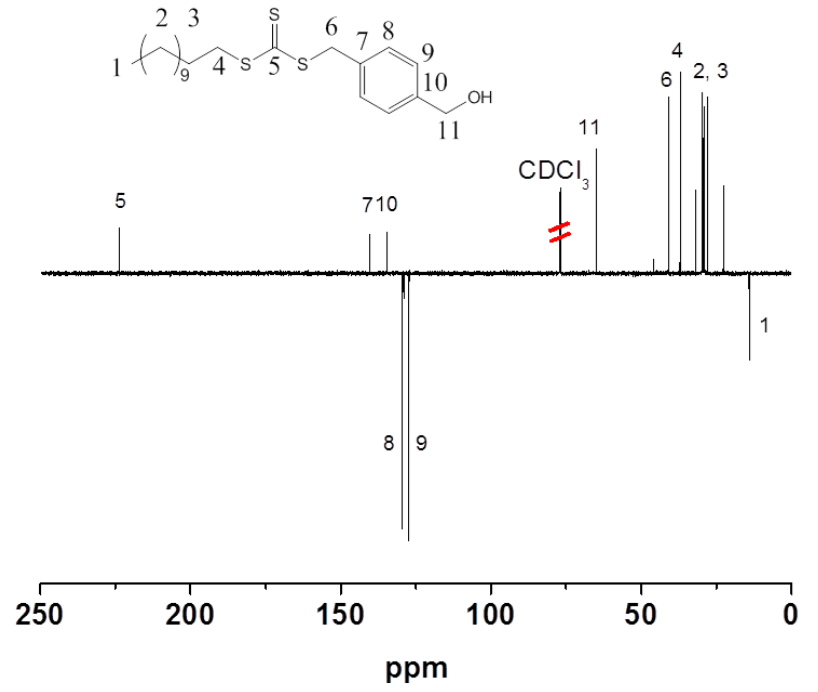

Figure 2.25. ^{13}C NMR spectrum of dual-headed initiator dodecyl 4-(hydroxymethyl) benzyl carbonotrithioate (150 MHz, $CDCl_3$).

2.5.4 Synthesis of poly(*L*-lactide) using ROP

Poly(*L*-lactide) were synthesized in a glove box under nitrogen atmosphere as reported previously.[44] Typically, for DP = 31, dual headed initiator, dodecyl 4-(hydroxymethyl) benzyl carbonotrithioate (92.7 mg, 0.23 mmol) and (-)-sparteine (40.1 µL, 0.17 mmol) were combined in one vial with *L*-lactide (1.01 g, 6.98 mmol) and 1-(3,5-bis(trifluoromethyl)phenyl)-3-cyclohexyl-thiourea (129.2 mg, 0.35 mmol) in another. Dichloromethane (4 mL and 6 mL for each vial respectively) was then added to each of the vials before the two solutions were mixed and left to stir at room temperature for 3 h. Product was precipitated in *n*-hexane three times before filtration and drying *in vacuo* to yield a yellow solid. ^{1}H NMR (400MHz, $CDCl_3$, ppm) δ = 7.36 - 7.30 (4H, m, H6 & H7), 5.40 - 5.30 (2H PLLA + 2H, m, H9 & H11 & H8), 4.61 (2H, s, H5), 4.40 - 4.30 (1H, m, H13), 3.37 (2H, t, $^{3}J_{H\text{-}H}$ = 7.5 Hz, H4), 1.66 - 1.48 (6H PLLA + 2H, m, H10 & H12 & H3), 1.34 - 1.18 (18H, br, H2), 0.88 (3H, t, $^{3}J_{H\text{-}H}$ = 6.5 Hz, H1); $Đ_M$ (SEC, THF with 2% TEA as eluent) = 1.07.

2.5.5 Synthesis of PLLA-*b*-PTHPA diblock copolymers using RAFT polymerization

The representative procedure of the synthesis of diblock copolymer **2** is as follows. THPA (2.504 g, 400 *eq*.) and $PLLA_{31}$ macro-initiator (0.195 g, 1 *eq*.) were dissolved in $CHCl_3$ (2.5 mL) and transferred into a dried ampoule before adding AIBN (65.8 µL of a 10 mg/mL $CHCl_3$ solution). The solution was degassed by three freeze-pump-thaw cycles and sealed under argon and then placed in a 60 °C oil bath with stirring for 2.5 h. The product was precipitated into *n*-hexane before being reprecipitated using the same solvent system a

further two times and dried *in vacuo* to give a yellow solid (67% conversion by ^{1}H NMR spectroscopy) with a high yield of 98%. The DP of PTHPA was determined by comparing with the DP of PLLA in ^{1}H NMR spectra in Figure 2.1. ^{1}H NMR (400MHz, $CDCl_3$, ppm) δ = 6.20 - 5.68 (1H PTHPA, br, H5), 5.26 - 5.04 (2H PLLA, m, H12 & H14), 3.96 - 3.58 (2H PTHPA, br, H9), 2.66 - 2.24 (1H PTHPA, br, H3), 2.18 - 1.36 (8H PTHPA & 6H PLLA, br m, H4 & H6 & H7 & H8 & H13 & H15); $Đ_M$ (SEC, THF with 2% TEA as eluent) = 1.13.

2.5.6 Crystallization-driven self-assembly of PLLA-*b*-PTHPA diblock copolymers to obtain cylindrical micelles

The self-assembly of various diblock copolymers was carried out by a solvent evaporation method. Typically, 0.5 mL of THF and 2 mL of water (resistivity 18.2 MΩ•cm) (*v* : *v* = 20 : 80) were added to 50 mg polymer inside a vial. Acetic acid (1 *eq*. to the DP of PTHPA) was also added to the mixture to facilitate the hydrolysis of THPA blocks. The vial was sealed with a needle inserted through the seal and the mixture was allowed to stir at 65 °C (above the T_g of PLLA)[54] for 30 h before being quenched by cooling in liquid nitrogen and subsequent lyophilization. The freeze-dried PLLA-*b*-PAA particles were then dissolved directly into water (0.25 mg/mL) and heated at 65 °C for 1 h to allow for well-dispersed nanostructures.

2.5.7 Changing the pH conditions of crystallization-driven self-assembly of $PLLA_{38}$-*b*-PAA_{333} diblock copolymers

Three separate CDSAs of $PLLA_{38}$-*b*-$PTHPA_{333}$ diblock copolymers were set up using the standard conditions described above. After 3 h, the pH values of two

of the solutions were adjusted to 5.7 and 8.3 respectively by addition of sodium hydroxide aqueous solution. The remaining solution was left with pH unchanged at 2.9. The three particle solutions were left for another 27 h at 65 °C under standard assembly conditions before being cooled in liquid nitrogen and lyophilized. The freeze dried particles were dissolved in water (resistivity 18.2 MΩ•cm) (*ca.* 15 mg/mL) and dialyzed against water for 2 days to remove sodium acetate salts.

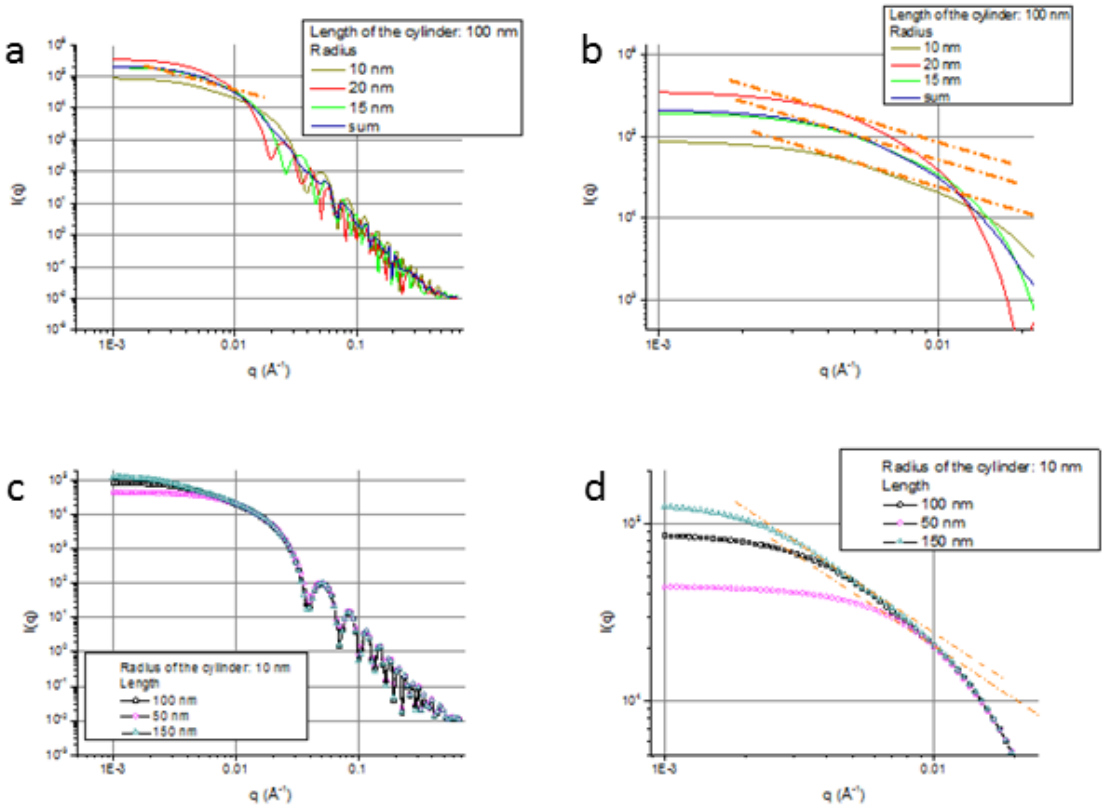

Figure 2.26. SAXS fitting of cylindrical nanoparticles with various radii for a fixed length (a and b, b is a zoom profile of a) and with various lengths for a fixed radius (c and d, d is a zoom profile of c). It is clearly visible that the q values range for which a slope of -1 is limited.

2.6 Acknowledgements

Dr. Nikos Petzetakis has kindly donated diblock copolymer, **3** used in this chapter. Dr. Anaïs Pitto-Barry in the group has kindly performed the SAXS analysis in Australian synchrotron and fitted all of the SAXS data in this chapter.

2.7 References

(1) Zhang, L. F.; Eisenberg, A. *Science* **1995,** 268, 1728-1731.

(2) Yu, K.; Eisenberg, A. *Macromolecules* **1996,** 29, 6359-6361.

(3) Blanazs, A.; Armes, S. P.; Ryan, A. J. *Macromol. Rapid Commun.* **2009,** 30, 267-277.

(4) Pounder, R. J.; Willcock, H.; Ieong, N. S.; O'Reilly, R. K.; Dove, A. P. *Soft Matter* **2011,** 7, 10987-10993.

(5) Lin, L. Y.; Lee, N. S.; Zhu, J. H.; Nystrom, A. M.; Pochan, D. J.; Dorshow, R. B.; Wooley, K. L. *J. Control. Release* **2011,** 152, 37-48.

(6) Robin, M. P.; Mabire, A. B.; Damborsky, J. C.; Thom, E. S.; Winzer-Serhan, U. H.; Raymond, J. E.; O'Reilly, R. K. *J. Am. Chem. Soc.* **2013,** 135, 9518-9524.

(7) Du, J. Z.; Armes, S. P. *J. Am. Chem. Soc.* **2005,** 127, 12800-12801.

(8) Du, J. Z.; O'Reilly, R. K. *Soft Matter* **2009,** 5, 3544-3561.

(9) Du, J. Z.; Armes, S. P. *Langmuir* **2009,** 25, 9564-9570.

(10) Du, J. Z.; Tang, Y. P.; Lewis, A. L.; Armes, S. P. *J. Am. Chem. Soc.* **2005,** 127, 17982-17983.

(11) Liu, J.; Thompson, Z. J.; Sue, H. J.; Bates, F. S.; Hillmyer, M. A.; Dettloff, M.; Jacob, G.; Verghese, N.; Pham, H. *Macromolecules* **2010,** 43, 7238-7243.

(12) Wang, X. S.; Wang, H.; Coombs, N.; Winnik, M. A.; Manners, I. *J. Am. Chem. Soc.* **2005,** 127, 8924-8925.

(13) Wang, H.; Wang, X. S.; Winnik, M. A.; Manners, I. *J. Am. Chem. Soc.* **2008,** 130, 12921-12930.

(14) Geng, Y.; Dalhaimer, P.; Cai, S. S.; Tsai, R.; Tewari, M.; Minko, T.; Discher, D. E. *Nat. Nanotechnol.* **2007,** 2, 249-255.

(15) Zhang, K.; Rossin, R.; Hagooly, A.; Chen, Z. Y.; Welch, M. J.; Wooley, K. L. *J. Polym. Sci., Part A: Polym. Chem.* **2008,** 46, 7578-7583.

(16) Li, Z.; Ma, J.; Lee, N. S.; Wooley, K. L. *J. Am. Chem. Soc.* **2011,** 133, 1228-1231.

(17) Huang, K.; Rzayev, J. *J. Am. Chem. Soc.* **2009,** 131, 6880-6885.

(18) Chen, Q. J.; Zhao, H.; Ming, T.; Wang, J. F.; Wu, C. *J. Am. Chem. Soc.* **2009,** 131, 16650-16651.

(19) He, W. N.; Xu, J. T.; Du, B. Y.; Fan, Z. Q.; Wang, X. S. *Macromol. Chem. Phys.* **2010,** 211, 1909-1916.

(20) Gilroy, J. B.; Gadt, T.; Whittell, G. R.; Chabanne, L.; Mitchels, J. M.; Richardson, R. M.; Winnik, M. A.; Manners, I. *Nature Chem.* **2010,** 2, 566-570.

(21) Wang, X. S.; Guerin, G.; Wang, H.; Wang, Y. S.; Manners, I.; Winnik, M. A. *Science* **2007,** 317, 644-647.

(22) He, W.-N.; Zhou, B.; Xu, J.-T.; Du, B.-Y.; Fan, Z.-Q. *Macromolecules* **2012,** 45, 9768-9778.

(23) Du, Z. X.; Xu, J. T.; Fan, Z. Q. *Macromol. Rapid Commun.* **2008,** 29, 467-471.

(24) Shen, L.; Wang, H.; Guerin, G.; Wu, C.; Manners, I.; Winnik, M. A. *Macromolecules* **2008,** 41, 4380-4389.

(25) Soto, A. P.; Gilroy, J. B.; Winnik, M. A.; Manners, I. *Angew. Chem. Int. Ed.* **2010,** 49, 8220-8223.

(26) Yusoff, S. F. M.; Gilroy, J. B.; Cambridge, G.; Winnik, M. A.; Manners, I. *J. Am. Chem. Soc.* **2011,** 133, 11220-11230.

(27) Rupar, P. A.; Cambridge, G.; Winnik, M. A.; Manners, I. *J. Am. Chem. Soc.* **2011,** 133, 16947-16957.

(28) Gaedt, T.; Schacher, F. H.; McGrath, N.; Winnik, M. A.; Manners, I. *Macromolecules* **2011,** 44, 3777-3786.

(29) He, F.; Gaedt, T.; Manners, I.; Winnik, M. A. *J. Am. Chem. Soc.* **2011,** 133, 9095-9103.

(30) Massey, J. A.; Temple, K.; Cao, L.; Rharbi, Y.; Raez, J.; Winnik, M. A.; Manners, I. *J. Am. Chem. Soc.* **2000,** 122, 11577-11584.

(31) Rupar, P. A.; Chabanne, L.; Winnik, M. A.; Manners, I. *Science* **2012,** 337, 559-562.

(32) Gadt, T.; Ieong, N. S.; Cambridge, G.; Winnik, M. A.; Manners, I. *Nat. Mater.* **2009,** 8, 144-150.

(33) Qiu, H.; Cambridge, G.; Winnik, M. A.; Manners, I. *J. Am. Chem. Soc.* **2013,** 135, 12180-12183.

(34) Schmelz, J.; Karg, M.; Hellweg, T.; Schmalz, H. *ACS Nano* **2011,** 5, 9523-9534.

(35) Schmelz, J.; Schedl, A. E.; Steinlein, C.; Manners, I.; Schmalz, H. *J. Am. Chem. Soc.* **2012,** 134, 14217-14225.

(36) Gwyther, J.; Gilroy, J. B.; Rupar, P. A.; Lunn, D. J.; Kynaston, E.; Patra, S. K.; Whittell, G. R.; Winnik, M. A.; Manners, I. *Chem. Eur. J.* **2013,** 19, 9186 - 9197.

(37) Patra, S. K.; Ahmed, R.; Whittell, G. R.; Lunn, D. J.; Dunphy, E. L.; Winnik, M. A.; Manners, I. *J. Am. Chem. Soc.* **2011,** 133, 8842-8845.

(38) Lazzari, M.; Scalarone, D.; Vazquez-Vazquez, C.; Lopez-Quintela, M. A. *Macromol. Rapid Commun.* **2008,** 29, 352-357.

(39) Schmalz, H.; Schmelz, J.; Drechsler, M.; Yuan, J.; Walther, A.; Schweimer, K.; Mihut, A. M. *Macromolecules* **2008,** 41, 3235-3242.

(40) Lee, C.-U.; Smart, T. P.; Guo, L.; Epps, T. H.; Zhang, D. *Macromolecules* **2011,** 44, 9574-9585.

(41) Fujiwara, T.; Miyamoto, M.; Kimura, Y.; Iwata, T.; Doi, Y. *Macromolecules* **2001,** 34, 4043-4050.

(42) Zhang, J.; Wang, L. Q.; Wang, H. J.; Tu, K. H. *Biomacromolecules* **2006,** 7, 2492-2500.

(43) Portinha, D.; Boue, F.; Bouteiller, L.; Carrot, G.; Chassenieux, C.; Pensec, S.; Reiter, G. *Macromolecules* **2007,** 40, 4037-4042.

(44) Petzetakis, N.; Dove, A. P.; O'Reilly, R. K. *Chem. Sci.* **2011,** 2, 955-960.

(45) Petzetakis, N.; Walker, D.; Dove, A. P.; O'Reilly, R. K. *Soft Matter* **2012,** 8, 3408-3414.

(46) Petzetakis, N.; Robin, M. P.; Patterson, J. P.; Kelley, E. G.; Cotanda, P.; Bomans, P. H. H.; Sommerdijk, N. A. J. M.; Dove, A. P.; Epps, T. H.; O'Reilly, R. K. *ACS Nano* **2013,** 7, 1120-1128.

(47) Patterson, J. P.; Sanchez, A. M.; Petzetakis, N.; Smart, T. P.; Epps, T. H.; Portman, I.; Wilson, N. R.; O'Reilly, R. K. *Soft Matter* **2012,** 8, 3322-3328.

(48) Vilgis, T.; Halperin, A. *Macromolecules* **1991,** 24, 2090-2095.

(49) Pan, P.; Kai, W.; Zhu, B.; Dong, T.; Inoue, Y. *Macromolecules* **2007,** 40, 6898-6905.

(50) Stoclet, G.; Seguela, R.; Lefebvre, J. M.; Rochas, C. *Macromolecules* **2010,** 43, 7228-7237.

(51) Pratt, R. C.; Lohmeijer, B. G. G.; Long, D. A.; Lundberg, P. N. P.; Dove, A. P.; Li, H. B.; Wade, C. G.; Waymouth, R. M.; Hedrick, J. L. *Macromolecules* **2006,** 39, 7863-7871.

(52) Hertler, W. R. *US Patent* **1991,** No. 5 072 029.

(53) O'Reilly, R. K.; Joralemon, M. J.; Hawker, C. J.; Wooley, K. L. *Chem. Eur. J.* **2006,** 12, 6776-6786.

(54) Becker, J. M.; Pounder, R. J.; Dove, A. P. *Macromol. Rapid Commun.* **2010,** 31, 1923-1937.

Chapter 3. Poly(lactide) Stereocomplexation-Triggered Morphological Transition of Cylindrical Nanoparticles

3.1 Abstract

Co-crystallization or stereocomplexation of polymers with different configurations or tacticities allows the formation of new materials with enhanced performance. Among them, the stereocomplexation of isotactic poly(*L*-lactide) (PLLA) and poly(*D*-lactide) (PDLA) has led to improved properties of the stereocomplex materials compared to each homochiral material. Although the stereocomplexation between PLLA and PDLA has been intensively explored in homopolymer blends, the study of stereocomplexation between block copolymers bearing poly(lactide)s in solution is limited. In this chapter, we report the preparation of stereocomplex micelles from a mixture of poly(*L*-lactide)-*b*-poly(acrylic acid) (PLLA-*b*-PAA) and poly(*D*-lactide)-*b*-poly(acrylic acid) (PDLA-*b*-PAA) diblock copolymers in water *via* crystallization-driven self-assembly (CDSA). During the formation of these stereocomplex micelles, an unexpected morphological transition resulted in the formation of dense crystalline spherical micelles rather than cylinders. Furthermore, the mixing of homochiral PLLA-*b*-PAA cylinders and PDLA-*b*-PAA cylinders led to cylinder disassembly and the formation of stereocomplex spherical micelles *via* a "unimer-exchange" mechanism, which demonstrates the utility of this morphological reorganization for triggered release applications. A similar transition was observed in a related PEO-*b*-PLLA/PEO-*b*-PDLA system and is also proposed to be applicable in a range of additional crystalline polymers. This new mechanism for morphological reorganization, through competitive crystallization and stereocomplexation, allows for new opportunities in controlled release and also delivery applications.

3.2 Introduction

Poly(lactide) has aroused great interest in the biomedical and pharmaceutical fields in the past few decades owing to its outstanding biodegradability, biocompatibility and low toxicity.[1-5] The cyclic lactide monomer presents two stereocenters and thus provides three stereoisomeric forms: *L*-lactide, *D*-lactide, and *meso*-lactide. The polymerization of *L*-lactide or *D*-lactide, in the absence of epimerization, leads to the formation of isotatic poly(*L*-lactide) (PLLA) and poly(*D*-lactide) (PDLA), which can co-crystallize to form a stereocomplex between the two polymer chains with opposite configurations. The stereocomplexation of poly(lactide) was first reported in 1987 by Ikada *et al.* who used differential scanning calorimetry (DSC) and wide-angle X-ray diffraction (WAXD) to study the stereocomplexation of different ratios of PLLA and PDLA blends.[6] It has been reported that the stereocomplex poly(lactide) crystallites are stabilized by CH_3•••O=C hydrogen-bonding interactions between the two poly(lactide) chains of opposite homochirality, resulting in a more compact conformation and more dense polymeric packing in comparison to the homochiral crystallites.[7] Stereocomplexation is of great interest in materials science as the stereocomplex formed between left-handed PLLA and right-handed PDLA polymeric helices has shown to impart improved mechanical and thermal properties to the resulting materials when compared to the equivalent homochiral polymers.[2, 6, 8, 9] Beyond homopolymer blends, the self-assembly of poly(lactide)-containing block copolymers in selective solvents can also induce stereocomplex formation which further improved the properties of resultant nanoparticles.[10-17] For instance, stereocomplexation of poly(*L*-lactide)-*b*-poly(ethylene glycol) (PLLA-*b*-PEG) and poly(*D*-lactide)-*b*-poly(ethylene glycol)

(PDLA-*b*-PEG) diblock copolymers resulted in enhanced stability of the resultant micellar constructs.[12] Stereocomplex micelles prepared from Y-shaped PEG-*b*-PLLA-*b*-PLLA and PEG-*b*-PDLA-*b*-PDLA miktoarm copolymers showed high loadings of paclitaxel.[14] The stereocomplexation of PLLA and PDLA has also enabled access to a wide variety of nanoparticle morphologies.[15, 16] For example, Hedrick and co-workers obtained patchy polymeric micelles from a mixture of poly(*L*-lactide)-*b*-poly(*N*-isopropylacrylamide) (PLLA-*b*-PNIPAAM) and PDLA-*b*-PEG diblock copolymers,[13] while Bouteiller and researchers observed cylindrical micelles by mixing poly(*L*-lactide)-*b*-poly(*ε*-caprolactone) (PLLA-*b*-PCL) and poly(*D*-lactide)-*b*-poly(*ε*-caprolactone) (PDLA-*b*-PCL) in THF.[10, 17]

In our previous studies,[18-21] we have shown PLLA-*b*-PAA or PDLA-*b*-PAA diblock copolymers with a large hydrophilic weight fraction (82%) can assemble into homochiral cylindrical micelles through a crystallization-driven self-assembly (CDSA) process in solution above the glass transition temperature (T_g) of the PLA block (typically 55-60 °C).[18] These cylindrical micelles possessed hollow cores, induced by the hydrogen-bonding interaction between the PLLA core and PAA corona during the slow drying process, and could subsequently be loaded with hydrophobic dyes.[19] In this chapter, the application of stereocomplexation in the CDSA process is explored. In an attempt to form more stable cylinders through stereocomplexation, self-assembly of a mixture of PLLA-*b*-PAA and PDLA-*b*-PAA diblock copolymers was explored and resulted in the unexpected formation of spherical micelles with stereocomplex cores. Furthermore, when mixed under identical CDSA conditions, the two pre-assembled PLLA-*b*-PAA and PDLA-*b*-PAA homochiral

cylinders were found to undergo a morphological transition into spherical micelles with a PLA stereocomplex core. This stereocomplexation induced reorganization was also demonstrated for a biocompatible PEO-*b*-PLA block copolymer system, and also through the addition of a PDLA-*b*-PAA unimer solution to a solution of PLLA-*b*-PAA cylinders with opposite homochirality. This new mechanism of structural reorganization provides a potential new trigger for controlled/targeted drug release in polymeric vehicles.

3.3 Results and discussion

3.3.1 Synthesis of precursor PLLA$_{31}$-*b*-PTHPA$_{332}$, 1, and PDLA$_{28}$-*b*-PTHPA$_{315}$, 2, diblock Copolymers

The diblock copolymers used in this chapter were prepared by a combination of ring-opening polymerization (ROP) of either *L*- or *D*-lactide with the highly selective metal-free thiourea/(-)-sparteine co-catalyst system and reversible addition-fragmentation chain transfer (RAFT) polymerization of tetrahydropyran acrylate (THPA) monomer, from a dual-headed initiator as reported previously (Scheme 3.1).[18, 21] Similar synthetic procedures were given in Chapter 2.

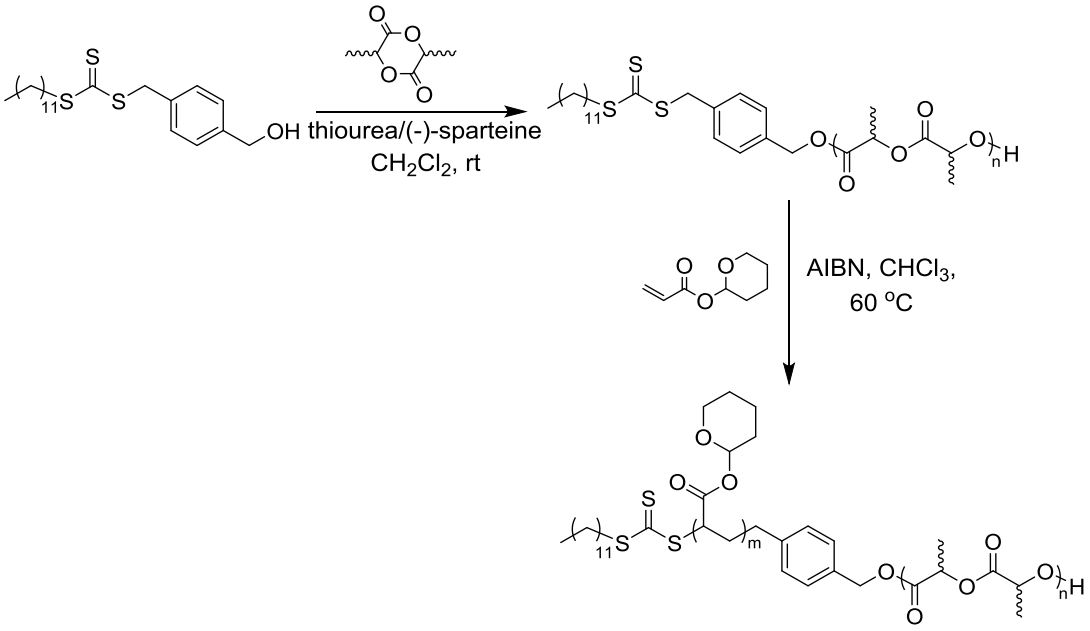

Scheme 3.1. Synthetic procedures of PLA-*b*-PTHPA diblock copolymers.

The compositions of the PLA macro-initiators and precursor PLA-*b*-PTHPA diblock copolymers were determined by ^{1}H NMR spectroscopy, resulting in PLLA$_{31}$ (**1'**), PDLA$_{28}$ (**2'**), PLLA$_{31}$-*b*-PTHPA$_{332}$ (**1**) and PDLA$_{28}$-*b*-PTHPA$_{315}$ (**2**) (Figure 3.1 and Figure 3.4). MALDI-ToF MS measurements of the PLA macro-

initiators were consistent with the expected molar mass and minimal transesterification was observed (Figure 3.3). All the poly(lactide) macro-initiators and diblock copolymers used in this study possess low dispersities ($Đ_M$ < 1.20) as determined by SEC analysis (Figure 3.2,Figure 3.5 and Table 3.1).

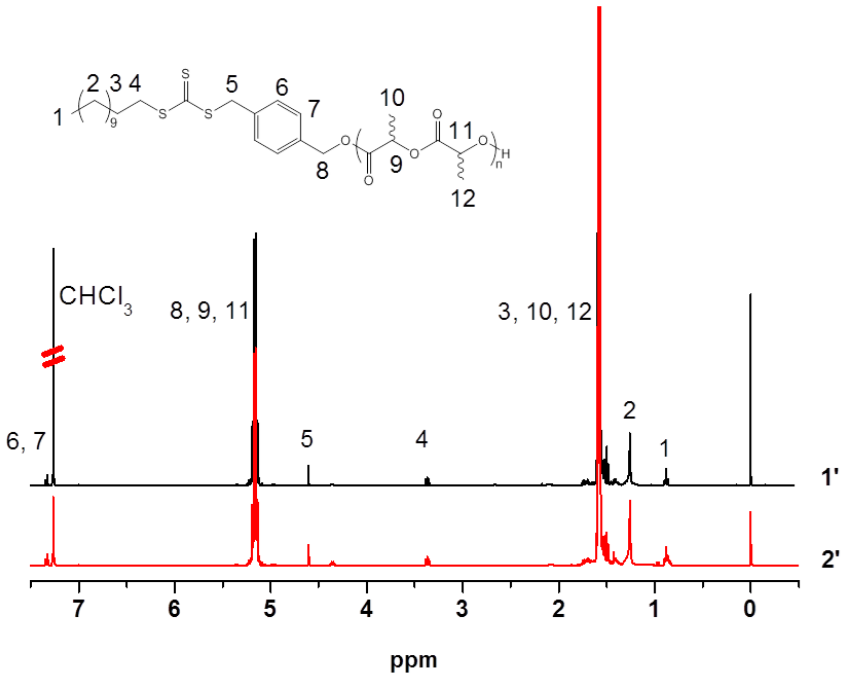

Figure 3.1. ^{1}H NMR spectra of PLLA, **1'** and PDLA, **2'** (400 MHz, $CDCl_3$).

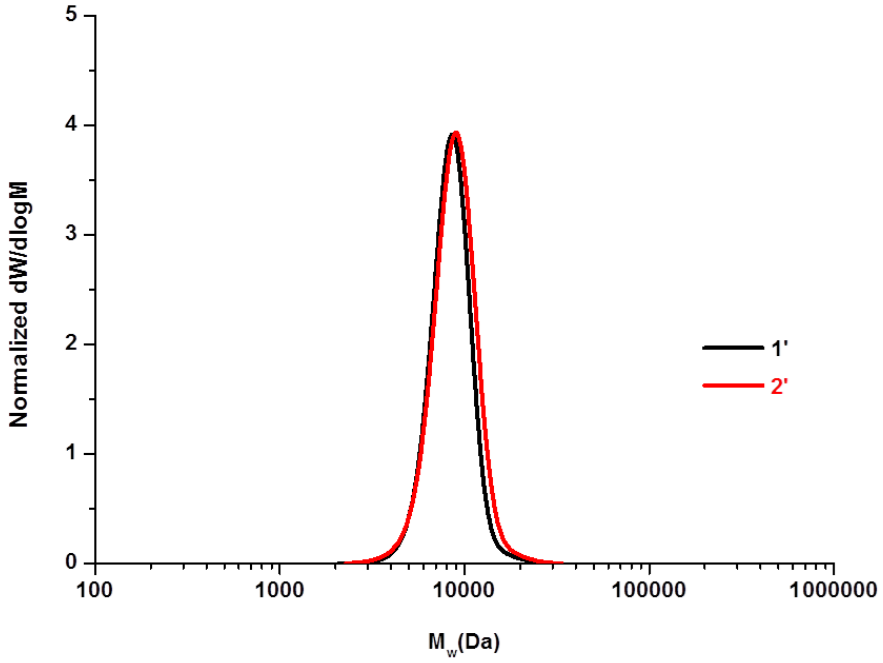

Figure 3.2. SEC chromatograms of PLLA, **1'** and PDLA, **2'** (THF with 2% TEA as eluent, RI detection).

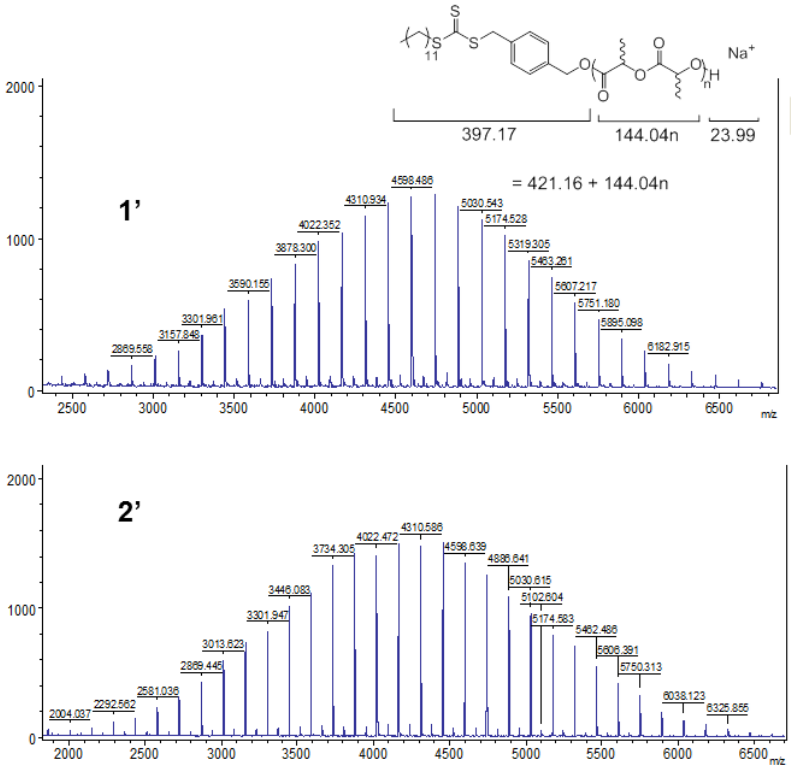

DP	Theoretical m/z	DP	Theoretical m/z
11	2005.6282	27	4310.3002
12	2149.6702	28	4454.3422
13	2293.7122	29	4598.3842
14	2437.7542	30	4742.4262
15	2581.7962	31	4886.4682
16	2725.8382	32	5030.5102
17	2869.8802	33	5174.5522
18	3013.9222	34	5318.5942
19	3157.9642	35	5462.6362
20	3302.0062	36	5606.6782
21	3446.0482	37	5750.7202
22	3590.0902	38	5894.7622
23	3734.1322	39	6038.8042
24	3878.1742	40	6182.8462
25	4022.2162	41	6326.8882
26	4166.2582		

Figure 3.3. MALDI-ToF spectra of macro-CTAs PLLA, **1'** and PDLA, **2'**, showing minimal transesterification.

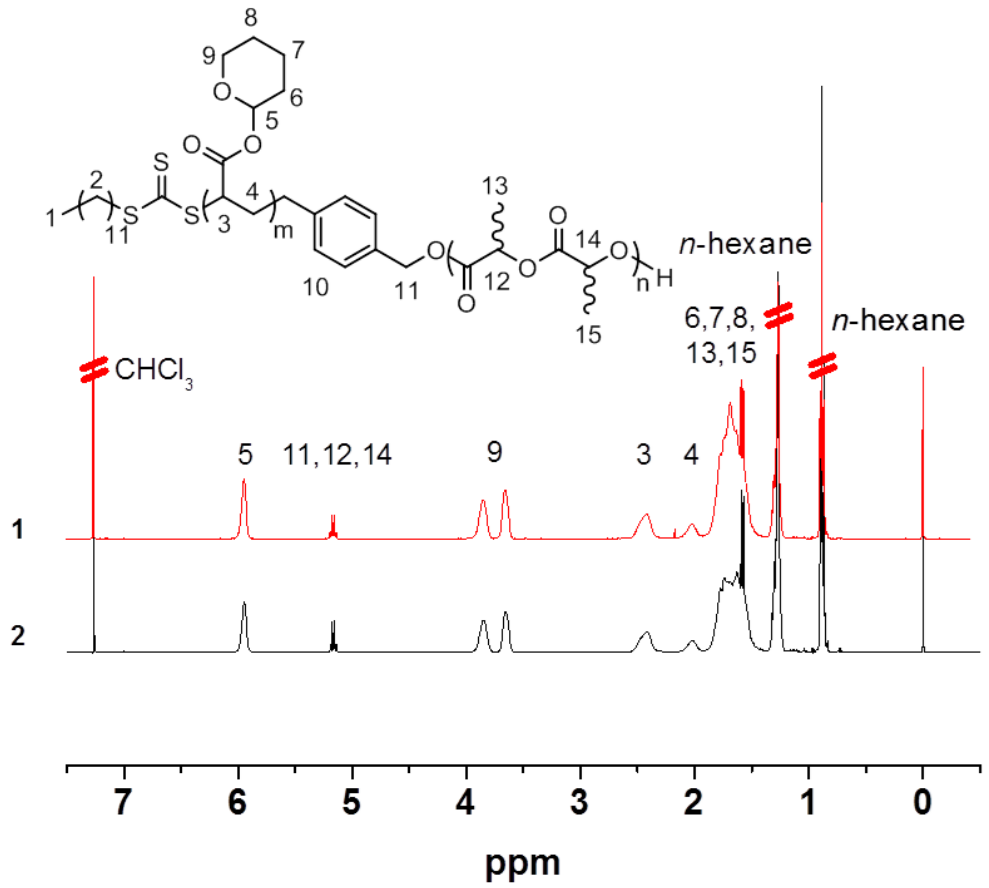

Figure 3.4. ^{1}H NMR spectra of diblock copolymers, **1** and **2** (400 MHz, $CDCl_3$).

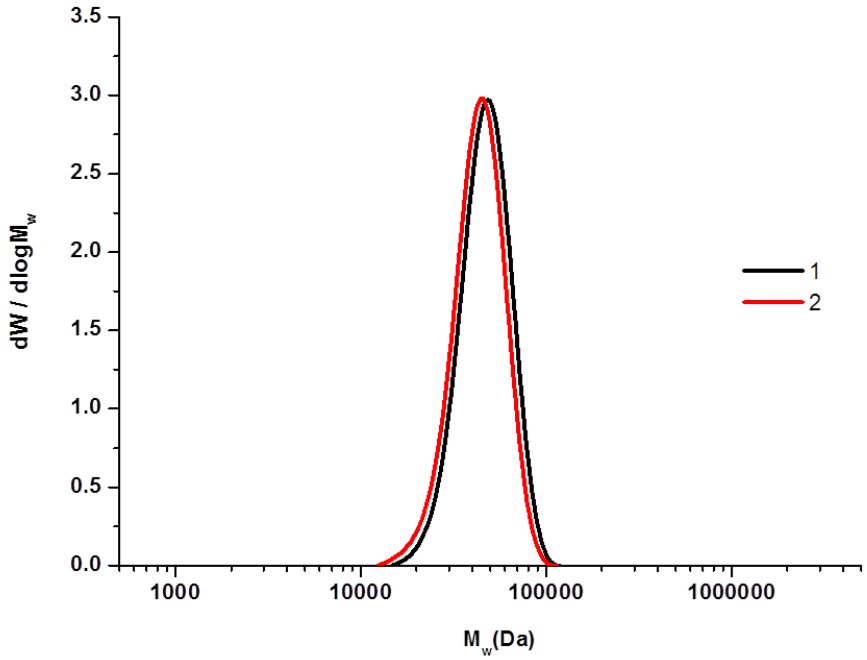

Figure 3.5. SEC chromatograms of **1** and **2** ($CHCl_3$ with 0.5% TEA as eluent, RI detection).

Table 3.1. Characterization data of poly(lactide) macro-CTAs and diblock copolymers

Polymer	M_n (kDa)[a]	$Đ_M$	Hydrophobic weight fraction (%)[d]
$PLLA_{31}$, **1'**	4.7	1.07[b]	—
$PDLA_{28}$, **2'**	4.3	1.08[b]	—
$PLLA_{31}$-*b*-$PTHPA_{332}$, **1**	54.9	1.10[c]	15.7
$PDLA_{28}$-*b*-$PTHPA_{315}$, **2**	52.0	1.11[c]	15.1

[a] Measured by ^{1}H NMR spectroscopy (400 MHz, $CDCl_3$). [b] Measured by THF SEC. [c] Measured by $CHCl_3$ SEC. [d] PLA weight fraction in the final PLA-*b*-PAA diblock copolymer.

3.3.2 Formation of stereocomplex particles achieved from the precursor diblock copolymers, 1 and 2

The exploration of stereocomplex formation of PLLA-*b*-PAA and PDLA-*b*-PAA was conducted using the identical CDSA conditions reported previously by the group and specified in Chapter 2.[18, 21] Specifically, **1** and **2** were mixed in an equal mass ratio in a vial before addition of a mixture of THF and H_2O (v_{THF}/v_{H2O} = 20/80), giving a final diblock copolymer concentration of 20 mg/mL. Acetic acid was added into the mixture to promote the hydrolysis of PTHPA into PAA and hence allow the formation of amphiphilic diblock copolymers. The sealed vial was pierced with a needle to allow the evaporation of THF during the self-assembly process. The temperature of the self-assembly was 65 °C, which is above the T_g of poly(lactide),[22] to allow the PLA blocks to move more freely and thus promote the co-crystallization of PLLA and PDLA. We have previously demonstrated that the PTHPA block can completely convert into PAA within the first 2 h of the self-assembly.[20]

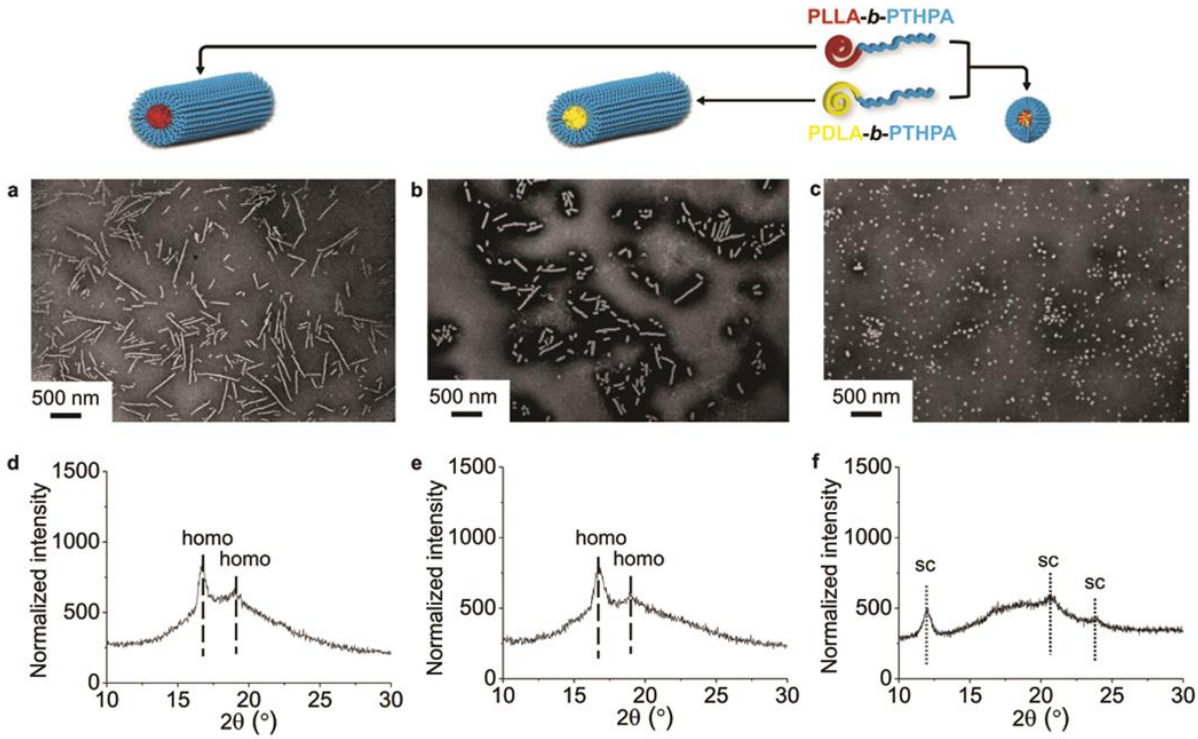

Figure 3.6. Characterization data of the nanostructures obtained from the self-assembly of deprotected diblock copolymers, **1** or/and **2**, showing the different morphologies and crystalline core nature for the homochiral cylinders and stereocomplex spheres. (a) TEM image of cylindrical micelles achieved from the self-assembly of the deprotected *L* enantiomer, **1**; (b) TEM image of cylindrical micelles achieved from the self-assembly of the deprotected *D* enantiomer, **2**; (c) TEM image of spherical micelles obtained from the mixture of the deprotected *L* and *D* enantiomers, **1** and **2**; (d and e) The homochiral cylinders showed Bragg peaks at 2θ values of 16.6° and 19.2° from WAXD diffractograms; (f) Stereocomplex spheres gave Bragg peaks at 2θ values of 12°, 20.6°, 23.8°. All of the particles were obtained after 30 h of self-assembly. TEM samples were prepared by slow drying and negatively stained using phosphotungstic acid (PTA).

After 30 h of self-assembly, spherical micelles (D_n= 49.7 nm) were observed using transmission electron microscopy (TEM) (Figure 3.6c). The observed spherical morphology was not expected as under the same conditions, the self-

assembly of homochiral PLLA-*b*-PAA (or PDLA-*b*-PAA) diblock copolymers lead to the formation of a cylindrical morphology (Figure 3.6a, 3.6b).[18-21] We had hypothesized that a more stable cylindrical structure would form as a result of the stereocomplexation of the diblock copolymers bearing PLLA or PDLA blocks as observed in a related system by Boutellier and co-workers.[10, 17] WAXD was used to confirm the successful co-crystallization of the two enantiomeric PLA blocks in the core domain. Notably, the appearance of an intense Bragg peak at a 2θ value of 12° (which belongs to the (001) plane) definitively proved formation of the crystalline stereocomplexation (Figure 3.6f), while the two homochiral cylinders obtained from deprotected **1** and **2** respectively showed a distinct crystalline Bragg peak at a 2θ value of 16.6° (which belongs to the (110)/(200) planes) that corresponds to homochirality (Figure 3.6d and Figure 3.6e).[2, 6]

The self-assembly process for the formation of stereocomplex spheres was further investigated by fourier transform infrared (FT-IR) spectroscopy (Figure 3.7). The vibration of the carbonyl group of poly(lactide) was found to shift to a lower wavenumber (from 1758 to 1750 cm^{-1}) after 3 h. Such a wavenumber shift is attributed to the rearrangement of the poly(lactide) chains from a disordered state to an ordered one throughout the stereocomplex formation.[10, 17] Following the stereocomplexation process by WAXD (Figure 3.8), an obvious stereocomplex Bragg peak at a 2θ value of 12° is observed after only 3 h, which indicates the fast formation of the stereocomplex micelles. Prolonged assembly under these conditions promoted the stereocomplexation of deprotected **1** and **2**, as evidenced by the increased intensity of the Bragg peak at a 2θ value of 12° as well as the slight increase in diameter of these

spheres, as observed by TEM (from D_n = 41.5 nm in Figure 3.9c to D_n = 49.7 nm in Figure 3.9f). A careful study of the TEM images during the self-assembly process (Figure 3.9b-3.9f) revealed an interesting phenomenon: a number of cylinders existed at the beginning of the self-assembly, but their lengths gradually decreased until the cylindrical morphology had almost disappeared after 30 h. Since the cylinders are believed to only self-assemble from the deprotected homochiral diblock copolymers, **1** or **2**, but not from the stereocomplex, we propose that the crystallization process is fast and leads to the resolution of the mixture into distinct *D* and *L* homochiral cylinders, which over time undergo a morphological transition into stereocomplex spheres.

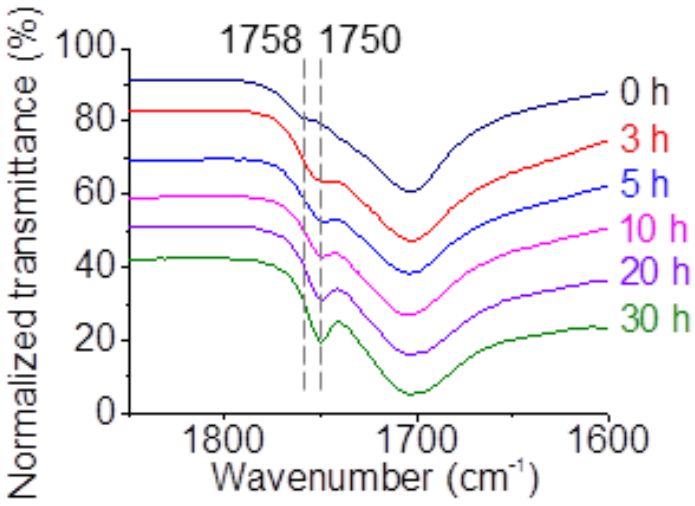

Figure 3.7. FT-IR spectra revealed that the wavenumber of the carbonyl group vibration of poly(lactide) shifted from 1758 to 1750 cm^{-1} over time during the self-assembly of deprotected homochiral polymers, **1** and **2**.

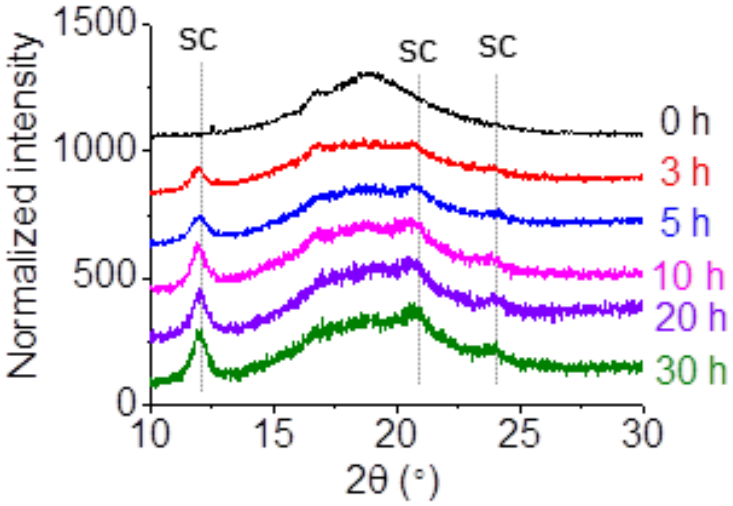

Figure 3.8. WAXD diffractograms showed that the peak for stereocomplex formation between homochiral polymers, **1** and **2**, increased over time.

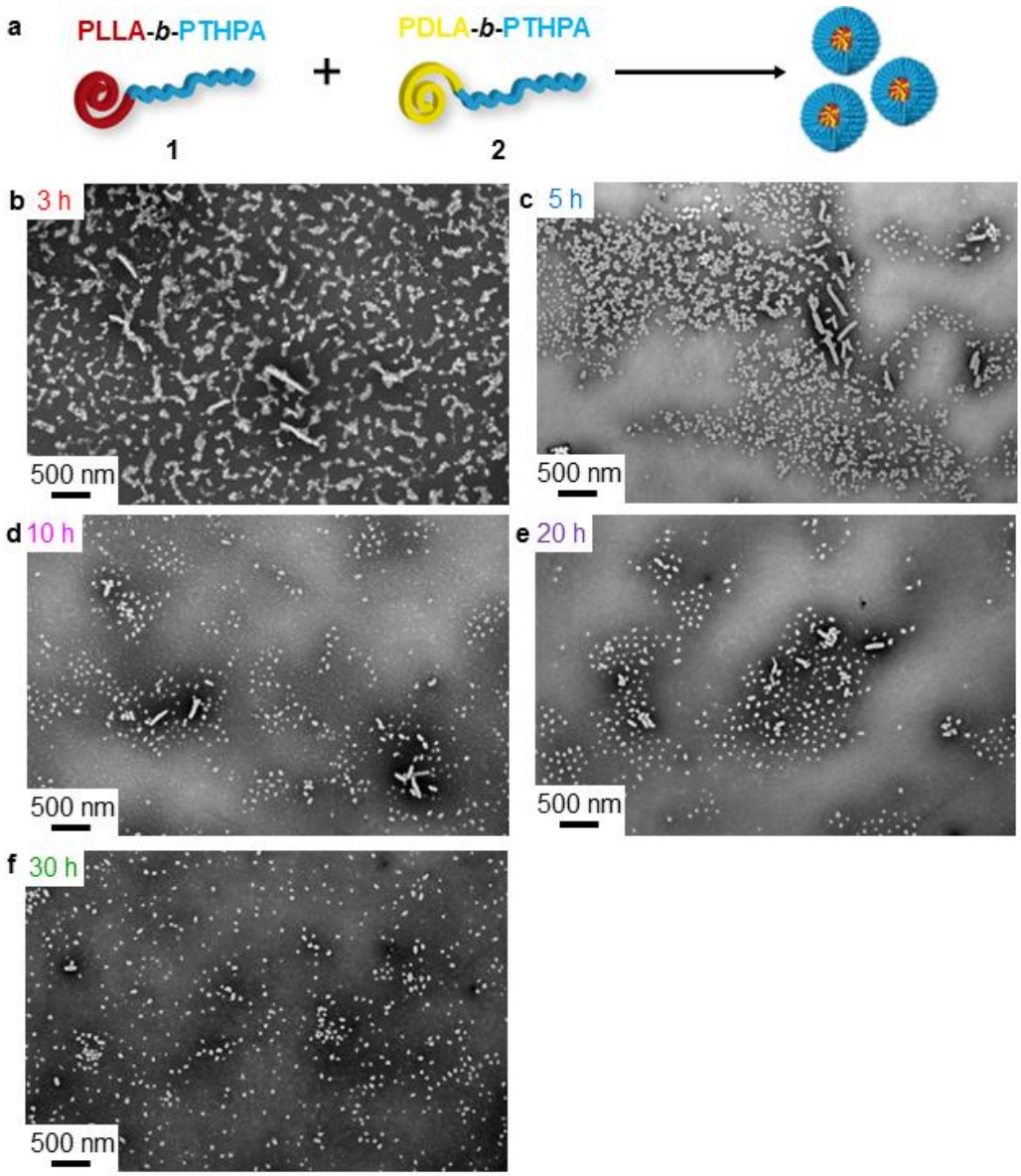

Figure 3.9. TEM characterization data of the formation of the stereocomplex spherical micelles from the homochiral polymers, **1** and **2**, as a function of time. (a) Schematic representation of the formation of stereocomplex spherical micelles from **1** and **2**. TEM images: (b) 3 h after starting the self-assembly; (c) after 5 h; (d) after 10 h; (e) after 20 h and (f) after 30 h. Cylindrical micelles obtained from the homochiral diblock copolymers, **1** or **2**, were found to decrease in length during self-assembly (c-g). TEM samples were prepared by slow drying and negatively stained using PTA.

3.3.3 Stereocomplexation-triggered morphological transition from homochiral cylinders to stereocomplex spheres

In order to explore this morphological transition in more detail and demonstrate its potential utility, separate solutions of homochiral cylinders, **3** (L_n = 194 nm, L_w/L_n = 1.22, W_n = 53 nm) and **4** (L_n = 188 nm, L_w/L_n = 1.21, W_n = 54 nm), were prepared from diblock copolymers, **1** and **2**, respectively (Figure 3.6a and 3.6b) under CSDA conditions for 30 h as described above. Subsequently, 1 mL (*ca*. 17 mg/mL) of each cylinder solution was mixed together with an additional 0.5 mL of THF, to mimic the starting self-assembly conditions described above (v_{THF}/v_{H2O} = 20/80). The solution was then heated at 65 °C with a needle added through the cap to allow the THF to evaporate (Figure 3.10a). By using such an approach, we observed a dramatic decrease in cylinder length and increase in the population of spherical micelles by TEM (Figure 3.10b-3.10f) which demonstrates the ability to trigger the morphological transition through the onset of stereocomplexation. Analysis by dynamic light scattering (DLS) also illustrated the decrease from *ca*. 300 nm to *ca*. 80 nm in the hydrodynamic diameters of the nanoparticles over time (Figure 3.11). *In-situ* synchrotron small-angle X-ray scattering (SAXS) further confirmed such a cylinder-to-sphere transition (Figure 3.12), with a decrease of the radius of the morphology as the curve inflexions move to higher *q* values with time. A comparison of the parameters obtained from the fitted SAXS curves (Table 3.2) revealed the presence of an increasing number of spheres, while the dimensions of the cylinders also decreased over time. These observations were in accordance with TEM and DLS results.

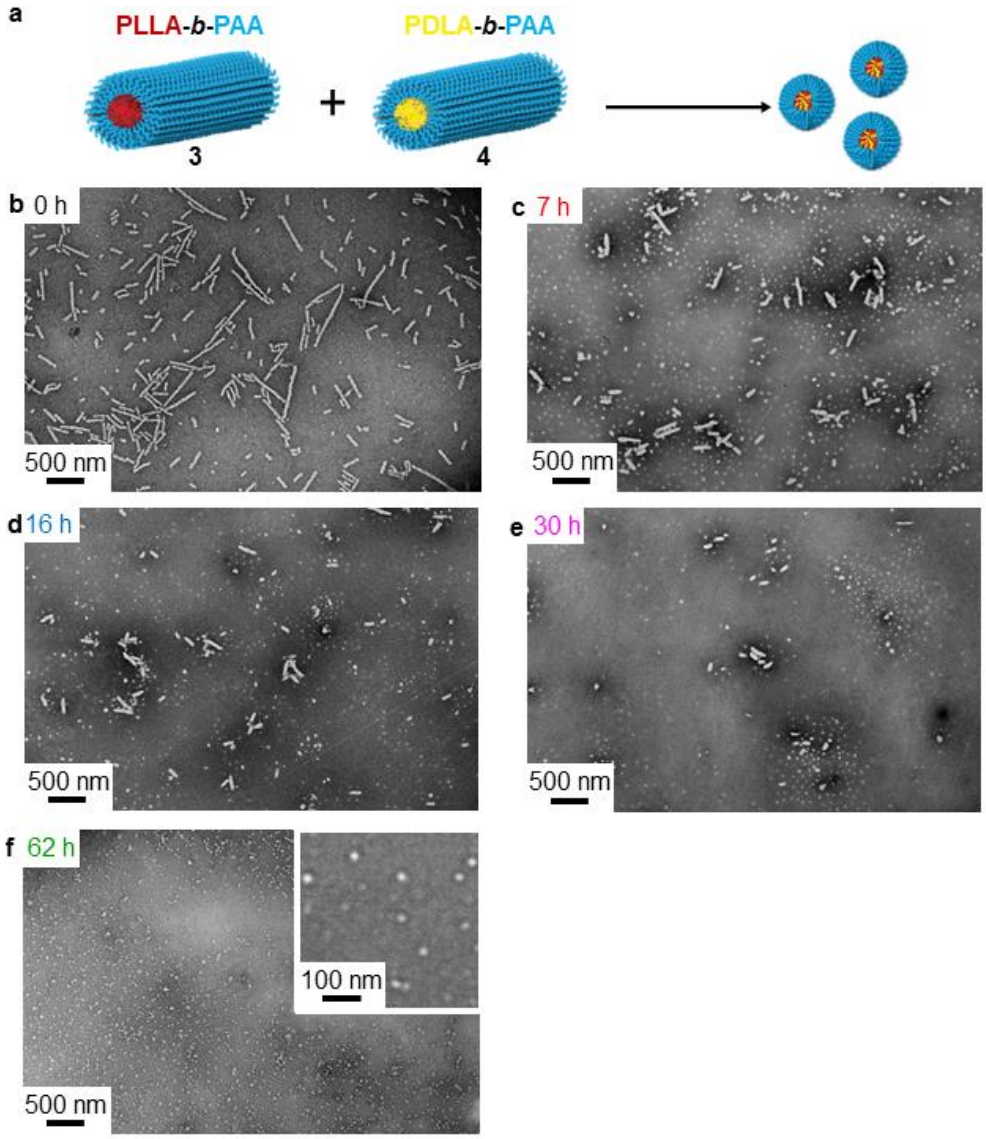

Figure 3.10. TEM images of the morphological transition when the two homochiral cylinders, **3** and **4**, were mixed at 65 °C with the addition of 0.5 mL fresh THF. (a) Schematic representation showing the morphological transition from homochiral cylinders, **3** and **4**, to stereocomplex spheres. (b-f) TEM images which illustrate the length of the cylindrical micelles decreased while the population of spherical micelles increased over time. TEM samples were prepared by slow drying and negatively stained using PTA.

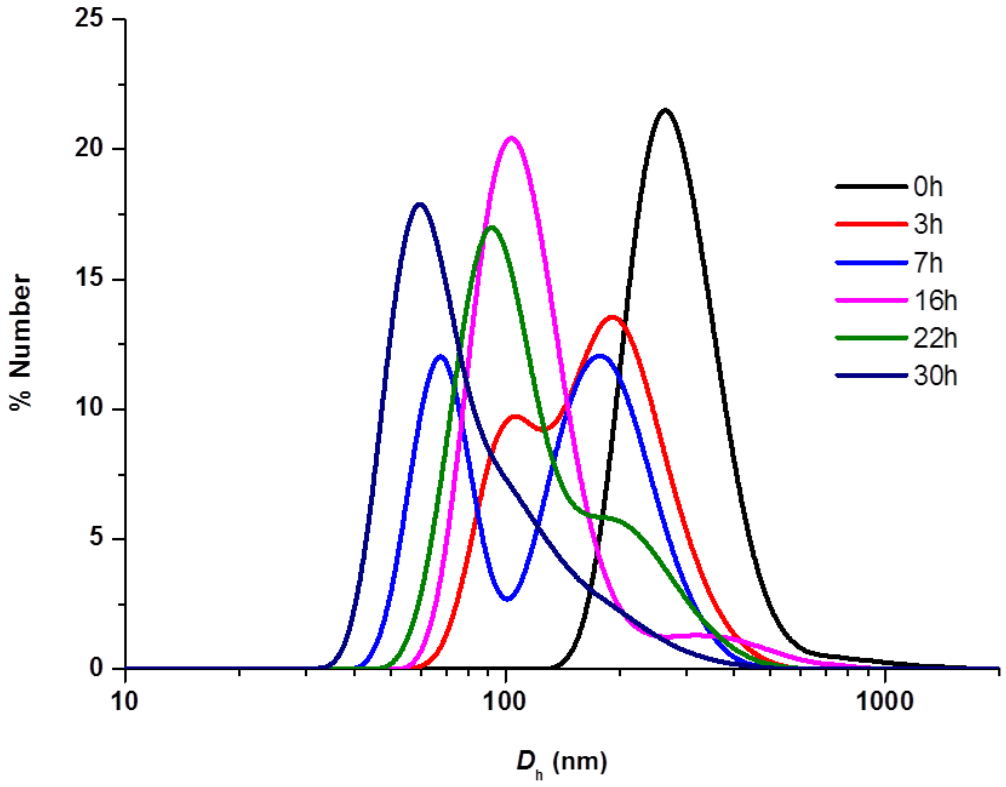

Figure 3.11. DLS data showing that the hydrodynamic diameter of the two homochiral cylinders, **3** and **4** (when mixed in a 1:1 ratio with the addition of 20% THF), decreased gradually when mixed together and heated at 65 °C over time.

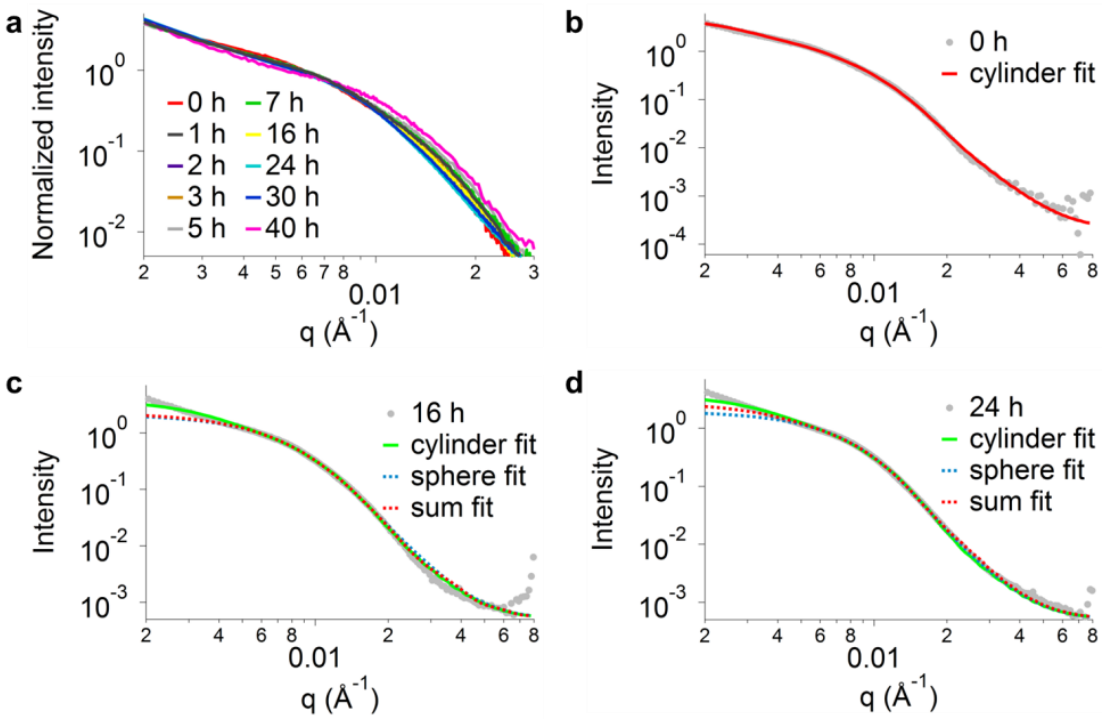

Figure 3.12. SAXS experimental profiles and fittings of the morphological transition from the two homochiral cylinders, **3** and **4**, to stereocomplex spheres at 65 °C with the addition of 0.5 mL fresh THF at the beginning of the self-assembly. (a) SAXS experimental profiles during the entire self-assembly process: a change of morphology is observed, with a decrease of the radius of the morphology as the curve inflexions move to higher *q* values with time. (b, c and d) Fitting of some experimental profiles with different models: cylinder (b) and a linear combination of sphere and cylinder (c and d).

Table 3.2. Detailed analysis of the fitted SAXS profiles given in Figure 3.12 for the assembly of the mixture of the two homochiral cylinders. The initial time point experiment profile (t = 0 h) has been fitted with a cylinder model, all the other subsequent profiles with the sum model

time (h)	length of cylinder (nm)	radius of cylinder (nm)	radius of sphere (nm)	scale ratio of cylinder:sphere[a]
0	191 ± 2	13 ± 0.1	-	-
3	169 ± 1	13 ± 3	12 ± 6	1:0.25
5	150 ± 5	25 ± 25	13 ± 4	1:5.75
7	146 ± 2	25 ± 4	14 ± 2	1:5
16	131 ± 10	13 ± 3	13 ± 2	1:120
24	129 ± 1	20 ± 2	12 ± 1	1: 33

[a] The scale ratio given by the sum model cannot be used as a ratio between the number of particles of each morphologies. It is related to the volume fraction of each morphology, and thus it is possible to observe trends in the evolution of the comparison of these two numbers.

FT-IR spectroscopic analysis was performed on samples taken throughout the cylinder-to-sphere transition to provide further evidence of stereocomplex formation (Figure 3.13). A wavenumber shift from 1758 to 1750 cm^{-1} was observed for the vibration of the carbonyl group of the poly(lactide) chains, which suggests the successful formation of stereocomplex micelles. By using WAXD analysis (Figure 3.14), a significant decrease in the intensity of the homochiral peak at a 2θ value of 16.6° and a gradual intensity increase of the stereocomplex peak at 2θ value of 12° were observed.

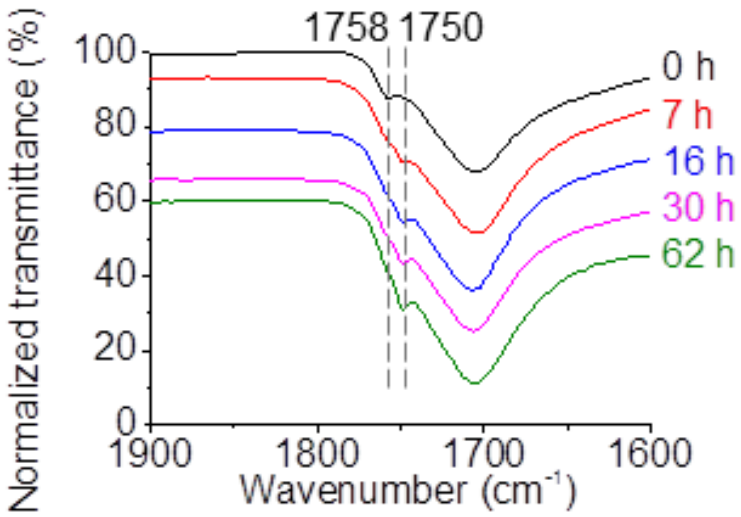

Figure 3.13. FT-IR spectra which reveal the wavenumber of the carbonyl group vibration of poly(lactide) shifted from 1758 to 1750 cm^{-1} during the cylinder-to-sphere transition (with the addition of THF).

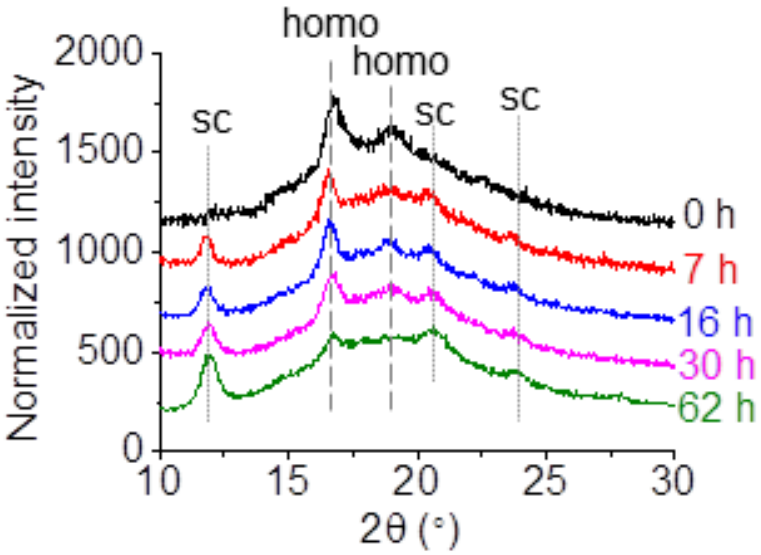

Figure 3.14. WAXD diffractograms illustrating that the intensity of stereocomplex Bragg peak at a 2θ value of 12° increased gradually while the intensity of homochiral Bragg peak at a 2θ value of 16.6° decreased significantly during the cylinder-to-sphere transition (with the addition of THF).

The same morphological transition from homochiral cylinders to stereocomplex spheres was also realized when **3** and **4** were mixed and heated without the addition of fresh THF. TEM (Figure 3.15) and SAXS (Figure 3.16 and Table 3.3) analysis confirmed that the lengths of cylinders decreased while spherical micelles formed over a longer time period (120 h). DLS proved that the hydrodynamic diameter decreased from *ca*. 300 nm to *ca*. 80 nm (Figure 3.17). Both the wavenumber shift from 1758 cm^{-1} to 1750 cm^{-1} observed by FT-IR spectroscopy (Figure 3.18) and the decrease of the intensity of the Bragg peak at a 2θ value of 16.6° by WAXD analysis (Figure 3.19) proved the changes of crystalline nature of this system. We propose that stereocomplexation is hindered without the presence of a good solvent for poly(lactide) (such as THF) which assists in chain folding and co-crystallization within the core domain, and to this end, a weak intensity of stereocomplexation Bragg peak was observed by WAXD (Figure 3.19). The dimensions of the stereocomplex spheres synthesized from unimers (D_n = 49.7 nm, Figure 3.9f) are much larger than those of the stereocomplex spheres achieved from the disassembly of cylinders (D_n = 22.0 nm for Figure 3.10f, D_n = 19.7 nm for Figure 3.15f) as indicated by TEM analysis. Since the stereocomplex core and PAA corona are both visible after staining with phosphotungstic acid (PTA), the crystalline stereocomplex core domain appears even smaller than that observed using negative staining.

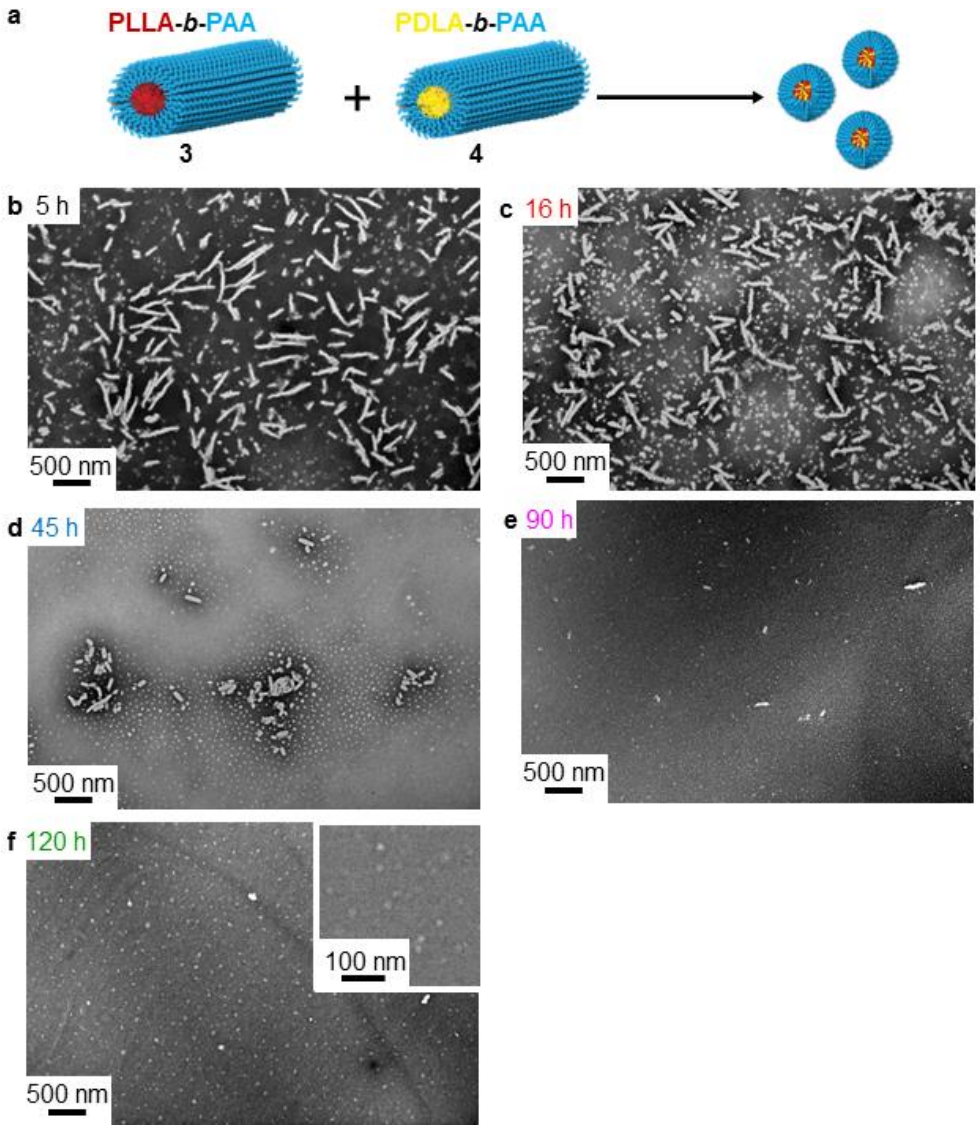

Figure 3.15. TEM images of the morphological transition when the two homochiral cylinders, **3** and **4**, were mixed at 65 °C without the addition of fresh THF. a, Schematic representation showing the morphological transition from homochiral cylinders, **3** and **4**, to stereocomplex spheres. b-f, TEM images which illustrate the length of the cylindrical micelles decreased while the population of spherical micelles increased over time. TEM samples were prepared by slow drying and negatively stained using PTA.

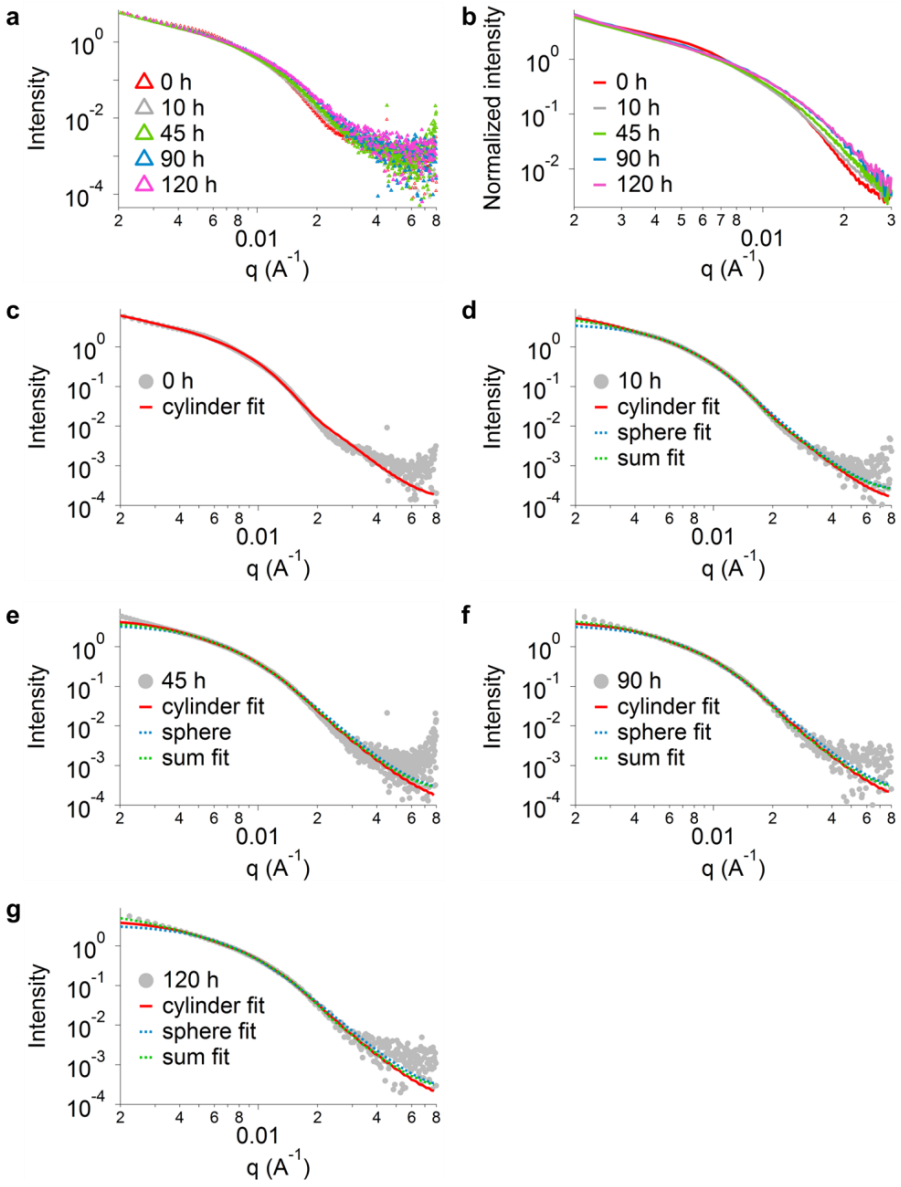

Figure 3.16. SAXS experimental profiles and fittings of the morphological transition from the two homochiral cylinders to stereocomplex spheres at 65 °C without the addition of fresh THF at the beginning of the self-assembly. a, SAXS experimental profiles during the entire self-assembly process. b, Expansion of Figure 3.16a in the *q* range of 0.002 to 0.03 $Å^{-1}$. c-g, Fittings of experimental profiles by using models “cylinder polyradius”, “poly core” and a linear combination of these two models. The fitted parameters are given in Table 3.3.

Table 3.3. Different parameters of the fitted SAXS profiles given in Figure 3.16. The initial time point experiment profile (t = 0 h) has been fitted with a cylinder model, all other profiles with the sum model

time (h)	length of cylinder (nm)	radius of cylinder (nm)	radius of sphere (nm)	scale ratio of cylinder:sphere[a]
0	190 ± 2	17 ± 1	—	—
5	183 ± 2	17 ± 0	19.2 ± 0.2	1:0.7
16	193 ± 7	17 ± 0	18.2 ± 0.7	1:0.8
45	147 ± 1	17 ± 0	16.5 ± 0.2	1:3.1
90	128 ± 6	17 ± 0	14.8 ± 0.5	1:3.8
120	62 ± 4	17 ± 0	14.0 ± 0.7	1:12.5

[a] The scale ratio given by the sum model cannot be used as a ratio between the number of particles of each morphologies. It is related to the volume fraction of each morphology, and thus it is possible to observe trends in the evolution of the comparison of these two numbers.

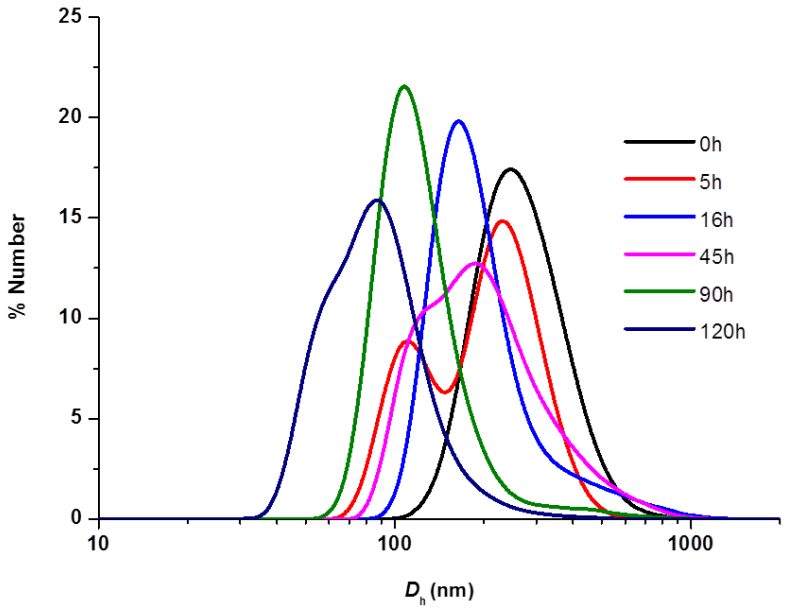

Figure 3.17. DLS data showing that the hydrodynamic diameter of the two homochiral cylinders, **3** and **4** (when mixed in a 1:1 ratio without the addition of THF), decreased gradually when mixed together and heated at 65 °C over time.

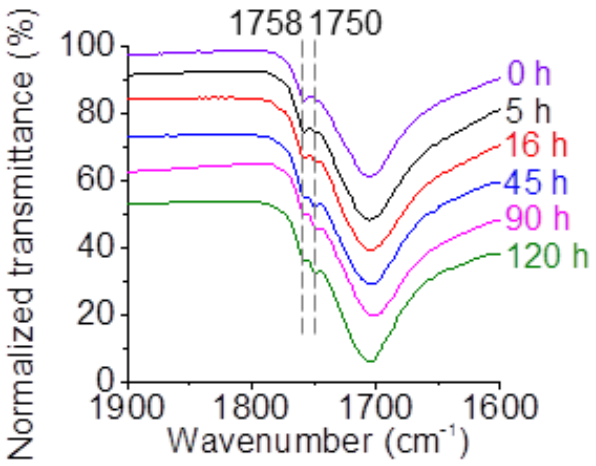

Figure 3.18. FT-IR spectra which reveal the wavenumber of the carbonyl group vibration of poly(lactide) shifted from 1758 cm^{-1} to 1750 cm^{-1} during the cylinder-to-sphere transition (without the addition of THF).

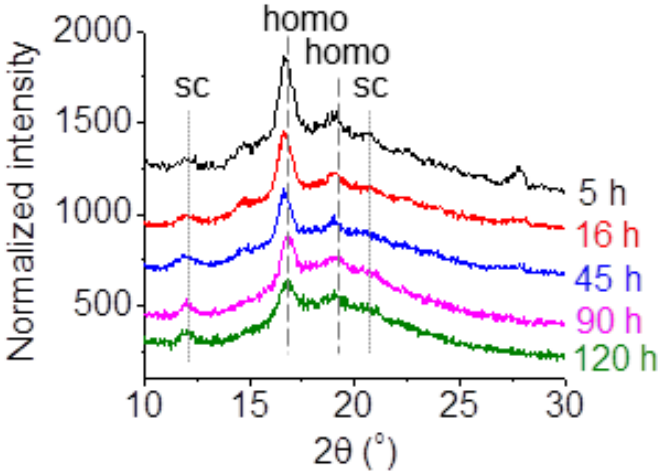

Figure 3.19. WAXD diffractograms showed that the intensity of the homochiral Bragg peak at a 2θ value of 16.6° decreased gradually while the intensity of stereocomplex Bragg peak at a 2θ value of 12° increased slightly during the cylinder-to-sphere transition (without the addition of THF).

The stereocomplex spherical micelles were further characterized using an aberration-corrected microscope at near focus conditions on graphene oxide (GO) supports, which are nearly electron transparent,[23] thus allowing particle analysis *via* the exit wave reconstruction (EWR) technique.[24] The sterocomplex micelles (Figure 3.21a, the same sample shown in Figure 3.10f) were also compared with amorphous spherical micelles prepared from PLLA-*b*-PAA (Figure 3.21d). Such amorphous spherical micelles were obtained by stopping the CDSA process of deprotected diblock copolymer, **1**, after 2.5 h of self-assembly when the morphology of the nanostructures is still spherical (as these amorphous spheres transformed into short crystalline cylindrical seeds very fast, we were not able to obtain pure enantiopure crystalline spheres to compare with stereocomplex spheres).[20] WAXD analysis confirmed the amorphous nature of such spherical micelles as no obvious Bragg peak at 2θ value of 16.6° was observed (Figure 3.20). Exit wave reconstruction (EWR) enabled a higher contrast and higher resolution image to be obtained from a focal series of TEM images and thus provided greater structural detail of the macromolecular nanostructures, despite the low contrast of these predominantly carbon-based materials.[24] EWR gives a phase image and an amplitude image; macromolecular nanostructures exhibit mainly phase contrast by TEM and so these structures are clearly resolved in the phase images. The square of the amplitude image (the intensity) gives contrast which is roughly related to the mass thickness of the macromolecular sample. By using EWR on unstained samples, a much clearer spherical shape was observed for both the stereocomplex and amorphous micelles in the phase images (Figure 3.21b and Figure 3.21e). The squared amplitude images from EWR (Figure 3.22a and

Figure 3.22b) revealed that the stereocomplex spherical micelles possessed a higher density than the amorphous spherical micelles; where the intensity relative to the background decreased by 8% for the former but only 3% for the latter (Figure 3.22c) (decreased intensity is due to increased scattering of the electron beam and hence implies increased mass thickness). The surface plots of EWR square amplitude images (Figure 3.21c *vs* Figure 3.21f) further proved that the stereocomplex micelles were more dense.

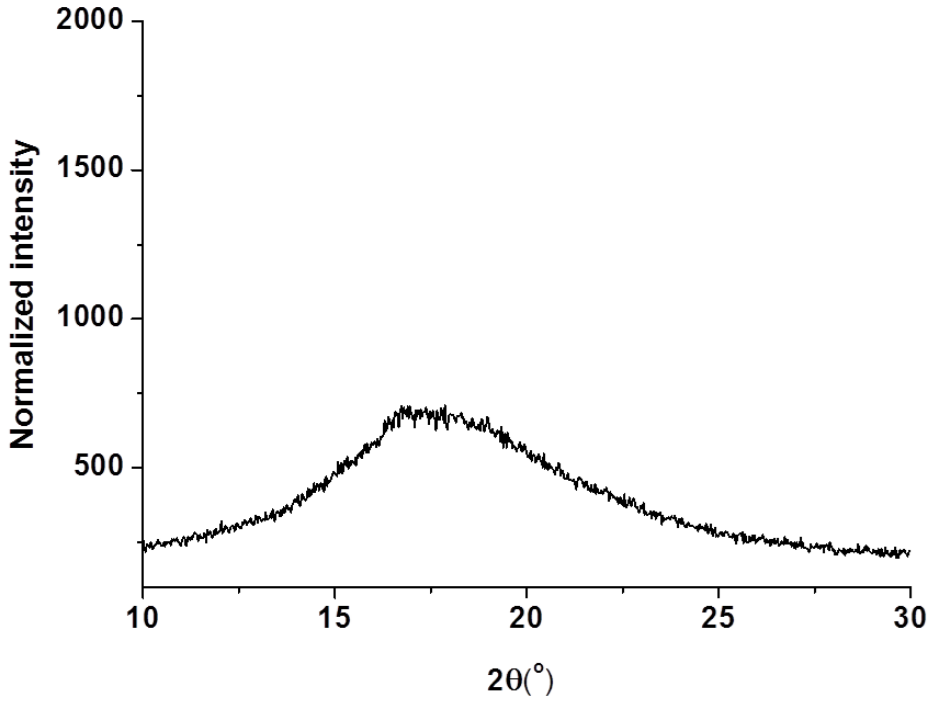

Figure 3.20. WAXD diffractogram showing the amorphous nature of spherical micelles obtained from the self-assembly of **1**.

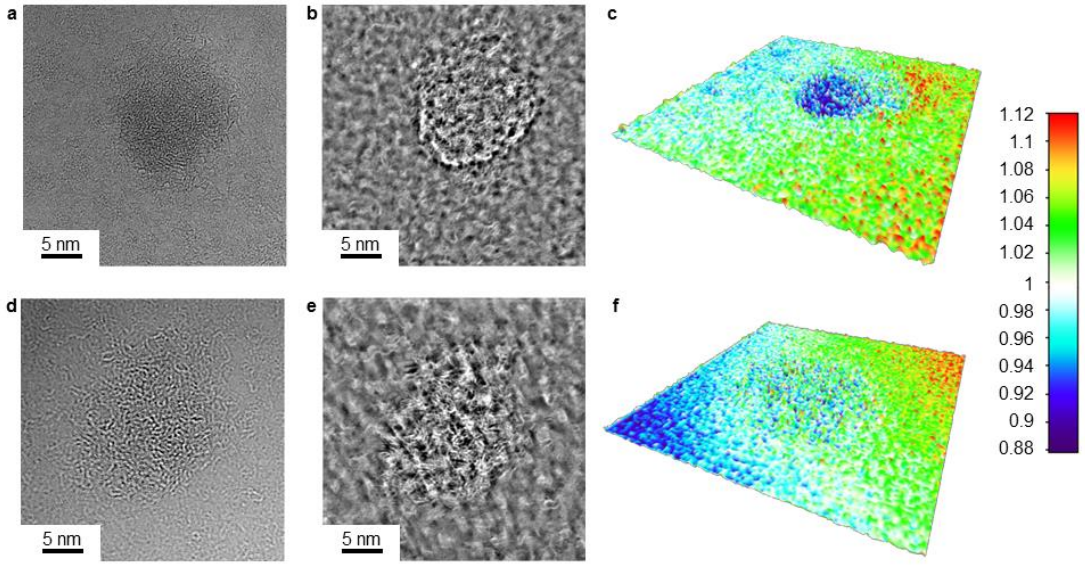

Figure 3.21. Characterizations of a stereocomplex spherical micelle (obtained from the mixture of homochiral cylinders, **3** and **4**) and an amorphous spherical micelle (obtained from the self-assembly of **1**). a, b and c, Near focus aberration-corrected atomic resolution microscope image, EWR phase image and surface plot representation of EWR square amplitude image of a stereocomplex sphere. d, e and f, Near focus aberration-corrected atomic resolution microscope image, EWR phase image and surface plot representation of EWR square amplitude image of an amorphous sphere. All of the images were obtained on GO supports.

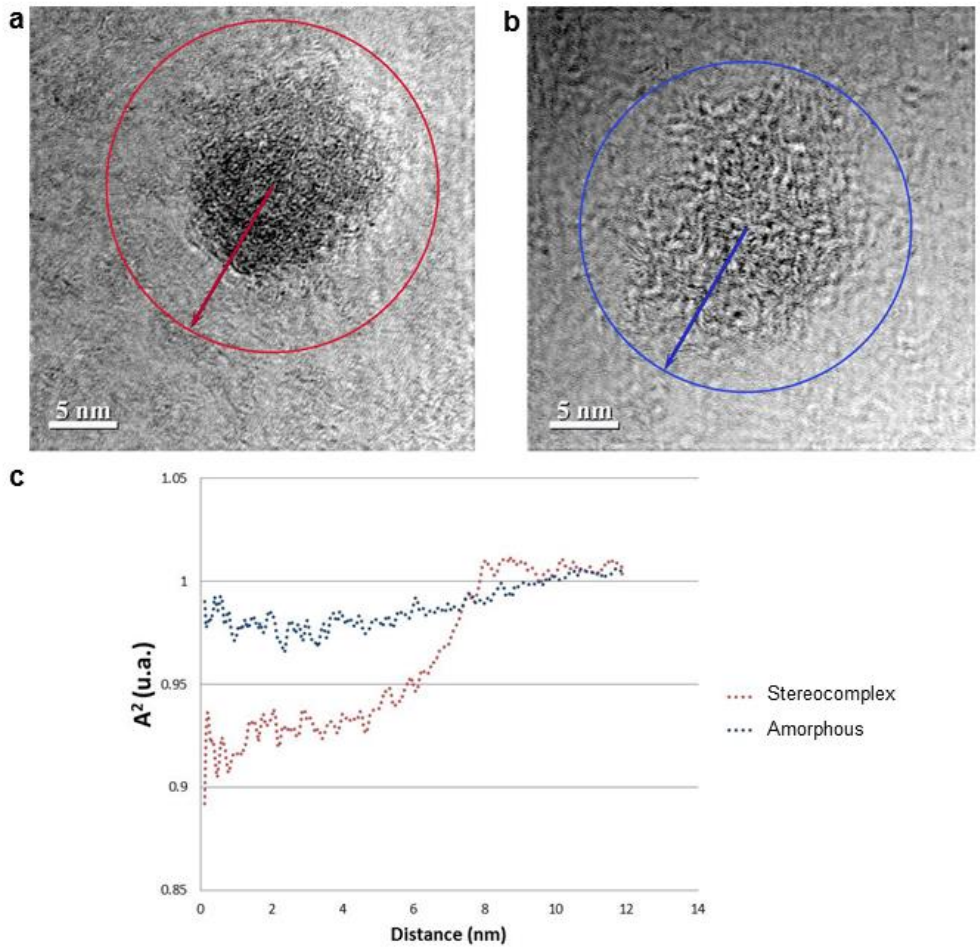

Figure 3.22. EWR images of the square amplitude of a stereocomplex spherical micelle (a, obtained from the mixture of homochiral cylinders, **3** and **4**) and an amorphous spherical micelle (b, obtained from the self-assembly of **1**) respectively. c, Radial plots from the middle of the structures to the GO support (red and blue curves for the stereocomplex micelle and amorphous micelle respectively).

To prove that the observed cylinder-to-sphere transition was a consequence of the onset of stereocomplexation, two control experiments were conducted using identical self-assembly conditions as described above, to monitor the changes in the homochiral cylinder, **3**, only. The homochiral cylindrical micelles were heated at 65 °C for an extended time at a high concentration (17 mg/mL). With no addition of fresh THF, the length of these cylinders stayed

approximately the same even after 120 h of heating, although some aggregation was observed by TEM analysis (Figure 3.23a-3.23c). This observation was supported by SAXS analysis (Figure 3.24, Table 3.4), which also indicated unchanged cylinder length as well as some aggregation after excessive heating. Moreover, no obvious changes in the intensity of the Bragg peak at a 2θ value of 16.6° were observed in the WAXD diffractograms over time (Figure 3.23d), again indicating the high stability of these cylinders. Interestingly, when the cylinder solution was exposed to 0.5 mL fresh THF (v_{THF}/v_{H2O} = 20/80) and heated at 65 °C, with a needle through the seal of the vial, the cylinder length decreased rapidly within the first few hours followed by the formation of large lamellar particles after 16 h, as observed by TEM analysis (Figure 3.25a-3.25e). Interestingly, numerous small “arms” were noticed protruding these lamellar micelles (Figure 3.25e). Such structural reorganization was further confirmed by SAXS analysis with an observed increase in the population of lamellar particles compared to the population of cylinders over the heating process (Figure 3.26 and Table 3.5). WAXD diffractograms of this system also indicated that the intensity of the homochiral peak at the 2θ value of 16.6° decreased after the addition of 0.5 mL fresh THF into the cylinder solution but recovered after another 30 h of heating under the self-assembly conditions (Figure 3.25f).

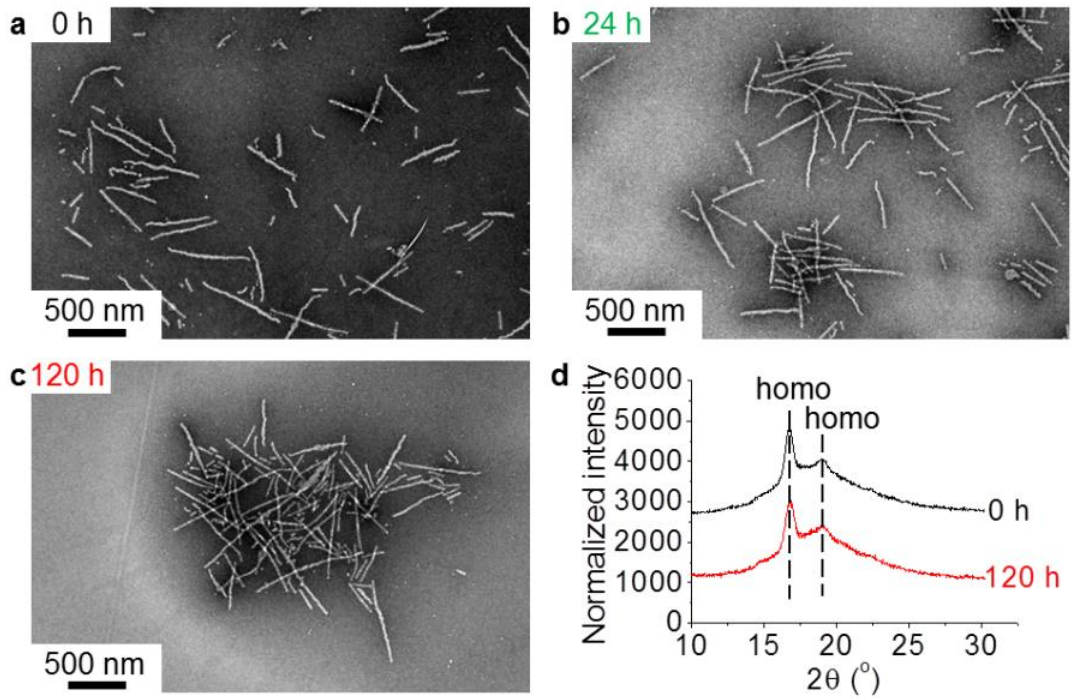

Figure 3.23. a-c, TEM images showing that the lengths of homochiral cylinders, **3**, did not change significantly when heated at 65 °C for 120 h. d, WAXD diffractograms showing there is no significant difference in the intensity of homochiral Bragg peak at 2θ 16.6° over this time. No stereocomplex Bragg peaks were observed during the entire self-assembly. TEM samples were prepared by slow drying and negatively stained using PTA.

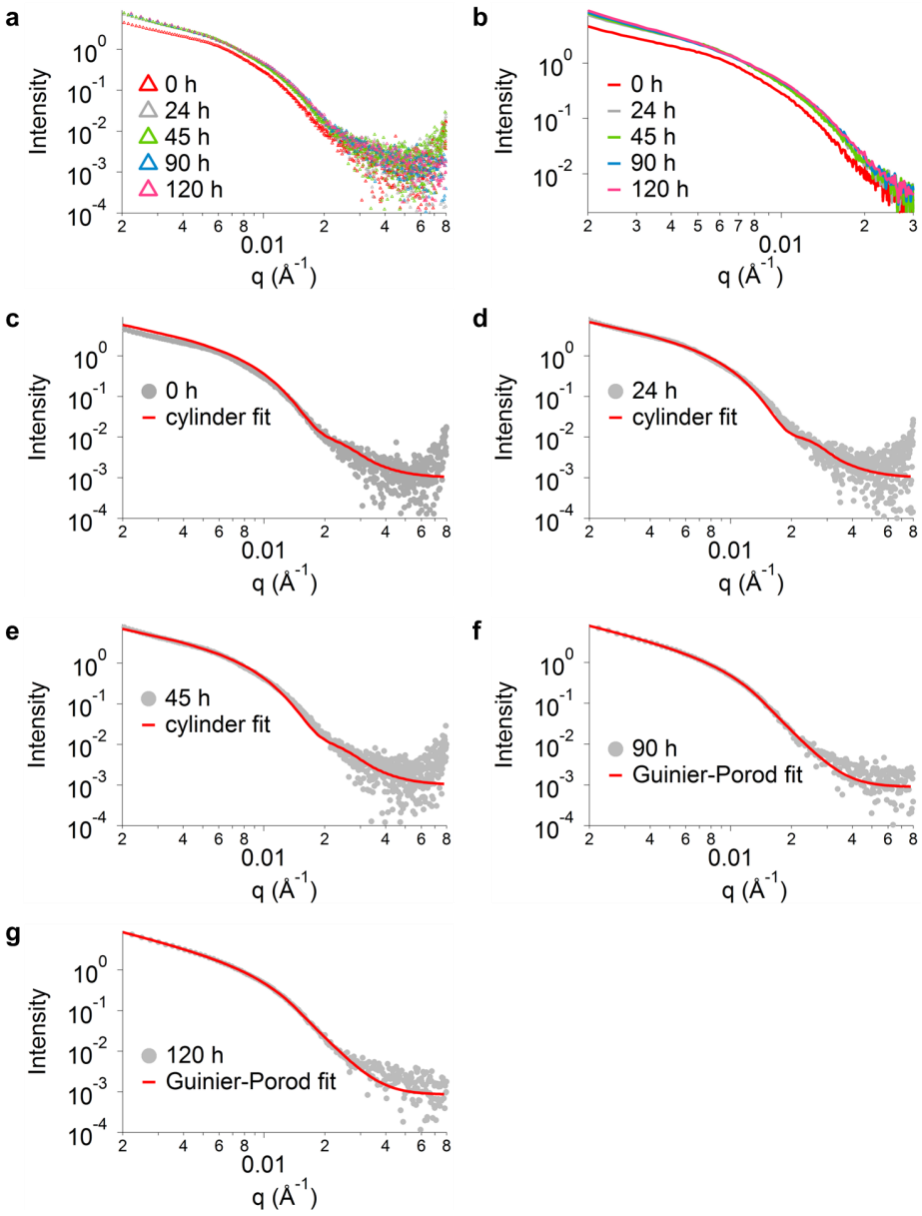

Figure 3.24. SAXS profiles and fittings showing that the size of cylindrical micelles, **3**, did not change obviously with heating. a, SAXS experimental profiles during the entire self-assembly process. b, Expansion of Figure 3.24a in the *q* range of 0.002 to 0.03 Å^{-1}. c-e, Fittings of experimental profiles by using the cylindrical model. f-g Fittings of experimental profiles by using the Guinier-Porod model; some aggregations of the particles were observed and the cylindrical model does not provide correct fits for 90 h and 120 h. The parameters of the fitted curves are listed in Table 3.4.

Table 3.4. Different parameters of the fitted SAXS profiles given in Figure 3.24 using a "cylinder polyradius" model. As fits were not valuable after 90 h, a simpler "Guinier-Porod" model was used to provide information on the general shape of the assemblies

time (h)	length of cylinder (nm)	radius of cylinder (nm)	dimensionality parameter[a]	shape[a]
0	255 ± 4	19 ± 0.0	2.16	Rod
5	254 ± 5	19 ± 0.0	2.09	Rod
10	275 ± 2	19 ± 0.0	2.09	Rod
16	256 ± 4	19 ± 0.0	2.05	Rod
24	272 ± 3	19 ± 0.0	1.96	Rod
45	277 ± 4	19 ± 0.0	1.94	Rod
63	240 ± 3	19 ± 0.0	1.86	Rod
90	1853 ± 69	19 ± 0.0	1.81	Rod+plate
120	2028 ± 65	19 ± 0.0	1.77	Rod+plate

[a] The dimensionality parameter is calculated as 3-s and is 3 for spherical objects, 2 for rods and 1 for plates. These values are obtained with a Guinier-Porod model.

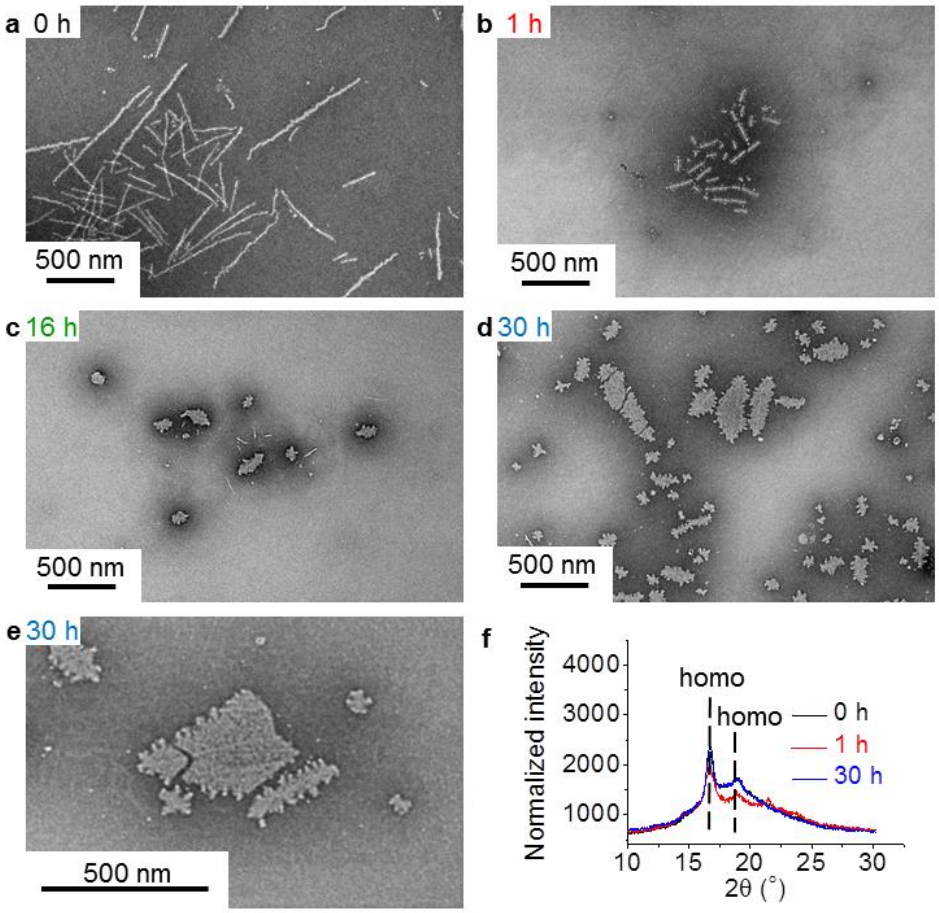

Figure 3.25. TEM images showing that the structure of cylinders, **3**, changed significantly over time, with heating at 65 °C and with the addition of 0.5 mL fresh THF: a, Cylindrical micelles before addition of fresh THF. b, The length of cylinders decreased dramatically due to dissolution in the THF/water mixture. c and d, The disassembled unimers gradually inserted into the undestroyed cylinders and lamellar structures were formed. e, Numerous small “arms” were noticed protruding from the lamellar micelles. f, Overlaid WAXD diffractograms showing that the intensity of the homochiral Bragg peak at 2θ 16.6° decreased after addition of fresh THF but recovered after 30 h due to unimer growth onto the short cylindrical seeds. No stereocomplexation peaks were observed during the self-assembly. TEM samples were prepared by slow drying and negatively stained by PTA.

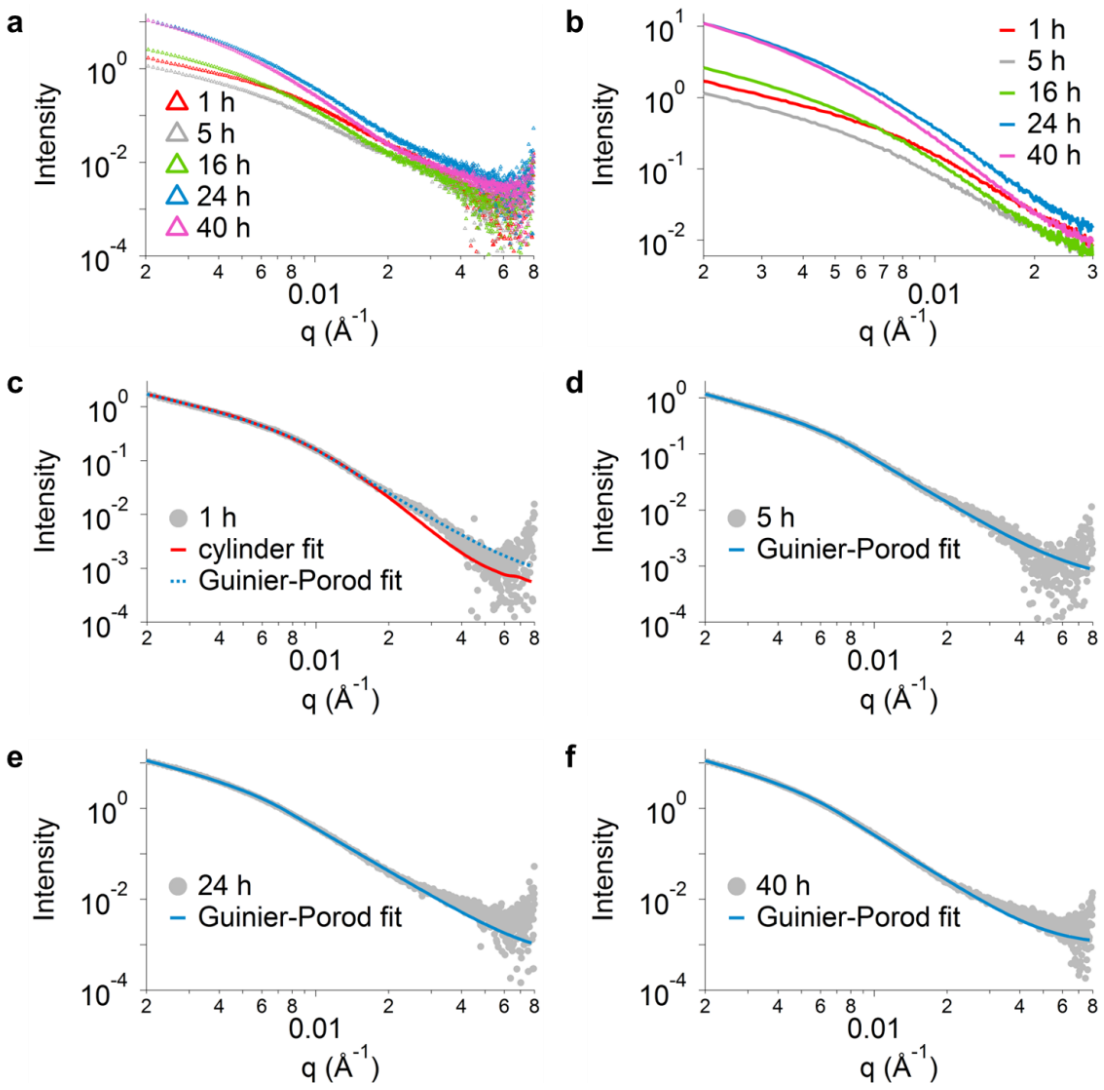

Figure 3.26. SAXS profiles and fittings showing that the structure of cylinders, **3**, changed significantly into lamellar particles over time after addition of 0.5 mL fresh THF and heating at 65 °C. a, SAXS experimental profiles during the entire self-assembly process. b, Expansion of Figure 3.26a in the *q* range of 0.002 to 0.03 Å^{-1}. c, Fittings of experimental profile using the cylindrical model and the Guinier-Porod. d-f Fittings of experimental profiles using the Guinier-porod model to provide basic information on the general shape of the assemblies. The cylindrical model does not provide a good fit after 5 h of heating. The parameters of the fitted curves are listed in Table 3.5.

Table 3.5. Different parameters of the fitted SAXS profiles given in Figure 3.26 using the Guinier-porod model

time (h)	R_g (nm)	dimensionality parameter[a]	shape[a]
0	16 ± 0.1	2.12	Rod
1	12 ± 0.1	1.97	Rod
5	15 ± 0.1	1.88	Rod+Plate
16	15 ± 0.1	1.81	Rod+Plate
24	16 ± 0.1	1.70	Rod+Plate
40	17 ± 0.1	1.60	Rod+Plate

[a] The dimensionality parameter is calculated as 3-s and is 3 for spherical objects, 2 for rods and 1 for plates.

To further expand the scope of the stereocomplexation-triggered morphological transition, a fully biocompatible PLA system (PEO_{454}-*b*-$PLLA_{29}$ cylinders and PEO_{454}-*b*-$PDLA_{26}$ cylinders) was also investigated. By mixing the two cylindrical micelles at 65 °C with addition of THF at the beginning of the self-assembly, a transition from crystalline cylinders to stereocomplex spheres was observed over a similar timeframe as evidenced by TEM and FT-IR analysis (Figure 3.27). We suggest that this new mechanism for nanostructure reorganization, which is triggered by stereocomplexation, highlights the potential utility of these PLA materials in delivery or sensing applications.

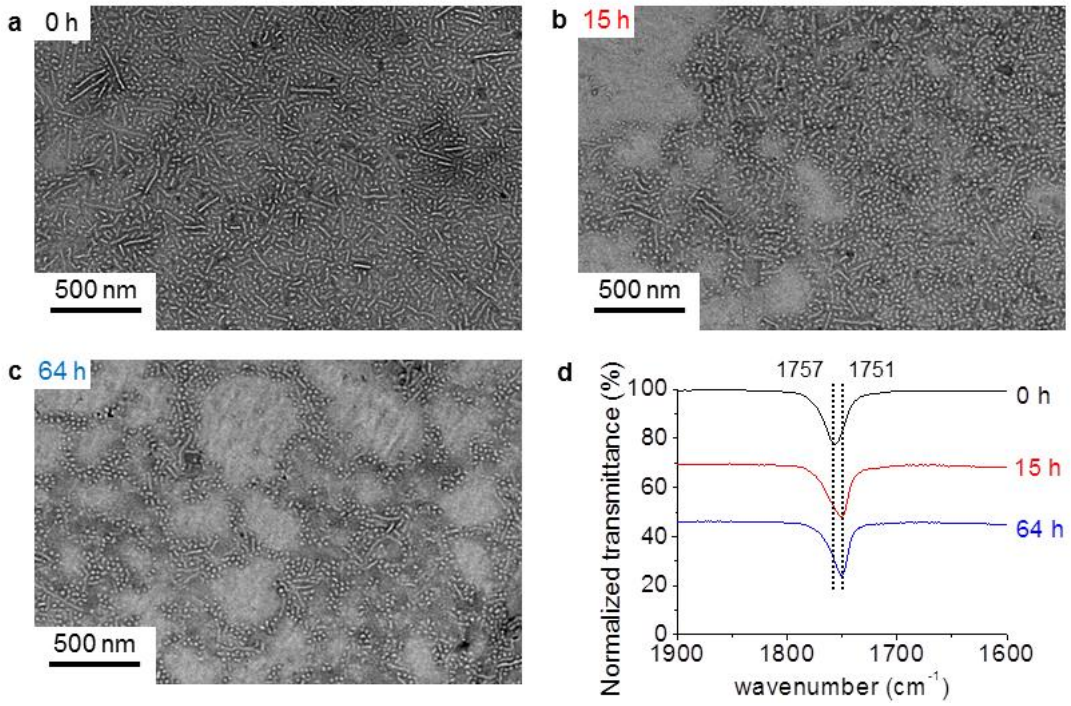

Figure 3.27. Characterizations of the morphological transition and changes to the crystalline core nature when the two homochiral PLLA-*b*-PEO cylinders and PDLA-*b*-PEO cylinders were mixed at 65 °C with the addition of 0.5 mL fresh THF. a-c, TEM images which illustrate the length of the cylindrical micelles decreased while the population of spherical micelles increased over time. d, FT-IR spectra which revealed the wavenumber of carbonyl group vibration of poly(lactide) shifted from 1757 cm^{-1} to 1751 cm^{-1} over time. TEM samples were prepared by slow drying and negatively stained by PTA.

3.3.4 Explanation of the morphological transition and the growth of PLLA-*b*-PAA (PDLA-*b*-PAA) cylinders based on a "unimer-exchange" mechanism

In our recent studies, we proved that the formation of PLLA-*b*-PAA cylinders underwent a sphere-to-rod transition by using TEM, DLS and SAXS analysis.[20, 21] Specifically, amorphous PLLA-*b*-PAA spherical micelles formed first, some of which then underwent a crystallization process to yield short crystalline seeds

and finally, unimer insertions into the two active ends of these short seeds resulted in bidirectional epitaxial growth to form cylinders.

The exact mechanism of cylinder growth in this system remained unclear, with two possible mechanisms suggested by Eisenberg *et al*. in the late 1990s, the "unimer-exchange" theory and the "adhesive fusion" theory.[25] In the "unimer-exchange" mechanism, unimers continuously insert into short cylindrical (or spherical) seeds and this will lead to cylinder growth, while the "adhesive fusion" mechanism suggests that several small cylinders (or spheres) directly merge into one long cylinder through fusion. For a long time, most of the evidence of the formation of cylindrical micelles supported the "adhesive fusion" mechanism as the intermediate morphologies between small cylinders (or spheres) and long cylinders were often observed by TEM analysis.[26, 27] However, several in-depth studies from the groups of Manners, Winnik and Schmalz proved the unimer-exchange mechanism to some extent by growing crystalline poly(ferrocenylsilane) (PFS) or poly(ethylene) (PE) block-containing unimers onto the corresponding crystalline cylinder seeds to yield longer cylinders.[28-30] Xu and co-workers observed both growth modes during the self-assembly of semicrystalline poly(*ε*-caprolactone)-*b*-poly(ethylene oxide) into cylindrical micelles in a mixture of H_2O and DMF.[31] It was found that unimers were highly mobile in solution and could easily add onto the two active ends of the cylindrical micelles. In comparison, the rate of "adhesive fusion" was far slower as it happened only when two cylinders collided and was inhibited due to the mismatch of the crystal planes of the two ends of the cylinders. In other words, the "unimer-exchange" mode was believed to be the dominant mode during the crystallization-driven self-assembly process.

In the present study, the observed morphological transition from homochiral cylinders into stereocomplex spheres can rationalise the growth of crystalline-coil PLLA-*b*-PAA (or PDLA-*b*-PAA) cylinders *via* “unimer-exchange”. Before the two homochiral cylinders, **3** and **4**, were mixed together, unimers exist in both cylinder solutions, although most of them have been consumed in the CDSA process. As the unimers possess very long hydrophilic blocks (85% by weight fraction) and the self-assembly temperature is above the T_g of the PLA core block, these unimers are expected to be highly dynamic. When the cylinder solutions were mixed without addition of fresh THF, stereocomplex micelles formed gradually from these dynamic unimers and both the *L* and *D* unimers became locked in the stereocomplex micelles. Simultaneously, stereocomplex micelles “retrieve” unimers from the already-formed cylinders and decreased cylinder length through “unimer-exchange” (Figure 3.15b-3.15f). Several studies have shown that crystals which result from the stereocomplexation of PLLA and PDLA displayed higher stability than crystals obtained from each single enantiopure polymer owing to the improved packing and strong interactions of the helical chains of opposite configurations.[2, 6, 7, 32] Therefore, stereocomplexation can be considered as the driving force for such a cylinder-to-sphere transition. In turn, the presence of cylindrical micelles also hindered the formation of stereocomplex particles, as evidenced by the small dimensions of stereocomplex spheres and the weak intensity of the sterocomplex Bragg peaks in the WAXD diffractograms (Figure 3.15f and Figure 3.19), as most of the unimers were not free in the solution but were “stored” in the cylinders. On the contrary, if the growth of PLLA-*b*-PAA cylindrical micelles followed the “adhesive fusion” process, cylinders should grow when they are mixed in

solution, however, this phenomenon was not observed. The control experiment of homochiral cylinder, **3**, further supports our hypothesis. Without the addition of fresh THF into **3**, the nanostructures could not grow in length even with prolonged heating as there was a low concentration of unimers in solution (Figure 3.23a-3.23c).

When THF (a common solvent for both blocks) was added into the mixture of homochiral cylinders, **3** and **4**, a number of cylindrical micelles were able to disassemble into *L* and *D* unimers which rapidly self-assembled into stereocomplex spheres (Figure 3.10c). Again, these stereocomplex spheres "retrieve" unimers from homochiral cylinders and further decreased cylinder length *via* "unimer-exchange". A higher intensity of the stereocomplexation peak was observed in the WAXD diffractograms as a consequence of the addition of a good solvent for poly(lactide) which assisted in chain folding and co-crystallization (Figure 3.14). The shortened cylindrical micelles should regrow into long cylinders if "adhesive fusion" was adopted, however, this phenomenon was not observed. In the case of the control experiment of homochiral cylinder, **3**, with addition of 0.5 mL fresh THF, some cylinders were destroyed into *L* unimers which could further insert into the remaining undestroyed cylindrical micelles and form large lamellar particles (Figure 3.25a-3.25e) as there was no competitive stereocomplexation process to inhibit their growth. The regrowth process revealed the random insertion of unimers into any area of the cylinders, observed as small "arms" protruding from around the cylindrical seeds by TEM analysis (Figure 3.25e). The addition of THF to the cylinder solution not only disassembled some cylinders but also led to the formation of shortened and highly dynamic cylinders, which enabled unimers to

grow anywhere on these precursor cylindrical seeds rather than only on the two active ends to yield lamellar particles. Again, if the formation of these lamellar micelles was based on the “adhesive fusion” mechanism, one would expect the formation of similar lamellar structures when both *L* and *D* cylinders were mixed, which has not been observed.

To further prove such a “unimer-exchange” process, *D* unimers (17 mg in 0.5 mL of THF) were directly added into an aqueous solution of *L* cylinders, **3**, (17 mg in 2 mL H_2O) followed by the evaporation of THF at 65 °C (Figure 3.28a). It was observed that the length of cylinder, **3**, decreased and spherical micelles were formed over time as evidenced by TEM (Figure 3.28) and DLS analysis (Figure 3.29). The wavenumber shift from 1758 cm^{-1} to 1749 cm^{-1} observed by FT-IR spectroscopy (Figure 3.30) and the decreasing intensity of the Bragg peak at a 2θ value of 16.6° with increasing intensity of the Bragg peak at a 2θ value of 12° in the WAXD diffractograms (Figure 3.31) confirmed that the crystalline nature of this system changed during the self-assembly process.

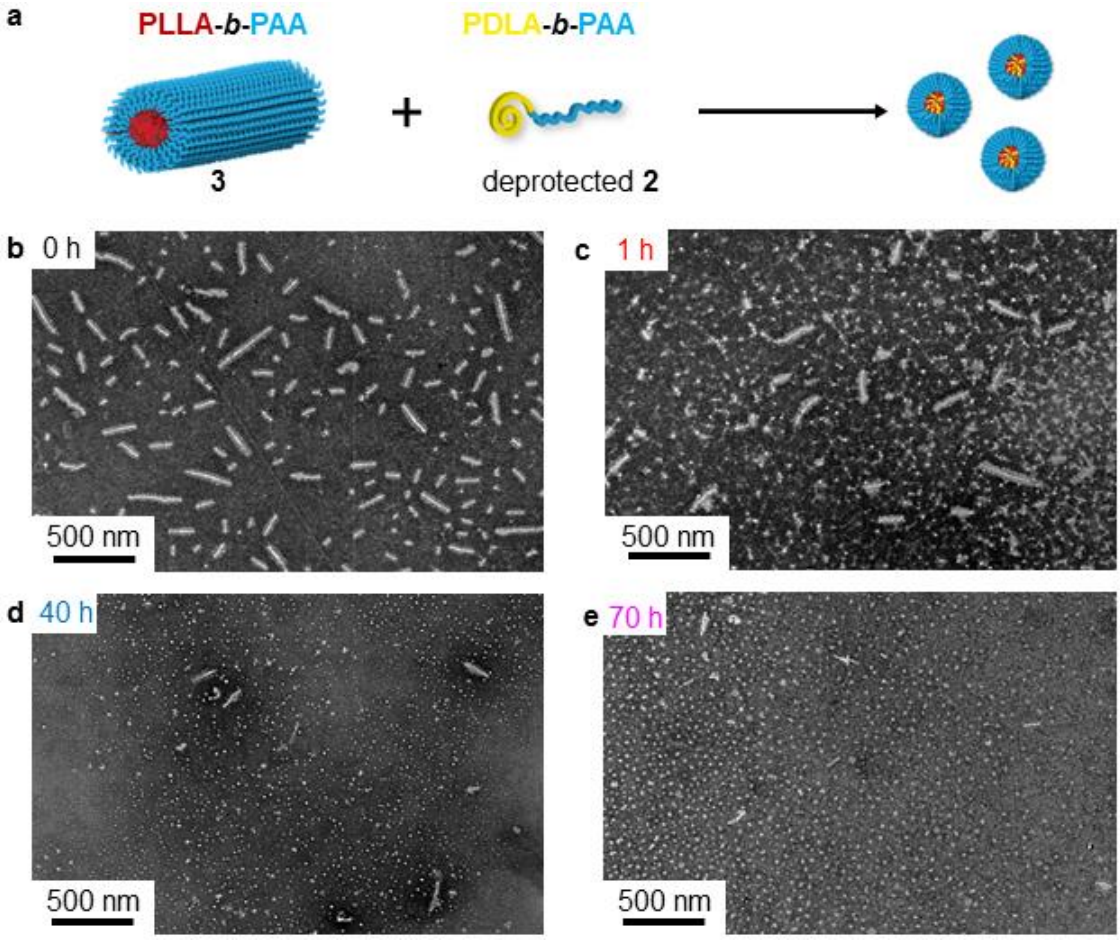

Figure 3.28. Characterizations of the morphological transition and the changes in the crystalline core nature when the THF solution of PDLA-*b*-PAA unimers was added into an aqueous solution of PLLA-*b*-PAA cylinder, **3**, at 65 °C. a, Schematic representation showing the morphological transition. b-e, TEM images which illustrate the length of the cylindrical micelles decreased while the population of spherical micelles increased over time. TEM samples were prepared by slow drying and negatively stained using PTA.

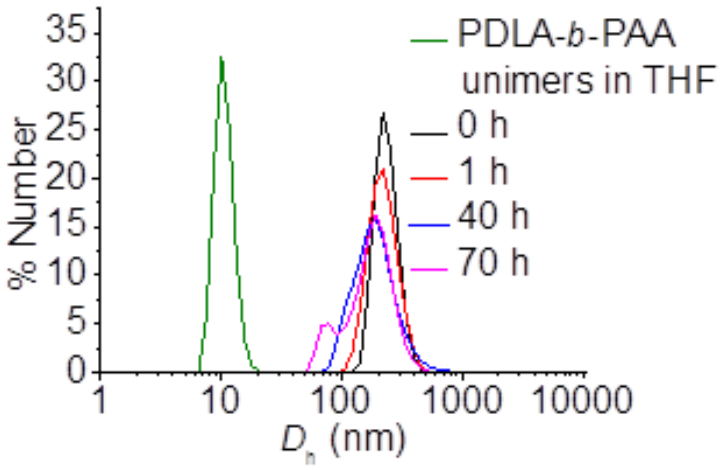

Figure 3.29. DLS data which indicate the morphological transition over time when the THF solution of PDLA-*b*-PAA unimers was added into an aqueous solution of PLLA-*b*-PAA cylinder, **3**, at 65 °C.

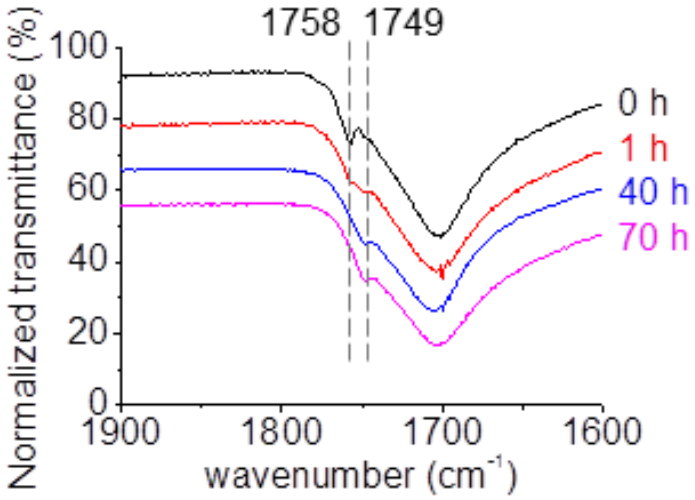

Figure 3.30. FT-IR spectra which reveal the wavenumber of the carbonyl group vibration of poly(lactide) shifted from 1758 cm^{-1} to 1749 cm^{-1} over time when the THF solution of PDLA-*b*-PAA unimers was added into an aqueous solution of PLLA-*b*-PAA cylinder, **3**, at 65 °C.

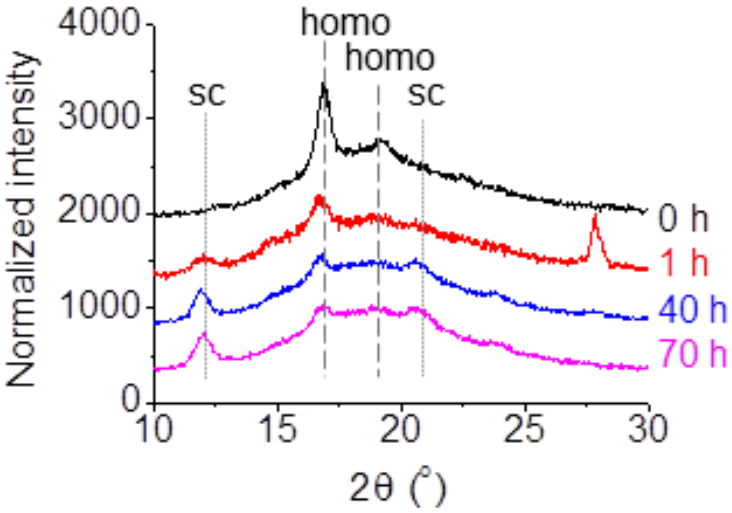

Figure 3.31. WAXD diffractograms showed that the intensity of the homochiral Bragg peak at a 2*θ* value of 16.6° decreased significantly while the intensity of stereocomplex Bragg peak at a 2*θ* value of 12° increased gradually when the THF solution of PDLA-*b*-PAA unimers was added into an aqueous solution of PLLA-*b*-PAA cylinder, **3**, at 65 °C.

While the exact reason of the formation of the spherical shapes of stereocomplex nanoparticles is not very clear, one hypothesis could be that the arrangement of stereocomplex crystals in the core domain of these nanostructures favoured a spherical morphology rather than a cylindrical morphology and most of the studies on stereocomplex nanoparticles to date have shown their spherical shapes.[13,15,16]

3.4 Conclusions

In summary, we observed that the stereocomplexation between the crystalline-coil PLLA-*b*-PAA and PDLA-*b*-PAA diblock copolymers formed spherical micelles instead of cylindrical micelles in an aqueous system. Surprisingly, the mixture of enantiopure PLLA-*b*-PAA cylinders and PDLA-*b*-PAA cylinders underwent a cylinder-to-sphere transition into stereocomplex spheres as proved by TEM, DLS, *in-situ* synchrotron SAXS, FT-IR and WAXD analysis. Such a morphological transition was not observed when enantiopure PLLA-*b*-PAA cylinders only were exposed to the identical self-assembly conditions without the presence of the opposite enantiopure PDLA-*b*-PAA cylinders. A similar transition was observed in a related PLLA-*b*-PEO and PDLA-*b*-PEO system and is also proposed to be applicable in a range of additional crystalline polymers. Both the mechanism of the cylinder-to-sphere transition in this system and the homochiral cylinder growth were proposed to occur by a "unimer-exchange" process. Such a "unimer-exchange" process was further confirmed when the addition of *D* unimers in THF solution into an aqueous solution of *L* cylinders led to the disassembly of the latter and the formation of the stereocomplex spherical micelles. We think that this fundamental study provides a deeper understanding of the balance of self-assembly forces in such PLA systems and suggest that this stereocomplexation-triggered reorganization may have potential applications in delivery or sensing.

3.5 Experimental section

3.5.1 Materials

Chemicals and solvents were used as purchased from Aldrich, Acros, Fluka, Fisher Chemical, Alfa Aesar or VWR. *L*-Lactide and *D*-lactide monomers were kindly donated by Corbion-Purac and were passed through a silica plug with dichloromethane as eluent to remove impurities and then dried over 3Å molecular sieves in dichloromethane. The lactide monomers were further purified by recrystallization in toluene before being stored in a glove box under an inert atmosphere. (-)-Sparteine was dried over CaH_2 before use and 1-(3,5-bis(trifluoromethyl)phenyl)-3-cyclohexyl-thiourea was prepared and purified as reported.[33] Tetrahydropyran acrylate (THPA) was synthesized and purified as described previously.[34] 2,2-azobis(isobutyronitrile) (AIBN) was recrystallized from methanol and stored at 4 °C.

3.5.2 Instrumentation

^{1}H nuclear magnetic resonance (^{1}H NMR) spectra were recorded on a Bruker spectrometer operating at a frequency of 400 MHz in $CDCl_3$. The chemical shifts are given in ppm with tetramethylsilane (TMS) as an internal reference. Size exclusion chromatography (SEC) was performed on an Agilent 1260 Infinity Multi**-**Detector SEC instrument equipped with refractive index and UV detectors with THF and 2% triethylamine as eluent at a flow rate of 1 mL/min. SEC data was calibrated by Cirrus GPC software with poly(styrene) (PS) standards.

Mass spectra were obtained by using a Bruker Ultraflex II Matrix-assisted laser desorption/ionization time of flight (MALDI-ToF) mass spectrometer**.** The MALDI-ToF samples were prepared as follows: *trans*-2-[3-(4-*tert*-butyl-phenyl)-2-methyl-2-propenylidene] malononitrile (DCTB) was used as a matrix while sodium trifluoroacetate (NaTFA) was used as a cationization agent. Typically, DCTB (20 µL of a 40 mg/mL HPLC grade THF solution), samples (20 µL of a 1 mg/mL HPLC grade THF solution) and NaTFA (20 µL of a 0.1 mg/mL HPLC grade THF solution) were successively added into a small centrifuge tube and mixed by a vortex mixer. Traces of mixture were deposited on a MALDI-ToF plate followed by solvent evaporation. The samples were measured in reflectron ion mode and calibrated by SpheriCal (1200 ~ 8000 g/mol) standards. The stained TEM images were obtained by using a JEOL 2000FX instrument operated at 200 kV. TEM samples were negatively stained by phosphotungstic acid (PTA, 2 wt%) on formvar/carbon grids (300 Mesh, Cu, Elektron Technology UK LTD). Typically, formvar/carbon grids were cleaned by air plasma from a glow-discharge system (2 min, 20 mA) which also improved the hydrophilicity of the grids. 20 µL of particle solution (0.25 mg/mL) was added onto the grid and the solution was blotted away after 2 min and then left to air-dry. 5 µL of a 2 wt% PTA solution was then added onto the grid to stain the particles and was blotted away after 30 s before air-drying. TEM images were analyzed by ImageJ software, and 200 particles were counted for each sample to obtain the number-average length (L_n) and to calculate weight-average length (L_w), number-average width (W_n) (for cylindrical micelles) and number-average diameter (D_n) (for spherical micelles). L_n, L_w, W_n and D_n were calculated by using the following equations:

$$L_n = \frac{\sum_{i=1}^{n} N_i L_i}{\sum_{i=1}^{n} N_i} \quad (1)$$

$$L_w = \frac{\sum_{i=1}^{n} N_i L_i^2}{\sum_{i=1}^{n} N_i L_i} \quad (2)$$

$$W_n = \frac{\sum_{i=1}^{n} N_i W_i}{\sum_{i=1}^{n} N_i} \quad (3)$$

$$D_n = \frac{\sum_{i=1}^{n} N_i D_i}{\sum_{i=1}^{n} N_i} \quad (4)$$

where L_i and W_i are the length and the width of each counted cylindrical micelle while D_i is the diameter of each counted spherical micelle. N_i is the number of the cylindrical micelles with the length of L_i and the width of W_i or the number of spherical micelles with the diameter of D_i.

TEM images on graphene oxide (GO) support (Figure 3.21 and Figure 3.22) were obtained by using an aberration-corrected JEOL JEM-ARM200F instrument operating at 80 kV with spherical aberration corrected tuned to approximately +1 μm and images were recorded on a Gatan SC-1000 Orius CCD camera. TEM samples were prepared using a freeze drying method using GO-covered TEM grids that provide a thin support which is almost electron transparent and gives excellent contrast.[23] Generally, one drop of each sample solution (5 μL of 0.1 mg/mL) was added onto the GO grid and was frozen using liquid nitrogen for 15 s. The grid was then placed into a small vial inside a flask and subsequently lyophilized. After lyophilization, the grid was collected for TEM analysis.

SAXS were carried on the SAXS/WAXS beamline at the Australian Synchrotron facility at a photon energy of 11 keV. The samples in solution were run using 1.5 mm diameter quartz capillaries. The reactions took place in heated vials, with the solutions circulating through the capillaries using a peristaltic pump. Such a setup allows living data to be collected *in-situ*, which provides real-time

insight into the overall self-assembly process and the evolution of the morphologies. The measurements were collected at a sample to detector distance of 7.364 m to give a q range of 0.002 to 1.14 $Å^{-1}$ (SAXS) where q is the scattering vector and is related to the scattering angle (2θ) and the photon wavelength (λ) by the following equation:

$$q = \frac{4\pi \sin\theta}{\lambda} \qquad (5)$$

Data were processed using ScatterBrain for radial integration, normalization, absolute scaling, and background subtraction: patterns were normalized to fixed transmitted flux using a quantitative beamstop detector; the scattering from a blank (H_2O) was measured in the same capillary and was subtracted for each measurement; the two-dimensional SAXS images were converted into one-dimensional SAXS profiles ($I(q)$ *versus* q) by circular averaging, where $I(q)$ is the scattering intensity. NIST SANS macros were used for SAXS data analysis using Igor Pro software.[35] The scattering length density of the solvent was calculated using the "scattering length density calculator" provided by the NIST Center for Neutron Research.[36] Limits for q range were applied for the fitting of SAXS data from 0.002 to 0.07 Å.

The hydrodynamic diameter (D_h) of different nanoparticles was determined by dynamic light scattering (DLS). Typically, scattering of a 0.25 mg/mL aqueous nanoparticle solution was measured in a Malvern Zetasizer NanoS instrument equipped with a 4 mW He-Ne 633 nm laser module at 25 °C. Measurements were carried out at a detection angle of 173° (back scattering) and the data was further analyzed by Malvern DTS 6.20 software. D_h was calculated by fitting the apparent diffusion coefficient in the Stokes-Einstein equation $D_h = kT/(3\pi\eta D_{app})$, where k is the Boltzmann constant, T is the temperature and η is the viscosity

of the solvent. D_h only coincides to the real hydrodynamic diameter when the measured sample is a solution of monodispersed spherical particles as D_{app} equals the translational diffusion (D_t). For cylindrical particles, owing to their anisotropy, the rotational diffusion is not negligible and contributes to the D_{app}. Therefore, the D_h measured for the cylindrical micelles only has a relative value and provides polydispersity information to detect multiple populations.

FT-IR spectra were obtained using a Perkin Elmer Spectrum 100 FT-IR. Scans from 550 to 4000 cm^{-1} were taken, and the spectra corrected for background absorbance.

WAXD was performed on a Panalytical X'Pert Pro MPD equipped with a $CuK\alpha_1$ hybrid monochromator as the incident beam optics. Generally, *ca*. 30 mg of self-assembled freeze-dried particles were placed in a 10 mm sample holder, and standard "powder" $2\theta-\theta$ diffraction scans were carried out in the angular range from 2θ 10° to 30° at room temperature.

3.5.3 Self-assembly of the mixture of 1 and 2 to realize stereocomplex particles

Identical self-assembly conditions that have been previously reported by the group to afford homochiral cylinders were utilized to obtain stereocomplex particles.[18, 21] A 1:1 mixture of **1** (25 mg) and **2** (25 mg) were added in 0.5 mL THF to 2 mL of H_2O (resistivity 18.2 MΩ·cm) (*v*/*v* = 20/80) in a vial and sealed with a needle through the seal. Acetic acid (1 equivalent *per* THPA block) was added into the mixture and the self-assembly was set up at 65 °C. After 30 h, the solution was quenched by cooling in liquid nitrogen and subsequently

lyophilized. The freeze-dried particles were then redispersed in H_2O (0.25 mg/mL) at room temperature for TEM and DLS analysis.

3.5.4 Crystallization-driven self-assembly of 1 or 2 to obtain homochiral cylindrical micelles, 3 or 4

The identical CDSA conditions described above were used to prepare cylindrical micelle, **3** or **4**, from either diblock copolymer, **1** or **2**, as previously reported.[18, 21] Generally, 0.5 mL THF and 2 mL H_2O (resistivity 18.2 MΩ·cm) were added to 50 mg of polymer inside a vial. Acetic acid (1 equivalent *per* THPA block) was also added to the mixture. The vial was sealed with a needle through the seal and the mixture was allowed to stir at 65 °C for 30 h before being quenched in liquid nitrogen and subsequent lyophilization. The freeze-dried particles were then dissolved directly into H_2O (0.25 mg/mL) at room temperature for TEM and DLS analysis.

3.5.5 Preparation of amorphous spheres from diblock copolymer, 1

Diblock copolymer, **1** (50 mg), was exposed to the identical CDSA conditions (v_{THF}/v_{H2O} = 20/80, acetic acid (1 equivalent per THPA block), evaporation of THF, 65 ◦C).[18, 21] After 2.5 h of self-assembly, as the morphology of the nanostructures is still a spherical structure (before the morphological transition into cylinder),[20] the nanoparticle solution was quenched by cooling in liquid nitrogen and subsequently lyophilized. The spherical morphology was confirmed by using HR-TEM (Figure 3.21d) and the amorphous core nature of these nanoparticles was evidenced using WAXD analysis (Figure 3.20).

3.5.6 Addition of PDLA-*b*-PAA unimers into PLLA-*b*-PAA cylinder, 3, to induce a cylinder-to-sphere morphological transition

Diblock copolymer, **2** (50 mg), was exposed to the identical CDSA conditions (v_{THF}/v_{H2O}=20/80, acetic acid (1 equivalent per THPA block), evaporation of THF, 65 °C). After 2.5 h, as the PTHPA block was completely hydrolyzed into PAA,[20] the solution was quenched by cooling in liquid nitrogen and subsequently lyophilized. The freeze-dried PDLA-*b*-PAA diblock copolymer (17 mg) was fully dissolved in THF (0.5 mL). DLS analysis confirmed that PDLA-*b*-PAA existed as unimer state in THF (Figure 3.29). 0.5 mL of the PDLA-*b*-PAA unimer THF solution was then added into 2 mL of an aqueous solution of PLLA-*b*-PAA cylinder, **3** (17 mg), in a vial. The vial was sealed with a needle through the seal and the mixture was allowed to stir at 65 °C. At different time intervals, the mixture was sampled and quenched by cooling in liquid nitrogen and subsequently lyophilized. The freeze-dried particles were then dissolved directly into H_2O (0.25 mg/mL) at room temperature for TEM and DLS analysis.

3.5.7 Synthesis and characterization of PEO-*b*-PLLA and PEO-*b*-PDLA diblock copolymers

The synthesis of PEO-*b*-PLLA and PEO-*b*-PDLA diblock copolymers were obtained by the ROP of *L*-lactide or *D*-lactide using poly(ethylene glycol) methyl ether (20 kDa) as the macro-initiator.[37] The compositions of these two diblock copolymers were confirmed by ^{1}H NMR spectroscopy (Figure 3.32 and Table 3.6) showing the methine resonance of PLA repeat units at δ = 5.26 - 5.14 ppm and methylene resonances of PEO repeat units at δ = 3.83 - 3.46 ppm. SEC

analysis confirmed narrow dispersities for both diblock copolymers ($Đ_M$ < 1.05, Figure 3.33 and Table 3.6).

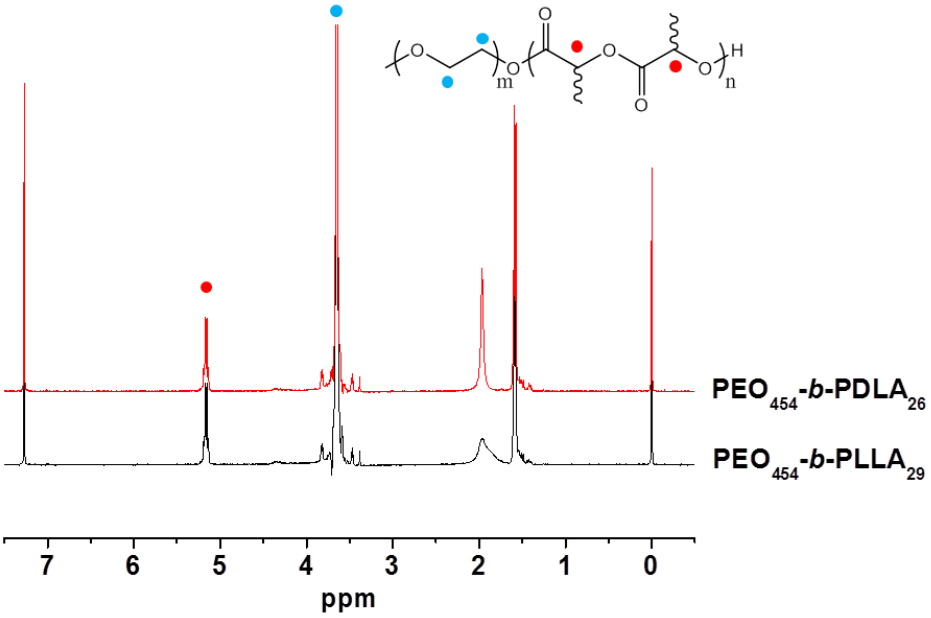

Figure 3.32. ^{1}H NMR spectra for PEO-*b*-PLLAand PEO-*b*-PDLA diblock copolymers (400 MHz, $CDCl_3$).

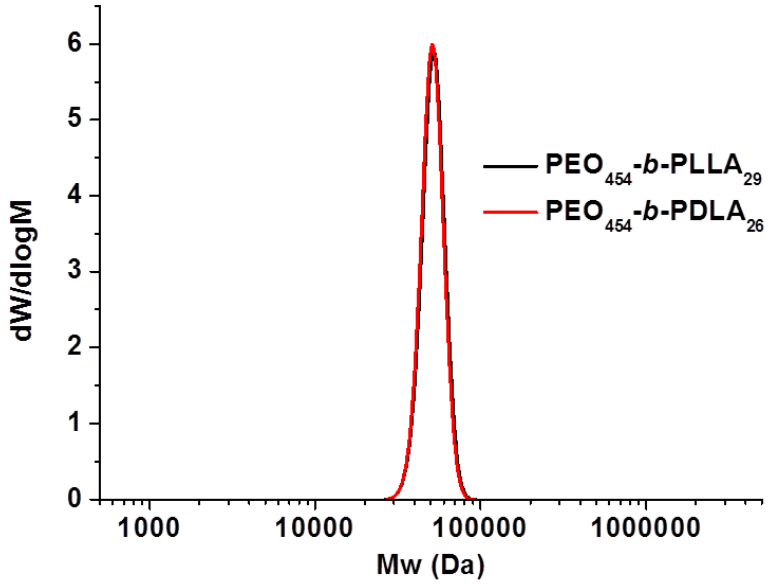

Figure 3.33. SEC chromatograms of PEO-*b*-PLLA and PEO-*b*-PDLA diblock copolymers ($CHCl_3$ with 0.5% TEA as eluent, RI detection).

Table 3.6. Characterization data PEO-*b*-PLLA and PEO-*b*-PDLA diblock copolymers

Polymer	M_n (kDa)[a]	$Đ_M$[b]
PEO_{454}-*b*-$PLLA_{29}$	24.2	1.03
PEO_{454}-*b*-$PDLA_{26}$	23.7	1.02

[a] Measured by ^1H NMR spectroscopy (400 MHz, $CDCl_3$). [b] Measured by $CHCl_3$ SEC.

3.5.8 Using stereocomplexation as a trigger to induce a morphological transition from the mixture of PEO-*b*-PLLA cylinders and PEO-*b*-PDLA cylinders

The homochiral PEO-*b*-PLLA cylinder and PEO-*b*-PDLA cylinder were prepared as previously reported by the group.[37] 1 mL of each cylinder solution (Note: the cylinder solution still co-existed with a number of spherical micelles) was directly mixed (20 mg/mL) before addition of 0.5 mL of THF. The mixture was sealed with a needle through the seal and the mixture was allowed to stir at 65 °C. At different time intervals, the mixture was sampled and quenched by cooling in liquid nitrogen and subsequently lyophilized. The freeze-dried particles were analyzed by FT-IR and dissolved directly into H_2O (0.25 mg/mL) at room temperature for TEM analysis.

3.6 Acknowledgements

Dr. Anaïs Pitto-Barry in the group has kindly synthesized PEO-*b*-PLA diblock copolymers and performed their CDSAs to prepare cylindrical micelles and performed the SAXS analysis at the Australian synchrotron and fitted all of the SAXS data in this chapter. Dr. Ana M. Sanchez and M. Adam Dyson from the Department of Physics at the University of Warwick performed the high resolution microscopy and its EWR analysis in this chapter.

3.7 References

(1) Jeong, B.; Bae, Y. H.; Lee, D. S.; Kim, S. W. *Nature* **1997,** 388, 860-862.

(2) Tsuji, H. *Macromol. Biosci.* **2005,** 5, 569-597.

(3) Oh, J. K. *Soft Matter* **2011,** 7, 5096-5108.

(4) Albertsson, A.-C.; Varma, I. K. *Biomacromolecules* **2003,** 4, 1466-1486.

(5) Uhrich, K. E.; Cannizzaro, S. M.; Langer, R. S.; Shakesheff, K. M. *Chem. Rev.* **1999,** 99, 3181-3198.

(6) Ikada, Y.; Jamshidi, K.; Tsuji, H.; Hyon, S. H. *Macromolecules* **1987,** 20, 904-906.

(7) Zhang, J.; Sato, H.; Tsuji, H.; Noda, I.; Ozaki, Y. *Macromolecules* **2005,** 38, 1822-1828.

(8) Tsuji, H.; Ikada, Y. *Polymer* **1999,** 40, 6699-6708.

(9) Fukushima, K.; Kimura, Y. *Polym. Int.* **2006,** 55, 626-642.

(10) Portinha, D.; Boue, F.; Bouteiller, L.; Carrot, G.; Chassenieux, C.; Pensec, S.; Reiter, G. *Macromolecules* **2007,** 40, 4037-4042.

(11) Nagahama, K.; Mori, Y.; Ohya, Y.; Ouchi, T. *Biomacromolecules* **2007,** 8, 2135-2141.

(12) Kang, N.; Perron, M. E.; Prud'homme, R. E.; Zhang, Y. B.; Gaucher, G.; Leroux, J. C. *Nano Lett.* **2005,** 5, 315-319.

(13) Kim, S. H.; Tan, J. P. K.; Nederberg, F.; Fukushima, K.; Yang, Y. Y.; Waymouth, R. M.; Hedrick, J. L. *Macromolecules* **2009,** 42, 25-29.

(14) Nederberg, F.; Appel, E.; Tan, J. P. K.; Kim, S. H.; Fukushima, K.; Sly, J.; Miller, R. D.; Waymouth, R. M.; Yang, Y. Y.; Hedrick, J. L. *Biomacromolecules* **2009,** 10, 1460-1468.

(15) Tan, B. H.; Hussain, H.; Leong, Y. W.; Lin, T. T.; Tjiu, W. W.; He, C. *Polym. Chem.* **2013,** 4, 1250-1259.

(16) Wolf, F. K.; Hofmann, A. M.; Frey, H. *Macromolecules* **2010,** 43, 3314-3324.

(17) Portinha, D.; Bouteiller, L.; Pensec, S.; Richez, A.; Chassenieux, C. *Macromolecules* **2004,** 37, 3401-3406.

(18) Petzetakis, N.; Dove, A. P.; O'Reilly, R. K. *Chem. Sci.* **2011,** 2, 955-960.

(19) Petzetakis, N.; Robin, M. P.; Patterson, J. P.; Kelley, E. G.; Cotanda, P.; Bomans, P. H. H.; Sommerdijk, N. A. J. M.; Dove, A. P.; Epps, T. H.; O'Reilly, R. K. *ACS Nano* **2013,** 7, 1120-1128.

(20) Petzetakis, N.; Walker, D.; Dove, A. P.; O'Reilly, R. K. *Soft Matter* **2012,** 8, 3408-3414.

(21) Sun, L.; Petzetakis, N.; Pitto-Barry, A.; Schiller, T. L.; Kirby, N.; Keddie, D. J.; Boyd, B. J.; O'Reilly, R. K.; Dove, A. P. *Macromolecules* **2013,** 46, 9074-9082.

(22) Becker, J. M.; Pounder, R. J.; Dove, A. P. *Macromol. Rapid Commun.* **2010,** 31, 1923-1937.

(23) Patterson, J. P.; Sanchez, A. M.; Petzetakis, N.; Smart, T. P.; Epps, T. H.; Portman, I.; Wilson, N. R.; O'Reilly, R. K. *Soft Matter* **2012,** 8, 3322-3328.

(24) Dyson, M. A.; Sanchez, A. M.; Patterson, J. P.; O'Reilly, R. K.; Sloan, J.; Wilson, N. R. *Soft Matter* **2013,** 9, 3741-3749.

(25) Zhang, L. F.; Eisenberg, A. *Macromolecules* **1999,** 32, 2239-2249.

(26) Zhang, J.; Wang, L. Q.; Wang, H. J.; Tu, K. H. *Biomacromolecules* **2006,** 7, 2492-2500.

(27) Blanazs, A.; Madsen, J.; Battaglia, G.; Ryan, A. J.; Armes, S. P. *J. Am. Chem. Soc.* **2011,** 133, 16581-16587.

(28) Wang, X. S.; Guerin, G.; Wang, H.; Wang, Y. S.; Manners, I.; Winnik, M. A. *Science* **2007,** 317, 644-647.

(29) Gilroy, J. B.; Gadt, T.; Whittell, G. R.; Chabanne, L.; Mitchels, J. M.; Richardson, R. M.; Winnik, M. A.; Manners, I. *Nat. Chem.* **2010,** 2, 566-570.

(30) Schmelz, J.; Schedl, A. E.; Steinlein, C.; Manners, I.; Schmalz, H. *J. Am. Chem. Soc.* **2012,** 134, 14217-14225.

(31) He, W.-N.; Zhou, B.; Xu, J.-T.; Du, B.-Y.; Fan, Z.-Q. *Macromolecules* **2012,** 45, 9768-9778.

(32) Brizzolara, D.; Cantow, H.-J.; Diederichs, K.; Keller, E.; Domb, A. J. *Macromolecules* **1996,** 29, 191-197.

(33) Pratt, R. C.; Lohmeijer, B. G. G.; Long, D. A.; Lundberg, P. N. P.; Dove, A. P.; Li, H. B.; Wade, C. G.; Waymouth, R. M.; Hedrick, J. L. *Macromolecules* **2006,** 39, 7863-7871.

(34) Hertler, W. R. *US Patent* **1991,** No. 5 072 029.

(35) Kline, S. *J. App. Cryst.* **2006,** 39, 895-900.

(36) Scattering Length Density Calculator http://www.ncnr.nist.gov/resources/ sldcalc.html (2014).

(37) Pitto-Barry, A.; Kirby, N.; Dove, A. P.; O'Reilly, R. K. *Polym. Chem.* **2014,** 5, 1427-1436.

Chapter 4. Fluorescent Aminobromomaleimide Functional Group Containing Cylindrical Micelles towards Bioimaging Contrast Agents

4.1 Abstract

In this chapter, a novel fluorescent aminobromomaleimide (ABM) fluorophore was designed and incorporated in a dual-headed initiator that combines ring-opening polymerization (ROP) and reversible addition-fragmentation chain transfer (RAFT) polymerization to yield poly(*L*-lactide)-*b*-poly(tetrahydropyran acrylate) (PLLA-*b*-PTHPA) diblock copolymer. Well-defined fluorescent cylindrical micelles were prepared from ABM containing PLLA-*b*-PTHPA diblock copolymers using a crystallization-driven self-assembly (CDSA) approach. In comparison, only ill-defined nanostructures were obtained from a fluorescent dithiomaleimide (DTM) functional group containing Y-shaped $(PLLA)_2$-*b*-PTHPA block copolymer when it was exposed to the identical CDSA condition. Such phenomenon was ascribed to the Y-shape structure of the DTM labeled polymer. Biocompatible poly(ethylene glycol) (PEG) was then directly grafted onto the poly(acrylic acid) PAA corona of the ABM labelled PLLA-*b*-PAA cylindrical micelles *via* amidation without affecting their morphologies. By using time-correlated single-photon counting (TCSPC) analysis, we noticed that the self-assembled ABM labeled nanostructures possessed significantly longer fluorescence lifetimes than their precursor polymers. Also, different morphologies of ABM labelled nanostructures affected their fluorescence lifetimes since poly(*DL*-lactide)-*b*-poly(acrylic acid) (PDLLA-*b*-PAA) spherical micelles showed longer fluorescence lifetime when compared to PLLA-*b*-PAA cylindrical micelles. This new fluorescent ABM functional handle has been demonstrated to be applicable to label various PLA containing polymers and cylindrical and spherical nanoparticles which can provide potential use in bioimaging.

4.2 Introduction

Fluorescent imaging techniques provide us with great opportunities to study specific biological processes and mechanisms both *in vitro* and *in vivo*.[1] Polymeric nanoparticles with core-shell structures have attracted significant attention as fluorescent contrast agents due to the ease of functionalization of the precursor polymers and their tuneable dimensions and shapes.[2, 3] Various strategies such as physical encapsulation of organic dyes[4] and functionalization of the nanoparticles in the core,[5] shell[6] and surface[7] have been utilized to prepare fluorescent polymeric nanoparticles. Recently, we have demonstrated that the dithiomaleimide (DTM) functional group is highly emissive and can be utilized to label both proteins and polymers.[8] In addition, incorporations of DTM functionalized acrylate (or methacrylate) monomers into the corresponding poly(acrylate)s (or poly(methacrylate)) during a reversible addition-fragmentation chain transfer (RAFT) copolymerization allowed various fluorescent copolymers with narrow dispersities to be obtained.[9] Furthermore, by modifying a dual headed ring-opening polymerization (ROP)/RAFT initiator with a DTM functional group at the junction (Scheme 4.1, initiator, **1**), a fluorescent amphiphilic poly(*DL*-lactide)-*b*-poly(triethylene glycol monomethyl ether acrylate) block copolymer was prepared that can further undergo self-assembly in water to yield spherical micelles.[10] These fluorescent spherical micelles with a fluorescent core-shell interface showed bright self-reporting properties and show promise as potential delivery agents.[10]

In comparison to spherical micelles, cylindrical micelles may possess advantages when used as self-reporting contrast agents due to their long dimensions, resulting in less opportunity to be captured by macrophages and

therefore longer circulation time *in vivo*.[11] Cylindrical nanoparticles can be achieved from the crystallization-driven self-assembly (CDSA) of crystalline or semi-crystalline poly(ferrocenylsilane),[12] poly(ethylene),[13] poly(3-hexylthiophene)[14] or poly(acrylonitrile)[15] block containing polymers. We have previously reported the successful preparation of semi-crystalline poly(lactide) (PLA) containing cylindrical micelles with tuneable dimensions and different corona blocks in aqueous systems.[16-18] More importantly, most fluorescent contrast agents reported to date showed spherical structures and only a few studies have reported fluorescent polymeric cylindrical micelles due to the narrow self-assembly window (within the region 1/3 ≤ packing parameter $p \leq 1/2$)[19] to access a cylindrical morphology. For instance, Discher *et al.*[11] physically encapsulated hydrophobic dyes inside the core of poly(ethylene glycol)-*b*-poly(caprolactone) cylindrical micelles and studied their interactions with human lung-derived epithelial cells,[11] however, the stability of these self-reporting contrast agents were limited due to self-quenching of the dye and possible leakage from the particle. Manners, Winnik and co-workers recently reported color-tuneable fluorescent cylinders prepared from 4,4-difluoro-4-bora-3a,4a-diaza-s-indacene (BODIPY) functionalized PFS-*b*-(PDMA-*r*-PVMS) block copolymers using a CDSA approach.[20] Furthermore, Monteiro *et al*. attached fluorescent Oregon green 488 maleimide and Streptavidin DyLight 550 probes onto the surface of functionalized poly(styrene)-*b*-poly(*N*-isopropylacrylamide) cylindrical micelles which were obtained by aqueous RAFT dispersion polymerization.[21]

To further explore fluorescent DTM nanoparticles, we decided to use a CDSA approach to drive DTM bearing poly(*L*-lactide)$_2$-*b*-poly(acrylic acid) (PLLA$_2$-*b*-

PAA) copolymers into fluorescent cylindrical micelles. However, as DTM initiator, **3** (Scheme 4.1), generated two PLLA arms and affected the chain folding process of PLLA during the CDSA, only ill-defined cylindrical micelles were achieved. Therefore, a fluorescent aminobromomaleimide (ABM) initiator, **4** (Scheme 4.1), that can generate only one PLLA arm was designed and explored instead (note that thiobromomaleimide species were found possess very weak fluorescence intensity)[8]. By using the CDSA, ABM containing PLLA-*b*-PAA diblock copolymers formed well-defined fluorescent cylindrical micelles. As our target is to use these fluorescent cylindrical micelles as bioimaging contrast agents, three triblock copolymers with different biocompatible coronal blocks, PHEA, PDMA and POEGA were also synthesized. However, none of these triblock copolymers self-assembled into well-defined cylindrical micelles. Therefore, direct PEGylation on the already formed fluorescent PLLA-*b*-PAA cylindrical micelles was performed without destroying the cylindrical morphologies. Time-correlated single-photon counting (TCSPC) analysis was performed to further compare the fluorescence lifetimes of various ABM polymeric materials.

4.3 Results and discussion

4.3.1 Synthesis of DTM containing Y-shaped $(PLLA)_2$-*b*-PTHPA block copolymers

To explore fluorescent DTM functional cylindrical nanoparticles, a fluorescent precursor Y-shaped poly(*L*-lactide)$_2$-*b*-poly(tetrahydropyran acrylate) ($(PLLA)_2$-*b*-PTHPA) block copolymer, **6**, (Scheme 4.2) was synthesized from a DTM functionalized dual headed ROP/RAFT initiator, **3**, that has been previously reported by the group (Scheme 4.1).[10] The DTM initiator, **3**, was prepared by the modification of the dual headed initiator, **1**, that has been described in Chapters 2 and 3. Firstly, **1** was reacted with 2,3-dibromomaleimide to give product, **2**, using the Mitsunobu reaction. Then, **2** was reacted with 2-mercaptoethanol by an addition/elimination reaction to give DTM initiator, **3**.[22] The successful synthesis of DTM initiator 3 was confirmed using ^{1}H NMR spectroscopy (400 MHz, CDCl3, Figure 4.1).

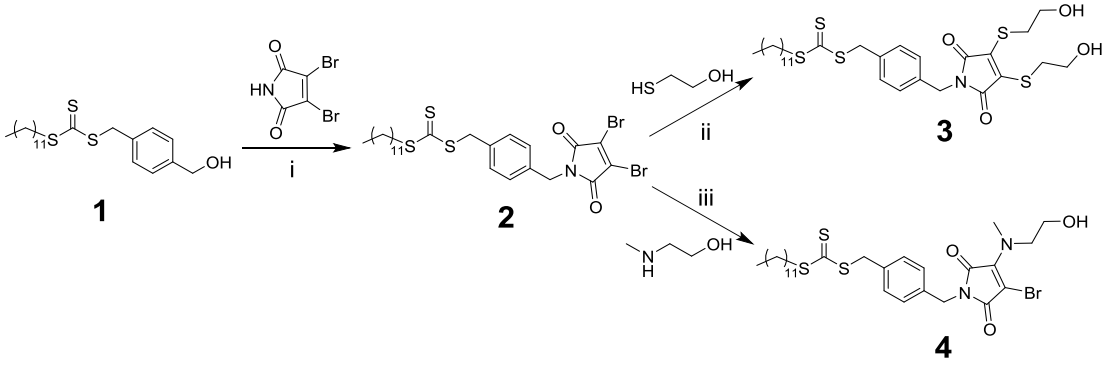

Scheme 4.1 Synthetic procedures of DTM and ABM functional group containing dual headed ROP/RAFT initiators. i) PPh_3, DIAD, neopentyl alcohol, THF, -78 °C 20 h; ii) TEA, THF, room temperature, 3 h; iii) Na_2CO_3, THF, room temperature, 4 h.

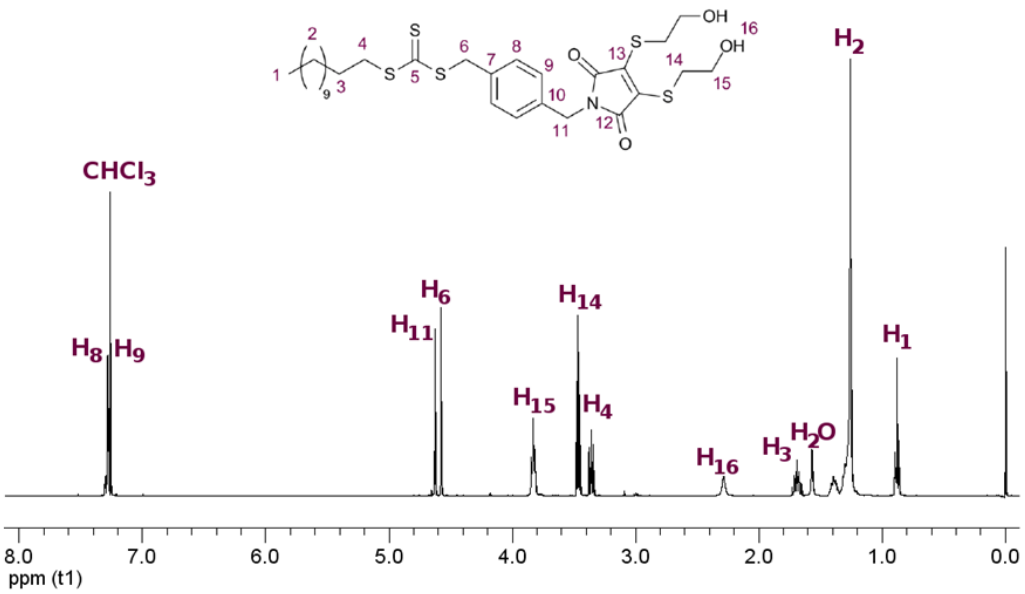

Figure 4.1. ^{1}H NMR spectrum (400 MHz, $CDCl_3$) of DTM dual-headed-initiator, **3**.[8]

The fluorescent precursor $(PLLA)_2$-*b*-PTHPA block copolymer, **6**, was achieved by a combination of ROP and RAFT polymerization using the DTM initiator, **3** (Scheme 4.2). Firstly, ROP of *L*-lactide was performed using the highly selective 1-(3,5-bis(trifluoromethyl)phenyl)-3-cyclohexyl-thiourea/(-)-sparteine co-catalyst system[23] and initiated from the two hydroxyl groups of DTM initiator, **3**. ^{1}H nuclear magnetic resonance (^{1}H NMR) spectroscopic analysis indicated the successful synthesis of $(PLLA)_2$, **5** (methine resonance of PLLA repeat units observed at δ = 5.36 - 4.94 ppm) (Figure 4.2).

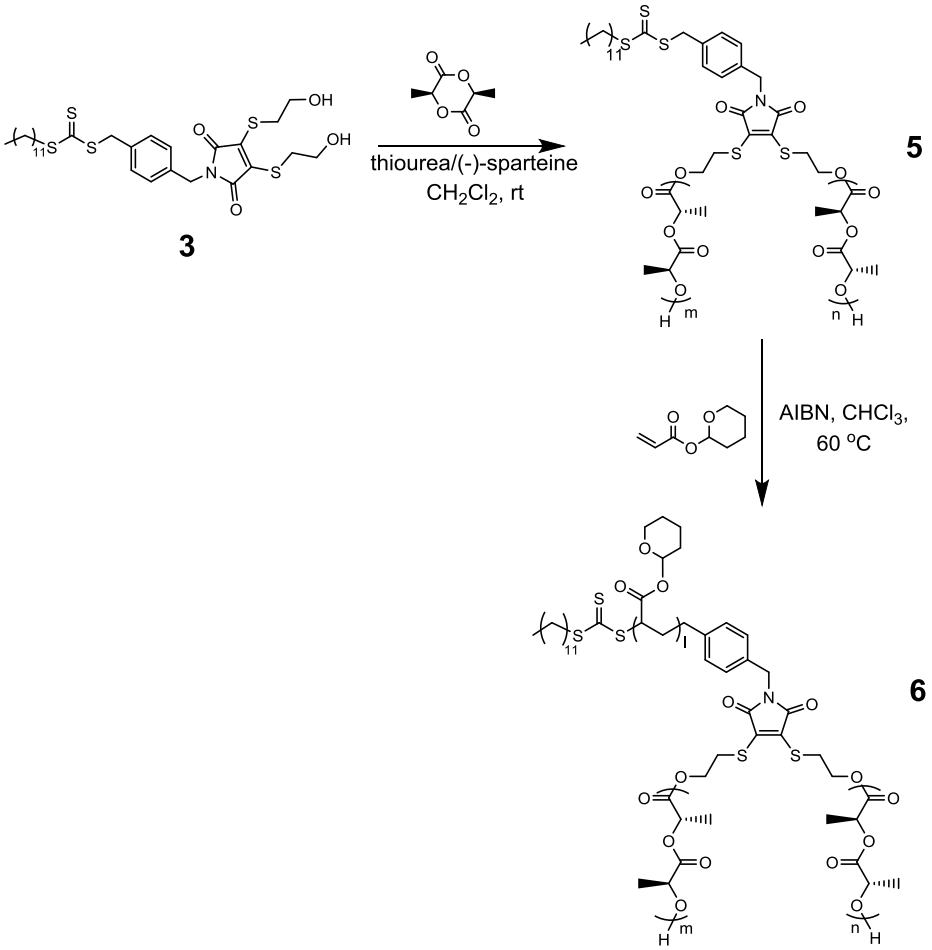

Scheme 4.2. Synthetic procedures of DTM functional $(PLLA)_2$-*b*-PTHPA diblock copolymer, **6**.

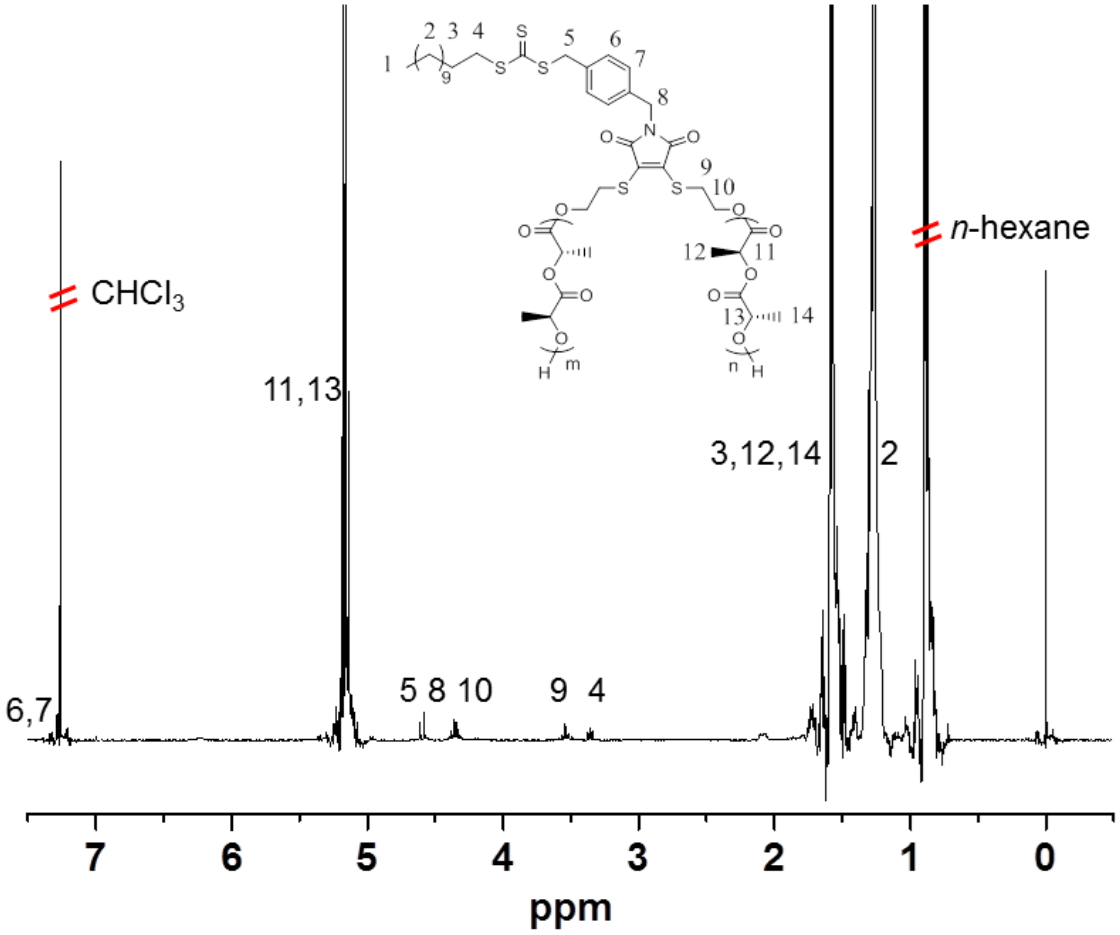

Figure 4.2. ^{1}H NMR spectrum (400 MHz, $CDCl_3$) of DTM containing $(PLLA)_2$ macro-initiator, **5**.

PTHPA was subsequently grown from the $(PLLA)_2$ macro-initiator, **5**, by RAFT polymerization of THPA as proven by ^{1}H NMR spectroscopic analysis showing the broad methine resonance of the tetrahydropyranyl protecting groups of PTHPA repeat units at δ = 6.40 - 5.60 ppm (Figure 4.3). The block compositions of the $(PLLA)_2$ macro-initiator, **5**, and precursor $(PLLA)_2$-*b*-PTHPA block copolymer, **6**, were found to be $(PLLA_{41})_2$ and $(PLLA_{41})_2$ -*b*-$PTHPA_{564}$ by ^{1}H NMR spectroscopy (Table 4.1). The block copolymer, **6**, was designed with a degree of polymerization (DP) of PLLA of 82 and hydrophobic weight fraction of 22.5% in order to access well-defined cylindrical nanostructures based on

the results in Chapter 2. Size exclusion chromatography (SEC) analysis revealed successful RAFT chain-extension and narrow dispersities of both polymers (Figure 4.4, Table 4.1).

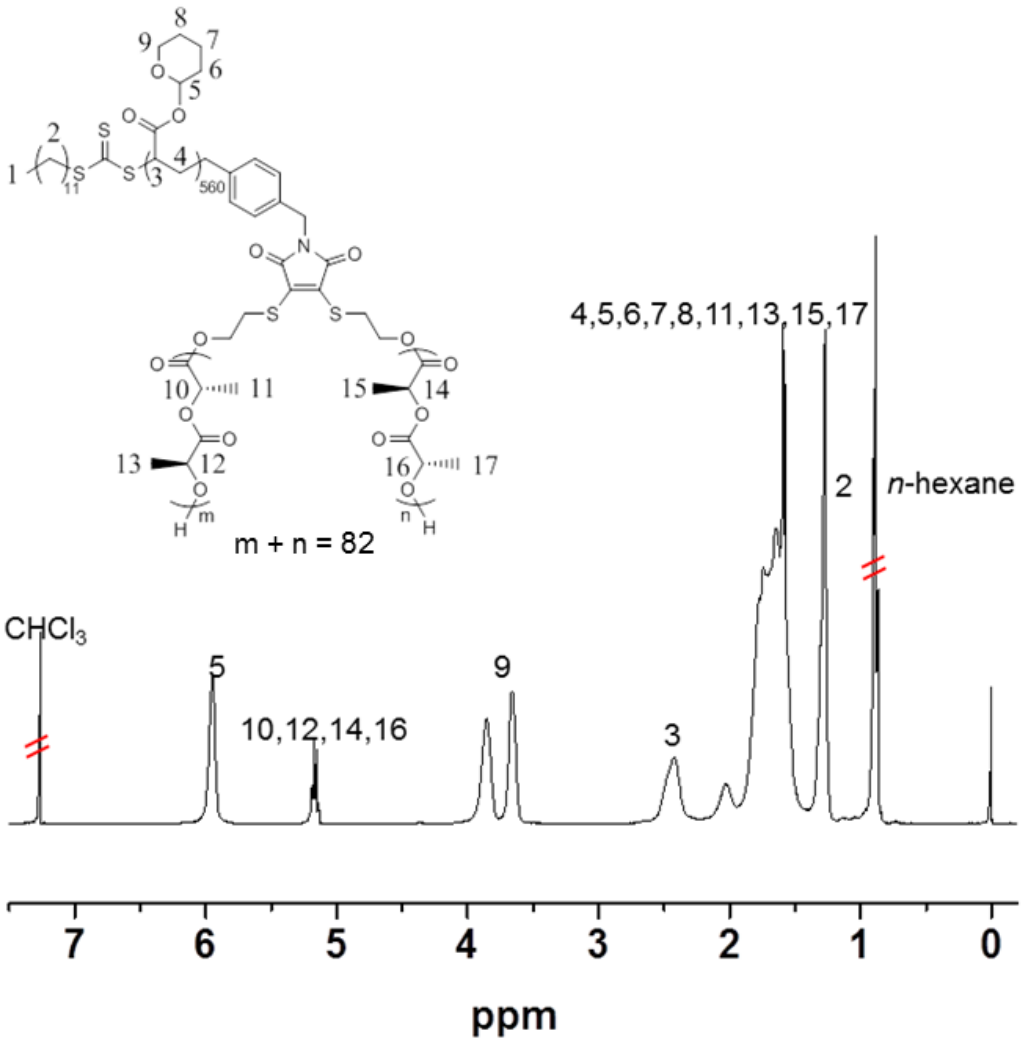

Figure 4.3. ^{1}H NMR (400 MHz, $CDCl_3$) spectrum of DTM containing $(PLLA)_2$-*b*-PTHPA diblock copolymer, **6**.

Table 4.1 Characterization data of $(PLLA)_2$, **5**, and $(PLLA)_2$-*b*-PTHPA, **6**, polymers

Polymer	M_n (kDa)[a]	$Đ_M$[b]	Hydrophobic weight fraction (%)[c]
$(PLLA_{41})_2$, **5**	12.4	1.09	—
$(PLLA_{41})_2$-*b*-$PTHPA_{564}$, **6**	100.5	1.30	22.5

[a] Measured by ^1H NMR spectroscopy in $CDCl_3$. [b] Measured by SEC analysis ($CHCl_3$ with 0.5% TEA as eluent). [c] PLLA weight fraction in the resultant PLLA-*b*-PAA diblock copolymer.

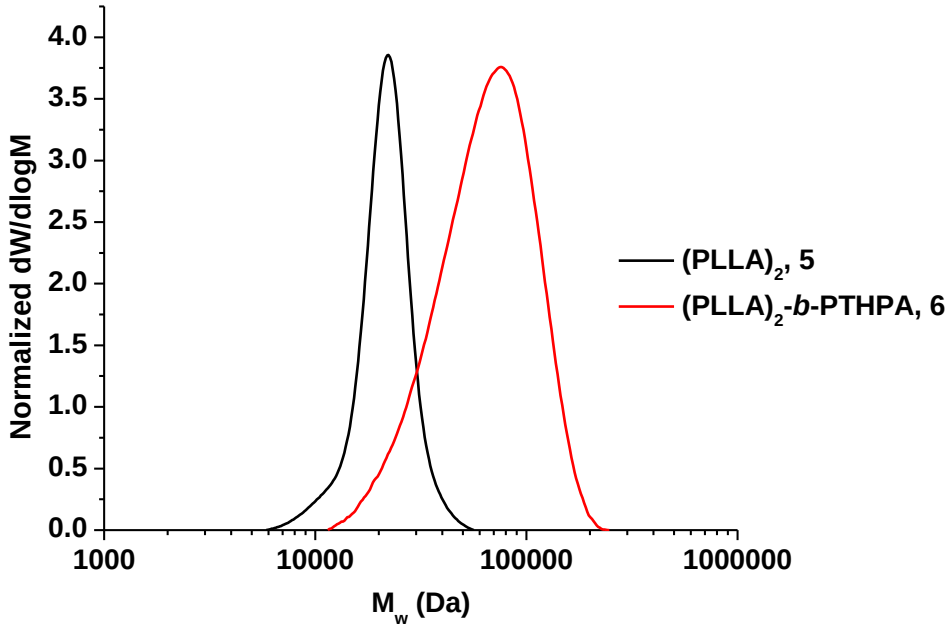

Figure 4.4. SEC chromatograms ($CHCl_3$ with 0.5% TEA as eluent, RI detector) of DTM containing $(PLLA)_2$ macro-initiator, **5**, and $(PLLA)_2$-*b*-PTHPA block copolymer, **6**.

4.3.2 Crystallization-driven self-assembly of DTM containing Y-shaped $(PLLA)_2$-*b*-PTHPA block copolymer, 6

The same self-assembly conditions described in Chapter 2 were utilized for the CDSA of fluorescent Y-shaped polymer, **6**.[16, 17] Specifically, a mixture of THF

and H_2O (v_{THF}/v_{H2O} = 20/80) was added to a vial containing block copolymer, **6**, to give a final block copolymer concentration of 20 mg/mL. Acetic acid (1 *eq*. to PTHPA block) was added to the mixture to promote the hydrolysis of PTHPA into PAA and hence allow the formation of amphiphilic block copolymers. The sealed vial was pierced with a needle to allow the evaporation of THF during the self-assembly process. The temperature of the self-assembly was set at 65 °C, which is above the T_g of poly(lactide),[24] to promote crystallization of the PLLA core block.

After 30 h of self-assembly, cylindrical micelles were observed by transmission electron microscopy (TEM) analysis (Figure 4.5), however, a number of lamellar micelles were noted to co-exist with these cylinders. Several experiments with varied concentrations of polymer, **6**, and solvent compositions during CDSA still failed to yield well-defined cylindrical micelles (data not given). As Y-shaped block copolymer, **6**, has a sufficient DP of PLLA and a hydrophobic weight fraction (22.5%) to induce CDSA, well-defined cylindrical structures were expected based on the results in Chapter 2. The reason for the formation of lamellar micelles could be attributed to the Y-shape structure of block copolymer, **6**, which has two crystallizable PLLA arms. During the unimer addition process in CDSA,[25] one PLLA arm of the unimer can fold into a cylindrical micelle seed while the other PLLA arm of the same unimer can fold into a second cylindrical micelle seed and therefore, the Y-shaped unimer may act as a “cross-linker” to generate large lamellar particles. Another possible reason could be the $(PLLA)_2$ homopolymers remained in the $(PLLA)_2$-*b*-PTHPA block copolymer (some tailing was observed in the SEC chromatograms in Figure 4.4) that affected the CDSA process to yield well-defined cylindrical

micelles. To overcome this “cross-linking” problem, an aminobromomaleimide (ABM) initiator, **4**, (Scheme 4.1) that can generate only one PLLA arm was designed and utilized instead (note that thiobromomaleimide was found to be not very fluorescent)[8]. Such an ABM initiator, **4**, is proposed to be fluorescent as similar aminomaleimide derivatives were proven to be fluorescent by Naka and Kato.[26]

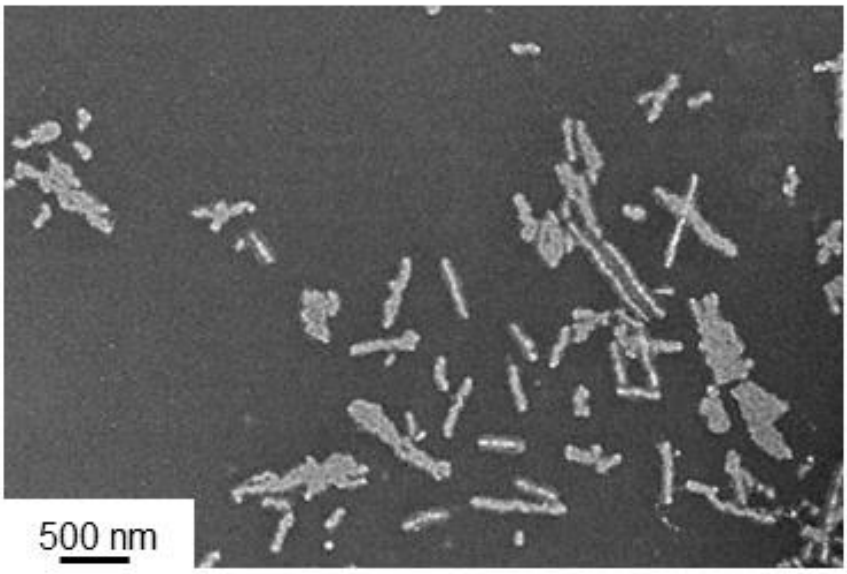

Figure 4.5. TEM image showing a large number of lamellar micelles co-existed with cylindrical micelles obtained from the CDSA of Y-shaped polymer, **6**. TEM sample was prepared by slow drying and negatively stained using PTA. Scale bar = 500 nm.

4.3.3 Synthesis and characterization of fluorescent ABM functional ROP/RAFT dual headed initiator, 4

As shown in Scheme 4.1, the dual headed ROP/RAFT initiator, **1**, was modified with 2,3-dibromomaleimide to give product, **2**, using the Mitsunobu reaction. **2** was subsequently reacted with 2-methylamino ethanol by an addition/elimination reaction in THF to give monoaminated ROP/RAFT dual

initiator, **4**.[22] The successful synthesis of ABM initiator, **4**, was proven using ^{1}H NMR spectroscopy (Figure 4.6) and ^{13}C NMR spectroscopy (Figure 4.7).

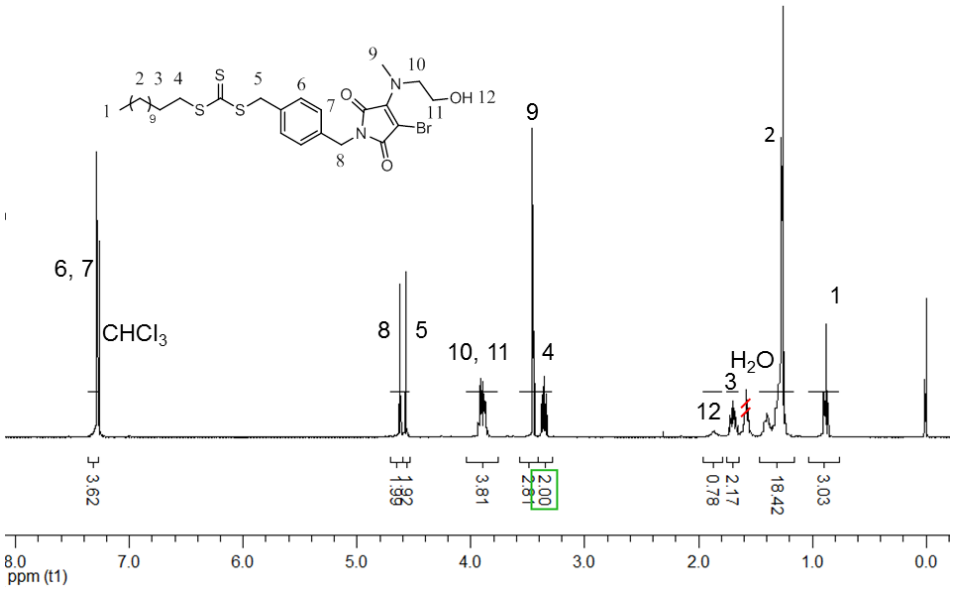

Figure 4.6. ^{1}H NMR (400 MHz, $CDCl_3$) spectrum of ABM containing initiator, **4**.

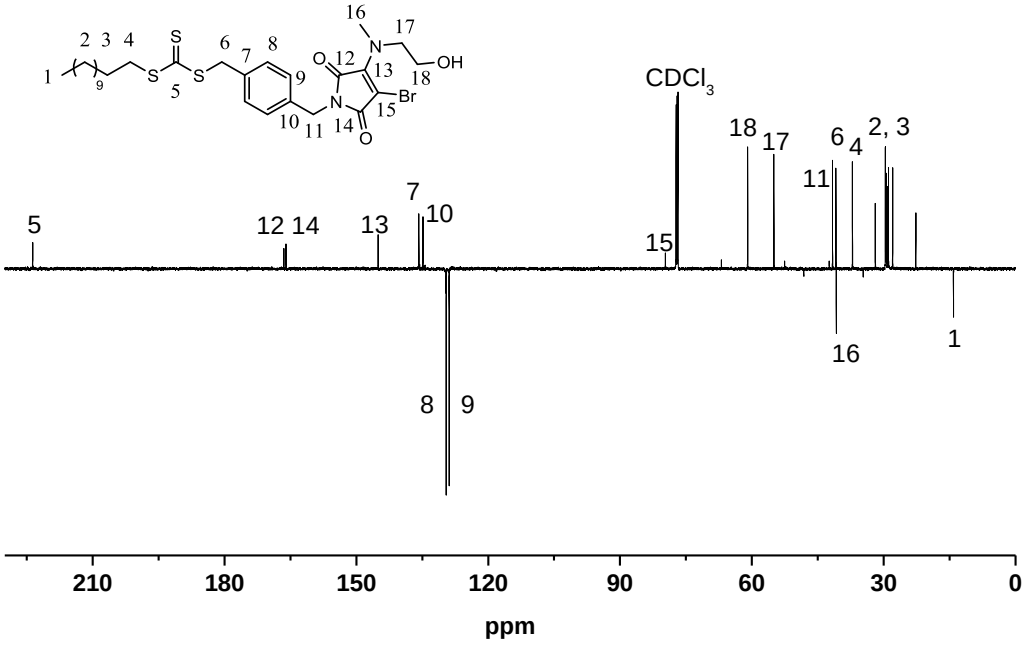

Figure 4.7. ^{13}C NMR (150 MHz, $CDCl_3$) spectrum of ABM containing initiator, **4**.

The fluorescence of ABM initiator, **4**, was confirmed by fluorescence spectroscopy, where the excitation spectrum of **4** in 1,4-dioxane (0.1 mM) exhibited excitation maxima at *ca*. 265 nm and 395 nm and the emission spectrum has a maximum of *ca*. 505 nm (Figure 4.8). Both the excitation and emission maxima of ABM initiator, **4**, were found to be slightly different to those of DTM species (excitation maxima at 265 and 415 nm, and the emission maxima at 520 nm) as reported by the group.[8]

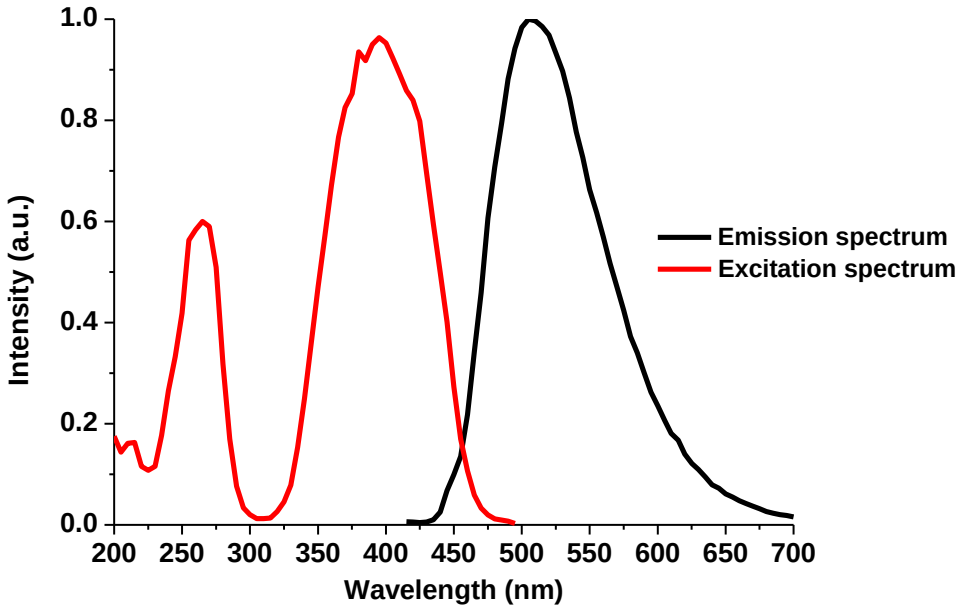

Figure 4.8. Excitation and emission spectra of ABM containing CTA, **4**, in 1,4-dioxane (0.1 mM).

4.3.4 Synthesis and characterization of fluorescent ABM containing PLLA-*b*-PTHPA

The fluorescent ABM containing PLLA-*b*-PTHPA diblock copolymer was achieved using the identical ROP/RAFT approach as described above but with the dual headed ABM initiator, **4**, instead of the DBM initiator, **3** (Scheme 4.3).

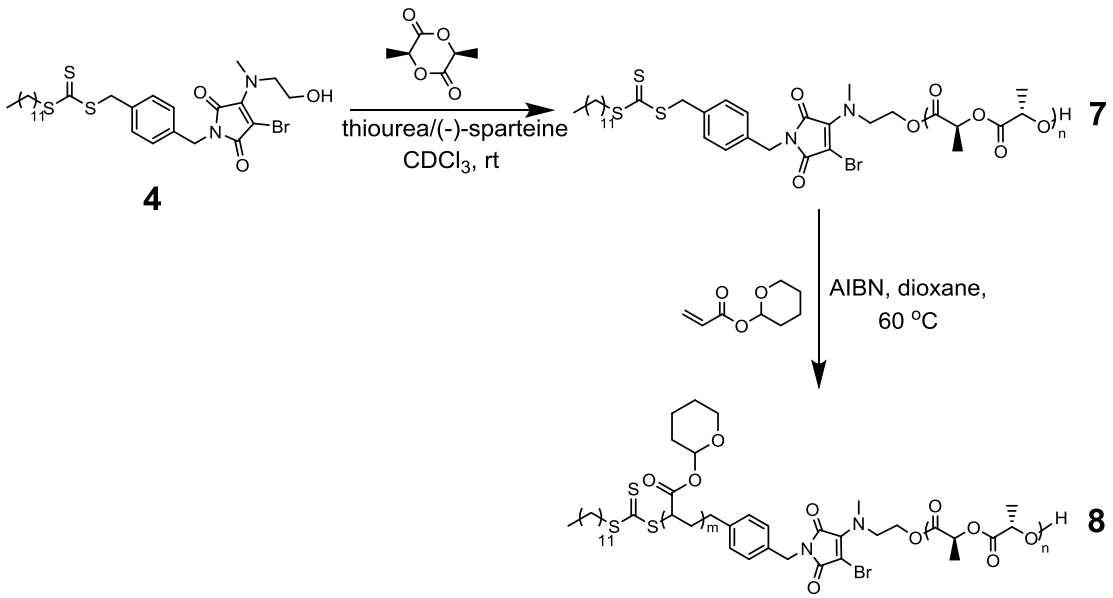

Scheme 4.3. Synthetic procedures for ABM containing PLLA-*b*-PTHPA diblock copolymer, **8**.

Firstly, ROP of *L*-lactide was performed using the highly selective thiourea/(-)-sparteine co-catalyst system. The polymerization rate was slightly slower with *ca*. 92% monomer conversion after 3.5 h (Figure 4.9), while it only took 3 h to reach nearly full monomer conversion using initiator, **1**, under the same ROP conditions. ^{1}H NMR spectroscopic analysis indicated the successful synthesis of ABM containing PLLA, **7** (methine resonance of PLLA repeat units observed at δ = 5.38 - 5.00 ppm) (Figure 4.10). MALDI-ToF measurement of polymer, **7**, was consistent with the expected molar masses of the PLLA repeat unit and minimal transesterification was observed (Figure 4.11). Furthermore, SEC analysis revealed the narrow dispersity of PLLA macro-initiator, **7** (Figure 4.13, Table 4.2).

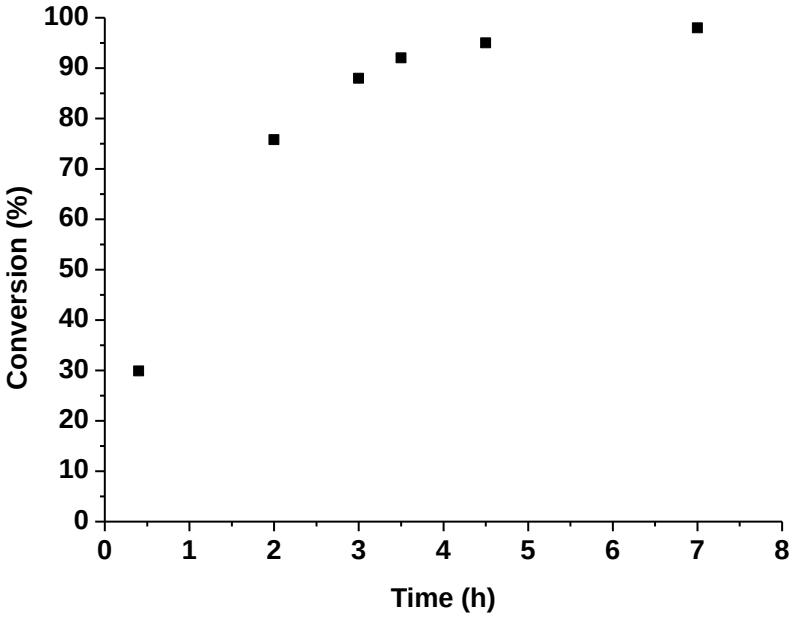

Figure 4.9. *L*-lactide monomer conversion as a function of time during the ROP using ABM initiator, **4**.

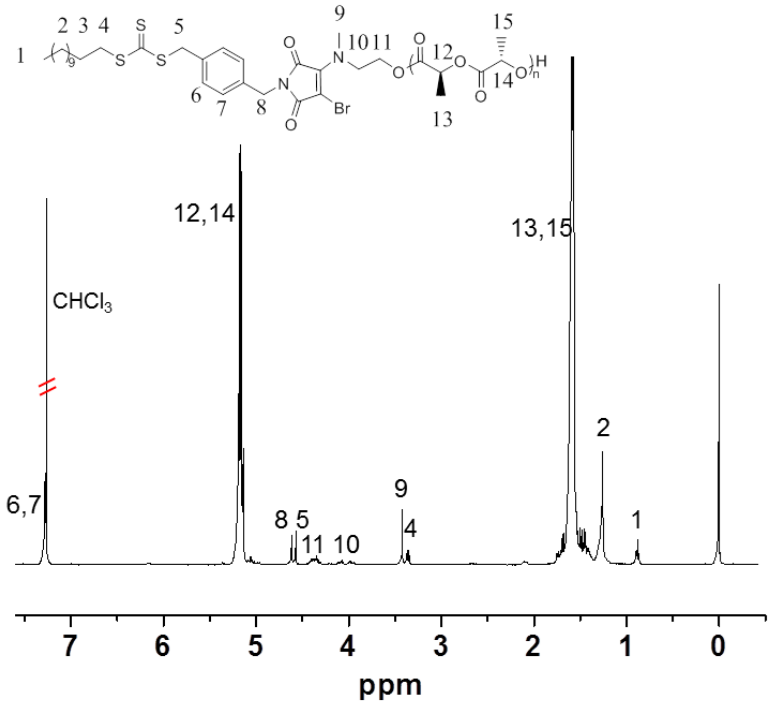

Figure 4.10. ^{1}H NMR (400 MHz, $CDCl_3$) spectrum of ABM group containing PLLA macro-initiator, **7**.

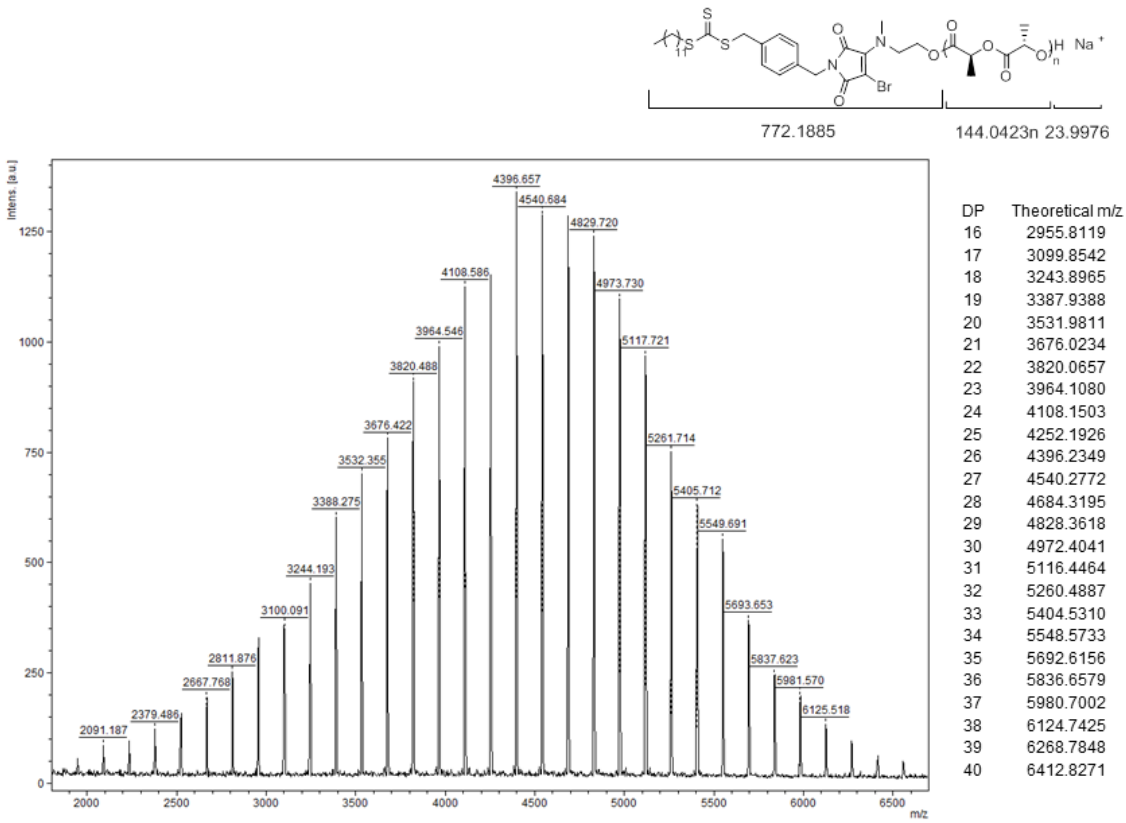

Figure 4.11. MALDI-ToF spectrum of ABM containing PLLA macro-initiator, **7**, showing minimal transesterification. Trans-2-[3-(4-tert-butyl-phenyl)-2-methyl-2-propenylidene] malononitrile (DCTB) was used as a matrix while sodium trifluoroacetate (NaTFA) was used as a cationization agent to prepare samples.

PTHPA was subsequently grown from the PLLA macro-initiator, **7**, using the RAFT polymerization of THPA. ^{1}H NMR spectroscopic analysis indicated the successful synthesis of ABM containing PLLA-*b*-PTHPA diblock copolymer, **8**, with the broad methine resonance of tetrahydropyranyl protecting groups of PTHPA repeat units at δ = 6.21 - 5.68 ppm (Scheme 4.3, Figure 4.12) and no deprotection of PTHPA block was observed during the RAFT polymerization. The diblock copolymer, **8**, (Table 4.2) was designed with a DP of PLLA of 32 and hydrophobic weight fraction of 20.8% in order to access well-defined cylindrical nanostructures based on the results in Chapter 2. SEC analysis

revealed the narrow dispersity of diblock copolymer, **8**, and successful chain-extension from PLLA macro-initiator, **7** (Figure 4.13, Table 4.2).

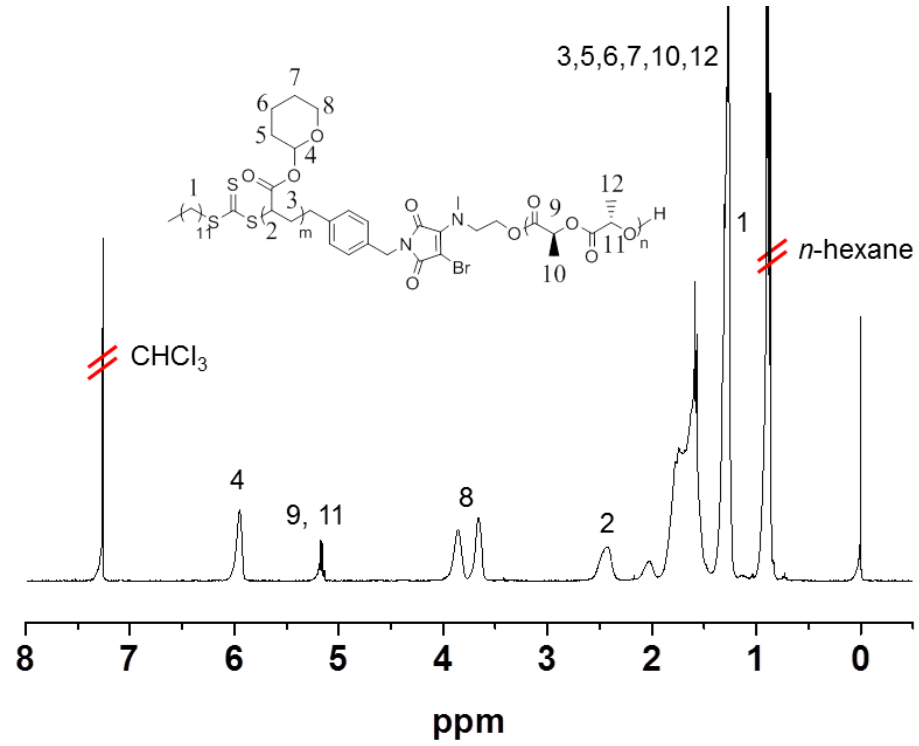

Figure 4.12. ^{1}H NMR (400 MHz, $CDCl_3$) spectrum of ABM group containing PLLA-*b*-PTHPA diblock copolymer, **8**.

Table 4.2. Characterization data of ABM containing PLLA macro-initiator, **7**, and PLLA-*b*-PTHPA diblock copolymer, **8**

Polymer	M_n **(kDa)**[a]	$Đ_M$[b]	**Hydrophobic weight fraction (%)**[c]
$PLLA_{32}$, **7**	5.2	1.06	—
$PLLA_{32}$-*b*-$PTHPA_{243}$, **8**	43.2	1.22	20.8

[a] Measured by ^{1}H NMR spectroscopy (400 MHz, $CDCl_3$). [b] Measured by $CHCl_3$ SEC.

[c] PLLA weight fraction in the final PLLA-*b*-PAA diblock copolymer.

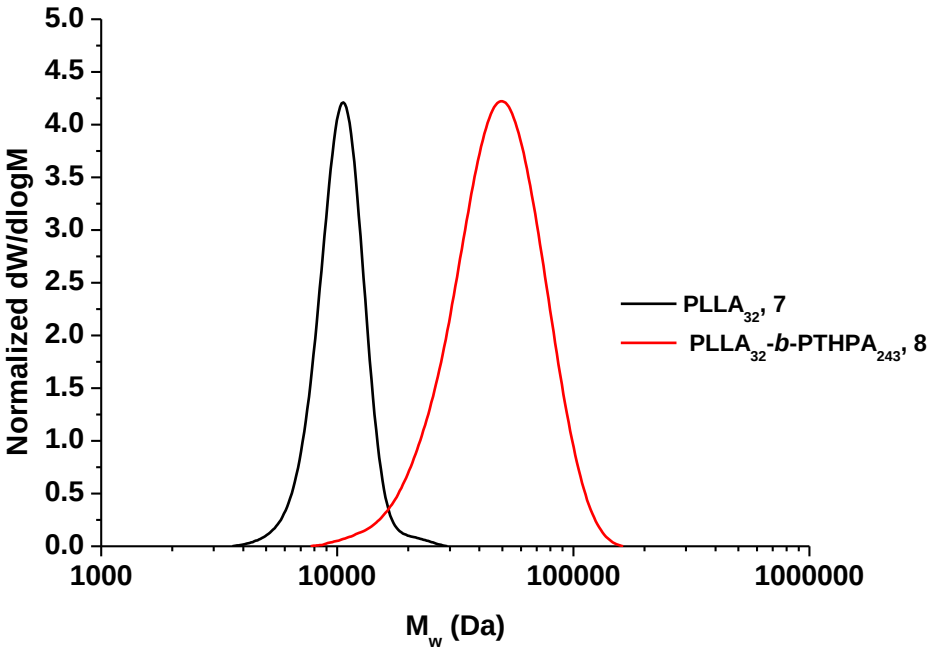

Figure 4.13. SEC chromatograms ($CHCl_3$ with 0.5% TEA as eluent) of ABM containing PLLA macro-initiator, **7**, and PLLA-*b*-PTHPA diblock copolymer, **8**.

The fluorescence of ABM containing diblock copolymer, **8**, was confirmed by fluorescence spectroscopy, where the excitation spectrum of, **8**, in 1,4-dioxane (0.1 mM) shows excitation maxima at *ca*. 260 nm and 395 nm and the emission spectrum gives a maximum at *ca*. 500 nm (Figure 4.14).

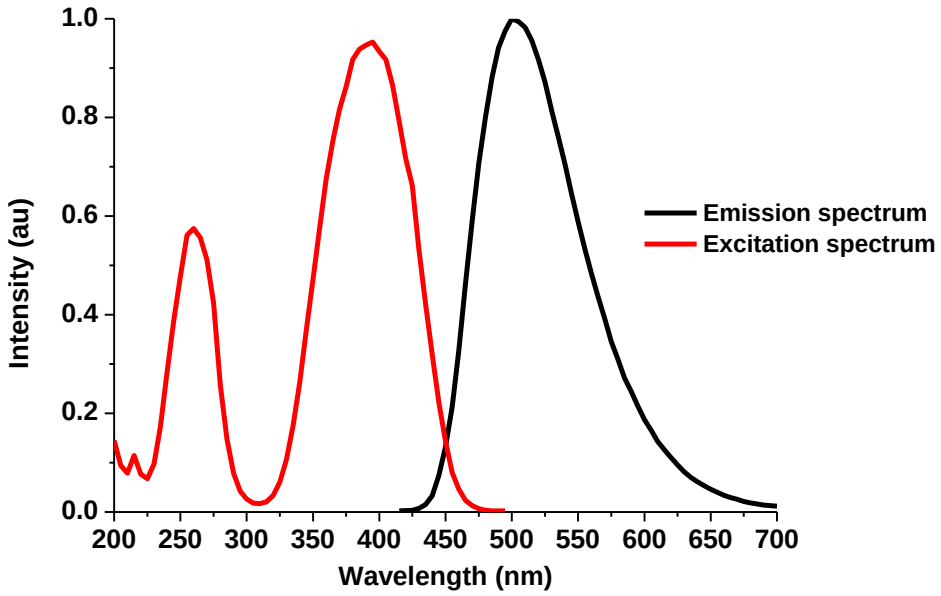

Figure 4.14. Excitation and emission spectra of ABM containing diblock copolymer PLLA-*b*-PTHPA, **8**, in 1,4-dioxane (0.1 mM).

4.3.5 Crystallization-driven self-assembly of ABM containing PLLA-*b*-PTHPA diblock copolymer, 8, to obtain cylindrical micelles

The CDSA of the fluorescent ABM containing PLLA-*b*-PTHPA diblock copolymer, **8**, was carried out using the identical conditions described above. Specifically, 0.5 mL of THF and 2 mL of H_2O (resistivity 18.2 MΩ·cm) were added to 50 mg of polymer inside a vial. Acetic acid (1 *eq*. *per* PTHPA block) was also added to the mixture to facilitate the hydrolysis of PTHPA to PAA. The vial was sealed with a needle through the seal and the mixture was allowed to stir at 65 °C.

After 6 h of self-assembly, cylindrical micelles were obtained as observed by TEM, while a large amount of spherical micelles were also noted (Figure 4.15a). The solution was therefore left for prolonged heating to promote the sphere-to-

rod transition,[25] however, after 25 h of self-assembly, only ill-defined cylindrical structures and a large number of spheres were observed (Figure 4.15b). It was hypothesized that the ABM functional group at the junction of the diblock copolymer, **8**, could be less stable over such a long period of heating at 65 °C, which affected the growth process of the cylindrical micelles.

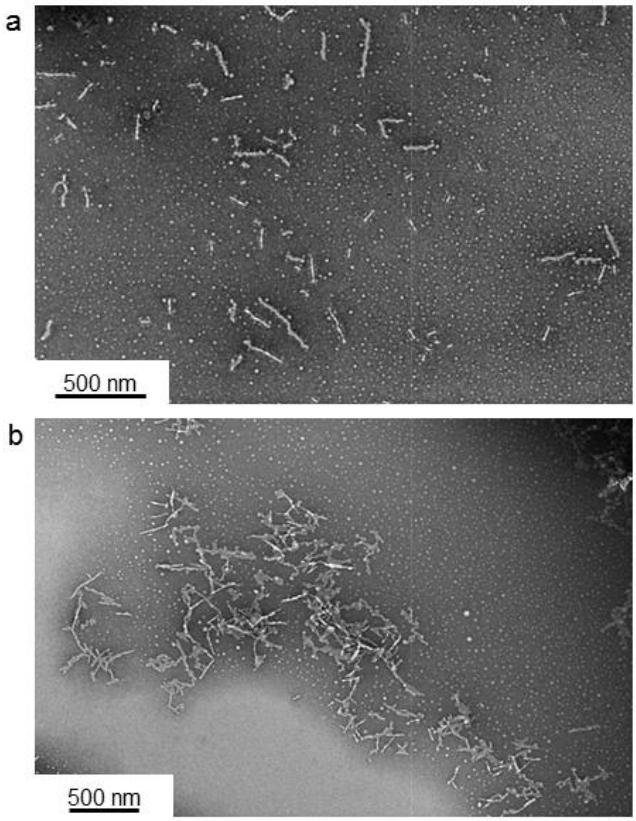

Figure 4.15. TEM images showing the self-assembled structures from ABM containing PLLA-*b*-PTHPA diblock copolymer, **8**, when the concentration was at 20 mg/mL at the beginning of CDSA. a, cylindrical micelles co-existing with spherical micelles were observed after 6 h; b, ill-defined cylindrical micelles were observed after 25 h. TEM samples were prepared by slow drying and negatively stained using PTA. Scale bar = 500 nm.

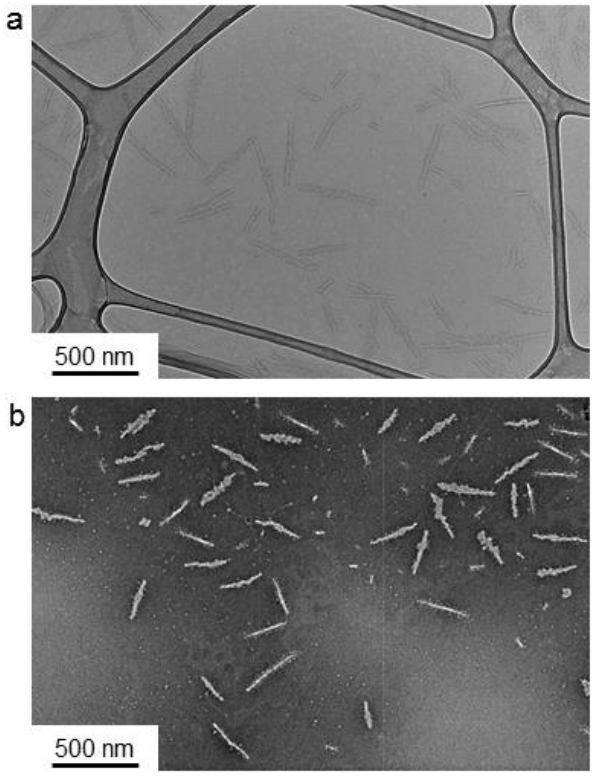

Figure 4.16. TEM images showing the cylindrical nanostructures, **9**, self-assembled from ABM containing PLLA-*b*-PTHPA diblock copolymer, **8**, when the concentration was at 10 mg/mL at the beginning of CDSA. a, prepared by a slow drying method on GO grid; b, prepared by a slow drying method followed by negative staining using PTA. Scale bar = 500 nm.

To overcome this problem, a lower concentration of diblock copolymer, **8**, (10 mg/mL instead of 20 mg/mL) was utilized so that the sphere-to-rod transition would be faster when the same amount of THF (20%) was present at the beginning of the CDSA. The CDSA process was also shortened to 6 h. After 6 h of heating at 65 °C with the evaporation of THF, well-defined cylindrical micelles, **9**, (L_n = 224 nm, L_w/L_n = 1.25, W_n = 49 ± 8 nm) were achieved as observed by TEM analysis (Figure 4.16). Dynamic light scattering (DLS) measurements showed only one population for such ABM containing cylindrical micelles (Figure 4.17). Interestingly, these cylindrical micelles which

were obtained only after 6 h of CDSA showed a very intense crystalline Bragg peak at a *2θ* value of 16.6° (which corresponds to the reflections of (110)/(200) planes in the crystalline domains of PLLA)[27] as proven by wide-angle X-ray diffraction (WAXD) analysis (Figure 4.18).

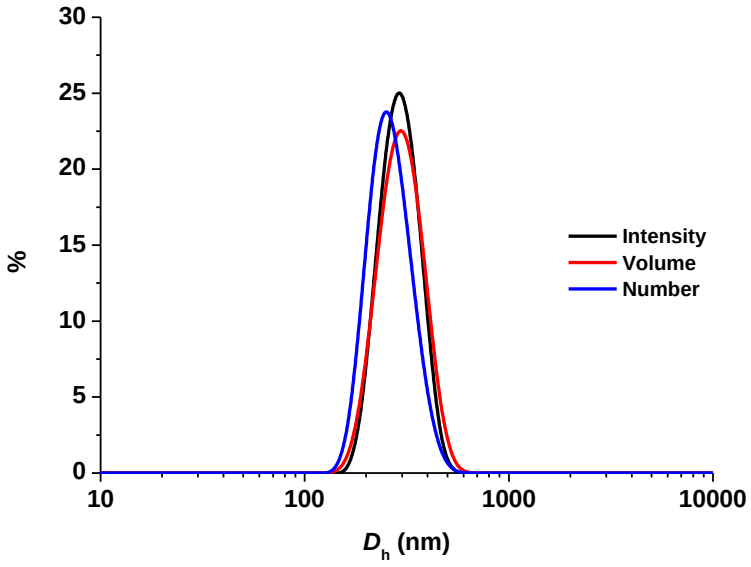

Figure 4.17. DLS data showing one population of PLLA-*b*-PAA cylindrical micelles, **9**.

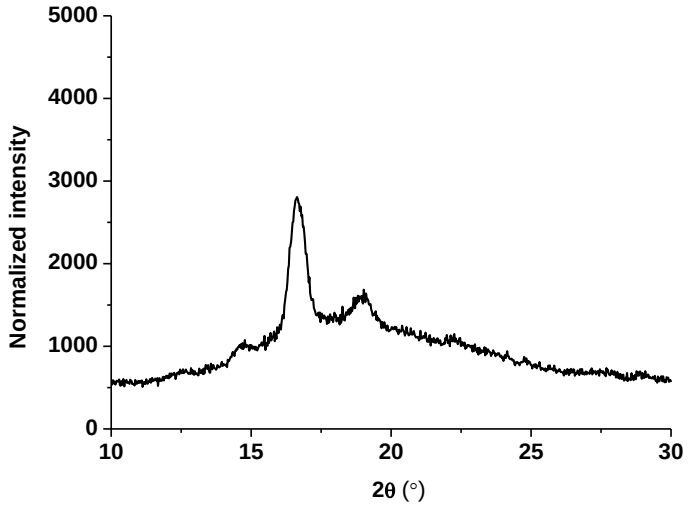

Figure 4.18. WAXD diffractogram showing the crystalline core nature of PLLA-*b*-PAA cylindrical micelles, **9**.

ABM containing PLLA-*b*-PAA cylindrical micelles, **9**, in H_2O (resistivity 18.2 MΩ·cm, 0.1 mg/mL) showed a similar excitation maximum at *ca*. 390 nm and emission maximum at *ca*. 505 nm (Figure 4.19) when compared to the precursor PLLA-*b*-PTHPA diblock copolymer, **8**, in 1,4-dioxane.

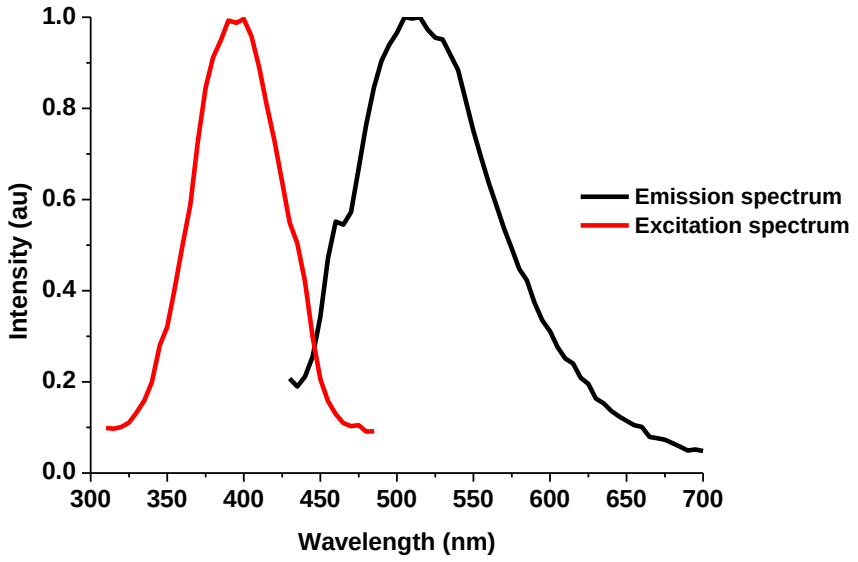

Figure 4.19. Excitation and emission spectra of ABM group containing PLLA-*b*-PAA cylindrical micelles, **9**, in H_2O (resistivity 18.2 MΩ·cm, 0.1 mg/mL).

4.3.6 Preparation of biocompatible ABM containing cylindrical micelles

To further utilize these fluorescent ABM containing PLLA-*b*-PAA cylindrical micelles as potential bioimaging contrast agents, a biocompatible polymer corona should be designed to shield the PAA shell. In our first attempt, three triblock copolymers with different biocompatible corona blocks, poly(2-hydroxyethyl acrylate) (PHEA), **10**, poly(*N*,*N*'-dimethylacrylamide) (PDMA), **11**, and poly(oligo(ethylene glycol) methyl ether acrylate) (POEGA), **12**, were synthesized through RAFT chain-extensions from PLLA-*b*-PTHPA diblock copolymer, **8** (Scheme 4.4, Table 4.3). The targeted hydrophobic weight

fractions of these triblock copolymers were *ca*. 18% (Table 4.3) in order to obtain well-defined cylindrical morphologies based on the results in Chapter 2.

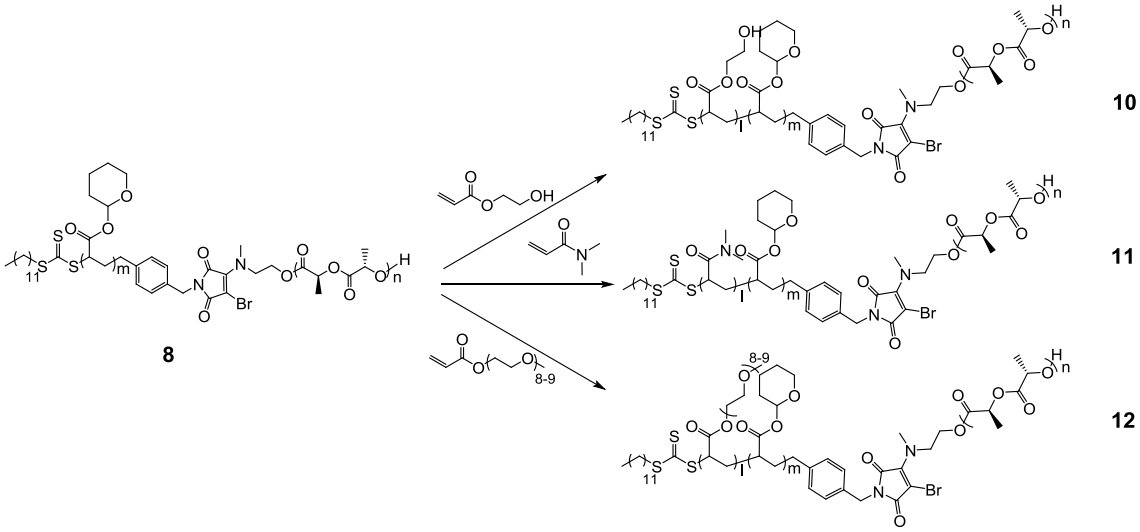

Scheme 4.4. Synthetic routes for different ABM containing triblock copolymers using RAFT polymerizations. All of the RAFT polymerizations were carried out in 1,4-dioxane with AIBN as a radical initiator at 60 °C.

Table 4.3. Characterization data of ABM containing triblock copolymers, **10**, **11** and **12**

Polymer	M_n (kDa)[b]	$Đ_M$	Hydrophobic weight fraction (%)[e]
$PLLA_{32}$-*b*-$PTHPA_{227}$-*b*-$PHEA_{35}$, **10**[a]	44.7	1.24[c]	18.4
$PLLA_{32}$-*b*-$PTHPA_{243}$-*b*-$PDMA_{38}$, **11**	46.9	1.22[d]	17.8
$PLLA_{32}$-*b*-$PTHPA_{243}$-*b*-$POEGA_{17}$, **12**	51.3	1.35[d]	15.2

[a] Triblock copolymer, **10,** was obtained by chain-extension from a similar $PLLA_{32}$-*b*-$PTHPA_{227}$ diblock copolymer to **8**. [b] Measured by ^{1}H NMR spectroscopy (400 MHz, $CDCl_3$). [c] Measured by DMF SEC. [d] Measured by $CHCl_3$ SEC. [e] PLLA weight fractions in the resultant PLLA-*b*-PAA-*b*-PHEA, PLLA-*b*-PAA-*b*-PDMA or PLLA-*b*-PAA-*b*-POEGA triblock copolymers.

^{1}H NMR spectroscopy showed successful synthesis of the three different triblock copolymers with the appearance of new resonances that correspond to

HEA, DMA or OEGA repeat units (Figure 4.20, Table 4.3), while SEC analysis proved their narrow dispersities (Figure 4.21, Table 4.3). However, when these three triblock copolymers were exposed to the successful CDSA conditions used to prepare cylindrical micelles, **9**, (10 mg/mL, v_{THF}/v_{H2O} = 20/80, 65 °C, evaporation of THF, 6 h), only ill-defined structures were obtained from **10** and **11**, while **12** formed relatively short cylindrical micelles (Figure 4.22). Several experiments with different concentrations of these triblock copolymers and solvent compositions were also performed, but unfortunately, no well-defined nanostructures were obtained (data not given). We propose that the PDMA could interact with the PAA shell block and inhibit the CDSA process to give ill-defined cylindrical micelles since PDMA was found to be a good proton acceptor[28] while the hydroxyl groups of the PHEA corona block could also interact with PAA shell block through possible hydrogen bonding interaction that further affected the CDSA process. We have previously noticed that the formation of PLLA-*b*-PEO cylindrical micelles was very slow and often took a few days to grow into long cylindrical micelles[18] and this phenomenon may explain the short dimensions of cylindrical micelles obtained from triblock copolymer, **12**, which has a similar POEGA coronal block.

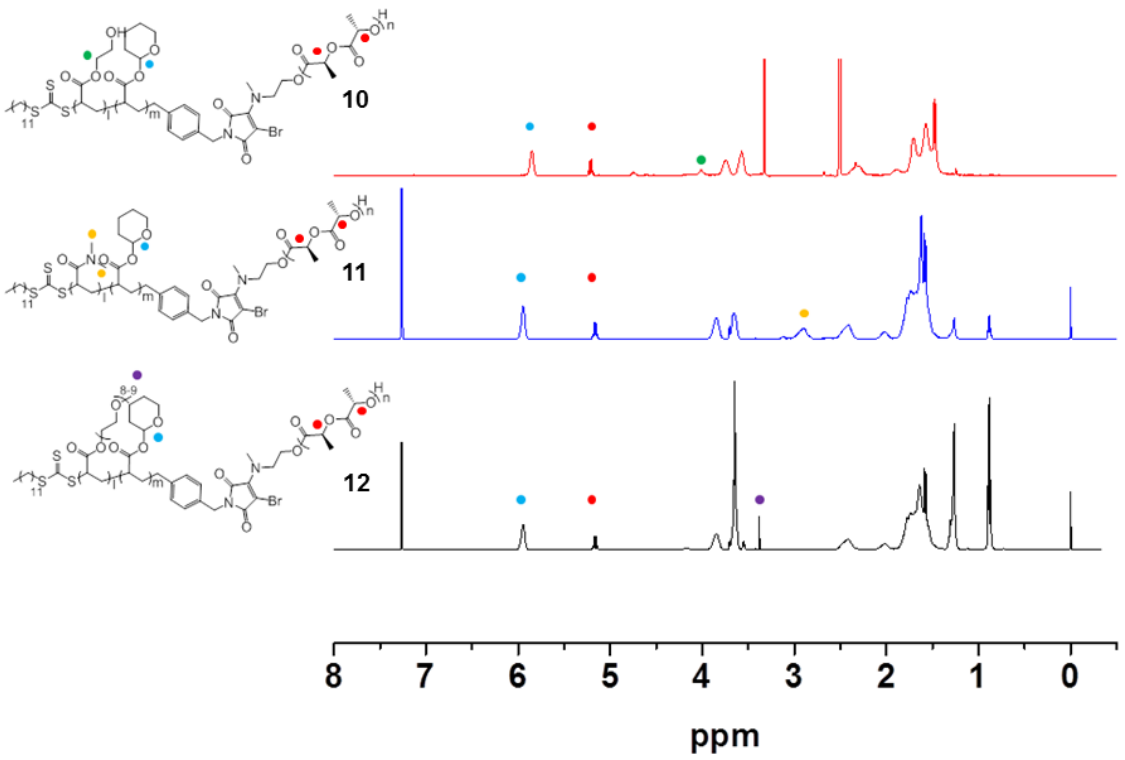

Figure 4.20. ^{1}H NMR (400 MHz) spectra of different ABM containing triblock copolymers (**10** in d_6-DMSO, **11** and **12** in $CDCl_3$).

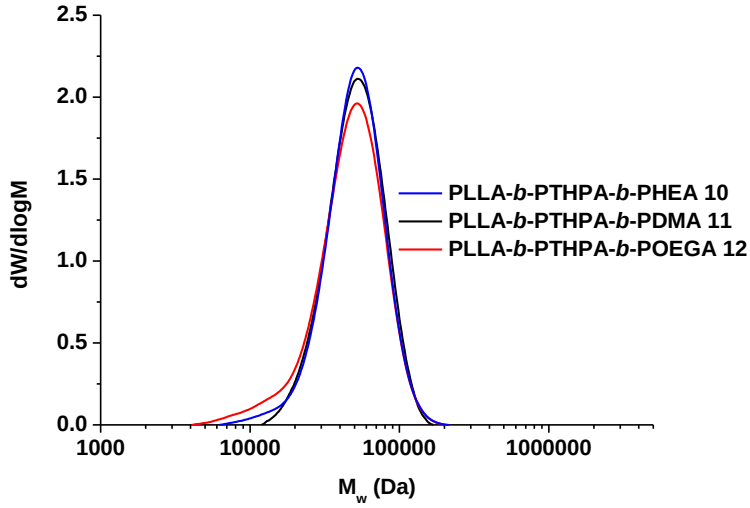

Figure 4.21. SEC chromatograms of different ABM group containing triblock copolymers (**10** and **12** were characterized in DMF with 5 mM NH_4BF_4 using PMMA as standards while **11** was characterized in $CHCl_3$ with 0.5% TEA using PS as standards, RI detector)

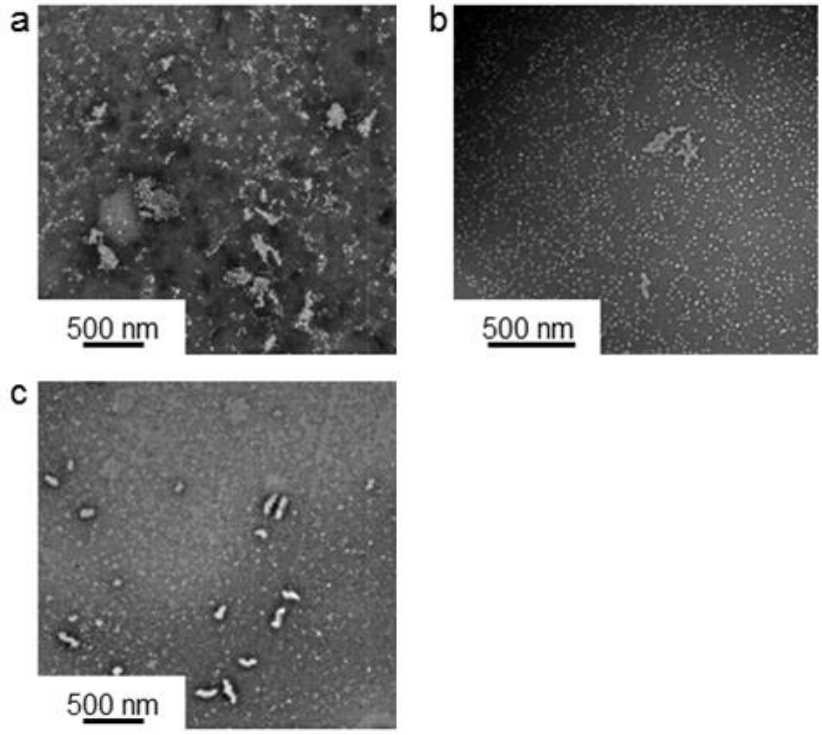

Figure 4.22. TEM images showing the ill-defined structures self-assembled from ABM containing triblock copolymers, **10** (a) and **11** (b) and short cylindrical micelles self-assembled from triblock copolymer, **12**. TEM samples were prepared by slow drying and negatively stained using PTA. Scale bar = 500 nm.

To obtain biocompatible cylindrical micelles without affecting their morphologies, direct PEGylation of the fluorescent PLLA-*b*-PAA cylindrical micelles, **9**, with amine-functional PEG was carried out using *N*-(3-dimethylaminopropyl)-*N'*-ethylcarbodiimide hydrochloride (EDC hydrochloride) as the coupling reagent in water[29] (Scheme 4.5). Two different grafting ratios of PEG *per* PAA chain were designed by varying the equivalents of PEG-NH_2. The grafting ratios of PEG *per* PAA chain were confirmed by ^{1}H NMR spectroscopic analysis (methylene resonances of PEG repeat units at δ = 3.83 - 3.45 ppm) and the compositions of such cylindrical micelles were $PLLA_{32}$-*b*-$(PAA_{0.93}$-*g*-$PEG_{0.07})_{243}$, **13**, and

$PLLA_{30}$-*b*-($PAA_{0.75}$-*g*-$PEG_{0.25}$)$_{229}$, **14**, (Figure 4.23) (note that **14** was obtained by PEGylation of similar $PLLA_{30}$-*b*-PAA_{229} cylindrical micelles to **9**).

Scheme 4.5. Direct PEGylation of the PLLA-*b*-PAA cylindrical micelles 9 using amidation with EDC hydrochloride as coupling agent to prepare biocompatible cylindrical micelles, **13** and **14**.

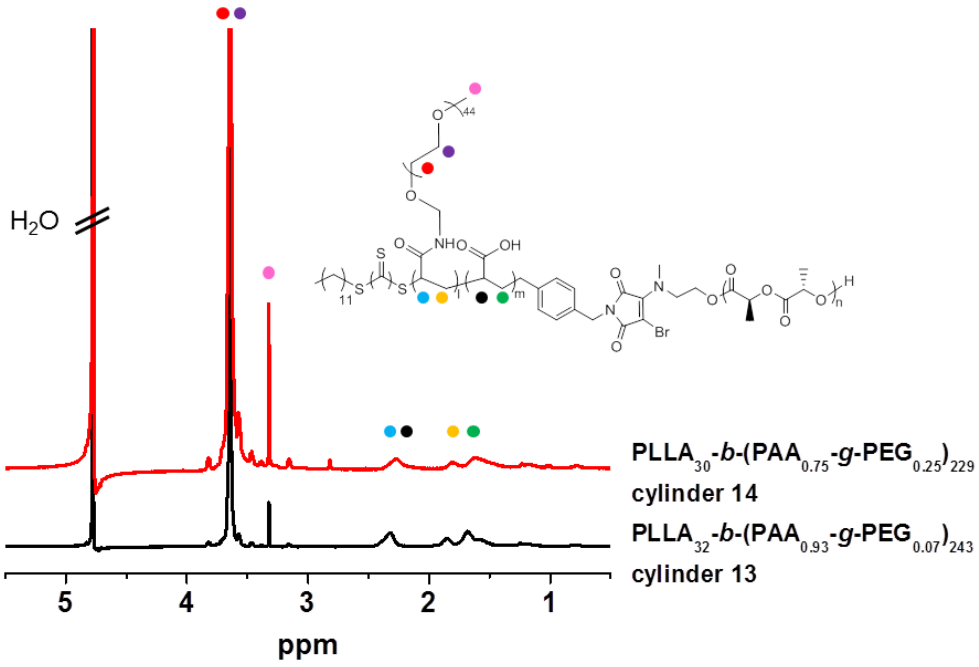

Figure 4.23. ^{1}H NMR (400 MHz) spectrum of PLLA-*b*-(PAA-*g*-PEG) cylindrical micelles, **13** and **14**, in D_2O.

TEM analysis proved that the cylindrical morphologies were retained after PEGylation (L_n = 232 nm , L_w/L_n = 1.22, W_n = 48 ± 9 nm for **13** and L_n =

222 nm , L_w/L_n = 1.24, W_n = 49 ± 7 nm for **14**) (Figure 4.24) and both the lengths and the widths of these cylindrical micelles were similar with those of cylindrical micelles, **9**, before PEGylation (L_n = 224 nm, L_w/L_n = 1.25, W_n = 49 ± 8 nm). It is also worth mentioning that the hydrophobic weight fraction of the PEGylated cylindrical micelles, **14**, is only 3.3%. The high stability of these cylindrical micelles at such a low hydrophobic weight fraction can be attributed to the crystalline core of these nanoparticles which locks in the cylindrical morphology and prevents disassembly. The zeta potential of PEGylated cylindrical micelles, **13**, did not change significantly when compared to that of cylindrical micelles, **9**, (-53.2 ± 3.37 mV) due to the low PEGylation ratio (7%). However, when the PEGylation ratio was increased to 25% (cylindrical micelles, **14**), an obvious change of zeta potential to a less negative value (-44.7 ± 4.77 mV) was observed. Such increase of zeta potential suggests that there were fewer negative charges in the system and further confirmed the successful PEGylation of the PAA shell.

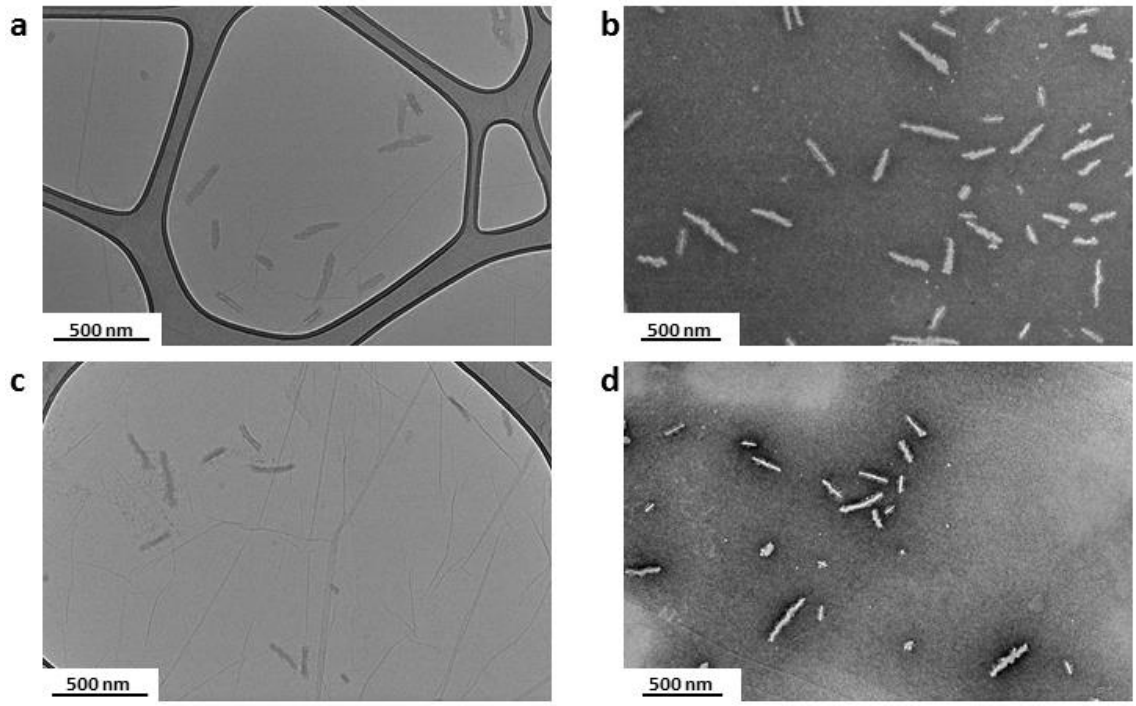

Figure 4.24. TEM images of ABM containing PEGylated cylindrical micelles, **13** (a, b) and **14** (c, d). a and c were prepared by a slow drying method on GO grid while b and d were prepared by a slow drying method followed by negative staining using PTA. Scale bar = 500 nm.

Using WAXD analysis, it was noted that the intensities of the Bragg peak at a *2θ* value of 16.6° of cylindrical micelles, **13** and **14**, were the same with that of cylindrical micelles, **9** (Figure 4.25), indicating that PEGylation had little effect on the core crystallinity of these cylindrical nanoparticles. The new Bragg peaks observed after PEGylation (*2θ* value of 19.0°, 23.2° and 26.1°) were generated from PEG crystallites rather than PLLA crystallites (Figure 4.25).

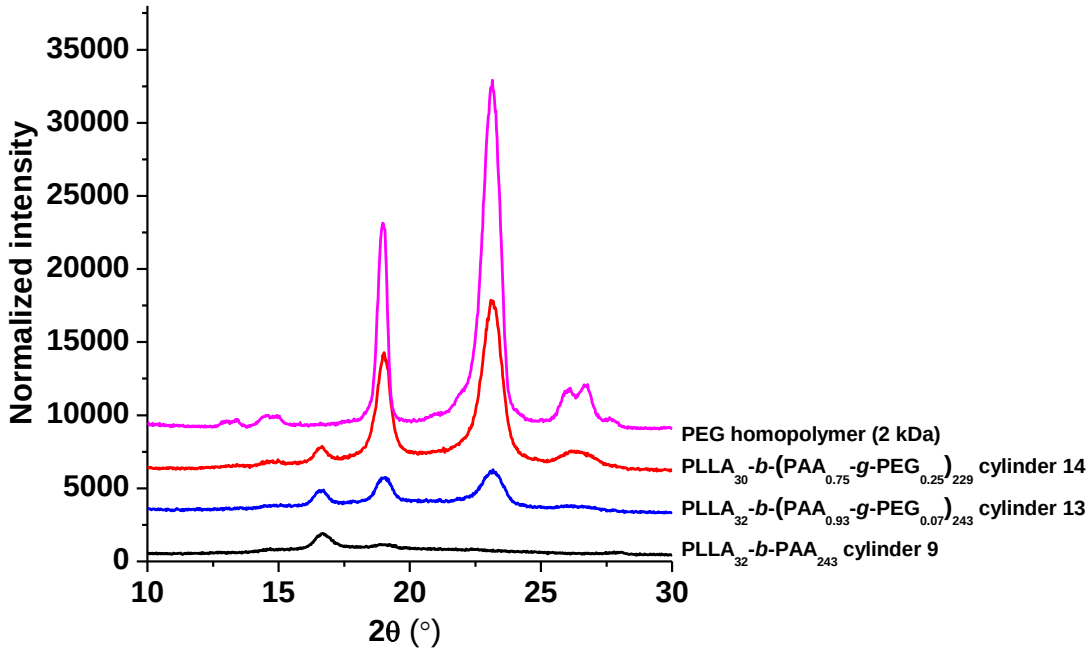

Figure 4.25. WAXD diffractograms of cylindrical micelles, **9**, **13**, **14** and PEG homopolymer (2 kDa).

The fluorescence of PEGylated cylindrical micelles, **14** was confirmed by fluorescence spectroscopy, where the excitation spectrum of **14** in water (0.1 mg/mL) exhibited excitation maxima at *ca*. 395 nm and the emission spectrum has a maximum of *ca*. 510 nm (Figure 4.26).

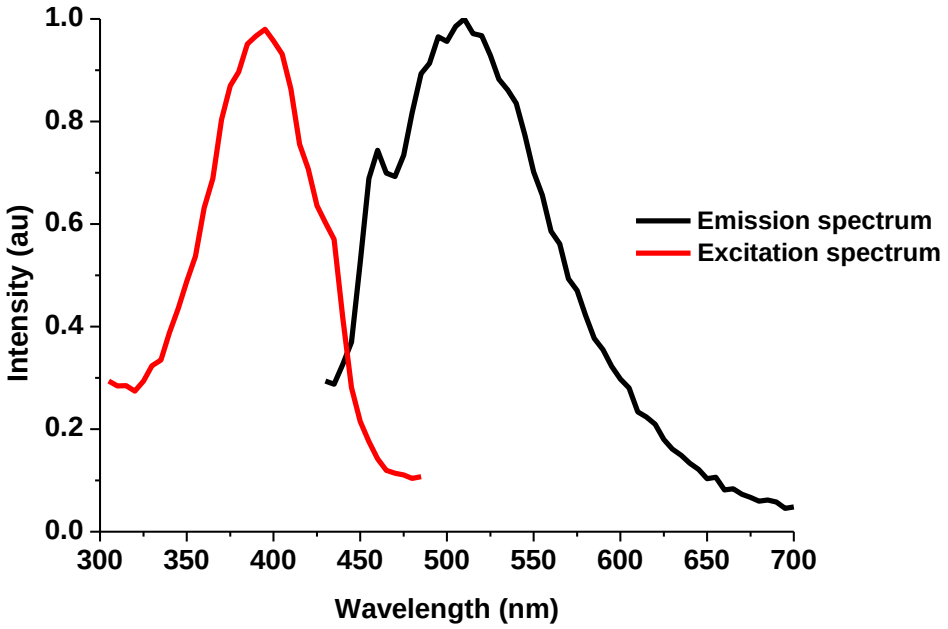

Figure 4.26. Excitation and emission spectra of ABM group containing PLLA-*b*-(PAA-*g*-PEG) cylindrical micelles, **14** in H_2O (resistivity 18.2 MΩ·cm, 0.1 mg/mL).

4.3.7 Fluorescence lifetime studies of various ABM containing materials

In order to determine fluorescence lifetime spectra of various ABM polymers and micelles, solution-state time-correlated single-photon counting (TCSPC) was performed. All experimentally obtained TCSPC spectra were fit to a sum of exponential decays, with deconvolution of the instrument response function (IRF),

$$I(t) = \sum_i A_i e^{-\frac{t}{\tau_i}} \qquad (1)$$

where *I* is the intensity of fluorescence, τ_i and A_i are the lifetime components and their amplitudes.

Intensity average lifetimes ($\tau_{Av,I}$) and amplitude average lifetimes ($\tau_{Av,A}$) were obtained from the fitting parameters according to the following equations,

$$\tau_{Av,I} = \frac{\sum A_i \tau_i^2}{\sum A_i \tau_i} \qquad (2)$$

$$\tau_{Av,A} = \frac{\sum A_i \tau_i}{\sum A_i} \qquad (3)$$

As can be seen from Figure 4.27 and Table 4.4, ABM containing diblock cylindrical micelles, **9**, and PEGylated cylindrical micelles, **14**, in H_2O showed a similar $\tau_{Av,I}$ of *ca*. 5 ns. In comparison, ABM containing initiator, **4**, and diblock copolymer, **8**, in 1,4-dioxane (a good solvent) possessed much shorter lifetimes (less than 2 ns) which can be ascribed to the non-emissive aggregation and solvent-collision effect, where such phenomenon was also observed between the DTM containing polymers and self-assembled nanostructures as previously reported.[10] To further explore whether different morphologies of nanoparticles affect the ABM fluorescence lifetime, ABM containing amorphous poly(*DL*-lactide)-*b*-poly(acrylic acid) (PDLLA-*b*-PAA) spherical micelles, **15**, (Figure 4.28 and Figure 4.29, D_n = 19.6 ± 2 nm) were prepared using a "solvent-switch" method. Interestingly, the ABM containing spherical micelles in H_2O displayed a longer decay (*ca*. 7 ns, Table 4.4) when compared to the cylindrical morphologies. It is proposed that spherical micelles have a higher interfacial curvature with a more crowded corona area than cylindrical micelles[19] and the ABM group at the interface is better protected from the aqueous environment. Thus, the ABM groups of spherical micelles have a decreased solvent-collision effect and therefore a longer fluorescence lifetime was observed. When the ABM containing PDLLA-*b*-PAA spherical micelle solution, **15**, was highly diluted (1×10^{-4} mg/mL), a dramatic decrease of fluorescence lifetime was observed (Table 4.4). Since the spherical morphology was believed to disassemble into unimers with dilution (below the critical micelle concentration), the solvent-

collision effect and non-emission aggregation of the ABM group increased and the fluorescence lifetime of PDLLA-*b*-PAA unimer became similar with that of PLLA-*b*-PTHPA diblock copolymer, **8**, in 1,4-dioxane. This phenomenon is very useful as the disassembly process of fluorescent ABM containing PDLLA-*b*-PAA spherical micelles, **15**, can be directly monitored using fluorescence lifetime imaging (FLIM) to explore specific biological processes for the use of these spherical micelles as fluorescent contrast agents or delivery vehicles *in vivo* or *in vitro*. It is also worth mentioning that the self-assembled ABM containing nanostructures possess shorter lifetimes than those of DTM species ($\tau_{Av,I}$ = 15 - 20 ns, $\tau_{Av,A}$ = 7.6 - 13 ns)[10] but longer lifetimes than many commonly used fluorescent small molecules.[30]

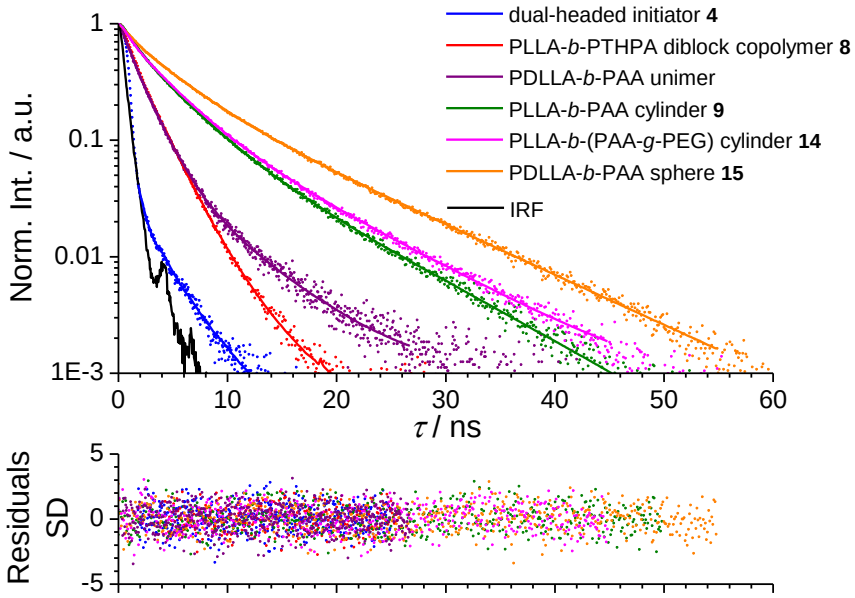

Figure 4.27. Fluorescence lifetime spectra of ABM containing dual-headed initiator, **4** (0.01 mM in 1,4-dioxane), PLLA-*b*-PTHPA diblock copolymer, **8** (0.01 mM in 1,4-dioxane), PDLLA-*b*-PAA unimer (0.1 μg/mL in water), PLLA-*b*-PAA cylinder, **9** (0.1 mg/mL in water), PLLA-*b*-(PAA-*g*-PEG) cylinder, **14** (0.1 mg/mL in water), and PDLLA-*b*-PAA sphere, **15** (0.1 mg/mL in water).

Table 4.4. Fitting parameters of fluorescence lifetime spectra in Figure 4.26 and the average fluorescence lifetimes of ABM containing initiator, polymers and various nanoparticles

Sample	A_1, τ_1	A_2, τ_2	A_3, τ_3	$\tau_{Av,I}$ (ns)	$\tau_{Av,A}$ (ns)
dual-headed initiator **4**	0.0166, 0.816	0.0025, 1.750	–	1.04	0.94
PLLA-*b*-PTHPA diblock copolymer **8**	0.6849, 0.123	0.1008, 1.754	0.0096, 3.684	1.52	0.37
PDLLA-*b*-PAA unimer	0.0472, 0.223	0.0278, 1.585	0.0017, 5.554	1.95	0.83
PLLA-*b*-PAA cylinder **9**	0.0657, 1.079	0.0619, 3.748	0.0151, 8.844	4.87	3.06
PLLA-*b*-(PAA-*g*-PEG) cylinder **14**	0.0823, 0.617	0.0626, 3.286	0.0210, 8.592	5.17	2.63
PDLLA-*b*-PAA sphere **15**	0.0625, 0.705	0.0540, 3.875	0.0305, 10.134	7.07	3.83

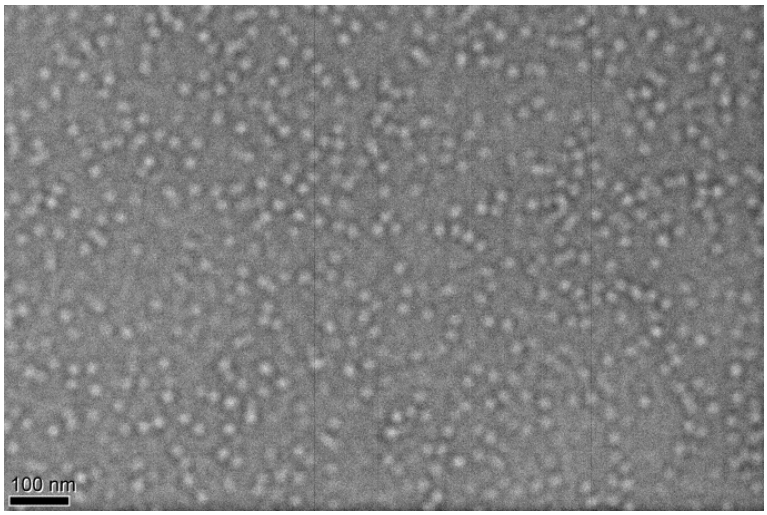

Figure 4.28 TEM image of $PDLLA_{31}$-*b*-PAA_{230} spherical micelles. Sample was prepared by a slow drying method followed by negative staining using PTA. Scale bar = 100 nm.

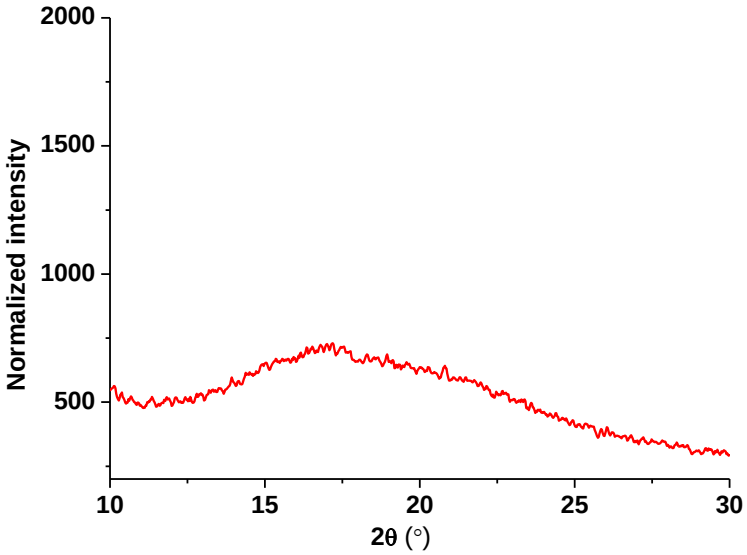

Figure 4.29 WAXD diffractogram showing the amorphous nature of PDLLA$_{31}$-*b*-PAA$_{230}$ spherical micelles.

4.4 Conclusions

In summary, a Y-shaped $(PLLA)_2$-*b*-PTHPA block copolymer was synthesized first from a fluorescent DTM modified dual-headed initiator to prepare fluorescent cylindrical micelles using a CDSA approach. However, only ill-defined nanostructures were obtained and the Y-shaped structure of such a polymer which has two PLLA arms was considered to affect the CDSA process. Therefore, an ABM containing dual-headed initiator that can generate only one PLLA arm was designed and synthesized. Well-defined fluorescent cylindrical micelles were realized from the ABM containing PLLA-*b*-PTHPA diblock copolymer using CDSA. Three different biocompatible polymers including PHEA, PDMA, POEGA were grown from the ABM containing PLLA-*b*-PTHPA diblock copolymer in order to prepare biocompatible cylindrical micelles, although none of these polymers resulted in well-defined cylinders. Thus, biocompatible PEG-NH_2 was directly grafted onto the PAA corona of ABM labelled PLLA-*b*-PAA cylindrical micelles *via* amidation without affecting their morphologies. From the fluorescence lifetime studies, it was found that ABM containing nanostructures possessed longer lifetimes than common fluorescent labels but shorter lifetimes than DTM species. The morphology of nanoparticles was found to affect the ABM fluorescence lifetime since spherical micelles had a longer lifetime over that of cylindrical micelles. This new fluorescent ABM handle can be successfully utilized to label various polymers and nanoparticles which provide potential use as bioimaging contrast agents.

4.5 Experimental section

4.5.1 Materials

Chemicals and solvents were used as purchased from Aldrich, Acros, Fluka, Fisher Chemical, Alfa Aesar or VWR. *L*-Lactide monomer was kindly donated by Corbion-Purac and was passed through a silica plug with dichloromethane (CH_2Cl_2) as eluent to remove impurities and then dried over 3Å molecular sieves in CH_2Cl_2. The lactide monomers were further purified by recrystallization in toluene before being stored in a glove box under an inert atmosphere. (-)-Sparteine was dried over CaH_2 before use and 1-(3,5-bis(trifluoromethyl)phenyl)-3-cyclohexyl-thiourea was prepared and purified as reported.[23] Tetrahydropyran acrylate (THPA) was synthesized and purified as described previously.[31] 2,2-azobis(isobutyronitrile) (AIBN) was recrystallized from methanol and stored at 4 °C. The dual-headed initiator, **1** and DTM initiator, **3** were synthesized as previously reported by the group.[8, 16]

4.5.2 Instrumentation

^{1}H nuclear magnetic resonance (^{1}H NMR) and ^{13}C NMR spectra were recorded on a 400 MHz or 600 MHz Bruker spectrometer in $CDCl_3$ unless otherwise stated. The chemical shifts are given in ppm with tetramethylsilane (TMS) as an internal reference. Size exclusion chromatography (SEC) was performed on an Agilent 1260 Infinity Multi**-**Detector SEC instrument equipped with refractive index and UV detectors with $CHCl_3$ and 0.5% triethylamine as eluent (unless stated otherwise) at a flow rate of 1 mL/min. SEC data was calibrated by Cirrus GPC software with PS or PMMA standards.

Mass spectra were obtained by using a Bruker Ultraflex II Matrix-assisted laser desorption/ionization time of flight (MALDI-ToF) mass spectrometer**.** The MALDI-ToF samples were prepared as follows: *trans*-2-[3-(4-*tert*-butyl-phenyl)-2-methyl-2-propenylidene] malononitrile (DCTB) was used as a matrix while sodium trifluoroacetate (NaTFA) was used as a cationization agent. Typically, DCTB (20 µL of a 40 mg/mL HPLC grade THF solution), sample (20 µL of a 1 mg/mL HPLC grade THF solution) and NaTFA (20 µL of a 0.1 mg/mL HPLC grade THF solution) were successively added into a small centrifuge tube and mixed by a vortex mixer. Traces of mixture were deposited on a MALDI-ToF plate followed by solvent evaporation. The samples were measured in reflectron ion mode and calibrated by SpheriCal (1200 ~ 8000 g/mol) standards. TEM images on graphene oxide (GO)[32] support were obtained by using JEOL 2000FX instrument operated at 200 kV. Generally, one drop of the sample solution (20 µL) was added onto a GO grid and after 2 min, the solution was blotted away before drying totally. The GO grids were prepared as follows: lacey carbon grids (400 Mesh, Cu, Elektron Technology UK LTD) were cleaned by air plasma from a glow-discharge system (2 min, 20 mA) to improve the hydrophilicity of the lacey carbon. One drop of GO solution (0.10 - 0.15 mg/mL) was deposited on each grid and left to air-dry totally. The stained TEM images were obtained by using a JEOL 2000FX instrument operated at 200 kV. TEM samples were negatively stained by phosphotungstic acid (PTA, 2 wt%) on formvar/carbon grids (300 Mesh, Cu, Elektron Technology UK LTD). Typically, formvar/carbon grids were cleaned by air plasma from a glow-discharge system (2 min, 20 mA) which also improved the hydrophilicity of the grids. 20 µL of particle solution (0.25 mg/mL) was added onto the grid and the solution was

blotted away after 2 min and then left to air-dry. 5 μL of a 2 wt% PTA solution was then added onto the grid to stain the particles and was blotted away after 30 s before air-drying. TEM images were analyzed by ImageJ software, and 200 particles were counted for each sample to obtain the number-average length (L_n) and to calculate weight-average length (L_w), number-average width (W_n) (for cylindrical micelles) and number-average diameter (D_n) (for spherical micelles). L_n, L_w, W_n and D_n were calculated by using the following equations:

$$L_n = \frac{\sum_{i=1}^{n} N_i L_i}{\sum_{i=1}^{n} N_i} \quad (4)$$

$$L_w = \frac{\sum_{i=1}^{n} N_i L_i^2}{\sum_{i=1}^{n} N_i L_i} \quad (5)$$

$$W_n = \frac{\sum_{i=1}^{n} N_i W_i}{\sum_{i=1}^{n} N_i} \quad (6)$$

$$D_n = \frac{\sum_{i=1}^{n} N_i D_i}{\sum_{i=1}^{n} N_i} \quad (7)$$

where L_i and W_i are the length and the width of each counted cylindrical micelle while D_i is the diameter of each counted spherical micelle. N_i is the number of the cylindrical micelles with the length of L_i and the width of W_i or the number of spherical micelles with the diameter of D_i.

The hydrodynamic diameter (D_h) of different nanoparticles was determined by dynamic light scattering (DLS). Typically, scattering of a 0.25 mg/mL aqueous nanoparticle solution was measured in a Malvern Zetasizer NanoS instrument equipped with a 4 mW He-Ne 633 nm laser module at 25 °C. Measurements were carried out at a detection angle of 173° (back scattering) and the data was further analyzed by Malvern DTS 6.20 software. D_h was calculated by fitting the apparent diffusion coefficient in the Stokes-Einstein equation $D_h = kT/(3\pi\eta D_{app})$, where k is the Boltzmann constant, T is the temperature and η is the viscosity of the solvent. D_h only coincides to the real hydrodynamic diameter when the

measured sample is a solution of monodispersed spherical particles as D_{app} equals the translational diffusion (D_t). For cylindrical particles, owing to their anisotropy, the rotational diffusion is not negligible and contributes to the D_{app}. Therefore, the D_h measured for the cylindrical micelles only has a relative value and provides polydispersity information to detect multiple populations.

The zeta potentials of various nanoparticles were measured by laser doppler micro-electrophoresis in a Malvern Zetasizer Nano-ZS instrument equipped with a 4 mW He-Ne 633 nm laser module at 25 °C. Typically, an electric field was applied to an aqueous solution of nanoparticles (1 mg/mL), which then moved with a velocity related to the zeta potential. This velocity was measured using a M3-PALS (Phase analysis Light Scattering) laser interferometric technique which enabled the calculation of electrophoretic mobility and the zeta potential. The data was analyzed by Malvern DTS 7.02 software.

WAXD was performed on a Panalytical X'Pert Pro MPD equipped with a CuKα_1 hybrid monochromator as the incident beam optics. Generally, *ca*. 30 mg of self-assembled freeze-dried particles were placed in a 10 mm sample holder, and standard "powder" 2θ - θ diffraction scans were carried out in the angular range from 2θ 10° to 30° at room temperature.

The excitation and emission spectra of various fluorescent samples were obtained using an Agilent Cary Eclipse fluorescence spectrophotometer. All of the samples were prepared in either 1,4-dioxane (spectroscopy degrade) or water (resistivity 18.2 MΩ•cm) at corresponding concentrations.

Time-correlated single-photon counting (TCSPC) was employed to obtain fluorescence lifetime spectra. This was performed with an Edinburgh Instruments FLS920Fluorescence Spectrometer fitted with a 376.2 nm EPL

69.7 ps pulsed diode laser and a 495 nm long pass emission filter. Samples were prepared in 10 mm quartz cells (Starna Cell). Instrument response functions (IRF) were determined from the scatter signal solution of Ludox HS-40 colloidal silica (3% particles in water wt/wt). All IRF deconvolved exponential fits were performed with FAST (Edinburgh) software. The number of exponents was selected for completeness of fit as determined by bootstrap chi-squared analysis. All experimentally obtained TCSPC spectra were fit to a sum of exponential decays, with deconvolution of the IRF. Average lifetimes were obtained from the fitting parameters according to the equations (2) and (3).

4.5.3 Synthesis of $(PLLA)_2$, 5 by ROP using DTM containing initiator, 3

$(PLLA)_2$ **5** was synthesized in a glove box under nitrogen atmosphere by ROP using DTM containing initiator, **3**. Generally, initiator, **3** (80.7 mg, 0.13 mmol) and (-)-sparteine (47.8 µL, 0.21 mmol) were combined in one vial with *L*-lactide (1.2 g, 8.3 mmol) and 1-(3,5-bis(trifluoromethyl)phenyl)-3-cyclohexyl-thiourea (154.2 mg, 0.42 mmol) in another. Dichloromethane (5 mL and 7 mL for each vial respectively) was then added to each of the vials before the two solutions were mixed and left to stir at room temperature for 3.5 h. Product was precipitated in *n*-hexane three times before filtration and dried *in vacuo* to yield a yellow solid. ^{1}H NMR (400MHz, $CDCl_3$, ppm, Figure 4.2) δ = 7.29 - 7.28 (4H, m, H6 & H7), 5.36 - 4.94 (2H PLLA, m, H11 & H13), 4.61 (2H, s, H5), 4.58 (2H, s, H8),4.45 - 4.28 (2H, m, H10), 3.60 - 3.48 (2H, m, H9), 3.36 (2H, t, $^3J_{H\text{-}H}$ = 7.5 Hz, H4), 1.66 - 1.48 (6H PLLA + 2H, m, H12 & H14 & H3), 1.32 - 1.22 (18H, br, H2); $Đ_M$ (SEC, $CHCl_3$ and 0.5% TEA as eluent) = 1.09.

4.5.4 Synthesis of Y-shaped DTM containing $(PLLA)_2$-*b*-PTHPA block copolymer, 6, using RAFT polymerization

THPA (2.5 g, 850 *eq*.) and $(PLLA)_2$ macro-initiator, **5** (0.232 g, 1 *eq*.) were dissolved in $CHCl_3$ (7.5 mL) and transferred into a dried ampoule before adding AIBN (30.9 µL of a 10 mg/mL $CHCl_3$ solution). The solution was degassed by three freeze-pump-thaw cycles and sealed under argon and then placed in a 60 °C oil bath with stirring for 8 h. The product was precipitated into *n*-hexane three times and dried *in vacuo* to give a yellow solid (42% conversion by ^{1}H NMR spectroscopy). The DP of PTHPA was determined by comparing with the DP of $(PLLA)_2$, **5**, in ^{1}H NMR spectra in Figure 4.2. ^{1}H NMR (400 MHz, $CDCl_3$, ppm, Figure 4.3) δ = 6.40 - 5.60 (1H PTHPA, br, H5), 5.30 - 5.04 (2H PLLA, m, H10 & H12 & H14 & H16), 4.28 - 3.20 (2H PTHPA, br, H9), 2.80 - 2.20 (1H PTHPA, br, H3), 2.18 - 1.36 (8H PTHPA & 6H PLLA, br m, H4 & H6 & H7 & H8 & H11 & H13 & H15 & H17); $Đ_M$ (SEC, $CHCl_3$ and 0.5% TEA as eluent) = 1.30.

4.5.5 Crystallization-driven self-assembly of DTM functional Y-shaped $(PLLA)_2$-*b*-PTHPA block copolymer, 6

The self-assembly of DTM functional Y-shaped PLLA-*b*-PTHPA block copolymer, **6**, was carried out using a solvent evaporation method. Typically, 0.5 mL of THF and 2 mL of water (resistivity 18.2 MΩ•cm) (*v* : *v* = 20 : 80) were added to 50 mg of polymer inside a vial. Acetic acid (1 *eq*. to the DP of PTHPA) was also added to the mixture to facilitate the hydrolysis of the PTHPA block. The vial was sealed with a needle inserted through the seal and the mixture was allowed to stir at 65 °C (above the T_g of PLLA)[24] for 30 h before being quenched by cooling in liquid nitrogen and subsequent lyophilization. The

freeze-dried PLLA-*b*-PAA particles were then dissolved directly into water (0.25 mg/mL) for TEM and DLS analysis.

4.5.6 Synthesis of fluorescent ABM functional group containing dual headed initiator, 4

The general synthetic procedures are given in Scheme 4.1. Firstly, dual headed initiator, **1** (4.00 g, 1 *eq*.), was dissolved in dry THF (100 mL) followed by the addition of triphenyl phosphine (PPh_3) (2.63 g, 1 *eq*.), diisopropyl azodicarboxylate (DIAD) (1.98 mL, 1 *eq*.) and neopentyl alcohol (0.44g, 0.5 *eq*.) under a flow of N_2. The solution was left in a dry ice/acetone bath for 30 min before slow addition of 2,3-dibromomaleimide (2.56 g, 1 *eq*.) to form product, **2**, *via* the Mistunobu reaction. The solution was then allowed to warm to room temperature and stirred for another 20 h before removal of THF *in vacuo* and purification by a silica column (dichloromethane : petroleum ether = 1 : 2). The excess solvent was removed *in vacuo* to give a yellow product, **2**, with a yield of 67%. ^{1}H NMR (400 MHz, $CDCl_3$, ppm, Figure 4.30) δ 7.36 - 7.28 (4H, m, H6 & H7), 4.68 (2H, s, H8), 4.61 (2H, s, H5), 3.36 (2H, t, $^3J_{H\text{-}H}$ = 7.5 Hz, H4), 1.73 - 1.65 (3H, m, H3), 1.43 - 1.21 (18H, m, H2), 0.88 (3H, t, $^3J_{H\text{-}H}$ = 7.0 Hz, H1); ^{13}C NMR (150 MHz, $CDCl_3$, ppm, Figure 4.31) δ 223.5 (C5), 163.6 (C12), 135.6 (C7), 134.6 (C10), 129.7 (C8), 129.5 (C13), 129.2 (C13), 42.8 (C11), 40.7 (C6), 37.2 (C4), 32-22 (C2 & C3), 14.1 (C1).

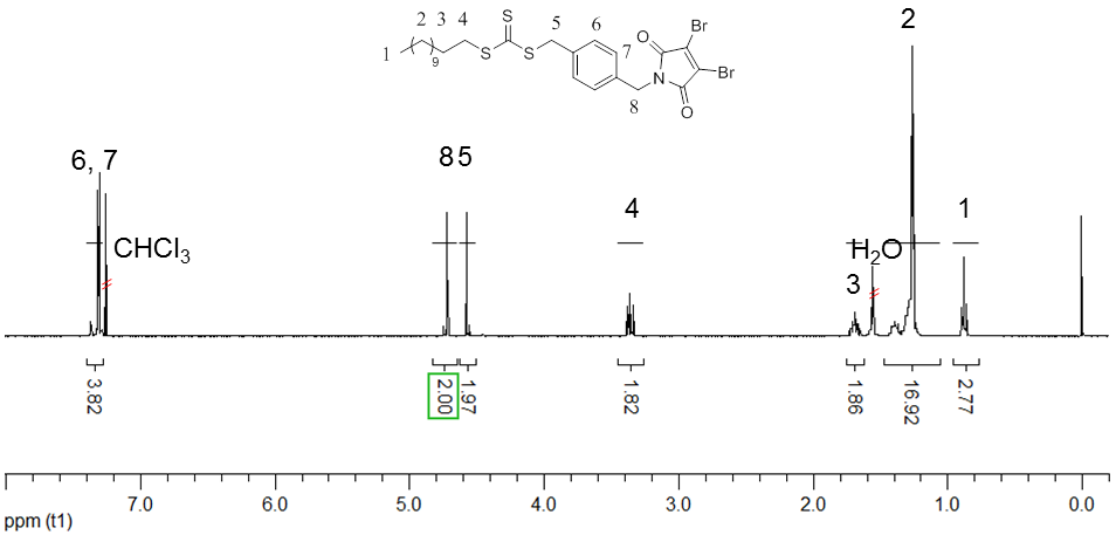

Figure 4.30. ^{1}H NMR (400 MHz, $CDCl_3$) spectrum of product, **2**.

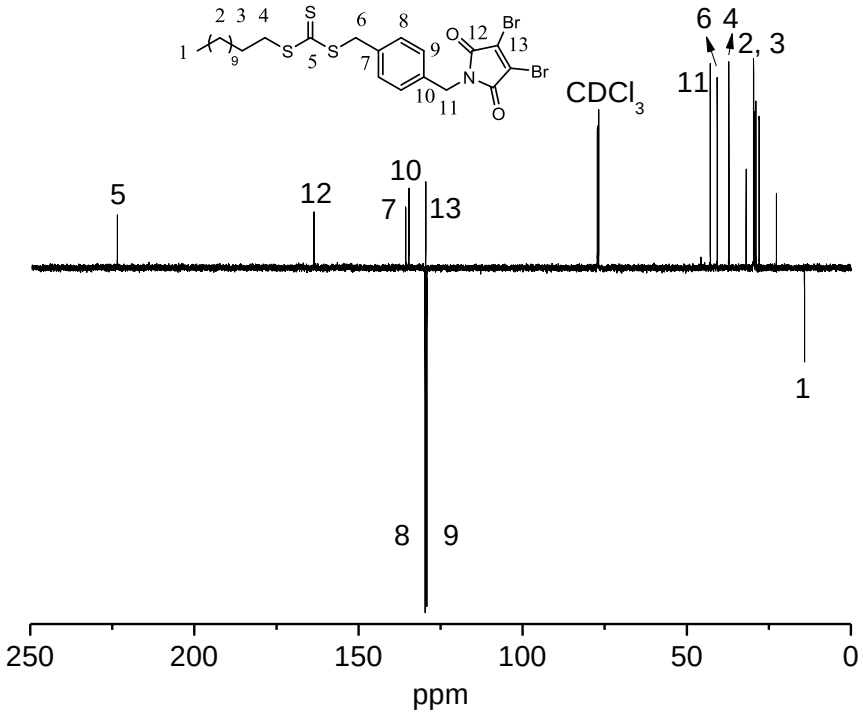

Figure 4.31. ^{13}C NMR (150 MHz, $CDCl_3$) spectrum of product, **2**.

Then, product, **2** (4.00 g, 1 *eq*.), and sodium carbonate (1.67 g, 2.5 *eq*.) were dissolved in 100 mL of THF followed by addition of 2-methylamino ethanol

(0.51 mL, 1 *eq*.). The solution was allowed to stir at room temperature for 2 h before removal of THF *in vacuo*. The solid was dissolved in 100 mL of CH_2Cl_2 and washed against water (2 × 100 mL). The organic layer was dried over magnesium sulphate before purification by a silica column using dichloromethane/acetone. The excess solvent was removed *in vacuo* to give a yellow ABM functional dual-headed initiator, **4**, with a yield of 85%. ^{1}H NMR (400 MHz, $CDCl_3$, ppm, Figure 4.6) δ 7.36 - 7.28 (4H, m, H6 & H7), 4.68 (2H, s, H8), 4.61 (2H, s, H5), 3.36 (2H, t, $^3J_{H\text{-}H}$ = 7.5 Hz, H4), 1.73 - 1.65 (3H, m, H3), 1.43 - 1.21 (18H, m, H2), 0.88 (3H, t, $^3J_{H\text{-}H}$ = 7.0 Hz, H1); ^{13}C NMR (150 MHz, $CDCl_3$, ppm, Figure 4.7) δ 223.6 (C5), 166.5 (C12), 166.0 (C14), 145.0 (C13), 135.8 (C7), 134.8 (10), 129.6 (C8), 128.9 (C9), 79.7 (C15), 61.0 (C18), 55.0 (C17), 41.7 (C11), 40.9 (C6), 40.8 (C16), 37.1 (C4), 32 - 22 (C2 & C3), 14.1 (C1). Elemental analysis: calculated (%) C 53.41, H 6.56, N 4.45, Br 12.69, S 15.27; found (%) C 53.59, H 6.55, N 4.40, Br 12.39, S 15.22. HR-MS: *m*/*z* calculated 651.1355; *m*/*z* found 651.1356 ($[M+Na]^+$).

4.5.7 Synthesis of ABM functional PLLA, 7, and PDLLA using ROP

PLLA **7** and $PDLLA_{31}$ were synthesized in a glove box under nitrogen atmosphere by ROP using ABM containing initiator, **4**. Typically, initiator, **4** (60.7 mg, 0.10 mmol), and (-)-sparteine (19.9 µL, 0.09 mmol) were combined in one vial with *L*-lactide (or *rac*-lactide) (0.5 g, 3.5 mmol) and 1-(3,5-bis(trifluoromethyl)phenyl)-3-cyclohexyl-thiourea (64.2 mg, 0.17 mmol) in another. $CDCl_3$ (2 mL and 3 mL for each vial respectively) was then added to each of the vials before the two solutions were mixed and left to stir at room temperature for 3.5 h. Product was precipitated in *n*-hexane three times before

filtration and dried *in vacuo* to yield a yellow solid. ^{1}H NMR (400 MHz, $CDCl_3$, ppm, Figure 4.10) δ 7.32 - 7.28 (4H, m, H6 & H7), 5.38 - 5.00 (2H PLLA, m, H12 & H14), 4.62 (2H, s, H8), 4.57 (2H, s, H5), 4.43 - 4.30 (3H, m, H11 & 1H from the methine proton of the last repeating unit of PLLA), 4.12 - 3.93 (2H, m, H10), 3.42 (3H, s, H9) 3.36 (2H, t, $^{3}J_{H\text{-}H}$ = 7.5 Hz, H4), 1.77 - 1.38 (6H PLLA + 2H, m, H10 & H12 & H3), 1.35 - 1.19 (18H, br, H2), 0.88 (3H, t, $^{3}J_{H\text{-}H}$ = 6.5 Hz, H1) ; $Đ_M$ of PLLA, **7** (SEC, $CHCl_3$ and 0.5% TEA as eluent) = 1.06 $Đ_M$ of $PDLLA_{31}$ (SEC, $CHCl_3$ and 0.5% TEA as eluent) = 1.07.

4.5.8 Synthesis of ABM containing PLLA-*b*-PTHPA, 8, and $PDLLA_{31}$-*b*-$PTHPA_{230}$ diblock copolymers using RAFT polymerization

Generally, THPA (3 g, 1000 *eq*.) and PLLA macro-initiator, **7** (or $PDLLA_{31}$ macro-initiator) (0.101 g, 1 *eq*.), were dissolved in 1,4-dioxane (3 mL) and transferred into a dried ampoule before adding AIBN (31.5 µL of a 10 mg/mL 1,4-dioxane solution). The solution was degassed by three freeze-pump-thaw cycles and sealed under argon and then placed in a 60 °C oil bath with stirring for 3 h. The product was precipitated into *n*-hexane three times and dried *in vacuo* to give a pale yellow solid (23% conversion by ^{1}H NMR spectroscopy). The DP of PTHPA was determined by comparing with the DP of PLLA in ^{1}H NMR spectrum in Figure 4.10. ^{1}H NMR (400 MHz, $CDCl_3$, ppm, Figure 4.12) δ 6.21 - 5.68 (1H PTHPA, br, H4), 5.27 - 5.06 (2H PLLA, m, H9 & H11), 3.85 - 3.66 (2H PTHPA, br, H8), 2.55 - 2.33 (1H PTHPA, br, H2), 2.07 - 1.45 (8H PTHPA & 6H PLLA, br m, H3 & H5 & H6 & H7 & H10 & H12); $Đ_M$ of PLLA-*b*-PTHPA, **8** (SEC, $CHCl_3$ and 0.5% TEA as eluent) = 1.22, $Đ_M$ of $PDLLA_{31}$-*b*-$PTHPA_{230}$ (SEC, $CHCl_3$ and 0.5% TEA as eluent) = 1.31.

4.5.9 Crystallization-driven self-assembly of ABM functional group containing PLLA-*b*-PTHPA diblock copolymer, 8

The self-assembly of ABM functional PLLA-*b*-PTHPA diblock copolymer, **8**, was carried out using a solvent evaporation method. Typically, 0.5 mL of THF and 2 mL of water (resistivity 18.2 MΩ•cm) (*v* : *v* = 20 : 80) were added to 25 mg of polymers inside a vial. Acetic acid (1 *eq*. to the DP of PTHPA) was also added to the mixture to facilitate the hydrolysis of the THPA blocks. The vial was sealed with a needle inserted through the seal and the mixture was allowed to stir at 65 °C for 6 h before being quenched by cooling in liquid nitrogen and subsequent lyophilization. The freeze-dried PLLA-*b*-PAA nanoparticles were then dissolved directly into water (0.25 mg/mL) for TEM and DLS analysis.

4.5.10 Synthesis of ABM containing triblock copolymers, 10, 11 and 12

ABM containing triblock copolymers $PLLA_{32}$-*b*-$PTHPA_{227}$-*b*-$PHEA_{35}$, **10**, $PLLA_{32}$-*b*-$PTHPA_{243}$-*b*-$PDMA_{38}$, **11**, and $PLLA_{32}$-*b*-$PTHPA_{243}$-*b*-$POEGA_{17}$, **12**, were synthesized using RAFT chain-extensions from PLLA-*b*-PTHPA diblock copolymer, **8**. Typically, for the synthesis of **11**, DMA (0.1 g, 200 *eq*.) and PLLA-*b*-PTHPA macro-initiator, **8** (0.22 g, 1 *eq*.), were dissolved in 1,4-dioxane (2 mL) and transferred into a dried ampoule before adding AIBN (16.5 µL of a 5 mg/mL 1,4-dioxane solution). The solution was degassed by three freeze-pump-thaw cycles and sealed under argon and then placed in a 60 °C oil bath with stirring for 2.25 h. The product was precipitated into *n*-hexane three times and dried *in vacuo* to give a pale yellow solid (19% conversion by ^{1}H NMR spectroscopy). ^{1}H NMR (400 MHz, $CDCl_3$, ppm, Figure 4.20) δ 6.17 - 5.70 (1H PTHPA, br, methine resonance of tetrahydropyranyl protecting groups), 5.28 -

5.05 (2H, m, methine resonance of PLLA backbones), 4.02 - 3.53 (2H, br, methylene resonances of tetrahydropyranyl protecting groups), 3.26 - 2.76 (6H, br, methyl resonances of PDMA) 2.55 - 2.33 (1H, br, methine resonance of PTHPA backbones), 2.17 - 1.40 (8H PTHPA & 6H PLLA, br m, methylene resonances of tetrahydropyranyl protecting groups and methyl resonances of PLLA); $Đ_M$ (SEC, $CHCl_3$ and 0.5% TEA as eluent) = 1.22.

4.5.11 Crystallization-driven self-assembly of ABM functional group containing triblock copolymers, 10, 11 and 12

The CDSA of ABM containing triblock copolymers, **10**, **11** and **12** was carried out using the identical self-assembly conditions as those used in the CDSA of diblock copolymer, **8**. Typically, 0.5 mL of THF and 2 mL of water (resistivity 18.2 MΩ•cm) (*v* : *v* = 20 : 80) were added to 25 mg of polymer inside a vial. Acetic acid (1 *eq*. to the DP of PTHPA) was also added to the mixture to facilitate the hydrolysis of the THPA blocks. The vial was sealed with a needle inserted through the seal and the mixture was allowed to stir at 65 °C for 6 h before being quenched by cooling in liquid nitrogen and subsequent lyophilization. The freeze-dried nanoparticles were then dissolved directly into water (0.25 mg/mL) for TEM and DLS analysis.

4.5.12 Direct PEGylation of ABM functional PLLA-*b*-PAA cylindrical micelles to prepare biocompatible cylinders

Generally, for the preparation of cylindrical micelles, **13** (grafting ratio of 7% of PEG *per* PAA), 15 mg of ABM containing PLLA-*b*-PAA cylindrical micelles, **9**, were dissolved in 15 mL of water followed by the addition of *N*-(3-

dimethylaminopropyl)-*N'*-ethylcarbodiimide hydrochloride (EDC hydrochloride) (4.6 mg, 0.15 *eq*. to the PAA block). Then an aqueous solution of methoxypoly(ethylene glycol) amine (PEG-NH_2) (2 kDa, 48.1 mg in 15 mL water) was added. The solution was allowed to stir at room temperature for 33 h before dialysis against water for 3 days to remove unreacted PEG-NH_2 and subsequent lyophilization. The freeze dried sample was dissolved in D_2O to analyze the grafting ratio of PEG using ^{1}H NMR spectroscopy (400 MHz, Figure 4.23).

4.5.13 Preparation of PDLLA-*b*-PAA spherical micelles

PDLLA-*b*-PAA spherical micelles were prepared using a "solvent-switch" method. Generally, $PDLLA_{31}$-*b*-$PTHPA_{230}$ diblock copolymer (25 mg) was added to a mixture of 1,4-dioxane / H_2O (2 mL / 0.5 mL) and acetic acid (3 *eq*. to PTHPA block) in a vial. The vial was well-sealed and heated at 65 °C for 6 h. ^{1}H NMR spectroscopy was used to confirm that the PTHPA block was fully deprotected into PAA. 11 mL of 1,4-dioxane was then added and the solution was allowed to stir at room temperature overnight. 12.5 mL of H_2O was slowly added to the solution (with a final concentration of 0.5 mg/mL of $PDLLA_{31}$-*b*-PAA_{230}) at room temperature using a peristaltic pump over 3 h and the solution was dialyzed against H_2O for 2 days before subsequent lyophilisation. TEM analysis confirmed the spherical morphology of such nanoparticles (Figure 4.28) while WAXD revealed their amorphous nature as no obvious Bragg peak was observed (Figure 4.29).

4.6 Acknowledgement

Dr. Mathew Robin in the group has kindly synthesized the DTM dual-headed initiator and performed the TCSPC analysis at University of Birmingham and fitted all of the fluorescence lifetime spectra data in this chapter.

4.7 References

(1) Leblond, F.; Davis, S. C.; Valdés, P. A.; Pogue, B. W. *J. Photochem. Photobiol. B* **2010,** 98, 77-94.

(2) Li, K.; Liu, B. *Chem. Soc. Rev.* **2014,** 43, 6570-6597.

(3) Elsabahy, M.; Wooley, K. L. *Chem. Soc. Rev.* **2012,** 41, 2545-2561.

(4) Wang, D.; Qian, J.; He, S.; Park, J. S.; Lee, K.-S.; Han, S.; Mu, Y. *Biomaterials* **2011,** 32, 5880-5888.

(5) Tian, Z.; Li, A. D. Q.; Hu, D. *Chem. Commun.* **2011,** 47, 1258-1260.

(6) Hansell, C. F.; O'Reilly, R. K. *ACS Macro Lett.* **2012,** 1, 896-901.

(7) Li, Q.; Zhang, L.; Bai, L.; Zhang, Z.; Zhu, J.; Zhou, N.; Cheng, Z.; Zhu, X. *Soft Matter* **2011,** 7, 6958-6966.

(8) Robin, M. P.; Wilson, P.; Mabire, A. B.; Kiviaho, J. K.; Raymond, J. E.; Haddleton, D. M.; O'Reilly, R. K. *J. Am. Chem. Soc.* **2013,** 135, 2875-2878.

(9) Robin, M. P.; O'Reilly, R. K. *Chem. Sci.* **2014,** 5, 2717-2723.

(10) Robin, M. P.; Mabire, A. B.; Damborsky, J. C.; Thom, E. S.; Winzer-Serhan, U. H.; Raymond, J. E.; O'Reilly, R. K. *J. Am. Chem. Soc.* **2013,** 135, 9518-9524.

(11) Geng, Y.; Dalhaimer, P.; Cai, S. S.; Tsai, R.; Tewari, M.; Minko, T.; Discher, D. E. *Nat. Nanotechnol.* **2007,** 2, 249-255.

(12) Gilroy, J. B.; Gadt, T.; Whittell, G. R.; Chabanne, L.; Mitchels, J. M.; Richardson, R. M.; Winnik, M. A.; Manners, I. *Nat. Chem.* **2010,** 2, 566-570.

(13) Schmelz, J.; Schedl, A. E.; Steinlein, C.; Manners, I.; Schmalz, H. *J. Am. Chem. Soc.* **2012,** 134, 14217-14225.

(14) Patra, S. K.; Ahmed, R.; Whittell, G. R.; Lunn, D. J.; Dunphy, E. L.; Winnik, M. A.; Manners, I. *J. Am. Chem. Soc.* **2011,** 133, 8842-8845.

(15) Lazzari, M.; Scalarone, D.; Vazquez-Vazquez, C.; Lopez-Quintela, M. A. *Macromol. Rapid Commun.* **2008,** 29, 352-357.

(16) Petzetakis, N.; Dove, A. P.; O'Reilly, R. K. *Chem. Sci.* **2011,** 2, 955-960.

(17) Sun, L.; Petzetakis, N.; Pitto-Barry, A.; Schiller, T. L.; Kirby, N.; Keddie, D. J.; Boyd, B. J.; O'Reilly, R. K.; Dove, A. P. *Macromolecules* **2013,** 46, 9074-9082.

(18) Pitto-Barry, A.; Kirby, N.; Dove, A. P.; O'Reilly, R. K. *Polym. Chem.* **2014,** 5, 1427-1436.

(19) Blanazs, A.; Armes, S. P.; Ryan, A. J. *Macromol. Rapid Commun.* **2009,** 30, 267-277.

(20) Hudson, Z. M.; Lunn, D. J.; Winnik, M. A.; Manners, I. *Nat. Commun.* **2014,** 5.

(21) Jia, Z.; Bobrin, V. A.; Truong, N. P.; Gillard, M.; Monteiro, M. J. *J. Am. Chem. Soc.* **2014,** 136, 5824-5827.

(22) Awuah, E.; Capretta, A. *J. Org. Chem.* **2011,** 76, 3122-3130.

(23) Pratt, R. C.; Lohmeijer, B. G. G.; Long, D. A.; Lundberg, P. N. P.; Dove, A. P.; Li, H. B.; Wade, C. G.; Waymouth, R. M.; Hedrick, J. L. *Macromolecules* **2006,** 39, 7863-7871.

(24) Becker, J. M.; Pounder, R. J.; Dove, A. P. *Macromol. Rapid Commun.* **2010,** 31, 1923-1937.

(25) Petzetakis, N.; Walker, D.; Dove, A. P.; O'Reilly, R. K. *Soft Matter* **2012,** 8, 3408-3414.

(26) Kato, T.; Naka, K. *Chem. Lett.* **2012,** 41, 1445-1447.

(27) Pan, P.; Kai, W.; Zhu, B.; Dong, T.; Inoue, Y. *Macromolecules* **2007,** 40, 6898-6905.

(28) Lassoued, A.; Djadoun, S. *Macromol. Symp.* **2014,** 336, 7-16.

(29) Zhang, K.; Rossin, R.; Hagooly, A.; Chen, Z.; Welch, M. J.; Wooley, K. L. *J. Polym. Sci. A Polym. Chem.* **2008,** 46, 7578-7583.

(30) Langhals, H.; Karolin, J.; B-A. Johansson, L. *J. Chem. Soc. Faraday Trans.* **1998,** 94, 2919-2922.

(31) Hertler, W. R. *US Patent* **1991,** No. 5 072 029.

(32) Patterson, J. P.; Sanchez, A. M.; Petzetakis, N.; Smart, T. P.; Epps, T. H.; Portman, I.; Wilson, N. R.; O'Reilly, R. K. *Soft Matter* **2012,** 8, 3322-3328.

Chapter 5. Core Functionalization of Polymeric Cylindrical Nanoparticles Using Photo-initiated Thiol-ene Radical Reactions

5.1 Abstract

In this chapter, *L*-lactide (LLA) and an allyl functional cyclic carbonate monomer, 5-methyl-5-allyloxycarbonyl-1,3-dioxan-2-one (MAC), were copolymerized using ring-opening polymerization (ROP) to introduce functional handles into the core block of an amphiphilic block copolymer, which was obtained by subsequent reversible addition-fragmentation chain transfer (RAFT) polymerization. Then, we aimed to prepare cylindrical micelles using crystallization-driven self-assembly (CDSA) of these functional amphiphilic block copolymers. It was found that the amphiphilic block copolymer which consists of a random structured P(LLA-*co*-MAC) core block failed to give a pure phase of cylindrical micelles as the incorporation of MAC destroyed the crystallizable PLLA polymer chain structure and affected the CDSA process. In comparison, the amphiphilic block copolymer which consists of a PLLA-*b*-PMAC core block yielded well-defined cylindrical micelles. In order to illustrate that these cylindrical micelles can be used as potential delivery vehicles, benzyl mercaptan was directly "clicked" onto the allyl groups of PMAC in the core block of these cylindrical micelles using a photo-initiated thiol-ene radical reaction with a high functionalization yield.

5.2 Introduction

To afford nanoparticles with different features and functions, chemical modification is often required. Functionalized nanoparticles can be achieved either by modification of the precursor amphiphilic polymers followed by self-assembly[1-3] or by direct functionalization of the self-assembled nanostructures.[4-6] For the former route, although it is more flexible to design a polymer for a specific target, this approach can be time-consuming and often requires multiple synthetic steps. In contrast, the post-assembly functionalization on micellar scaffolds is a faster and more versatile route as it avoids the synthesis and polymerization of the new functional monomers and optimization of multiple self-assembly conditions. Click-type reactions such as the Diels-Alder reaction,[7] thiol-ene reaction,[8, 9] copper-catalyzed azide-alkyne cycloaddition (CuAAC) reaction[10] and tetrazine-norbornene reaction[11] are often used for the chemical modifications. Among them, the thiol-ene radical reaction displays outstanding reaction properties as it has a rapid reaction rate and allows reactions between a wide range of thiols and alkenes and it is insensitive to oxygen or water.[12] Thiol-ene radical reactions have been applied to numerous areas including the functionalization of polymers,[13-15] modification of substrate surfaces[16] and preparation of hydrogels.[17]

In spite of their biodegradability, biocompatibility and low toxicity.[18-22] poly(lactide)s (PLAs) are often unfunctionalized and therefore their potential biomedical applications with special targets are limited. Although functionalized PLAs can be synthesized by the ring-opening polymerization (ROP) of functionalized cyclic lactide monomers,[23] an alternative approach to introduce functional handles into PLAs is to copolymerize lactide with functionalized

carbonate monomers using ROP methods.[8, 24, 25] Cyclic carbonate monomers can be easily synthesized using cyclization reactions between functionalized diols and triphosgene or ethyl chloroformate.[26] To date, a variety of functional carbonate monomers have been synthesized to fulfil different requirements (Figure 5.1).[27]

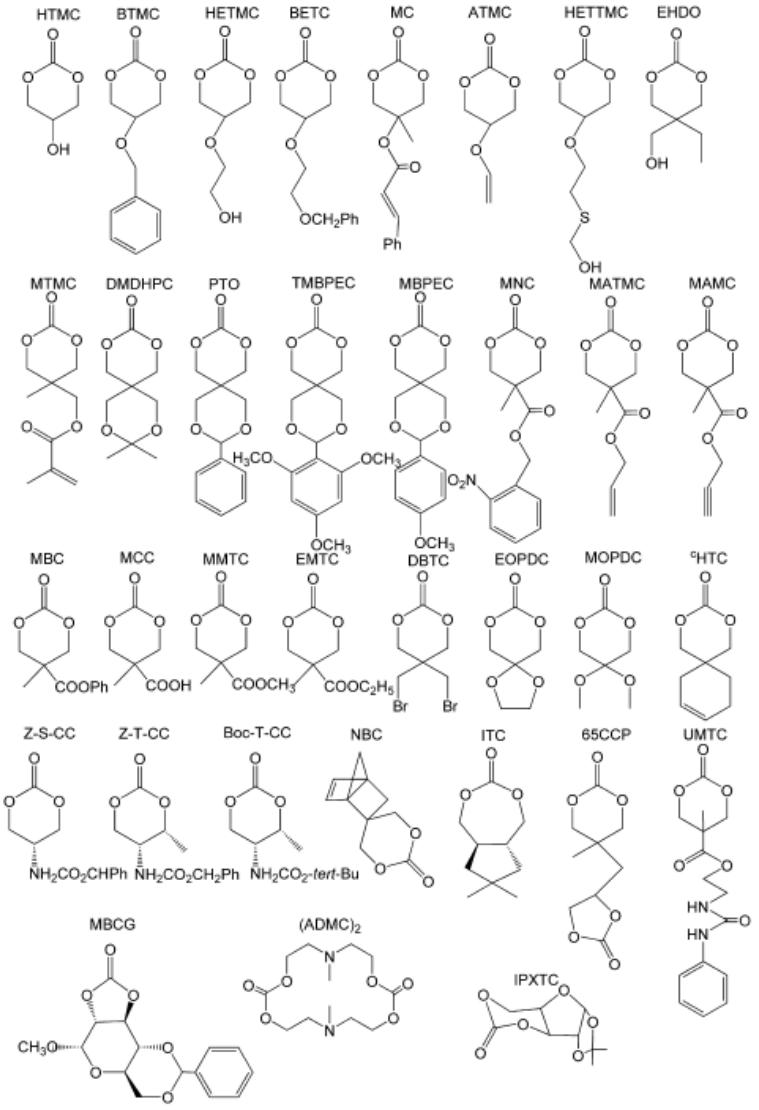

Figure 5.1. Various functional carbonate monomers.[27]

In our previous studies[28, 29] and in Chapters 2, 3 and 4 of this thesis, we have described the preparation of poly(*L*-lactide) (PLLA) and poly(*D*-lactide) (PDLA) containing cylindrical micelles, however, their potential use as functional

delivery vehicles for small molecules has not yet been illustrated. Since both PLLA and PDLA are semi-crystalline, the incorporation of small molecules in the PLLA or PDLA domains of nanoparticles by physical encapsulation is very challenging and very low loadings of small molecules in the self-assembled nanoparticles were often achieved.[30] Herein, we aimed to copolymerize LLA and an allyl functional cyclic carbonate, 5-methyl-5-allyloxycarbonyl-1,3-dioxan-2-one (MAC),[25, 31] so that the allyl group can be used as a versatile handle for further modification, for example, for the radical addition of functional thiols.[9] By subsequent reversible addition-fragmentation chain-transfer (RAFT) polymerization of tetrahydropyran acrylate (THPA) from a dual-headed initiator, several P(LLA-*co*-MAC)-*b*-PTHPA block copolymers with different MAC ratios were synthesized. However, when these block copolymers were exposed to crystallization-driven self-assembly (CDSA) conditions, a pure phase of cylindrical micelles was found difficult to achieve. It is proposed that the incorporation of MAC in PLLA destroyed the crystallization ability of the core block and hindered the formation of well-defined cylindrical micelles. To overcome this problem, a core forming diblock PLLA-*b*-PMAC, which was then chain-extended with PTHPA to form a triblock copolymer was synthesized. This triblock was utilized to form well-defined cylindrical micelles *via* CDSA. To demonstrate that these cylindrical nanoparticles can be functionalized with small molecules, benzyl mercaptan was attached to the core domain of these cylindrical micelles using photo-initiated thiol-ene radical reactions to realize a high functionalization yield.

5.3 Results and discussion

5.3.1 Copolymerization of LLA and MAC using ROP

To introduce functional handles in PLLA, the ROP of a mixture of LLA and MAC was performed using the 1-(3,5-bis(trifluoromethyl)phenyl)-3-cyclohexyl-thiourea/(-)-sparteine co-catalyst system from a dual-headed initiator that has been described in Chapters 2 and 3 (Scheme 5.1). In our first attempt, a molar fraction ratio of f_{LLA} : f_{MAC} = 0.55 : 0.45 was used and we aimed to obtain 10% MAC incorporation in the resultant copolymer. After 4.5 h, we observed that LLA reached 87% conversion and MAC reached 9% conversion with 11% MAC incorporation in the final copolymer (Figure 5.2, as determined by ^{1}H NMR spectroscopy). Due to the much slower polymerization rate of MAC when compared to that of LLA, a random P(LLA-*co*-MAC) copolymer rather than a statistical copolymer was considered to be obtained. The composition of the copolymer was confirmed by integration of the methine resonance of the PLLA repeat units at δ = 5.36 - 4.96 ppm and the methylene resonances of the PMAC repeat units in the backbone at δ = 4.45 - 4.22 ppm (Figure 5.3), giving a copolymer P($LLA_{0.89}$-*co*-$MAC_{0.11}$)$_{55}$, **1**. SEC analysis confirmed the narrow dispersity of such a copolymer (Figure 5.5, Table 5.1). By using differential scanning calorimetry (DSC) analysis, we noticed that the glass transition temperature (T_g) and the melting temperature (T_m) of copolymer, **1**, showed lower values (38 °C and 111 °C respectively) when compared to the $PLLA_{31}$ homopolymer used in Chapter 2 ($PLLA_{31}$ T_g : 51 °C, $PLLA_{31}$ T_m : 137 °C). This phenomenon was due to the incorporation of PMAC which has a low T_g at -26.4 °C and no melting transition.[9]

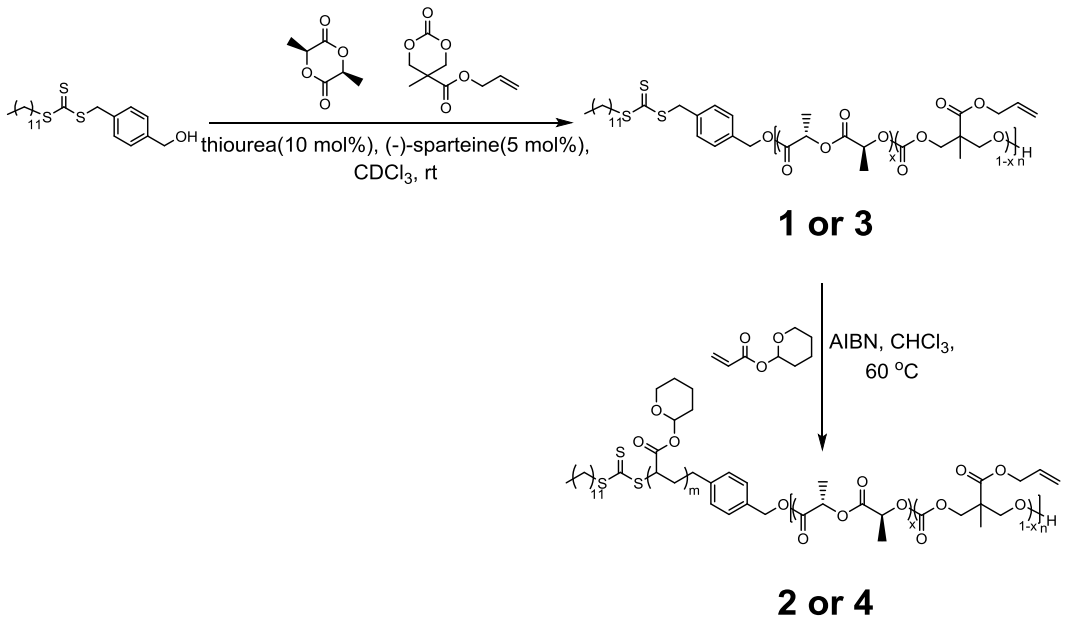

Scheme 5.1. Synthetic procedures of P(LLA-*co*-MAC)-*b*-PTHPA copolymers using a combination of ROP and RAFT polymerization.

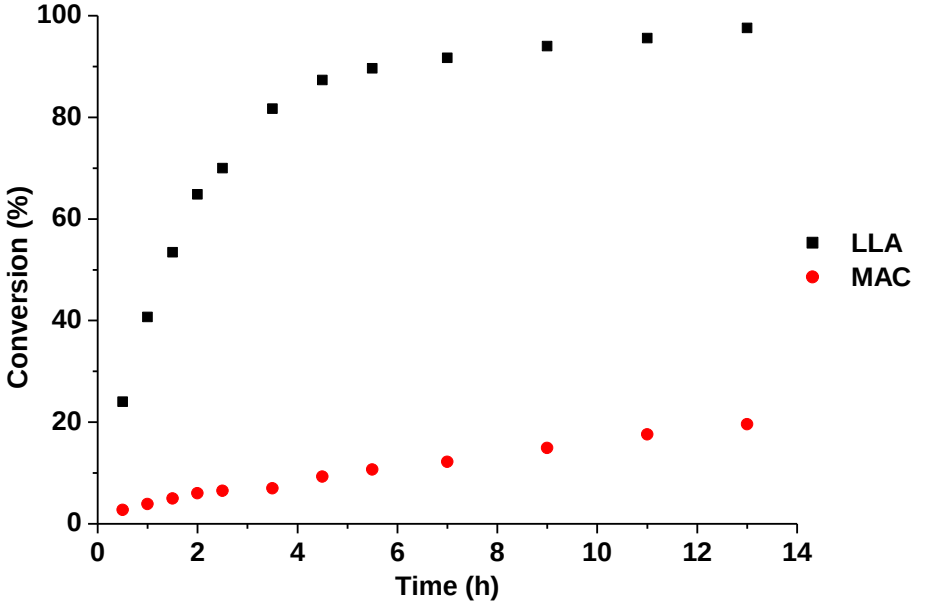

Figure 5.2. Kinetic study showing conversions of LLA and MAC against time. The molar fraction ratio between the two monomers was f_{LLA} : f_{MAC} = 0.55 : 0.45.

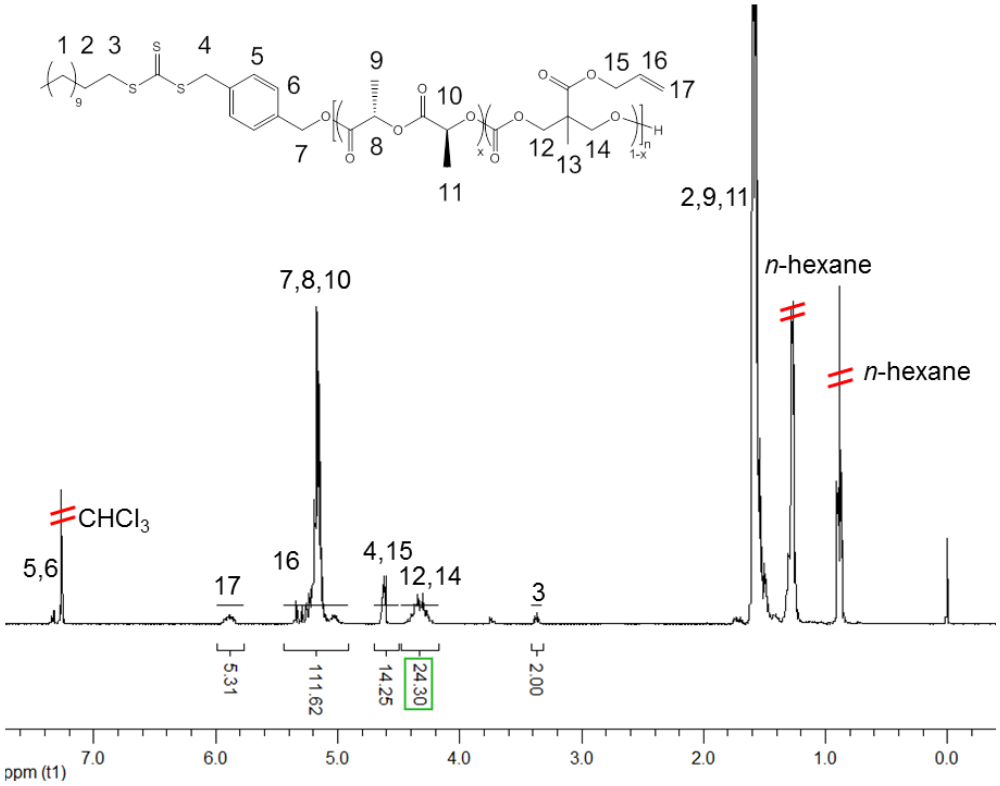

Figure 5.3. ^{1}H NMR spectrum (400 MHz, $CDCl_3$) of P(LLA-*co*-MAC) copolymer, **1**.

Table 5.1. Characterization data of P(LLA-*co*-MAC) and P(LLA-*co*-MAC)-*b*-PTHPA polymers

Polymer	M_n **(kDa)**[a]	$Đ_M$[b]	T_g **(°C)**[c]	**Hydrophobic %wt**[d]
$P(LLA_{0.89}\text{-}co\text{-}MAC_{0.11})_{55}$, **1**	8.7	1.04	38	–
$P(LLA_{0.89}\text{-}co\text{-}MAC_{0.11})_{55}\text{-}b\text{-}PTHPA_{477}$, **2**	83.1	1.31	–	17.0
$P(LLA_{0.95}\text{-}co\text{-}MAC_{0.05})_{41}$, **3**	6.4	1.05	45	–
$P(LLA_{0.95}\text{-}co\text{-}MAC_{0.05})_{41}\text{-}b\text{-}PTHPA_{232}$, **4**	42.6	1.19	–	26.5

[a] Measured by ^{1}H NMR spectroscopy (400 MHz, $CDCl_3$) . [b] Measured by SEC analysis ($CHCl_3$ with 0.5% TEA as eluent, RI detection). [c] Measured by DSC analysis. [d] PLLA weight fraction in the P(LLA-*co*-MAC)-*b*-PAA diblock copolymer.

5.3.2 Synthesis of P(LLA-*co*-MAC)-*b*-PTHPA block copolymer, 2, using RAFT polymerization

PTHPA was subsequently grown from the P(LLA-*co*-MAC) copolymer, **1**, using RAFT polymerization of THPA (Scheme 5.1). ^{1}H NMR spectroscopic analysis indicated the successful synthesis of P(LLA-*co*-MAC)-*b*-PTHPA block copolymer, **2**, with the broad methine resonance of the tetrahydropyranyl protecting groups of PTHPA repeat units at δ = 6.19 - 5.72 ppm (Figure 5.4). The hydrophobic weight fraction was targeted at 17.0% in order to access well-defined cylindrical nanostructures based on the results in Chapter 2. SEC analysis revealed a narrow dispersity of diblock copolymer, **2**, and successful chain-extension from the P(LLA-*co*-MAC) macro-initiator, **1** (Figure 5.5, Table 5.1).

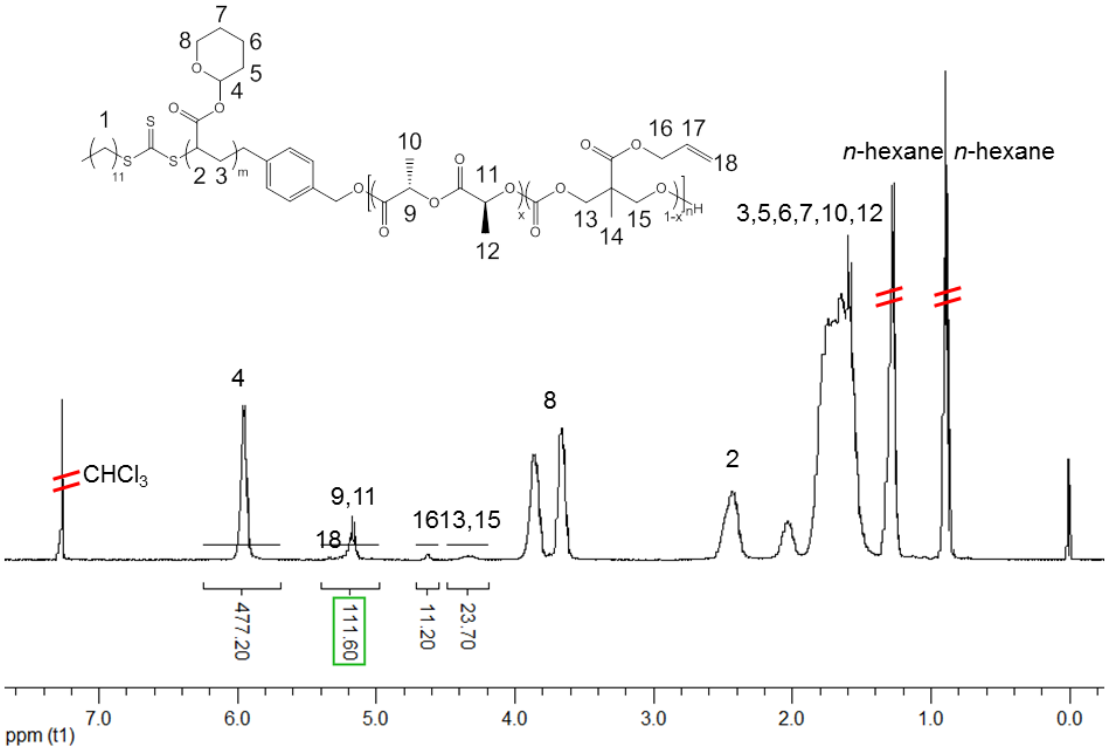

Figure 5.4. ^{1}H NMR spectrum (400 MHz, $CDCl_3$) of P(LLA-*co*-MAC)-*b*-PTHPA diblock copolymer, **2**.

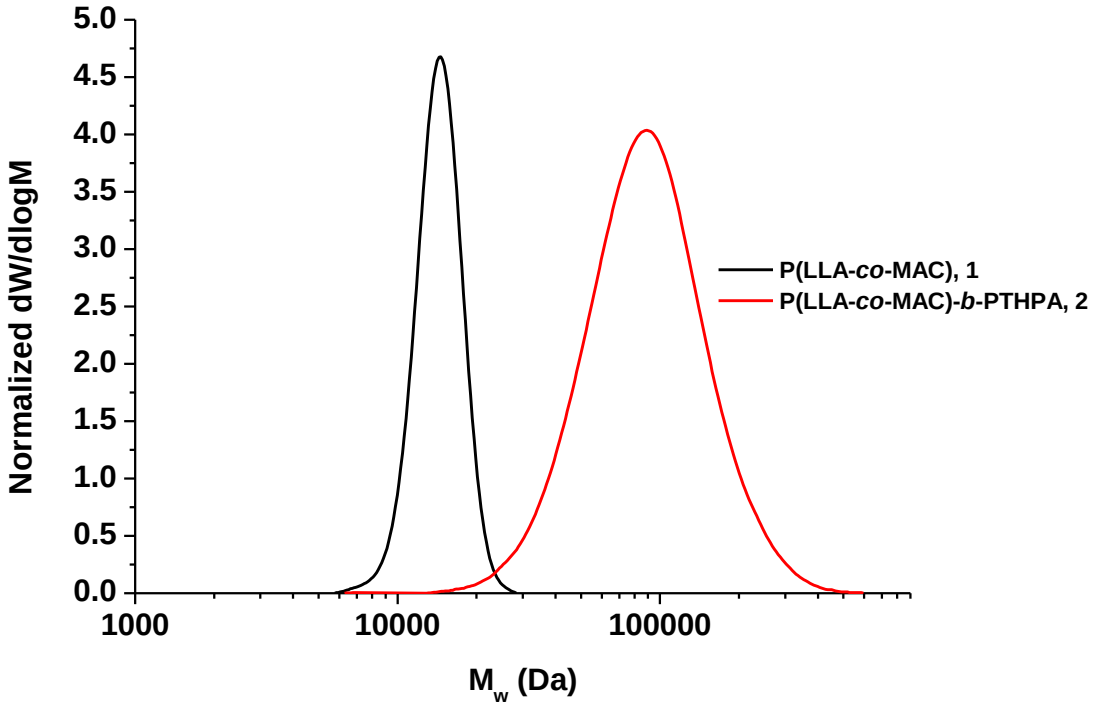

Figure 5.5. SEC chromatograms ($CHCl_3$ with 0.5% TEA as eluent, RI detection) of P(LLA-*co*-MAC), **1**, and P(LLA-*co*-MAC)-*b*-PTHPA, **2**.

5.3.3 Crystallization-driven self-assembly of P(LLA-*co*-MAC)-*b*-PTHPA copolymer, 2

The CDSA of the P(LLA-*co*-MAC)-*b*-PTHPA copolymer, **2**, was performed using the identical conditions described in Chapter 2. Generally, 0.5 mL of THF and 2 mL of H_2O (resistivity 18.2 MΩ·cm) were added to 50 mg of polymer inside a vial. Acetic acid (1 *eq*. to each PTHPA unit) was added to the mixture to promote the hydrolysis of PTHPA to PAA and we have previously demonstrated that the PTHPA block can completely convert into PAA within the first 2 h of the self-assembly.[32] The vial was sealed with a needle through the seal to allow the evaporation of THF and the mixture was allowed to stir at 65 °C (above the T_g of P(LLA-*co*-MAC) core block).[28]

After 30 h of CDSA, only spherical micelles were observed by TEM analysis (Figure 5.6a). This was not expected as under the same conditions, the self-assembly of PLLA-*b*-PAA diblock copolymers with similar hydrophobic weight fraction lead to the formation of a cylindrical morphology (see Chapter 2). The WAXD diffractogram of the nanoparticles indicated their amorphous nature as no obvious crystalline Bragg peak was observed (Figure 5.6b). Interestingly, when the CDSA temperature was lowered to 55 °C, a small portion of cylindrical micelles were formed although spherical micelles were still the primary morphology observed (Figure 5.6c). However, WAXD analysis again revealed the absence of any obvious crystalline Bragg peaks for this system (Figure 5.6d). A number of CDSA experiments were performed in which varied concentrations of polymer or solvent compositions were explored, however these all failed to yield pure cylindrical micelles (data not given). It is proposed that the incorporation of MAC inhibited the ability of the PLLA chain to crystallize during the CDSA process, so these P(LLA-*co*-MAC)-*b*-PAA spheres were not able to form crystalline micelle seeds and thus the expected sphere-to-cylinder transition was not observed.[32] A recent study by Pugh *et al*. has shown that the copolymers synthesized from a mixture of LLA and 2-bromo-3-hydroxypropionic acid (BA) were amorphous as analyzed using DSC, when more than 5% BA was incorporated in the resultant copolymers.[33] This result may also indicate that the P(LLA-*co*-MAC) copolymer with 10% MAC incorporated was not crystalline enough to induce a CDSA to prepare well-defined cylindrical micelles.

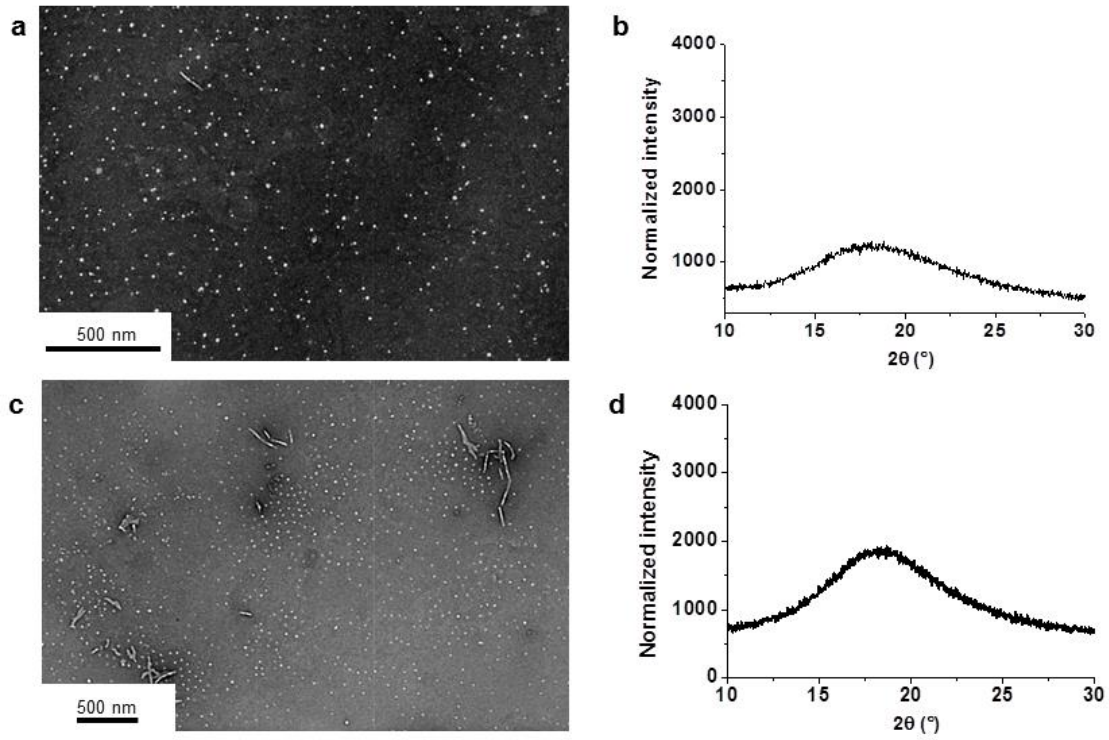

Figure 5.6. TEM images showing the resulting morphologies and WAXD diffractograms showing the amorphous nature of the nanoparticles obtained from the CDSA of P(LLA-*co*-MAC)-*b*-PTHPA diblock copolymer, **2**, at 65 °C (a and b) or 55 °C (c and d). TEM samples were prepared by slow drying and negatively stained by PTA. Scale bar = 500 nm.

Therefore, in attempt to improve the crystallization ability of the PLLA copolymer domain, a lower molar fraction of MAC (*ca.* 5%) was incorporated in the precursor diblock copolymer, **3**, which once again was chain-extended using RAFT to yield $P(LLA_{0.95}\text{-}co\text{-}MAC_{0.05})_{41}\text{-}b\text{-}PTHPA_{232,}$ **4** (Table 5.1). After exposure to the identical CDSA conditions (20 mg/mL, v_{THF}/v_{H2O} = 20/80, evaporation of THF, 1 *eq*. to each PHTPA block) at 55 °C for 30 h, diblock copolymer, **4**, yielded more cylindrical micelles than observed under identical conditions using **2**, however, there were still a large number of spherical micelles visible in the TEM analysis (Figure 5.7c). Although the WAXD

diffractogram indicated that the system was indeed crystalline (Figure 5.7d), a pure phase of cylindrical micelles could not be achieved. Several CDSA experiments with varied ratios of THF and water (v_{THF}/v_{H2O} = 10/90 and 30/70) were also performed, but spherical micelles were always observed to co-exist with cylindrical micelles by TEM (Figure 5.7a and 5.7e).

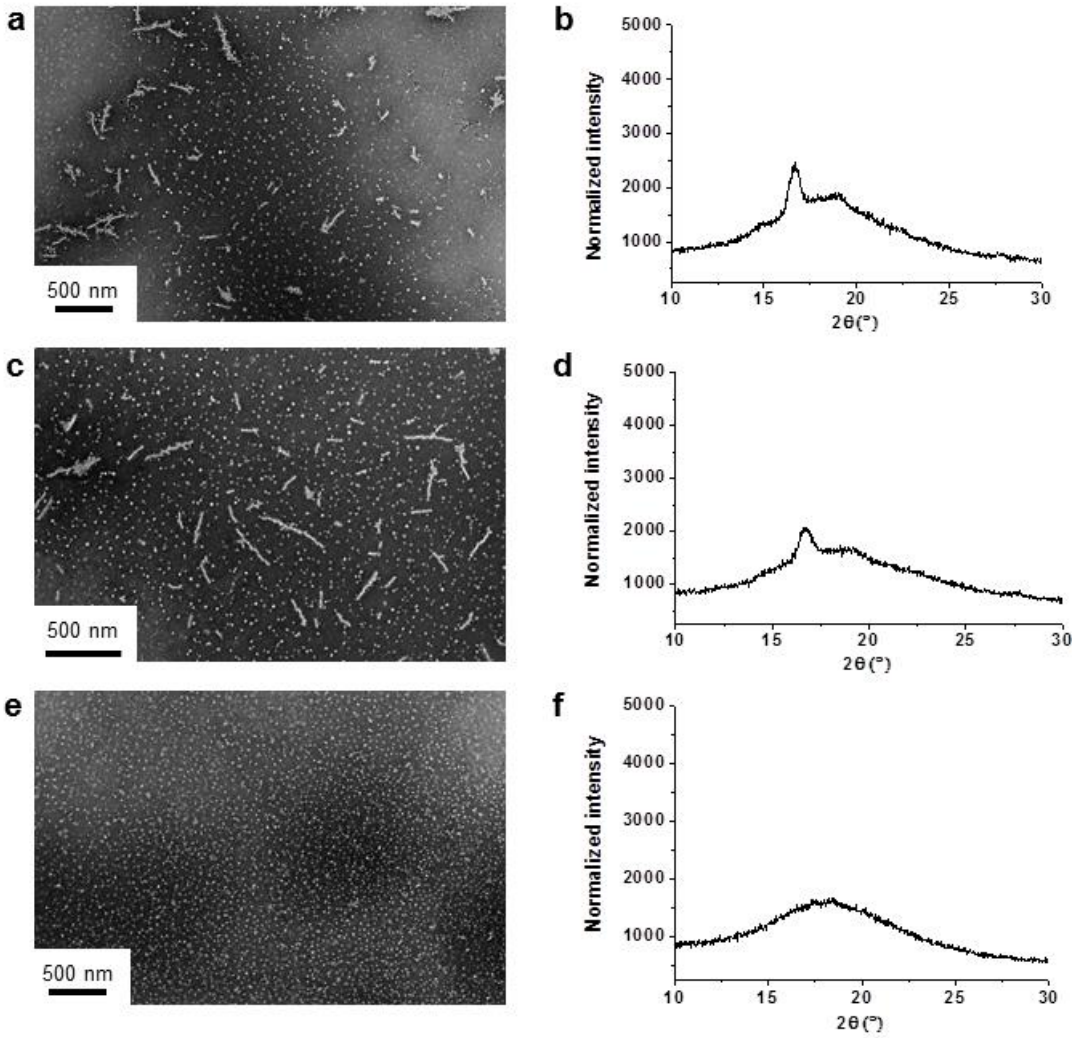

Figure 5.7. TEM images showing the nanostructures obtained from the CDSA of P(LLA-*co*-MAC)-*b*-PTHPA diblock copolymer, **4**, and WAXD diffractograms showing the crystalline/amorphous nature of these nanostructures at varied ratios of THF and H_2O (a and b : v_{THF}/v_{H2O} = 10/90, c and d : v_{THF}/v_{H2O} = 20/80, e and f : v_{THF}/v_{H2O} = 30/70). TEM samples were prepared by slow drying and negatively stained by PTA. Scale bar = 500 nm.

It seems that even 5% incorporation of MAC in the PLLA block was enough to affect the crystallization process of the spherical micelles formed at the beginning of CDSA procedure and hence these spherical micelles failed to transit into cylindrical micelles. Therefore, we decided to synthesize a diblock core block, PLLA-*b*-PMAC, so that the crystallization ability of PLLA would be guaranteed while also introducing functional handles into a second outer core domain of the resultant cylindrical micelles.

5.3.4 Synthesis of PLLA-*b*-PMAC-*b*-PTHPA triblock copolymer, 6

The synthesis of the PLLA-*b*-PMAC-*b*-PTHPA triblock copolymer is outlined in Scheme 5.2. Firstly, ROP of MAC was carried out using the thiourea (10 mol%) and (-)-sparteine (5 mol%) co-catalyst system from the dual-headed initiator in $CDCl_3$. The targeted degree of polymerization (DP) of PMAC was 4 and after 1 h, the conversion of the MAC monomer had reached 92% as confirmed by ^{1}H NMR spectroscopy (Figure 5.8). A solution of LLA in $CDCl_3$ was then added to the crude PMAC solution with a further addition of thiourea (5 mol%) and (-)-sparteine (2.5 mol%) co-catalyst for the ROP of LLA. After 3 h, the conversion of the LLA monomer reached 90% as confirmed by ^{1}H NMR spectroscopy and the polymerization was stopped. ^{1}H NMR spectroscopic analysis confirmed the successful synthesis of PMAC-*b*-PLLA diblock copolymer, **5** with the methylene resonance of the PMAC backbone observed at δ = 4.45 - 4.22 ppm and the methine resonance of the PLLA repeat units observed at δ = 5.36 - 4.96 ppm (Figure 5.9). SEC analysis showed a narrow dispersity for the PLLA-*b*-PMAC diblock copolymer ($Đ_M$ = 1.08, Figure 5.11).

PLLA-*b*-PMAC diblock copolymer, **5**, possessed a similar T_g with that of P(LLA-*co*-PMAC) random copolymer, **1**, at 38 °C but a higher T_m at 141 °C as determined by DSC analysis.

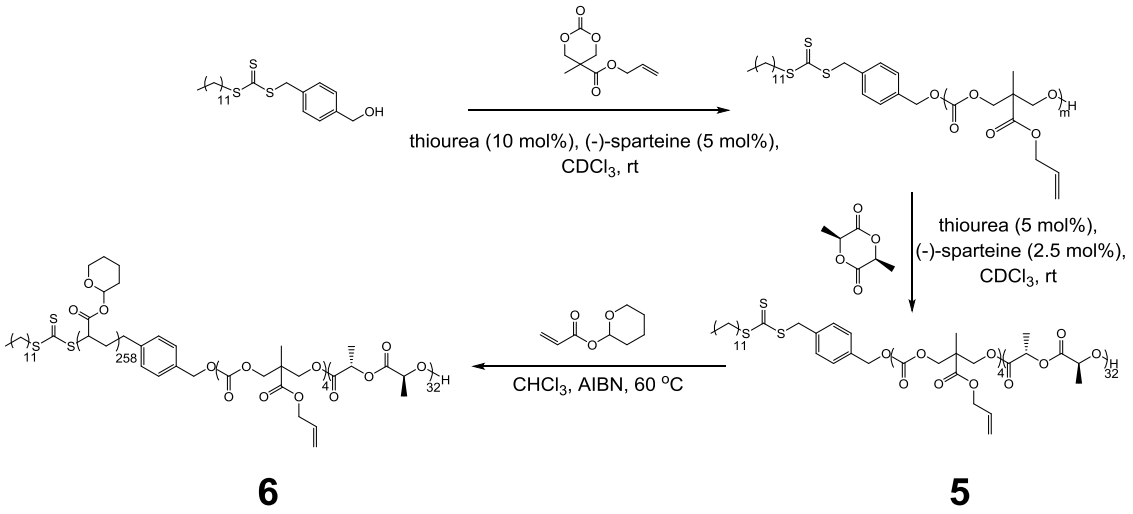

Scheme 5.2 Synthetic procedures of PLLA-*b*-PMAC-*b*-PTHPA triblock copolymer, **6**.

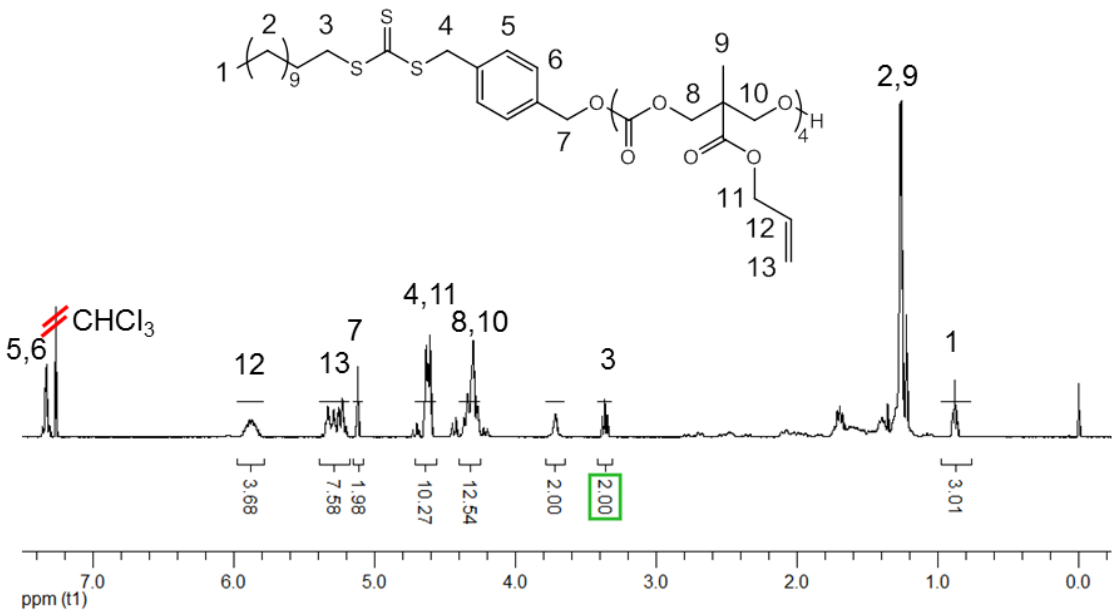

Figure 5.8. ^{1}H NMR spectrum (400 MHz, $CDCl_3$) of unpurified PMAC homopolymer.

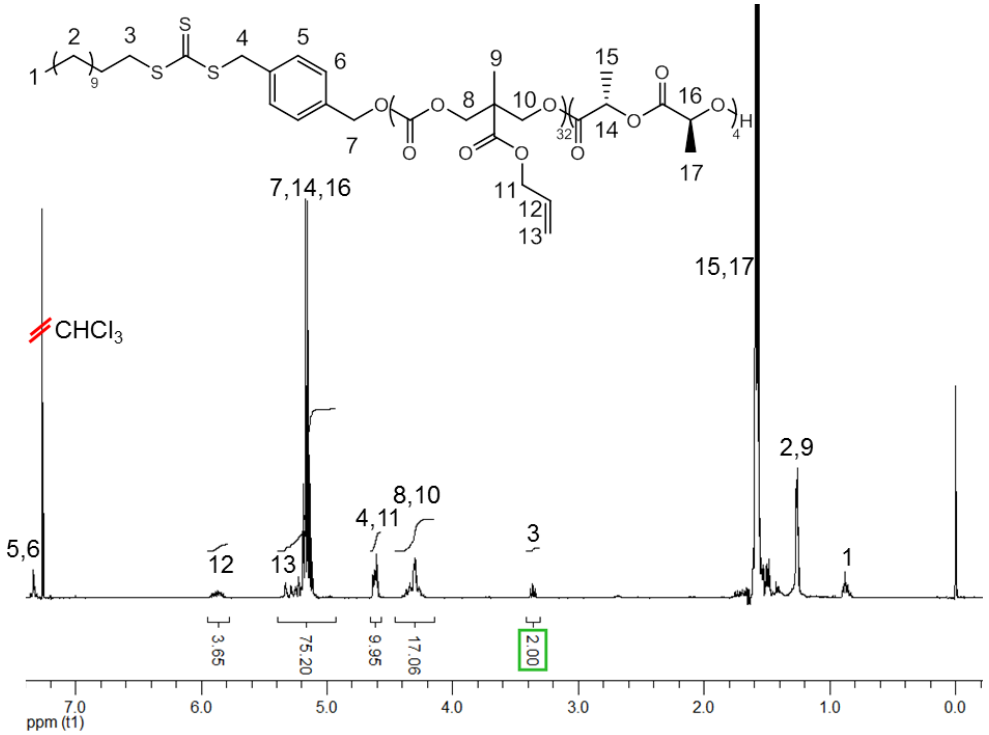

Figure 5.9. ^{1}H NMR spectrum (400 MHz, $CDCl_3$) of PLLA-*b*-PMAC diblock copolymer, **5**.

Table 5.2. Characterization data of PLLA-*b*-PMAC diblock copolymer, **5**, and PLLA-*b*-PMAC-*b*-PTHPA triblock copolymer, **6**

Polymer	M_n **(kDa)**[a]	$Đ_M$[b]	T_g **(°C)**[c]
$PLLA_{32}$-*b*-$PMAC_4$, **5**	5.8	1.07	38
$PLLA_{32}$-*b*-$PMAC_4$-*b*-$PTHPA_{258}$, **6**	46.1	1.27	–

[a] Measured by ^{1}H NMR spectroscopy (400 MHz, $CDCl_3$). [b] Measured by SEC analysis ($CHCl_3$ with 0.5% TEA as eluent). [c] Measured by DSC analysis.

The PTHPA block was then grown from the PLLA-*b*-PMAC macro-initiator, **5**, using RAFT polymerization as previously described (Scheme 5.2). ^{1}H NMR spectroscopic analysis indicated the successful synthesis of $PLLA_{32}$-*b*-$PMAC_4$-*b*-$PTHPA_{258}$ triblock copolymer, **6**, with the broad methine resonance of the

tetrahydropyranyl protecting groups of the PTHPA repeat units at δ = 6.20 - 5.70 ppm (Figure 5.10). The triblock copolymer was designed with a DP of PLLA of 32 and a hydrophobic weight fraction of 22.5% in order to access well-defined cylindrical nanostructures based on the results presented in Chapter 2. SEC analysis revealed the narrow dispersity of the triblock copolymer ($Đ_M$ = 1.27) and successful chain-extension from PLLA-*b*-PMAC macro-initiator, **5** (Figure 5.11, Table 5.2).

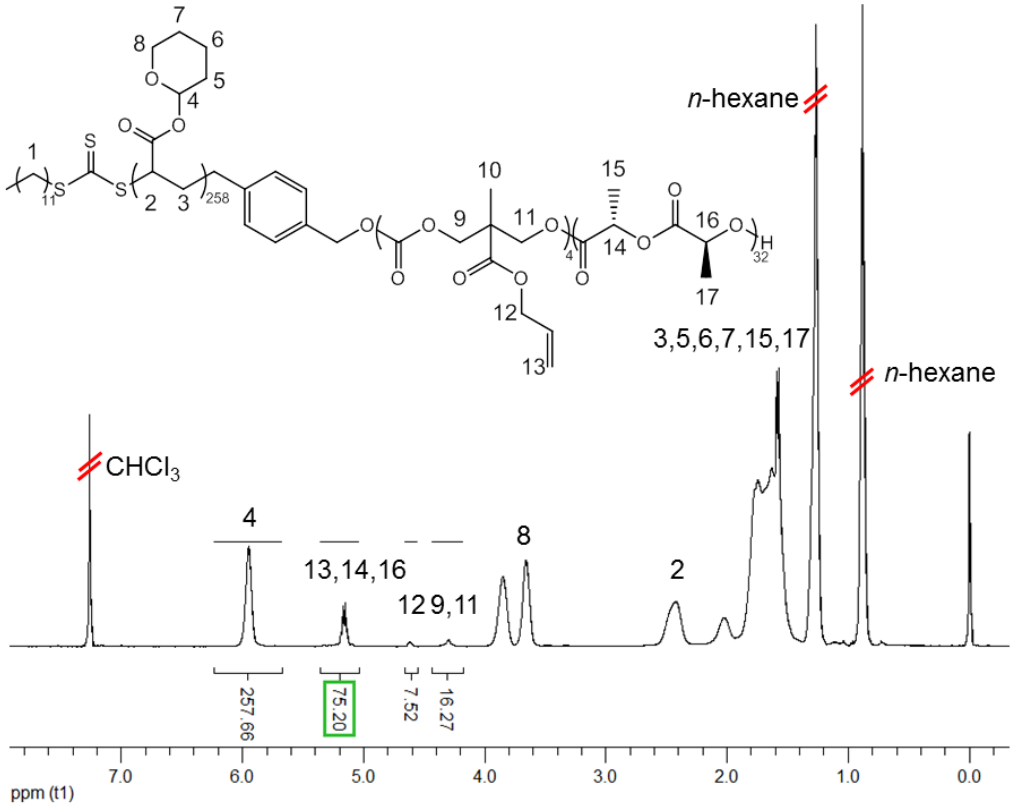

Figure 5.10. ^{1}H NMR spectrum (400 MHz, $CDCl_3$) of PLLA-*b*-PMAC-*b*-PTHPA triblock copolymer, **6**.

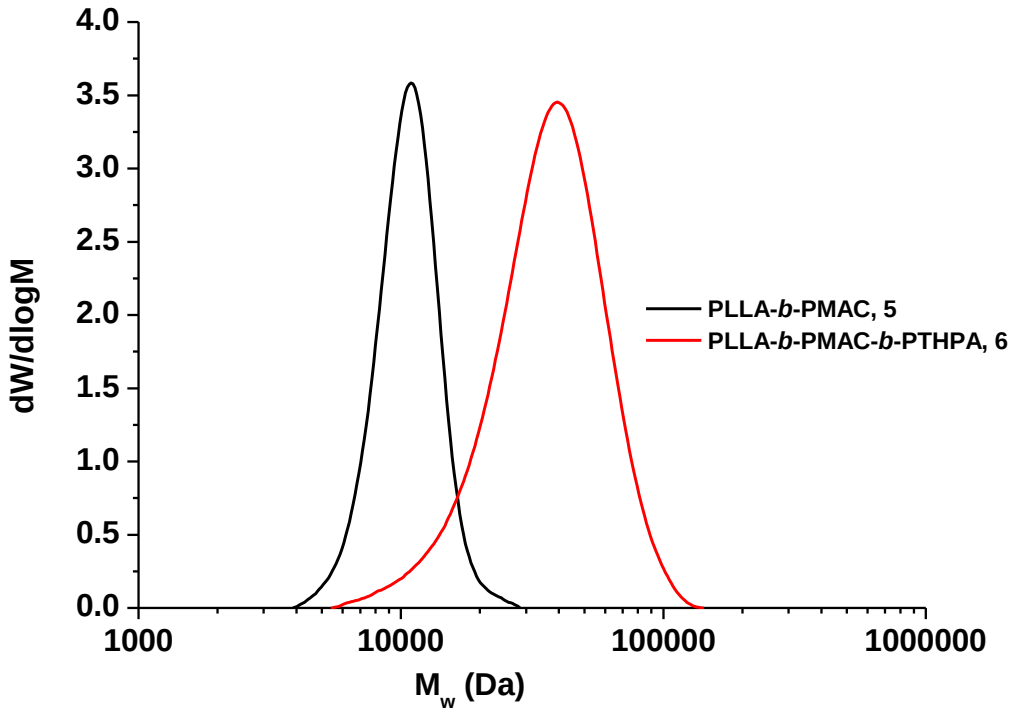

Figure 5.11. SEC chromatograms ($CHCl_3$ with 0.5% TEA as eluent, RI detection) of PLLA-*b*-PMAC diblock copolymer, **5** and PLLA-*b*-PMAC-*b*-PTHPA triblock copolymer, **6**.

5.3.5 Crystallization-driven self-assembly of PLLA-*b*-PMAC-*b*-PTHPA triblock copolymer, 6

The CDSA of the PLLA-*b*-PMAC-*b*-PTHPA triblock copolymer, **6**, was performed using the identical conditions described above with 20% THF at 55 °C. After 30 h, well-defined PLLA-*b*-PMAC-*b*-PAA cylindrical micelles, **7**, were obtained as confirmed by TEM analysis (L_n = 221 nm, L_w/L_n = 1.17, W_n = 52 ± 5 nm, Figure 5.12). DLS analysis showed only one size population of the assemblies (Figure 5.13). An intense crystalline Bragg peak at a 2θ value of

16.6° was observed in the WAXD diffractogram (Figure 5.14), indicating the crystalline core nature of these nanoparticles.

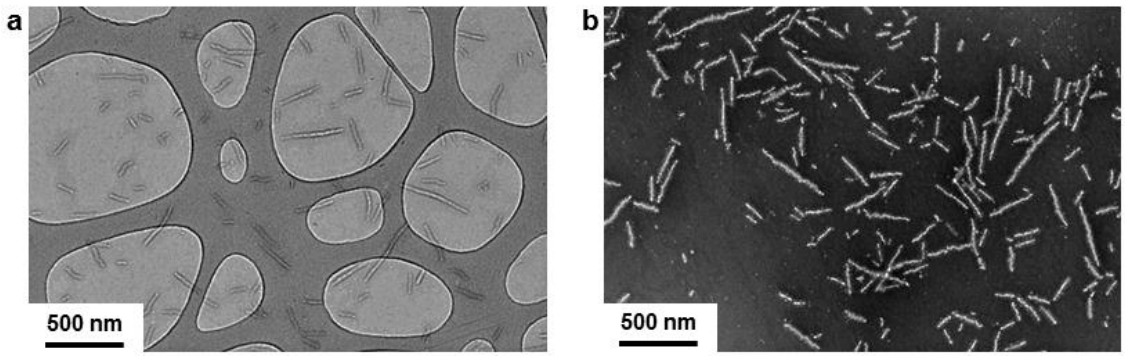

Figure 5.12. TEM images showing the PLLA-*b*-PMAC-*b*-PAA cylindrical micelles, **7**. a, prepared by a slow drying method on GO grid;[34] b, prepared by a slow drying method followed by negative staining using PTA. Scale bar = 500 nm.

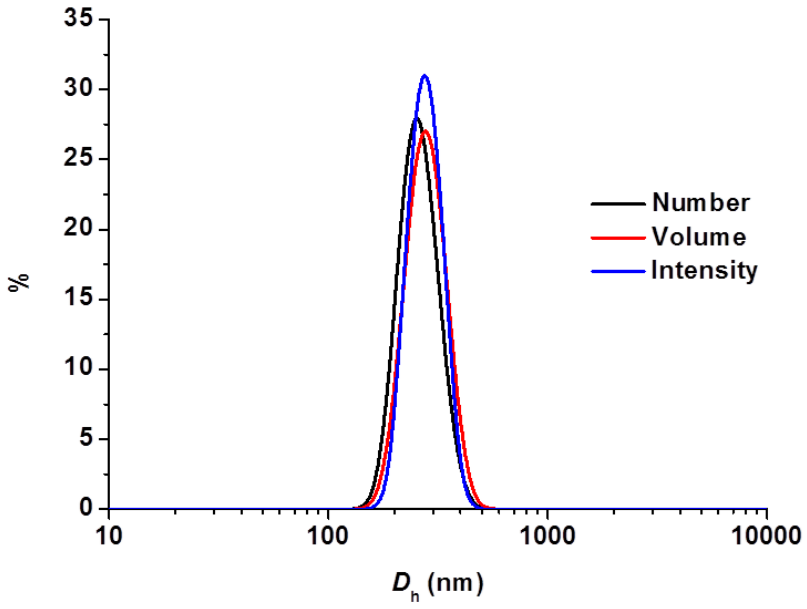

Figure 5.13. DLS data showing the distribution of PLLA-*b*-PMAC-*b*-PAA cylindrical micelles, **7** ($D_{h,\,av}$ = 268 nm, PD = 0.038).

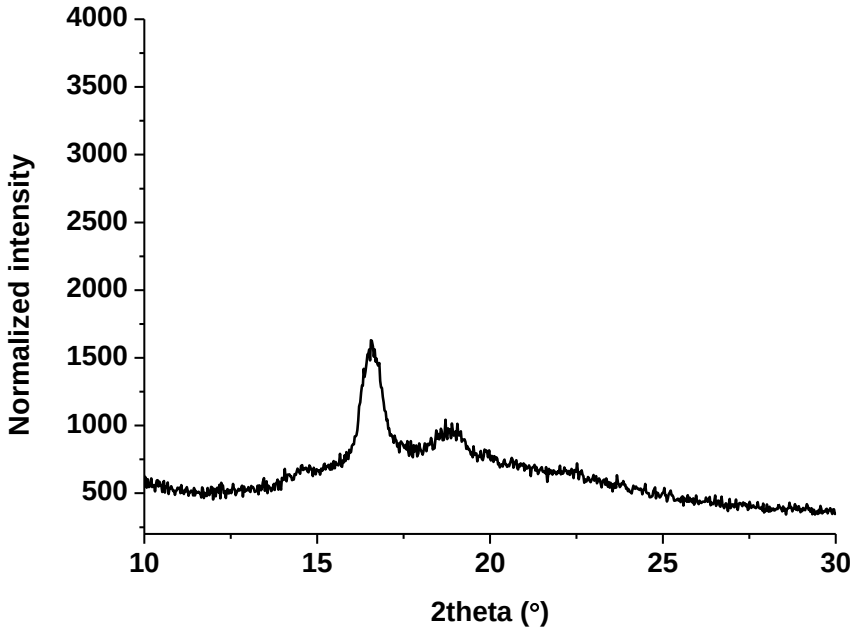

Figure 5.14. WAXD diffractogram showing the crystalline nature of the PLLA-*b*-PMAC-*b*-PAA cylindrical micelles, **7**.

5.3.6 Core functionalization of PLLA-*b*-PMAC-*b*-PAA cylindrical micelles, 7, using photo-initiated thiol-ene radical reactions

In order to show that the PLLA-*b*-PMAC-*b*-PAA triblock cylindrical micelles, **7**, can be functionalized with small molecules, benzyl mercaptan was "clicked" onto the allyl groups of PMAC in the self-assembled cylindrical nanoparticles using photo-initiated thiol-ene radical reactions[15] under a range of different conditions (Table 5.3).

Table 5.3. Functionalization of PLLA-*b*-PMAC-*b*-PAA cylindrical micelles, **7**, with benzyl mercaptan under different conditions using photo-initiated thiol-ene radical reactions

Concentration of cylindrical micelles in H_2O (mg/mL)	Solvent	Benzyl mercaptan (*eq*.)	UV initiator (*eq*.)	Functionalization ratio (%)[a]
3	—	10	2	74
3	THF	10	2	73
3	1,4-dioxane	10	2	74
3	THF	15	5	76
1.5	THF	10	2	55

[a]Measured by ^{1}H NMR spectroscopy (400 MHz, d_6-DMSO).

Generally, a mixture of an aqueous solution of cylindrical micelles (3 mg/mL), benzyl mercaptan (10 *eq*. to each allyl group) and 2-benzyl-2-(dimethylamino)-4'-morpholinobutyrophenone UV initiator (2 *eq*. to each allyl group) was exposed to UV irradiation for 1 h. The solution was then dialyzed against 2% 1,4-dioxane in water (resistivity 18.2 MΩ•cm) overnight and then H_2O for 2 days before subsequent lyophilization. For ^{1}H NMR spectroscopic analysis, the freeze-dried nanoparticles were further dissolved in DMSO and precipitated in diethyl ether three times to completely remove traces of unreacted thiol (note that the nanoparticles were disassembled into unimers in DMSO and therefore this step was avoided in the preparation of TEM samples in order to enable the study of their nanostructures). The disassembled polymers were then dissolved in d_6-DMSO for the ^{1}H NMR spectroscopic analysis to calculate the functionalization ratio. As can be seen in Figure 5.15 and Table 5.3, a functionalization ratio of 74% was obtained with the characteristic aromatic resonance of benzyl mercaptan observed at δ = 7.33 - 7.14 ppm. To make

benzyl mercaptan and the UV initiator more accessible to the core of the cylindrical micelles to realize a higher functionalization ratio, a small amount of THF or 1,4-dioxane (0.2 mL) was added into the mixture (Table 5.3), however, no obvious improvement in functionalization degree was observed in these experiments. A further increase of the amount of benzyl mercaptan (15 *eq*. to each allyl group) and UV initiator (5 *eq*. to each allyl group) failed to further improve the functionalization ratio significantly. It is proposed that some allyl groups can be physically trapped in the crystalline PLLA core of the cylindrical micelles during CDSA and therefore it is difficult to completely functionalize all of the allyl groups. In comparison, the unassembled PLLA-*b*-PMAC-*b*-PAA triblock copolymer can be easily modified with benzyl mercaptan to realize a full functionalization ratio using the photo-initiated thiol-ene radical reaction in 1,4-dioxane with 10 *eq*. of benzyl mercaptan and 0.5 *eq*. of UV initiator being used (Figure 5.16). This further proved our hypothesis that the allyl groups of PMAC in the cylindrical nanoparticles were physically inaccessible. TEM analysis confirmed that the PLLA-*b*-PMAC-*b*-PAA cylindrical micelles, **7**, did not change their size or morphology after functionalization with benzyl mercaptan (Figure 5.17) and the dimensions remained nearly the same (L_n = 217 nm, L_w/L_n = 1.12, W_n = 55 ± 7 nm).

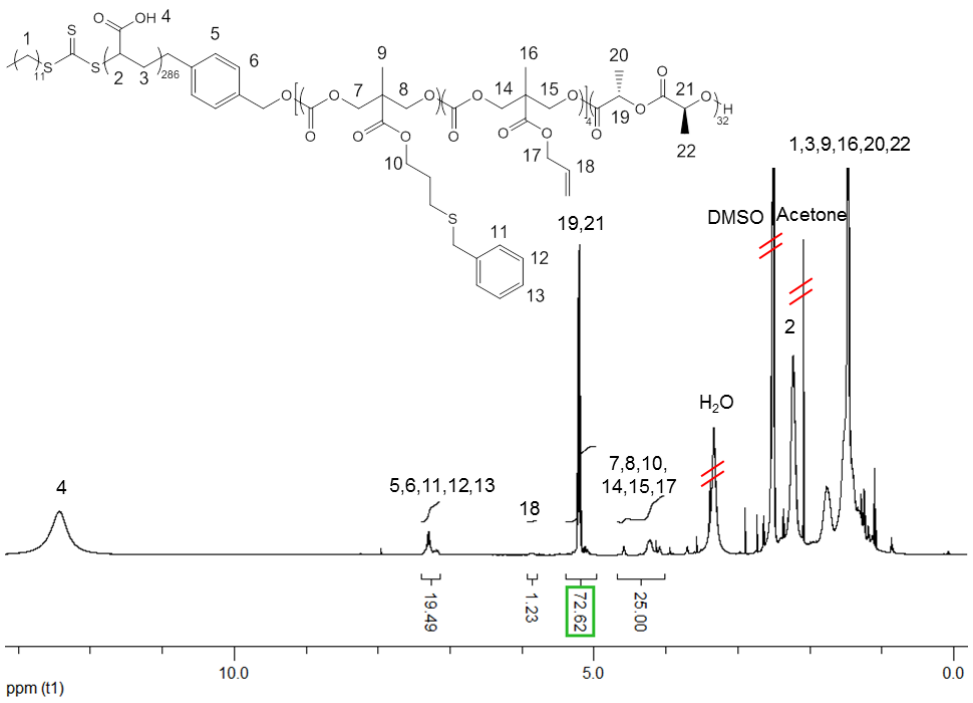

Figure 5.15. ^{1}H NMR spectrum (500 MHz, d_6-DMSO) of functionalized PLLA-*b*-PMAC-*b*-PAA cylindrical micelles, **7**.

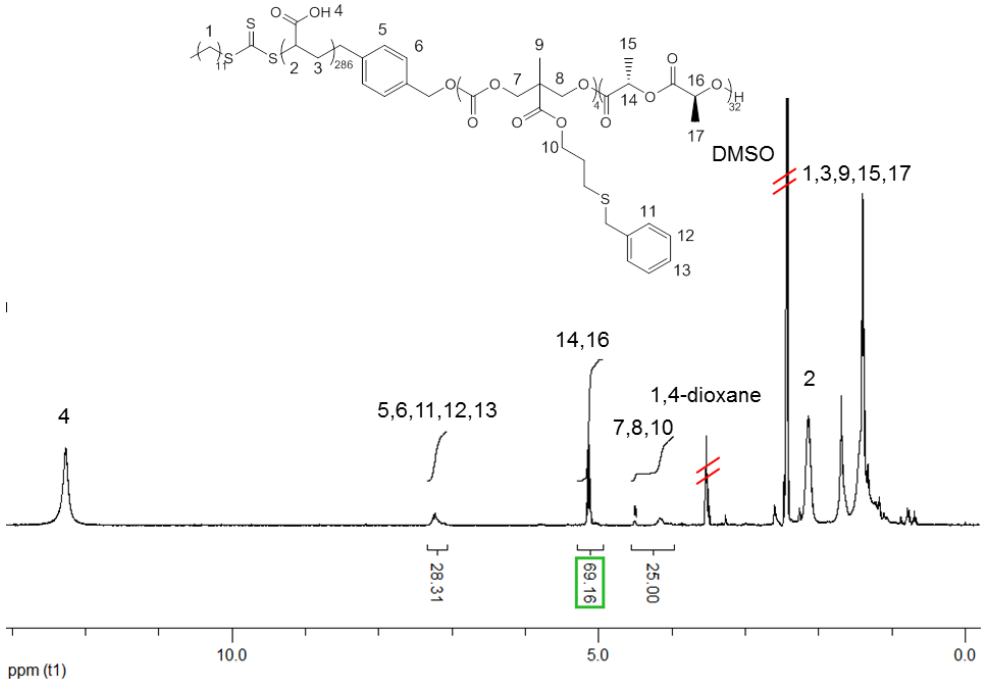

Figure 5.16. ^{1}H NMR spectrum (400 MHz, d_6-DMSO) of functionalized PLLA-*b*-PMAC-*b*-PAA triblock copolymers.

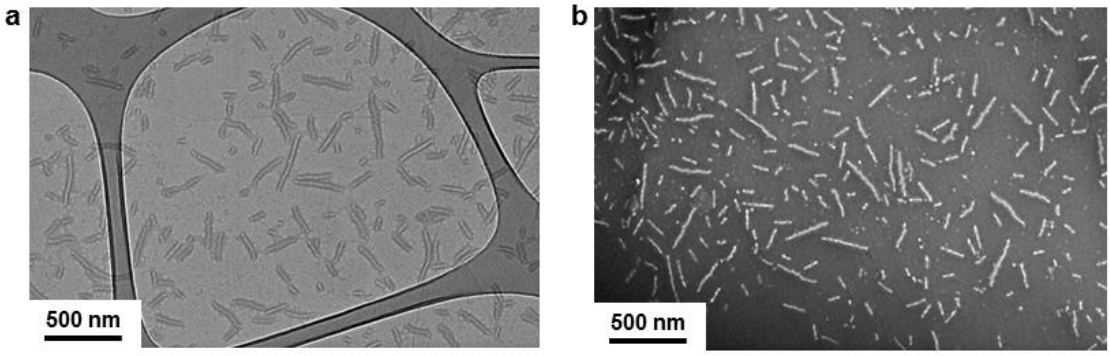

Figure 5.17. TEM image showing the unchanged morphologies of PLLA-*b*-PMAC-*b*-PAA cylindrical micelles, **7**, after functionalization with benzyl mercaptan. a, prepared by a slow drying method on GO grid; b, prepared by a slow drying method followed by negative staining using PTA. Scale bar = 500 nm.

5.4 Conclusions

In summary, we have successfully copolymerized LLA with an allyl functional cyclic carbonate monomer (MAC) to incorporate reactive handles in the core domain of the resultant self-assembled nanostructures. The amphiphilic copolymer which consists of a random structured LLA and MAC core block failed to give a pure phase of cylindrical micelles as the incorporation of MAC disrupted the crystallization of the PLLA polymer chains and affected the CDSA process. In comparison, the amphiphilic copolymer which consists of a diblock PLLA-*b*-PMAC core yielded well-defined cylindrical micelles. By using photo-initiated thiol-ene radical reactions, benzyl mercaptan was “clicked” onto the allyl groups of PMAC in the self-assembled PLLA-*b*-PMAC-*b*-PAA cylindrical micelles with a high functionalization ratio.

5.5 Experimental section

5.5.1 Materials

Chemicals and solvents were used as purchased from Aldrich, Acros, Fluka, Fisher Chemical, Alfa Aesar or VWR. LLA monomer was kindly donated by Corbion-Purac and was passed through a silica plug with dichloromethane (DCM) as eluent to remove impurities and then dried over 3Å molecular sieves in DCM. LLA monomer was further purified by recrystallization in toluene before being stored in a glove box under an inert atmosphere. (-)-Sparteine was dried over CaH_2 before use and 1-(3,5-bis(trifluoromethyl)phenyl)-3-cyclohexyl-thiourea was prepared and purified as reported.[35] Tetrahydropyran acrylate (THPA) was synthesized and purified as described previously.[36] MAC monomer was synthesized as reported[25] and was dried over 3Å molecular sieves in DCM. 2,2-Azobis(isobutyronitrile) (AIBN) was recrystallized from methanol and stored at 4 °C.

5.5.2 Instrumentation

^{1}H nuclear magnetic resonance (^{1}H NMR) spectra were recorded on a Bruker spectrometer operating at a frequency of 400 MHz in $CDCl_3$ (unless stated otherwise). The chemical shifts are given in ppm with tetramethylsilane (TMS) as an internal reference. Size exclusion chromatography (SEC) was performed on an Agilent 1260 Infinity Multi-Detector SEC instrument equipped with refractive index and UV detectors with $CHCl_3$ and 0.5% triethylamine as eluent at a flow rate of 1 mL/min. SEC data was calibrated by Cirrus GPC software with PS or PMMA standards.

Differential scanning calorimetry (DSC) analysis was performed using a Mettler Toledo DSC1 star system. Samples were run at a heating or cooling ramp of 10 °C/min in triplicate in series under a nitrogen atmosphere in 40 µL aluminum crucibles. T_g and T_m of various samples were obtained in the first runs.

The stained transmission electron microscopy (TEM) images were obtained by using a JEOL 2000FX instrument operated at 200 kV. TEM samples were negatively stained by phosphotungstic acid (PTA, 2 wt%) on formvar/carbon grids (300 Mesh, Cu, Elektron Technology UK LTD). Typically, formvar/carbon grids were cleaned by air plasma from a glow-discharge system (2 min, 20 mA) which also improved the hydrophilicity of the grids. 20 µL of particle solution (0.25 mg/mL) was added onto the grid and the solution was blotted away after 2 min and then left to air-dry. 5 µL of a 2 wt% PTA solution was then added onto the grid to stain the particles and was blotted away after 30 s before air-drying.

TEM images on graphene oxide (GO) support were also obtained using a JEOL 2000FX instrument operated at 200 kV. Generally, one drop of the sample solution (20 µL) was added onto a GO grid and after 2 min, the solution was blotted away before drying totally. The GO grids were prepared as follows: lacey carbon grids (400 Mesh, Cu, Elektron Technology UK LTD) were cleaned by air plasma from a glow-discharge system (2 min, 20 mA) to improve the hydrophilicity of the lacey carbon. One drop of GO solution (0.10 - 0.15 mg/mL) was deposited on each grid and left to air-dry totally.

The hydrodynamic diameter (D_h) of different nanoparticles was determined by dynamic light scattering (DLS). Typically, scattering of a 0.25 mg/mL aqueous nanoparticle solution was measured in a Malvern Zetasizer NanoS instrument

equipped with a 4 mW He-Ne 633 nm laser module at 25 °C. Measurements were carried out at a detection angle of 173° (back scattering) and the data was further analyzed by Malvern DTS 6.20 software. D_h was calculated by fitting the apparent diffusion coefficient in the Stokes-Einstein equation $D_h = kT/(3\pi\eta D_{app})$, where k is the Boltzmann constant, T is the temperature and η is the viscosity of the solvent. D_h only coincides to the real hydrodynamic diameter when the measured sample is a solution of monodispersed spherical particles as D_{app} equals the translational diffusion (D_t). For cylindrical particles, owing to their anisotropy, the rotational diffusion is not negligible and contributes to the D_{app}. Therefore, the D_h measured for the cylindrical micelles only has a relative value and provides polydispersity information to detect multiple populations.

WAXD was performed on a Panalytical X'Pert Pro MPD equipped with a CuKα_1 hybrid monochromator as the incident beam optics. Generally, *ca*. 30 mg of self-assembled freeze-dried particles were placed in a 10 mm sample holder, and standard "powder" 2θ - θ diffraction scans were carried out in the angular range from 2θ 10° to 30° at room temperature.

Photo-initiated thiol-ene radical reactions were carried out in a Metalight QX1 light box equipped with 12 x 9 W bulbs with a peak output at 365 nm for 1 h. Typically, samples were typically placed 10 cm away from the source with the bulbs arranged concentrically around them.

5.5.3 Synthesis of P(LLA-*co*-MAC), 1, using ROP

P(LLA-*co*-MAC), **1**, was synthesized in a glove box under nitrogen atmosphere by ROP from the dual-headed initiator, dodecyl 4-(hydroxymethyl) benzyl carbonotrithioate (Scheme 5.1). Generally, dual headed initiator (28.0 mg,

0.07 mmol) and (-)-sparteine (74.9 µL, 0.32 mmol) were combined in one vial with LLA (0.506 g, 3.51 mmol), MAC (0.576 g, 2.88 mmol) and 1-(3,5-bis(trifluoromethyl)phenyl)-3-cyclohexyl-thiourea (0.237 g, 0.64 mmol) in another vial. $CDCl_3$ (5.628 mL and 5 mL for each vial respectively) was then added to each of the vials before the two solutions were mixed and left to stir at room temperature for 4.5 h. Benzoic acid (5 mg) was added to the solution to stop the ROP. Product was precipitated in methanol three times before filtration and drying *in vacuo* to yield a pale yellow solid. ^{1}H NMR (400 MHz, $CDCl_3$, ppm, Figure 5.3) δ = 7.35 - 7.33 (4H, m, H5 & H6), 5.93 - 5.84 (2H, m, H17), 5.36 - 4.96 (2H PLLA + 1H PMAC + 2H, m, H8 & H10 & H16 & H7), 4.62 - 4.61 (2H + 2H PMAC, m, H4 & H15), 4.45 - 4.22 (4H PMAC, m, H12 & H14), 3.37 (2H, t, $^3J_{H\text{-}H}$ = 7.5 Hz, H3), 1.75 - 1.37 (6H PLLA + 2H, m, H9 & H11 & H2), 1.32 - 1.22 (3H PMAC + 18H, br, H13 & H1); $Đ_M$ (SEC, $CHCl_3$ with 0.5% TEA as eluent) = 1.08.

5.5.4 Synthesis of P(LLA-*co*-MAC)-*b*-PTHPA block copolymer, 2, using RAFT polymerization of THPA

Typically, THPA (1.5 g, 1600 *eq*.) and P(LLA-*co*-MAC) macro-initiator, **1** (52.9 mg, 1 *eq*.), were dissolved in $CHCl_3$ (1.5 mL) and transferred into a dried ampoule before adding AIBN (19.7 µL of a 5 mg/mL $CHCl_3$ solution). The solution was degassed by three freeze-pump-thaw cycles and sealed under argon and then placed in a 60 °C oil bath with stirring for 1.5 h. The product was precipitated into *n*-hexane before being reprecipitated using the same solvent system a further two times and dried *in vacuo* to give a yellow solid (29% conversion by ^{1}H NMR spectroscopy). ^{1}H NMR (400 MHz, $CDCl_3$, ppm, Figure

5.4) δ = 6.19 - 5.72 (1H PTHPA, br, H4), 5.36 - 5.00 (2H PLLA + 2H PMAC, m, H9 & H11 & H18), 4.67 - 4.59 (2H PMAC, m, H16), 4.49 - 4.28 (4H PMAC, m, H13 & H15), 4.00 - 3.50 (2H PTHPA, br, H8), 2.65 - 2.25 (1H PTHPA, br, H2), 2.21 - 1.39 (8H PTHPA + 6H PLLA, br, H3 & H5 & H6 & H7 & H10 & H12), 1.39 - 1.20 (18H + 3H PMAC, br, H1 & H14); $Đ_M$ (SEC, $CHCl_3$ with 0.5% TEA as eluent) = 1.31.

5.5.5 Crystallization-driven self-assembly of P(LLA-*co*-MAC)-*b*-PTHPA block copolymer, 2

The self-assembly of P(LLA-*co*-MAC)-*b*-PTHPA block copolymer, **2**, was performed by a solvent evaporation method. Typically, 0.5 mL of THF and 2 mL of water (v_{THF} : v_{H2O} = 20 : 80, unless otherwise stated) were added to 50 mg of polymer inside a vial. Acetic acid (1 *eq*. to each PTHPA block) was also added to the mixture to facilitate the hydrolysis of THPA. The vial was sealed with a needle inserted through the seal and the mixture was allowed to stir at 65 °C or 55 °C (above the T_g of PLLA)[37] for 30 h before being quenched by cooling in liquid nitrogen and subsequent lyophilization. The freeze-dried nanoparticles were then dissolved directly into water (0.25 mg/mL, resistivity 18.2 MΩ•cm) for TEM analysis.

5.5.6 Synthesis of PMAC homopolymer and PLLA-*b*-PMAC diblock copolymer, 5, using ROP

$PMAC_4$ was synthesized in a glove box under nitrogen atmosphere using ROP from the dual-headed initiator, dodecyl 4-(hydroxymethyl) benzyl carbonotrithioate (Scheme 5.2). Typically dual-headed initiator (39.9 mg,

0.1 mmol) and (-)-sparteine (4.7 µL, 0.02 mmol) were combined in one vial with MAC (80.0 mg, 0.4 mmol) and 1-(3,5-bis(trifluoromethyl)phenyl)-3-cyclohexyl-thiourea (14.8 mg, 0.04 mmol) in another. $CDCl_3$ (0.2 mL and 0.2 mL for each vial respectively) was then added to each of the vials before the two solutions were mixed and left to stir at room temperature for 1 h. Then, LLA (0.46 g, 3.2 mmol), thiourea (44.4 mg, 0.12 mmol) and (-)-sparteine (14.2 µL, 0.06 mmol) were dissolved in 4.2 mL of $CDCl_3$ and the solution was directly added to the crude PMAC solution. The polymerization was allowed to stir at room temperature for 3 h. Product was precipitated in *n*-hexane three times before filtration and drying *in vacuo* to yield a pale yellow solid. ^{1}H NMR (400 Hz, $CDCl_3$, ppm, Figure 5.9) δ = 7.36 - 7.31 (4H, m, H5 & H6), 5.93 - 5.81 (2H, m, H12), 5.36 - 4.98 (2H PLLA + 1H PMAC + 2H, m, H14 & H16 & H12 & H7), 4.63 - 4.60 (2H + 2H PMAC, m, H4 & H11), 4.40 - 4.22 (4H PMAC, m, H8 & H10), 3.36 (2H, t, $^3J_{H\text{-}H}$ = 7.5 Hz, H3), 1.75 - 1.41 (6H PLLA, H15 & H17), 1.35 - 1.19 (3H PMAC + 18H, br, H9 & H2); $Đ_M$ (SEC, $CHCl_3$ with 0.5% TEA as eluent) = 1.08.

5.5.7 Synthesis of PLLA-*b*-PMAC-*b*-PTHPA triblock copolymer, 6, using RAFT polymerization of THPA

Typically, THPA (2 g, 800 *eq*.) and PLLA-*b*-PMAC macro-initiator (93.1 mg, 1 *eq*.) were dissolved in $CHCl_3$ (2 mL) and transferred into a dried ampoule before adding AIBN (26.3 µL of a 10 mg/mL $CHCl_3$ solution). The solution was degassed by three freeze-pump-thaw cycles and sealed under argon and then placed in a 60 °C oil bath with stirring for 2.5 h. The product was precipitated into *n*-hexane three times and dried *in vacuo* to give a pale yellow solid (31%

conversion by ^{1}H NMR spectroscopy). ^{1}H NMR (400 MHz, $CDCl_3$, ppm, Figure 5.10) δ = 6.20 - 5.70 (1H PTHPA, br, H4), 5.35 - 5.00 (2H PLLA + 2H PMAC, m, H14 & H16 & H13), 4.67 - 4.56 (2H PMAC, m, H12), 4.43 - 4.18 (4H PMAC, m, H9 & H11), 4.10 - 3.56 (2H PTHPA, br, H8), 2.73 - 2.23 (1H PTHPA, br, H2), 2.21 - 1.39 (8H PTHPA + 6H PLLA, br, H3 & H5 & H6 & H7 & H15 & H17), 1.38 - 1.16 (18H + 3H PMAC, br, H1 & H10); $Đ_M$ (SEC, $CHCl_3$ with 0.5% TEA as eluent) = 1.27.

5.5.8 Crystallization-driven self-assembly of PLLA-*b*-PMAC-*b*-PTHPA triblock copolymer, 6

The self-assembly of PLLA-*b*-PMAC-*b*-PTHPA triblock copolymer, **6**, was performed by a solvent evaporation method. Typically, 0.5 mL of THF and 2 mL of water (v_{THF} : v_{H2O} = 20 : 80) were added to 50 mg of polymer inside a vial. Acetic acid (1 *eq*. to each PTHPA block) was also added to the mixture to facilitate the hydrolysis of THPA. The vial was sealed with a needle inserted through the seal and the mixture was allowed to stir at 55 °C for 30 h before being quenched by cooling in liquid nitrogen and subsequent lyophilization. The freeze-dried nanoparticles were then dissolved directly into water (0.25 mg/mL) for TEM and DLS analysis.

5.5.9 Functionalization of PLLA-*b*-PMAC-*b*-PAA cylindrical micelles, 7, using photo-initiated thiol-ene radical reactions

Generally, benzyl mercaptan and 2-benzyl-2-(dimethylamino)-4'-morpholinobutyrophenone UV initiator were directly added to an aqueous solution of PLLA-*b*-PMAC-*b*-PAA cylindrical micelles (3 mg/mL). 0.2 mL of THF

or 1,4-dioxane was then added into the mixture (or without any further addition of organic solvent according to Table 5.3). The mixture was allowed to stir at room temperature for 1 h before exposure to UV irradiation for 1 h. The mixture was then dialyzed against 2% 1,4-dioxane in water (resistivity 18.2 MΩ•cm) overnight and then H_2O for 2 days before subsequent lyophilization. The freeze-dried nanoparticles were directly dissolved in water (resistivity 18.2 MΩ•cm) for TEM analysis. For ^{1}H NMR spectroscopic analysis, the freeze-dried nanoparticles were dissolved in DMSO and precipitated in diethyl ether three times to completely remove unreacted thiols before being dried *in vacuo*. ^{1}H NMR (500 MHz, d_6-DMSO, ppm, Figure 5.15) δ = 13.6 - 11.2 (1H PAA, br, H4), 7.46 - 7.14 (5H benzyl mercaptan + 4H dual-headed initiator, m, H5 & H6 & H11 & H12 & H13), 5.93 - 5.79 (1H unfunctionalized PMAC, m, H18), 5.37 - 5.95 (2H PLLA, m, H19 & H21), 4.70 - 4.00 (6H PMAC, br, H7 & H8 & H10 & H14 & H15 & H17), 2.35 - 2.12 (1H PAA, br, H2), 1.94 - 1.08 (2H PAA + 6H PLLA + 3H PMAC + 18H dual-headed initiator, br, H1 & H3 & H9 & H16 & H20 & H22).

5.5.10 Functionalization of PLLA-*b*-PMAC-*b*-PAA triblock copolymers using photo-initiated thiol-ene radical reactions

Firstly, the precursor PLLA-*b*-PMAC-*b*-PTHPA triblock copolymer was added to a mixture of 1,4-dioxane and H_2O (2 mL and 0.5 mL respectively) with a further addition of acetic acid (3 *eq*. to each PTHPA block). The mixture was then sealed in a vial and heated at 65 °C to deprotect the PTHPA block. After 12 h, full deprotection was achieved as confirmed by ^{1}H NMR spectroscopy analysis. The mixture was precipitated in *n*-hexane before being reprecipitated using the

same solvent system a further two times and dried *in vacuo*. Benzyl mercaptan (10 *eq*. to each allyl group) and 2-benzyl-2-(dimethylamino)-4'-morpholinobutyrophenone UV initiator (0.5 *eq*. to each allyl group) were then added to PLLA-*b*-PMAC-*b*-PAA triblock copolymers (25 mg) in 1,4-dioxane (0.5 mL). The mixture was exposed to UV irradiation for 1 h before being precipitated in *n*-hexane three times and dried *in vacuo*. ^{1}H NMR (400 MHz, d_6-DMSO, ppm, Figure 5.16) δ = 12.7 - 11.7 (1H PAA, br, H4), 7.38 - 7.00 (5H benzyl mercaptan + 4H dual-headed initiator, m, H5 & H6 & H11 & H12 & H13), 5.27 - 4.95 (2H PLLA, m, H14 & H16), 4.60 - 3.95 (6H PMAC, br, H7 & H8 & H10), 2.31 - 2.01 (1H PAA, br, H2), 1.86 - 1.02 (2H PAA + 6H PLLA + 3H PMAC + 18H dual-headed initiator, br, H1 & H3 & H9 & H15 & H17).

5.6 References

(1) Sun, G.; Hagooly, A.; Xu, J.; Nyström, A. M.; Li, Z.; Rossin, R.; Moore, D. A.; Wooley, K. L.; Welch, M. J. *Biomacromolecules* **2008,** 9, 1997-2006.

(2) Robin, M. P.; Mabire, A. B.; Damborsky, J. C.; Thom, E. S.; Winzer-Serhan, U. H.; Raymond, J. E.; O'Reilly, R. K. *J. Am. Chem. Soc.* **2013,** 135, 9518-9524.

(3) Cotanda, P.; Lu, A.; Patterson, J. P.; Petzetakis, N.; O'Reilly, R. K. *Macromolecules* **2012,** 45, 2377-2384.

(4) Hansell, C. F.; O'Reilly, R. K. *ACS Macro Lett.* **2012,** 1, 896-901.

(5) Jia, Z.; Bobrin, V. A.; Truong, N. P.; Gillard, M.; Monteiro, M. J. *J. Am. Chem. Soc.* **2014,** 136, 5824-5827.

(6) O'Reilly, R. K.; Hawker, C. J.; Wooley, K. L. *Chem. Soc. Rev.* **2006,** 35, 1068-1083.

(7) Shi, M.; Wosnick, J. H.; Ho, K.; Keating, A.; Shoichet, M. S. *Angew. Chem. Int. Ed.* **2007,** 46, 6126-6131.

(8) Onbulak, S.; Tempelaar, S.; Pounder, R. J.; Gok, O.; Sanyal, R.; Dove, A. P.; Sanyal, A. *Macromolecules* **2012,** 45, 1715-1722.

(9) Tempelaar, S.; Mespouille, L.; Dubois, P.; Dove, A. P. *Macromolecules* **2011,** 44, 2084-2091.

(10) O'Reilly, R. K.; Joralemon, M. J.; Hawker, C. J.; Wooley, K. L. *Chem. Eur. J.* **2006,** 12, 6776-6786.

(11) Hansell, C. F.; Espeel, P.; Stamenović, M. M.; Barker, I. A.; Dove, A. P.; Du Prez, F. E.; O'Reilly, R. K. *J. Am. Chem. Soc.* **2011,** 133, 13828-13831.

(12) Hoyle, C. E.; Bowman, C. N. *Angew. Chem. Int. Ed.* **2010,** 49, 1540-1573.

(13) Geng, Y.; Discher, D. E.; Justynska, J.; Schlaad, H. *Angew. Chem. Int. Ed.* **2006,** 118, 7740-7743.

(14) Diehl, C.; Schlaad, H. *Macromol. Biosci.* **2009,** 9, 157-161.

(15) Chen, G.; Amajjahe, S.; Stenzel, M. H. *Chem. Commun.* **2009**, 1198-1200.

(16) Jonkheijm, P.; Weinrich, D.; Köhn, M.; Engelkamp, H.; Christianen, P. C. M.; Kuhlmann, J.; Maan, J. C.; Nüsse, D.; Schroeder, H.; Wacker, R.; Breinbauer, R.; Niemeyer, C. M.; Waldmann, H. *Angew. Chem. Int. Ed.* **2008,** 120, 4493-4496.

(17) Truong, V. X.; Barker, I. A.; Tan, M.; Mespouille, L.; Dubois, P.; Dove, A. P. *J. Mater. Chem. B* **2013,** 1, 221-229.

(18) Jeong, B.; Bae, Y. H.; Lee, D. S.; Kim, S. W. *Nature* **1997,** 388, 860-862.

(19) Tsuji, H. *Macromol. Biosci.* **2005,** 5, 569-597.

(20) Oh, J. K. *Soft Matter* **2011,** 7, 5096-5108.

(21) Albertsson, A.-C.; Varma, I. K. *Biomacromolecules* **2003,** 4, 1466-1486.

(22) Uhrich, K. E.; Cannizzaro, S. M.; Langer, R. S.; Shakesheff, K. M. *Chem. Rev.* **1999,** 99, 3181-3198.

(23) Gerhardt, W. W.; Noga, D. E.; Hardcastle, K. I.; García, A. J.; Collard, D. M.; Weck, M. *Biomacromolecules* **2006,** 7, 1735-1742.

(24) Chen, X.; McCarthy, S. P.; Gross, R. A. *Macromolecules* **1998,** 31, 662-668.

(25) Hu, X.; Chen, X.; Xie, Z.; Liu, S.; Jing, X. *J. Polym. Sci. A Polym. Chem.* **2007,** 45, 5518-5528.

(26) Tempelaar, S.; Mespouille, L.; Coulembier, O.; Dubois, P.; Dove, A. P. *Chem. Soc. Rev.* **2013,** 42, 1312-1336.

(27) Feng, J.; Zhuo, R. X.; Zhang, X. Z. *Prog. Polym. Sci.* **2012,** 37, 211-236.

(28) Petzetakis, N.; Dove, A. P.; O'Reilly, R. K. *Chem. Sci.* **2011,** 2, 955-960.

(29) Pitto-Barry, A.; Kirby, N.; Dove, A. P.; O'Reilly, R. K. *Polym. Chem.* **2014,** 5, 1427-1436.

(30) Liang, H.; Chen, S.; Chen, M.; Lee, P.; Chen, C.; Sung, H. *Bioconjugate Chem.* **2006,** 17, 291-299.

(31) Hu, X.; Chen, X.; Wei, J.; Liu, S.; Jing, X. *Macromol. Biosci.* **2009,** 9, 456-463.

(32) Petzetakis, N.; Walker, D.; Dove, A. P.; O'Reilly, R. K. *Soft Matter* **2012,** 8, 3408-3414.

(33) Wang, P. Stereopure functionalized poly(lactic acid). M.Sc., University of Akron, United States, **2013**.

(34) Patterson, J. P.; Sanchez, A. M.; Petzetakis, N.; Smart, T. P.; Epps, T. H.; Portman, I.; Wilson, N. R.; O'Reilly, R. K. *Soft Matter* **2012,** 8, 3322-3328.

(35) Pratt, R. C.; Lohmeijer, B. G. G.; Long, D. A.; Lundberg, P. N. P.; Dove, A. P.; Li, H. B.; Wade, C. G.; Waymouth, R. M.; Hedrick, J. L. *Macromolecules* **2006,** 39, 7863-7871.

(36) Hertler, W. R. *US Patent* **1991,** No. 5 072 029.

(37) Becker, J. M.; Pounder, R. J.; Dove, A. P. *Macromol. Rapid Commun.* **2010,** 31, 1923-1937.

General Conclusions and Outlook

In **Chapter 1** of this thesis, we have detailed several polymerization techniques especially RAFT polymerization and ROP which were widely used throughout this thesis to prepare polymers with good controls. Besides, CDSA which was the main concept and method to prepare various cylindrical nanoparticles in this thesis was specifically discussed.

In **Chapter 2,** we have explored the window to access PLLA-*b*-PAA cylindrical nanoparticles and expanded the window by 20% of hydrophobic weight fraction. And such a broad window to access PLLA-*b*-PAA cylindrical nanostructures has allowed us to prepare various PLA containing cylindrical nanoparticles in the following chapters. The successful change of dimensions of various PLLA-*b*-PAA cylindrical nanoparticles was also given by simply tuning the DP of PLLA and/or PAA based on CDSA approach. We have further discussed the relationship between PLLA core block and the crystallinity of resultant cylindrical nanoparticles.

In **Chapter 3**, we have studied the co-assembly of PLLA and PDLA containing diblock copolymers in an aqueous system. Interestingly, stereocomplex spheres instead of expected stereocomplex cylindrical morphologies were obtained when the two isomers were exposed to CDSA conditions. We have also observed an unexpected morphological transition from homochiral cylindrical micelles to stereocomplex spherical micelles which was proposed to follow a “unimer-exchange” mechanism. We think that this stereocomplexation-triggered reorganization may have potential applications in delivery or sensing.

In the following two chapters, we focused more on the applications of PLA containing polymers and nanoparticles. For example, **in Chapter 4**, we have

successfully labelled PLA containing polymers and nanoparticles using DTM or ABM fluorescent functional handles and compared their different fluorescent properties. Biocompatible PEGylated PLLA-*b*-PAA cylindrical micelles were also obtained which may have potential applications as bioimaging contrast agents.

In **Chapter 5**, we have successfully incorporated an allyl-functional cyclic carbonate monomer MAC in the PLLA core block of resultant nanoparticles. We noticed that a random P(LLA-*co*-MAC) core block was not crystalline enough to drive CDSA to realize cylindrical nanoparticles. In comparison, a PLLA-*b*-PMAC core block can successfully yield cylindrical nanoparticles. Benzyl mercaptan was then chemically attached to the cores of these cylindrical micelles using photo-initiated thiol-ene radical reactions with a good functionalization yield, illustrating their potential applications as delivery vehicles.

In the future, there are several points that could be improved. For example, although the cylindrical nanoparticles throughout this thesis have relatively narrow dispersities (L_w/L_n < 1.30), our group is currently working on the preparation of monodisperse cylinder system by growing unimers on the well-defined cylindrical seeds using CDSA. Also, we should explore other biocompatible coronal block of cylinders rather than PAA in the case of biomedical applications. Furthermore, subsequent *in vitro* or *in vivo* tests of fluorescent cylindrical nanoparticles described in **Chapter 4** are required to examine their biocompatibility. For **Chapter 5**, some other thiols including fluorescent dyes or model drugs are also needed to be “clicked” onto the core domains of cylindrical nanoparticles to show their potential applications as delivery vehicles.